Spectral Analysis of Embolic Signals

by

Ana Isabel Pereira Martins Leiria

Thesis submitted to the

University of Algarve

for the degree of

Doutor no ramo de Engenharia Electrónica e Computação, especialidade de Processamento de Sinal

Área Departamental de Engenharia Electrónica e de Computação

Faculdade de Ciências e Tecnologia

Universidade do Algarve

January 2005

RESUMO

Os parâmetros espectrais do sinal Doppler são usados na caracterização de fluxo sanguíneo. No caso particular do fluxo em artéria cerebral média, a caracterização pode incluir a detecção e classificação de embolias.

Para este efeito pretende-se estudar o desempenho de métodos de análise espectral, nomeadamente os que tenham demonstrado bons resultados quando aplicados a sinais Doppler em outras artérias. Para melhor quantificar o desempenho dos estimadores espectrais, é necessário conhecer à priori as características particulares do sinal, facto que se pretende como objectivo final deste estudo.

No sentido de disponibilizar sinais-referência para a análise do desempenho dos estimadores espectrais na detecção de embolias, foi desenvolvido um simulador de sinais de artéria cerebral média, com e sem embolias. Como entradas do simulador são utilizadas curvas médias extraídas de sinais clínicos, recorrendo a um algoritmo criado para o efeito, o *Sequential Phase Shift Averaging*. São também definidas pelo utilizador características dos êmbolos, tais como, velocidade, dimensão efectiva e potência devolvidas pela instrumentação ultra-sónica.

Durante este estudo considerou-se o fluxo sanguíneo caracterizado por quatro parâmetros espectrais: frequência máxima, frequência média, raiz quadrada de meia largura de banda, e, variação da potência ultra-sónica ao longo do tempo; este último como sendo o mais relevante para a identificação e diferenciação dos êmbolos.

Recorrendo aos sinais simulados, e, analisando os espectros dos sinais de fluxo sem embolias, verifica-se que a *Short Time Fourier Transform* estima melhor os parâmetros espectrais referidos do que a distribuição tempo-frequência de *Choi-Williams* ou o método paramétrico tempo-frequência de Covariância Modificada. A análise de espectros de sinais simulados de fluxo com embolias demonstra uma performance idêntica entre os métodos de análise temporal e a *Short Time Fourier Transform*, esta na versão em que o espectro do ciclo cardíaco é composto por elevada taxa de sobreposição de espectros de segmentos desse ciclo. Esta condicionante associada à constatação de que uma mesma embolia é captada distintamente consoante

o local do ciclo cardíaco em observação induziu a criação de uma nova representação espectral.

A representação proposta, de nome *Space-frequency representation*, permite a identificação visual da passagem do êmbolo pela janela de observação ultra-sónica. A pesquisa da existência do êmbolo é feita em função da velocidade sanguínea máxima instantânea, e a visualização da potência ultra-sónica por ele retornada é dimensionada adaptativamente de acordo com a relação espaço-frequência instantânea calculada. Esta metodologia permitirá introduzir vantagens significativas no diagnóstico clínico da circulação do fluxo sanguíneo em artéria cerebral média.

ABSTRACT

Doppler spectrum parameters are used to characterize blood flow. In the particular case of the middle cerebral artery, the characterization may include detection and classification of emboli.

To achieve so, study of the performance of spectral estimator methods, namely those that have produced good results when applied to Doppler signals belonging to other arteries, was deemed. For accurate quantification of the spectral estimators' performance, a priori knowledge of the signals characteristics is required, which in fact is the final goal of this work.

In order to produce reference-signals to enable analysis of the spectral estimators performance when detecting emboli, a middle cerebral artery signal simulator was developed, with the possibility of including emboli signals. The simulator considered as inputs the mean curves extracted from clinical signals. An algorithm specially developed to do so, the so-called, Sequential Phase Shift Algorithm, computed these mean curves. The simulator user should also specify emboli characteristics such as velocity, effective dimension and power backscattered by the ultrasound instrumentation.

During this study, blood flow was characterized by four spectral parameters: maximum frequency, mean frequency, root mean squared bandwidth, and, ultrasonic power variation over time; the latter being considered as the most relevant for identification and differentiation among emboli.

Making use of the simulated signals, and analysing the spectra of the signals without emboli, we may conclude that the Short Time Fourier Transform estimates the spectral parameters required for embolic analysis with more accuracy than the time-frequency distribution of Choi-Williams or the parametric time-frequency Modified Covariance method. Analysis of the spectra obtained from the simulated signals with emboli demonstrates that the time analysis methods perform similarly to the Short Time Fourier Transform, when the latter is used to compute the spectrum of the whole cardiac cycle by computation of highly superimposed spectra of segments of that cardiac cycle. This constraint, in association with the fact that the same embolus is backscattered

differently according to the place within the cardiac cycle under observation, lead to the development of a new spectral representation.

The proposed representation, named Space-frequency representation, enables the visual identification of the travelling embolus on the ultrasound window of observation. The search for the existence of an embolus is computed based on the instantaneous maximum blood flow velocity, and the visual representation of the backscattered power is adaptively dimensioned according to the instantaneous space-frequency relationship computed. This methodology enables significant improvement on the clinical diagnosis about blood flow in middle cerebral artery.

Ás minhas queridas avós
Natália, Tidi e Teresa

Mas quando alguém se lembrou
Querer mostrar-me, não me opus:
É fraca a luz que vos dou,
Mas afinal sempre é luz.

in *Este Livro que Vos Deixo…,* Volume I, de António Aleixo

ACKNOWLEDGMENTS

I would like to acknowledge

Universidade do Algarve, for the timely opportunity to conduct this work and for the leave of absence that made it possible;

PRODEP III (Programa de Desenvolvimento Educativo para Portugal), Medida 5, Acção 5.3;

CRUP/Treaty of Windsor for the financial support to the visits made, under the Acções Integradas Luso-Britânicas, to the Medical Physics Department of the Leicester University, UK;

the Medical Physics Department of the Leicester University, for the support of the work conducted there during my visits;

CYTED (Programa de Cooperación Científica y Tecnológica) for sponsoring RITUL (Rede Ibero-Americana de Tecnologias de Ultrasom) and the collaboration with several research groups with common goals;

UNESCO, for the financial support to MAGIAS (Métodos Avanzados de Generación de Imágenes Acústicas).

I would like to express my most sincere thanks

to Prof. Doutora Maria da Graça Ruano and Professor David H. Evans for their supervision, critical suggestions, advices, motivation and patience throughout the course of this work;

to Engª Margarida Madeira e Moura for her friendship, interest and support in all the phases of this work. Without her help it would have been very difficult to overcome some of the problems in the course of this work;

to Professor Wagner Coelho de Albuquerque and to Professor Eduardo Moreno for their most valuable advices and encouragement when I most needed it;

to my mother and my brothers José and Manuel for their constant support and love, and to my dearest nephews Manuel and Rita for their comprehension and patience;

to my father for his advices, his involvement and love.

CONTENTS

FIGURES

TABLES

ACRONYMS AND SYMBOLS

$a(m)$	Parameters of the AR model
$A(t)$	Amplitude of $x(t)$
$A(z)$	z transform of the AR branch of an ARMA model
$a^b(m)$	AR backward linear prediction coefficient
ACF	Autocorrelation function
ACS	Autocorrelation sequence
A_E	Amplitude of the signal of the embolus
$a^f(m)$	AR forward linear prediction coefficient
AR	Autoregressive
ARMA	Autoregressive moving average
ARMC	Autoregressive modified covariance
A_{vl}	Axial length of the sample volume
$B(f)$	Amplitude of the signal $X(f)$
$b(m)$	Parameters of the MA model
$B(z)$	z transform of the MA branch of an ARMA model
BCS_b	Backscattering cross-section of an erythrocyte
Bd	Rms half bandwidth
$b_f(t)$	Rms bandwidth function
$b_t(t)$	Bandwidth of time varying filter
c	Velocity of sound
$C(t,f)$	MGM straight line
CW	Continuous wave Doppler
CWD	Choi-Williams Distribution
$c_{xx}(\tau)$	Co-variance function of the process $x(t)$
$d(t,f)$	vertical distances between $\Gamma(t,f)$ and $C(t,f)$
DCWD	Discrete CWD

D_E	Duration of the ES
DFT	Discrete Fourier transform
E	Total energy
$e^b(n)$	Backward linear prediction error
ECG	Electrocardiogram
$e^f(n)$	Forward linear prediction error
E_N	Window power density
ES	Embolic Signal
f	Frequency index
f_d	Doppler frequency
f_E	Mean frequency of the ES
FFT	Fast Fourier transform
FIR	Finite impulse response
f_L	Low frequency for MGM
fm	Mean frequency
$f_m(t)$	Mean frequency function
$f_{MAX}(t)$	Measured maximum frequency function
f_n	Normalized frequency
f_r	Received frequency
f_s	Sampling frequency
f_t	Transmitted frequency
FT	Fourier transform
$h(t)$	Linear causal filter
$h(t,\varsigma)$	Time-varying filter
$H(z)$	z domain transfer function
H_{ae}	Haematocrit
hbr	Theoretical heart rate
k	Discrete frequency index
K_D	Predetermined part of the Doppler equation
$k_{\max}(t)$	Registered maximum frequency
L	Ratio between power of the embolus and power per unit of A_{vl}
M	CWD range for autocorrelation
MA	Moving average

MCA	Middle cerebral arteries
MEP	Measured embolic power
Mf	Maximum frequency
MGM	Modified geometric method
n	Discrete time index
N	Window length
N_c	Number of cardiac cycles
N_{hc}	Number of complete half cycles
n_{RI}	Refractive index
p	Number of poles of the ARMA model
$P(f)$	Power spectral density
$P(f,t)$	Power spectral density in time-frequency domain
$p(t)$	Power variation over time function
$P_{AR}(f,t)$	AR power spectrum
P_B	Power backscattered by blood
P_E	Power backscattered by the embolus
PFS	Pulse-foot-seeking algorithm
P_N	Power of noise
PRF	Pulse repetition frequency
PSA	Phase shift algorithm
PSD	Power spectrum density
pv	Power variation over time
PW	Pulse wave Doppler
q	Number of zeros of the ARMA model
r	Correlation coefficient
$R'_x(t,\tau)$	Generalized time-indexed autocorrelation function
$r'_{xx}(\tau)$	Autocorrelation temporal mean of the process $x(t)$
RF	Radio-frequency
$r_{gauss}(t)$	Random Gaussian variable function
rms	Root mean square
RMSE	Root mean square error
$r_n(t)$	White Gaussian noise signal
r_v	Radius of the vessel

$R_x(t,\tau)$	Instantaneous autocorrelation function
R_{xx}	Autocorrelation matrix
$r_{xx}(\tau)$	Autocorrelation of the process $x(t)$
$r_{xy}(\tau)$	Cross-correlation between the processes $x(t)$ and $y(t)$
s	Axial space
S_E	Effective axial length of the embolus
SF	Space-frequency
SF-DCWD	Space-Frequency Discrete Choi-Williams Distribution
SF-STFT	Space-frequency Short Time Fourier Transform
SF-STMC	Space-Frequency Short Time Modified Covariance
SNR	Signal to noise ratio
SPS	Sequential Phase Shift Averaging
STFT	Short Time Fourier Transform
STMC	Short Time Modified Covariance
SVL	Sample volume length
t	Continuous time index
T	Period
TCD	Transcranial Doppler
TFD	Time-frequency distribution
$t_g(f)$	Group delay
T_s	Sampling period
$u(t)$	Spectral parameter variation over time
$U(t)$	Deterministic component of $u(t)$
$u'(t)$	Random component of $u(t)$
$u_s(t)$	Spectral parameter variation over independent samples
v	Velocity
$v(t)$	ARMA input sequence
$V(t)$	Maximum velocity at time t
v_E	Velocity of the embolus
V_{HM}	Averaged diastolic velocity
V_m	Lowest maximum velocity in the signal
V_M	Highest maximum velocity in the signal
Vol_b	Volume of blood in a sample volume

Vol_c	Average volume of one erythrocyte
w	SF velocity weighting factor
$w(t)$	Window function
$w_E(t)$	Embolus amplitude weighting factor
WF	Wang and Fish simulator
WFA	Waveform main features averaging
W_{pack}	Packing factor
WSS	Wide sense stationary process
$X(f)$	Spectral representation of the signal $x(t)$
$x(t)$	Generic time domain discrete signal
$X(z)$	z transform of $x(n)$
$x^b(n)$	Backward linear prediction of $x(n)$
$x_b(t)$	Blood signal
$x_D(t)$	Direct flow in Doppler ultrasound signal
$x_e(t)$	Signal of the embolus
$x^f(n)$	Forward linear prediction of $x(n)$
$x_F(t)$	Phase component of $x_D(t)$
$x_I(t)$	Complex component of $x(t)$
$x_Q(t)$	Quadrature component of $x_D(t)$
$x_R(t)$	Real component of $x(t)$
$x_w(t)$	Windowed signal
$y_{AM}(t)$	Amplitude modulation function
$y_{FM}(t)$	Frequency modulation function
β_e	Adiabatic compressibility of erythrocytes
β_p	Adiabatic compressibility of plasma
$\Gamma(t,f)$	Integrated Doppler power spectrum
ΔE	Fractional energy
Δs	Axial space resolution
ΔT	Bounded time period
Δt	Time cell
$\Delta\omega$	Frequency cell
$\phi(\xi,\tau)$	TFD kernel function
θ_i	Ultrasound incidence angle

θ_r	Ultrasound reflection angle
θ_R	Ultrasound refraction angle
λ	Wavelength
μ_x	Mean value of the process $x(t)$
ξ	Frequency lag
ρ	Mean squared error
ρ^b	Mean squared backward linear prediction error
ρ_e	Density of blood
ρ^f	Mean squared forward linear prediction error
ρ_p	Density of plasma
σ	CWD scaling factor
σ_x	Standard deviation of the process $x(t)$
σ_x^2	Variance of the process $x(t)$
τ	Time lag
υ	Measure of the size of an aggregate scattering unit
$\varphi(t)$	Phase of the signal $x(t)$
$\Phi(t)$	Deterministic phase of the Doppler signal
Φ_{bs}	Backscattering coefficient of blood
$\psi(f)$	Phase of the signal $X(f)$
$\Psi(t,\tau)$	TFD autocorrelation domain kernel
ω	Angular frequency
ω	Angular frequency
$\omega_i(t)$	Instantaneous frequency

1 INTRODUCTION

1.1 MOTIVATION

Recent technological developments together with the emergence of new diseases incentive the association of engineering and medicine areas to synergistically search the solution of clinical problems. The work developed in these areas leads to methods of higher accuracy in diagnosis, and encourages research aiming the solution of new challenges. Developments that have occurred in Doppler ultrasound instrumentation are an example of the successful application of engineering in medical vascular diagnosis.

Clinical Doppler instrumentation and the corresponding mathematical models became particularly relevant tools, because they allow the use of non-invasive methods in the measurement of blood flow characteristics.

The study of blood flow has been an important area of research both in medicine and in engineering. This research field includes, among other goals, the detection, and characterization of emboli in the cerebral circulation. In particular, transcranial Doppler (TCD) ultrasound instrumentation provides the assessment of blood flow information from intracranial arteries, namely from middle cerebral arteries (MCA), where cerebral embolic events can be observed.

This issue is especially relevant because cardiovascular diseases are the major cause of mortality in Portugal, as well as in the rest of Europe. Ischemic stroke, predominantly due to cerebral embolism [Zuillen *et al.*, 1998], is one of the most important disorders, highly contributing to these statistics. The accurate detection and classification of emboli in brain blood circulation might help the prevention of such strokes.

Nowadays, many clinical and hospital units are provided with TCD instrumentation. These devices enable emboli detection, but still present some difficulties in identifying micro-emboli.

Correct characterisation of blood flow and cerebral emboli by TCD instrumentation depends on the precision obtained by the spectral estimation process. Most TCD equipment uses conventional spectral estimation methods based on the application of Short Time Fourier Transform (STFT). STFT present well identified limitations might lead to inaccurate quantitative measurements especially when small embolus detection is required.

Several published studies have reported the improvement in blood flow spectral estimation with methods other than the STFT. Most of these studies have used simulated Doppler ultrasound signals to test the alternative spectral estimators, and several arteries were analysed [Ruano, 1992] [Cardoso *et al*., 1996a] [Matos *et al.*, 2000] [Guo *et al*., 1994] [Leiria, 2000] [García-Nocetti *et al.*, 2001].

Detection and classification of embolic events in blood have been associated with time-domain processing and with time-frequency processing. The study and development of alternative estimators can help the choice of the best approach to process embolic signals (ES). Some studies on this subject can be found in [Fan, Evans, 1994], [Guetbi *et al*., 1997], [Girault *et al*., 2000], [Smith et al., 1996], [Smith et al., 1997], [Smith et al., 1998] and [Furui et al., 1999].

Although techniques allowing ultrasonic emboli detection and characterisation have been reported in the literature, these reports are scarce and do not convey a unique approach.

ESs are very complex and demand optimised methods and methodologies. The work hereby described envisages overcoming these issues and presents a structured approach to the assessment of blood flow, including, but not being restricted to, the detection and classification (characterisation) of emboli.

1.2 GOALS

The ultimate goal of this work is the improvement of emboli characterization in the MCA, when transcranial Doppler ultrasound instrumentation is employed. The strategy planned to reach this target includes three intermediate goals:

- The development of a MCA Doppler ultrasound signals simulator, with and without embolic occurrences. This will provide a reference signal for blood flow characterization through the analysis and development of spectral estimation methods;
- The statistical evaluation of time-frequency estimators. The simulated signals will be used as reference signals to enable the spectral estimators' assessment in terms of precision and accuracy of spectral parameters considered relevant for clinical diagnosis;
- Finally, the performance evaluation of the estimator previously identified when applied to real clinical signals; its ability to detect and classify emboli will be assessed.

1.3 THESIS OUTLINE

The research work developed is organized into eight chapters.

The present chapter provides a brief overview of the thesis outline and the motivation of these studies. The major contributions of this research work are also summarized on this chapter.

Chapter 2 reviews general issues related to the analysis of spectral ESs. This chapter includes a description of Doppler ultrasound instrumentation, anatomy and blood composition, mathematical characterization of Doppler ultrasound blood flow signals, and the state of art of embolic characterization and detection.

Accurate spectral representation of ESs requires knowledge of the appropriate spectral estimator to be applied to the blood signal when it is free of emboli in order to enable differentiating the spectral properties when emboli are present. Therefore, chapters 3 and 4 are concerned with embolic free blood flow signals and the description of the study dedicated to these spectra.

Chapter 3 describes the simulation of embolic free blood flow signals in MCA. The chapter starts by justifying the use of simulated signals, basing the justification on theoretical issues and revising the main Doppler signals simulated reported in the bibliography. The simulator adopted in the current work is then presented. Characterization of MCA signals' spectra and the description of the main spectral parameters and clinical indicators are described. An innovative algorithm for averaging Doppler blood flow parameters is reported on this chapter. The new algorithm was

developed based on two other existing methods (published in literature) but taking into account the MCA characteristics so that the averaging procedure could be obtained with better performance and considering other reference spectral parameters than the maximum frequency. Practical work is then reported, including the description of tests and results obtained when evaluating the modified averaging methods. Finally, the identification and description of the averaged parameters that will constitute the reference spectral parameters signals employed as inputs to the simulator are described, followed by the evaluation of the accuracy of the signals simulator.

Spectral analysis is addressed in Chapter 4. This chapter includes the description of the spectral estimators STFT, Choi-Williams Distribution (CWD) and Short Time Modified Covariance (STMC). The discrete formulation and application of these methods to simulated MCA blood flow signals is described. The results' evaluation according to the relevant spectral parameters is also accomplished leading to the choice of the best estimator. This chapter also includes a study on the relevance of each parameter on the performance of the method.

Chapter 5 reports the simulation and processing of ESs. An overview of the main features of emboli detection and characterization is followed by the description of the simulation process. The best-performed spectral estimator is compared to time-domain analysis results.

The results obtained and reported in the previous chapter, induced the development of a new method for spectral representation of Doppler signals, the space-frequency representation, described in Chapter 6. The mathematical formalization of the new method, its application to the simulated ESs, and its comparison with the STFT and time-domain processing are also included in Chapter 6.

Chapter 7 presents the results of the application of the statistical evaluation of STFT, time-domain processing and the space-frequency version of the STFT, to clinical signals.

In Chapter 8 general conclusions taken from this work are drawn. Guidelines for future work are also suggested.

Figure 1.1 shows the practical work addressed in each chapter of the thesis.

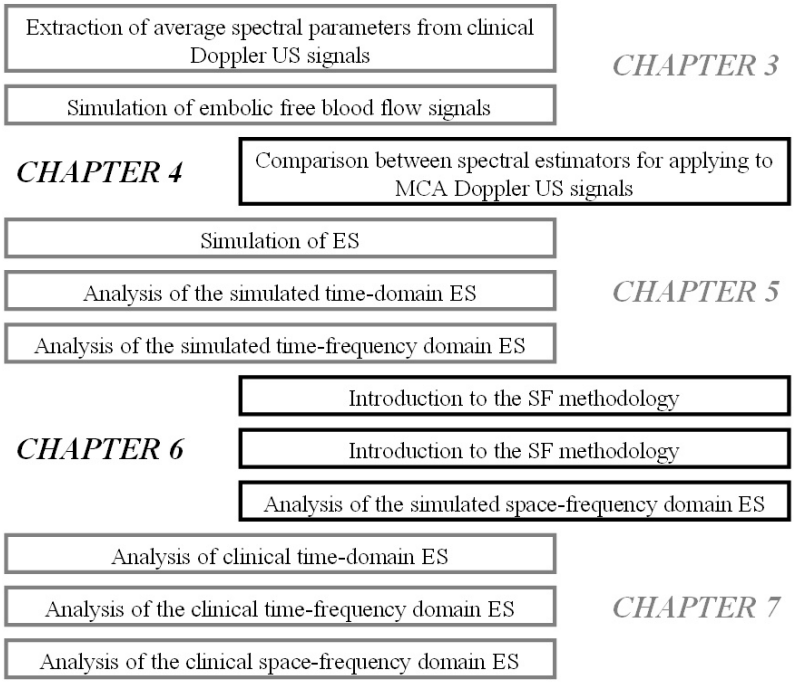

Figure 1.1 – Practical work addressed in each chapter of the thesis.

1.4 ORIGINAL CONTRIBUTIONS

The main contributions of this thesis may be summarized as follows:

- Method and algorithm for representing a spectrogram in the space-frequency domain

  The mathematical formulation and computational implementation of an innovative space-frequency blood flow representation; Statistical accuracy of the proposed method overcomes the accuracy obtained with traditional and time-frequency methods.

- Methods and algorithms for simulating MCA ultrasound blood flow signals and embolic signals

  The development of a MCA Doppler ultrasound signal simulator, employing a new averaging algorithm, where the input data is able to accept clinical Doppler signals, including the variation of clinical ultrasound power spectra during the cardiac cycle; The simulator includes the possibility of adding to the MCA signals embolic events with user-defined time location and power spectral characteristics.

- Quantification of the influence of the spectral estimators parameters on the accuracy of the estimation

The spectral parameters accuracy and its influence on the general spectral estimator accuracy was studied; these influences were rated according to the grade of influence each parameter had on the global method performance; the study has been applied to both signals with emboli or emboli-free; These hierarchies enabled the definition of fine tuned MCA blood flow spectral estimators.

- Method and algorithm for computing the average signal from random time-variable signals

The development of an innovative technique for averaging stochastic non-stationary signals, composed by consecutive segments with different lengths but similar periodic characteristics.

So far, these contributions were reported in:

Leiria Ana, Ruano M. G., Evans D. H., *Blood Flow Signals Characterization***,** 12th New England Doppler Conference, Artimino, Florence, May 2003

Leiria Ana, Moura M. M. M., Ruano M. Graça, *Time-Variable Blood Flow Averaged Waveforms*, Controlo 2004 - Sixth Portuguese Conference on Automatic Control, Vol. 2, pp. 625-629, Faro, Portugal, June 2004

Leiria Ana, Moura M. M. M., Solano Julio, Ruano M. Graça, Evans David H., *Middle Cerebral Artery Blood Flow: Accurate Time-Frequency Evaluation*, Anais do IIICLAEB'2004/XIXCBEB'2004 - Conferência Latino-Americana de Engenharia Biomédica, pp. 1095-1098, João Pessoa, Brazil, September 2004

Leiria Ana, Moura M. M. M., Evans David H., Ruano M. Graça, *Time-Variable Blood Flow Averaged Waveforms*, submitted to International Journal of Systems Science, 1st October 2004

2 BACKGROUND

2.1 INTRODUCTION

This chapter summarizes the fundamental issues related with the main subjects involved in spectral analysis of ESs: Doppler ultrasound, spectral analysis, and embolic analysis. The characterization of ultrasound waves and the concepts, techniques and methods associated with TCD ultrasound instrumentation are reviewed. A few anatomical aspects related to blood flow, such as the circulatory system, heart and blood vessels, are presented. Blood is described as the main source of information for Doppler ultrasound diagnosis. The Doppler signal is mathematically characterized and the procedures used to extract the required clinical information are outlined. Finally, the concepts related to embolic Doppler signals' processing are exposed.

2.2 DOPPLER ULTRASOUND

Ultrasound is being increasingly employed for diagnosis purposes since it allows the visualisation of the interior of the human body. Ultrasound instrumentation exploiting the Doppler effect allows monitoring of the moving structures within the body, for example fetal movement and blood flow. TCD equipment, in particular, is used for identification of emboli in the MCA.

A wave is a movement of energy defined as a periodic repetition of a disturbance from a normal or equilibrium condition [Evans, McDicken, 2000].

A sound wave is a mechanical wave travelling through matter. The propagation of ultrasound is due to the action among the atoms in the medium. That action is

transmitted to other atoms, along with a loss of energy. This loss of energy determines the length the wave can travel within the medium.

Ultrasound is a sound wave with frequencies above the human audible range of frequencies, i.e., above 20 kHz. Diagnostic ultrasound devices emit ultrasound waves into the human body, and collect and analyse the echoes returned by the structures reached by the wave.

The piezoelectric effect and the interaction between the ultrasound wave and the medium are physical phenomena directly related to diagnostic ultrasound. The former allows controlling the ultrasonic wave and interpreting its echoes while the physical phenomena affect the interpretation of the returned echoes.

When some solids suffer a mechanical pressure, they produce small electric charges, the so-called piezoelectric effect. Therefore, the incidence of ultrasound waves on a piezoelectric crystal originates a transmission of electric impulses susceptible of being electronically processed.

This is a reversible effect since when some voltage is applied to a piezoelectric solid, it suffers a mechanical distortion, and accordingly, if an alternating current is applied to the crystal, the electric field will create oscillations (surface compression and rarefaction) and produce ultrasonic waves.

This property is very useful when applied to diagnostic ultrasound, and it is used to generate (inverse piezoelectric effect) and receive (piezoelectric effect) electronically controlled ultrasound waves (Figure 2.1).

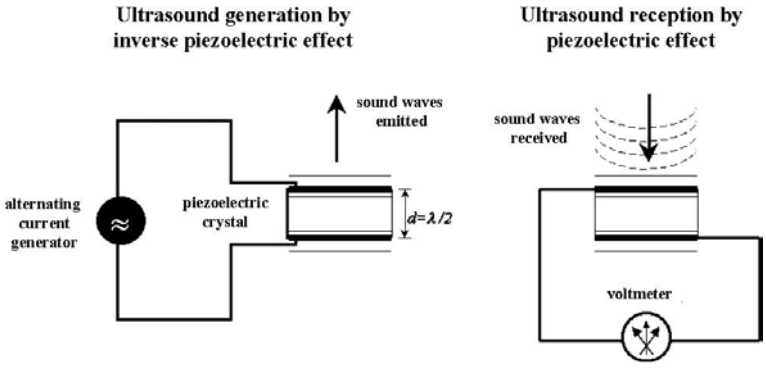

Figure 2.1 – Piezoelectric effect and inverse piezoelectric effect

When the ultrasound waves enter the human body, three main phenomena occur and affect the posterior interpretation of the returned echoes. These are reflection, refraction, and absorption.

When a wave crosses a medium and reaches a plane interface, part of the wave is reflected and part is refracted.

Reflection occurs when ultrasound reaches a surface with small irregularities and walls with higher dimensions than the wavelength. In this case, the incidence angle (θ_i) and the reflection angle (θ_r) are the same [Evans, McDicken, 2000].

However, if the medium has discontinuities with lower or equal dimension than the wavelength of the ultrasound, some of that wave's energy will scatter in several directions, as illustrated in Figure 2.2. Those discontinuities may be caused by changes on density or compressibility of the medium.

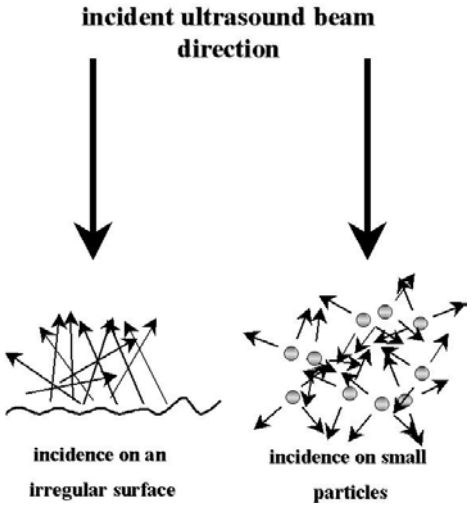

Figure 2.2 – Scatter concept

Refraction and reflection are represented in Figure 2.3.

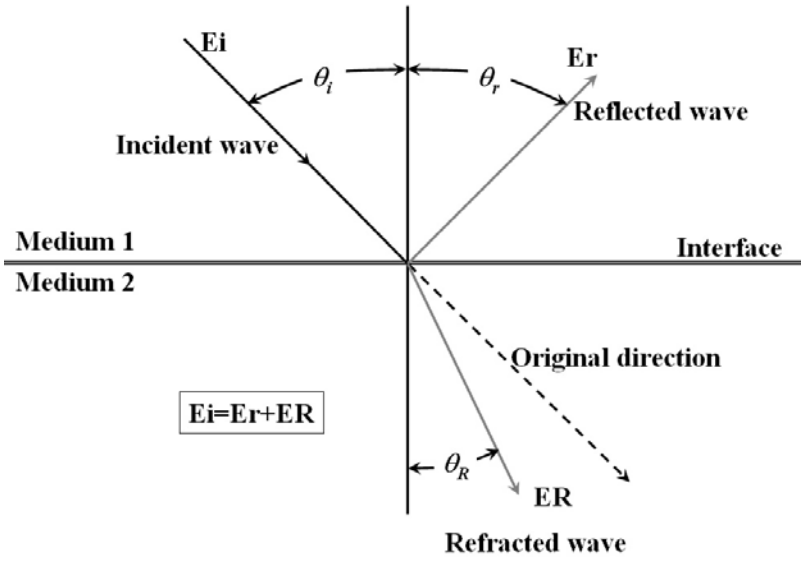

Figure 2.3 – Reflection and refraction of the sound waves on plane surfaces

Refraction is the deviation suffered by a beam of sound waves when it crosses the frontier between two mediums with different sound propagation velocities. According to the Snell's Law, the refraction angle (θ_R) is related to the velocities in both media (c_1 and c_2) by [Fish, 1990]:

$$\frac{\sin(\theta_i)}{\sin(\theta_R)} = \frac{c_1}{c_2} = n_{RI} \tag{2.1}$$

where, n_{RI} is the refractive index.

Ultrasound absorption occurs when sound is converted into heat energy. This results in a decrease of intensity of the ultrasound as it travels through the medium.

Dispersion, reflection, and absorption are the main causes of ultrasound attenuation. Higher transmitted frequencies produce more attenuation, decrease the penetration capability, but improve the skill of imaging near structures with increased resolution. The choice of the transmitting frequency depends on the depth willing to be reached and the resolution to be sought.

Doppler ultrasound is one of the techniques associated with ultrasound diagnosis. Systems that make use of the Doppler effect can extract phase information from the echoes returned by moving structures in the body and produce images, blood velocity spectra and estimates of several heamodynamic quantities.

This technology is mostly used in medicine, in the analysis of the blood flow behaviour to find possible disease patterns.

Examples of Doppler systems are Continuous Wave Doppler (CW), Pulse Wave Doppler (PW), Multigate Doppler system, Duplex scanning that combines PW or CW with B-Mode scanning systems, and Colour Flow Imaging that combines a Multigate Doppler system with B-scanning system [Hoskins *et al.*, 1999].

The Doppler effect is a physical principle observed from the relative movement between a source of waves and an observer. The frequency measured by the observer is different from the emitted frequency. If the source and the observer are moving close to each other, the frequency that reaches the observer will be higher than the emitted frequency. Otherwise, if the observer and the source are moving away from each other, the frequency measured by the observer will be lower than the emitted frequency. The signal representing the difference between the emitted and the received signals is called the Doppler signal.

This principle is the foundation of Doppler ultrasound diagnosis. In Doppler ultrasound systems, an ultrasound beam is emitted using a transmitting transducer towards the target to be analysed; then the ultrasound waves echoed by the moving targets will be caught by a receiving transducer and compared with the emitted waves to compute the Doppler signal.

In what concerns diagnosis, one should consider the combination of two Doppler effects: the source (transducer) as a static subject and the target (blood cells) is considered as a moving structure and the opposite effect, this is, the source (blood cells) is considered moving, and the target (transducer) is assumed static.

Figure 2.4 shows the relationship between the emitted and the received frequencies according to the movement of the target. In the figure, the letters T and R identifies the transmitting and receiving transducers, respectively. The transmitted frequency is represented by f_t and the received frequency by f_r.

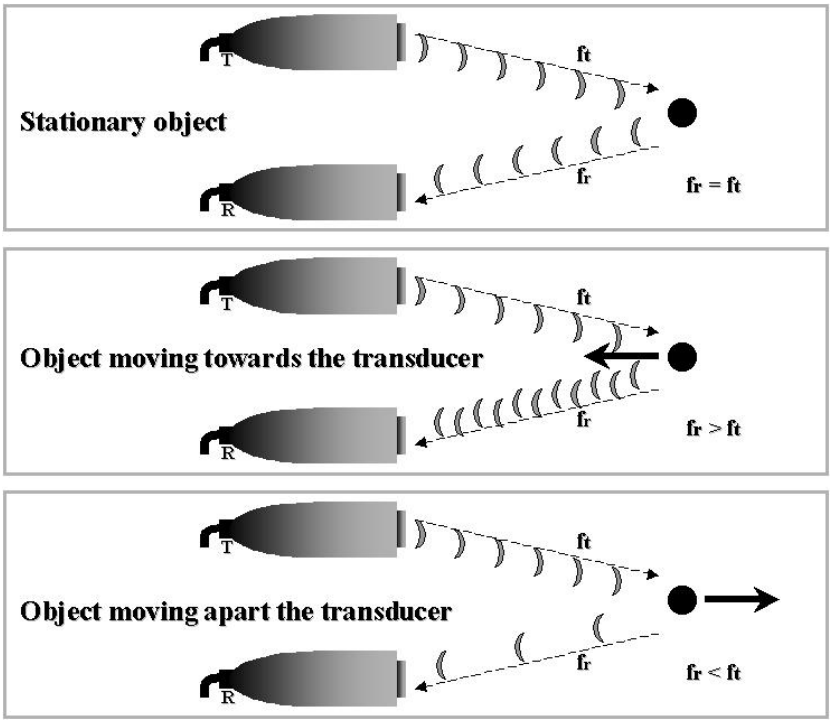

Figure 2.4 – Principle of operation of Doppler ultrasound in diagnosis

Doppler signals can be represented by the Doppler equation,

$$f_d = f_t - f_r = 2 f_t \frac{v \cos(\theta_i)}{c} \tag{2.2}$$

where f_d, f_t and f_r are respectively the Doppler frequency, the transmitted and received frequencies, respectively, v is the velocity of the target, θ_i the angle between

the ultrasound beam and the direction of the moving target and c is the velocity of the sound on the medium[1].

The values of f_t, θ_i and c are known. Therefore, the target velocity can be found if the Doppler frequency is also known,

$$v = \frac{K_D f_d}{\cos(\theta_i)} \tag{2.3}$$

$$K_D = const = \frac{c}{2 f_t} \tag{2.4}$$

The angle θ_i must be carefully chosen. The ideal value of θ_i to determine the velocity of a fluid inside a tube should be 0º, because equation (2.4) becomes

$$v = K_D f_d \,. \tag{2.5}$$

However, the echoes returned by the walls of the tube would make the analysis impracticable. The choice of an angle lower than 15º is generally considered a good solution, since equation (2.5) can still be used, disregarding a small error[2]. Any other applicable[3] value for θ_i must be well known to allow the correct determination of the flow velocity.

The Doppler angle is represented in Figure 2.5.

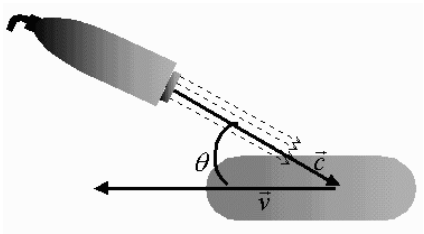

Figure 2.5 – Doppler angle

2.3 DOPPLER ULTRASOUND INSTRUMENTATION

Piezoelectric transducers in Doppler ultrasound instrumentation may generate pulses of ultrasound waves (that are propagated to the organ to be examined), or receive

[1] The sound velocity depends on the medium, the density, and the compressibility. In soft tissues, its value is assumed to be within the range bounded by 1540ms^{-1} and 1600ms^{-1}.

[2] $\cos(15º) \simeq 0.97$

[3] 90º, for instance is not applicable because the flow does not present any velocity component in that direction.

echoes from those waves (created by reflection and dispersion effects) and transform those echoes into electrical impulses. When the Doppler effect is used in association, quantitative analysis of the blood velocity or embolus detection is allowed.

When a wave is transmitted at a known frequency in direction to a specific vessel, the targets (mainly red blood cells) will reflect the wave, originating several echoes. When those echoes are compared with the transmitted frequency according to (2.2), the velocity of the targets can be found from (2.3).

In medical applications, the transmission frequency is usually in the range of 2 to 10 MHz, depending on the depth demanded and the sort of tissues that the ultrasound will cross [Evans, McDicken, 2000].

Two main classes of Doppler ultrasound equipment can be considered, according to the instrument's operating method: CW and PW Doppler.

CW Doppler ultrasound machines use two transducers, where one emits ultrasound waves continuously, and the other receives the echoes from those waves. There is no theoretical limit for the reachable depth. The main disadvantage of this mode of operation is the lack of precision in determining the depth of the organs that are generating the echoes. This drawback can be avoided with the PW Doppler technique, where a transducer working on two periods is used.

Figure 2.6 represents the PW Doppler equipment operation on a simplified block diagram. The oscillator in the figure generates a wave with a specified frequency that will be sent to the body through the transducer, and the same transducer will receive the echoes from this wave. The timing circuits will regulate the periods during which the transmitting gate is opened (during that time the transducer operates as an emitter) and closed (when the transducer works as a receiver). The depth of the target interrogated can be found from the time delay between the emitted and the received pulses. The wave collected is amplified and demodulated, reducing part of the artefacts originated by the reflecting particles [Fish, 1992].

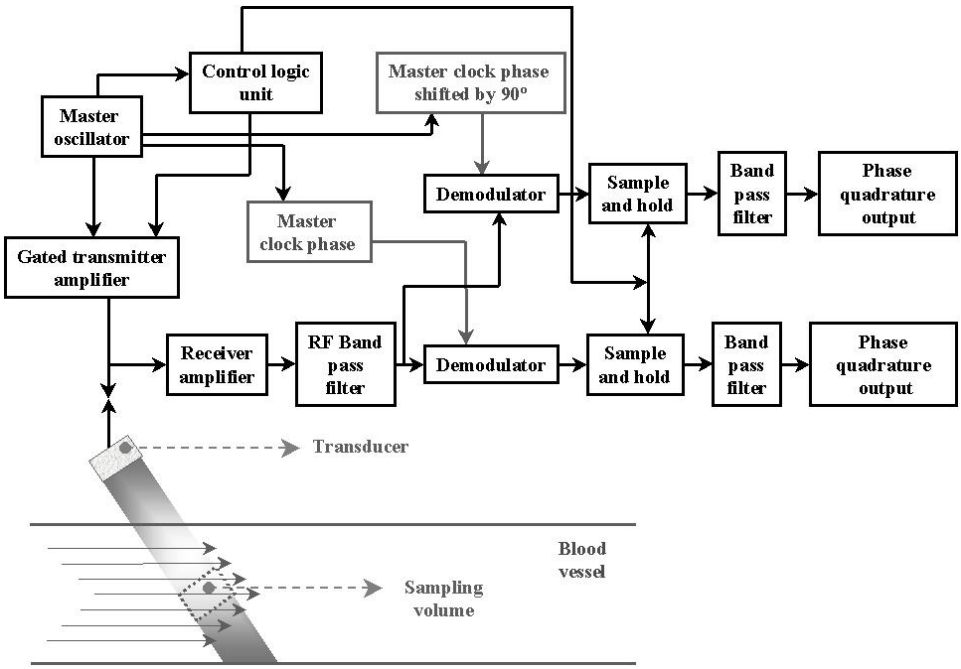

Figure 2.6 – Simplified scheme of Pulsed Wave Doppler equipment.

The major drawback of the PW system is the Nyquist limit: the maximum detectable frequency is half the rate of the wave's emitting repetition (the sampling frequency (f_s) or Pulse Repetition Frequency (PRF)). Therefore, as the target's depth increases, the PRF has to decrease to allow the echoes to be received, and only low frequencies (or targets' velocities) can be detected in deep vessels.

Transcranial Doppler PW instrumentation allows the insonation of the basal portions of the major cerebral arteries.

Figure 2.7 shows an excerpt of an MCA signal obtained with TCD.

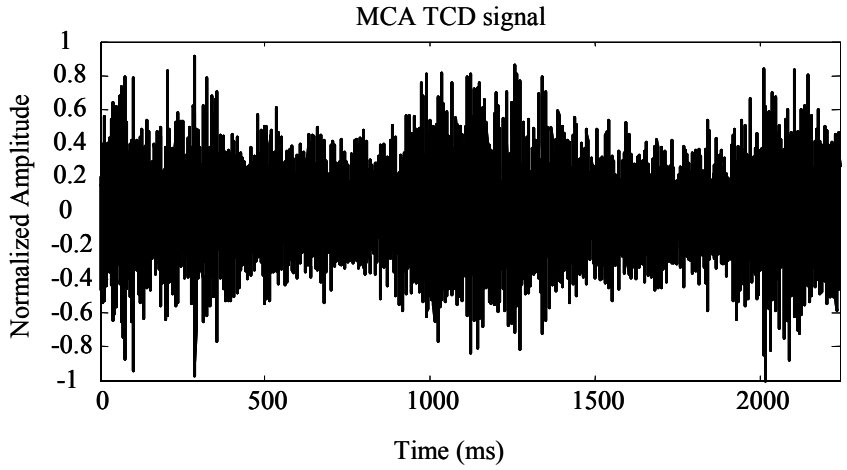

Figure 2.7 – Excerpt of an MCA TCD signal

Doppler ultrasound analysis of cerebral arteries located under the skull, present some technical difficulties. The first problem is that the bony skull greatly attenuates ultrasound beams. In addition, cerebral blood vessels are small and tightly packed together, which complicates the identification of a vessel or its location. In most cases, the vessels locations and identification must be deduced from the Doppler signals [Zuilen *et al.*, 1998].

Instead of frequency values between 5 and 8 MHz, used in ordinary medical ultrasound Doppler diagnosis applications, TCD instrumentation operates around 2 MHz to enable the penetration of the skull; however, even such frequencies cannot adequately penetrate most bones.

For most purposes, the only part of the skull that provides a suitable ultrasonic "window" is the thinnest portion of the squamous part of the temporal bone, just in front of the ear (see Figure 2.8). This transtemporal window is generally used to insonate the vessels of the circle of Willis.

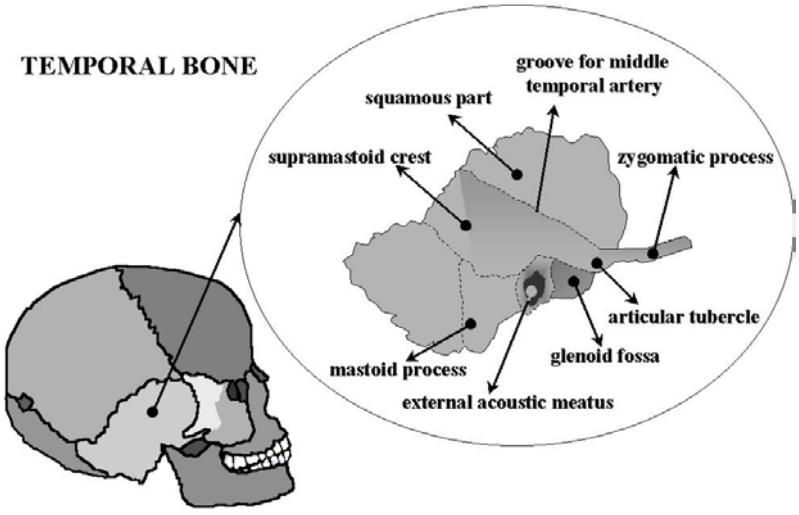

Figure 2.8 – Temporal bone structure

Some remarks should be made on the use of this window. The variability of the bone's thickness (depending on the age, gender, and ethnic group of the patient), varies the quality of the Doppler signal. The transtemporal window can be localised quite anteriorly (close to the vertical portion of the zygomatic bone) or, more frequently, posteriorly (close to the pinna of the ear). The vessels that can be examined through this window include the terminal portion of the internal carotid artery, its bifurcation into the middle and the anterior cerebral arteries, and the posterior cerebral artery. Sometimes the communicating arteries (either anterior or posterior) can also be

sampled, but they are more dependent upon the haemodynamic variability of the circle of Willis.

The use of PW Doppler allows controlling the three-dimensional sample volume, through the adjustment of the length of the pulse.

2.4 BLOOD FLOW

In the current study, TCD signals are obtained from blood flow in MCA. To identify what is expected from these signals, it is important to characterize blood composition and movement.

The blood circulation is divided into two different circuits illustrated in Figure 2.9.

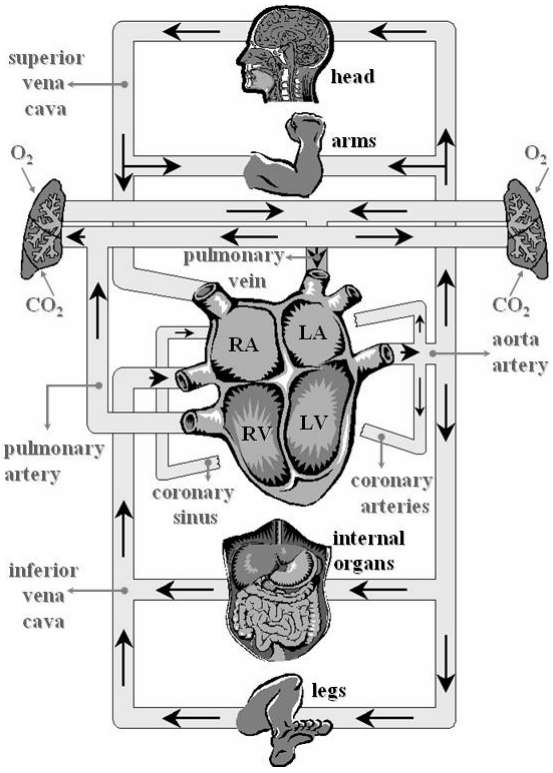

Figure 2.9 – Simplified scheme of the cardiovascular system

The first circuit is called the systemic circulation, and starts when oxygenated blood leaves the heart and goes into a big artery, the aorta, which conducts the blood to all parts of the body. As the blood gets in touch with anatomic elements, it supplies oxygen and several substances for the nutrition of those elements, and receives by exchange carbon dioxide, water and several non-assimilated substances. The venae cavae lead the deoxygenated blood to heart again. The pulmonary circulation starts here,

when the blood is driven out to the pulmonary alveoli, through the pulmonary artery. There, the blood gets rid of the carbon dioxide while receives new oxygen from the air in the lungs. The pulmonary veins drive the blood back to heart before the start of a new cycle.

In both circulations, the arteries and the veins communicate by means of systems with very thin channels called capillary vessels. Those vessels are responsible for the osmotic exchanges between the blood and the environmental medium.

Essentially, two halves compose the heart: the left heart containing the oxygenated blood and the right heart containing the deoxygenated blood. Each of those parts has two chambers. The superior chambers are the atria, and the inferior chambers are the ventricles (Figure 2.10).

At the end of the systemic circulation cycle, the blood enters the heart's right side and fills the right atrium. The pressure increase in the atrium forces the opening of the tricuspid valve, and most of the blood is let out into the right ventricle. Electric impulses, generated in the heart, force the right atrium to contract driving out the remaining blood.

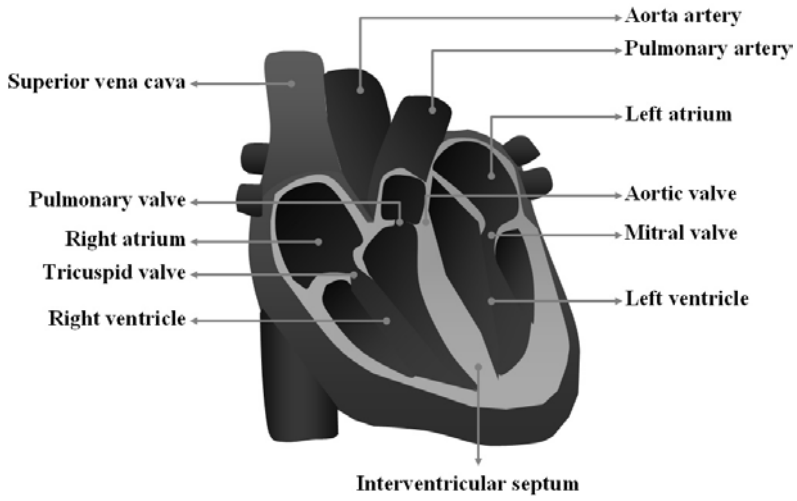

Figure 2.10 – Heart

When the ventricular pressure surpasses the atrium pressure, the tricuspid valve closes, and the pulmonary valve opens, allowing the blood to flow out of the heart. The right ventricle contracts due to electric impulses.

The pulmonary artery conducts blood to the lungs, where the blood makes the necessary exchanges. Using the pulmonary vein, the blood enters the left atrium of the heart. Due to the increase of pressure on the atrium, the mitral valve opens and lets the

blood go to the left ventricle. The left atrium contracts because of the electric impulses, and the remaining blood is forced out to the left ventricle.

Also due to electric impulses, the heart contracts deriving a difference of pressures that makes the mitral valve close, and the aortic valve open. The blood goes to the aorta and from there to the rest of the body. A new cardiac cycle starts with the blood returning to the heart.

The events in the heart give shape to the Doppler blood flow signal and its parameters, although this shape gets smoother as the blood moves away from the heart. To recognize what is expected from the signal at any time, the main phases of a heartbeat (depicted in Figure 2.11) will be further analysed next.

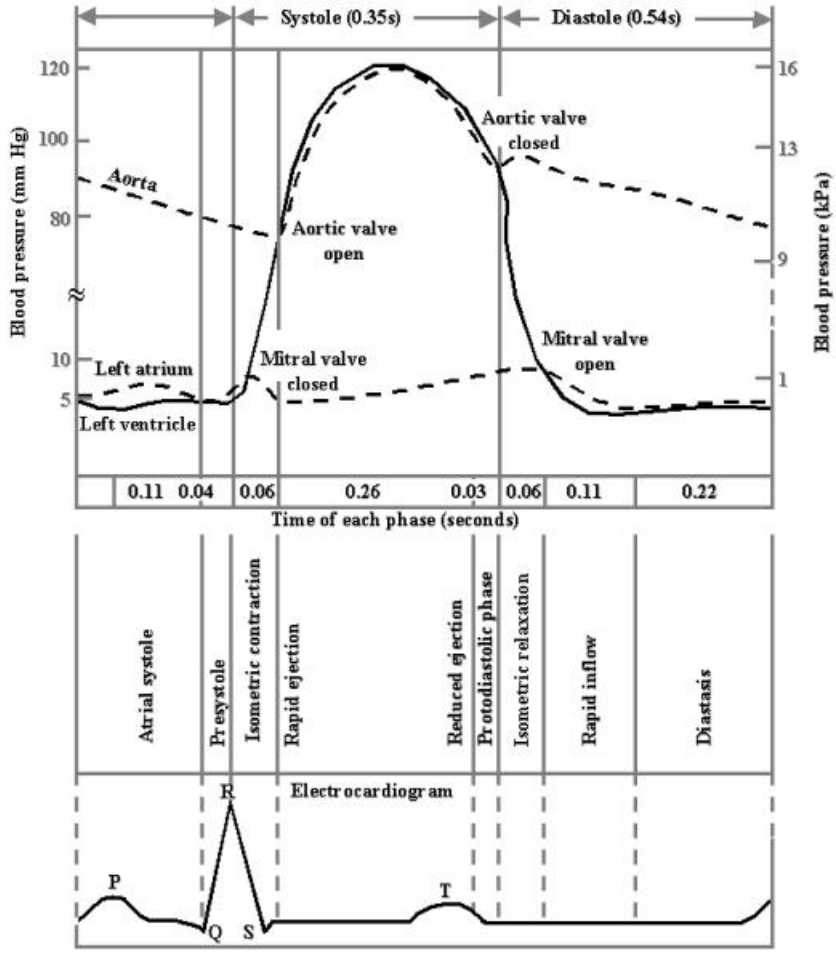

Figure 2.11 – Blood pressure varying as a function of time

The left ventricle contraction corresponds to an abrupt increase of the ventricular pressure and to the consequent close of the mitral valve. The aortic valve remains closed until the left ventricle and the aorta get to similar pressures. When that condition is satisfied, the ejection period starts. During the first third part of this phase (period of

rapid ejection), about 70% of the blood in the ventricle leaves the chamber. The remaining emptying time is called the period of reduced ejection.

During the ejection, the arterial pressure increases due to the income of blood in the aorta.

After the systole, the ventricle relaxes. The reduction of pressure in the ventricle and the high arterial pressure would force the blood to return towards the left ventricle. The aortic valve closes avoiding this return.

Meanwhile, the pressure of the left atrium increases, the arterial pressure gets higher than the ventricular pressure, the mitral valve opens, allowing the blood passage into the ventricle.

At this time, a period of rapid inflow of the ventricle starts. This period is due to differences of pressure, and lasts about one third of the total inflow phase. The phase of reduced inflow due to electric impulses will follow. A new cycle starts with a new ventricular contraction, induced by the electric impulses.

2.4.1 BLOOD VESSELS

Blood vessels present different anatomy, according to their function and physiologic requirements. Depending on the anatomy, they can be classified as arteries, arterioles, capillaries, venules and veins.

Arteries have large dimensions near the heart (to support high blood flow rates); however, they become narrower, as they start being successively divided and giving off branches.

The arterial walls are thick and have a considerable quantity of elastic fibres. Due to this constitution the arteries are able to carry the blood away from the heart under high-pressure, smoothing the pressure wave delivered by the heart, and support the sudden intake of blood ejected from the heart during systole.

Arterioles have a smooth muscle in their walls, so that they can be dilated or constricted. This property allows them to control the amount of blood that will be delivered to the different parts of the body.

The capillaries are the smallest vessels and a single layer of endothelial cells composes their walls.

Finally, venules and veins have thinner walls than their arterial counterparts do, because the blood pressure is much lower.

The MCA is the largest branch of the internal carotid artery. The MCAs are connected to the two anterior cerebral arteries through the anterior communication arteries, and to the two posterior cerebral arteries through the posterior communicating arteries (see Figure 2.12). This system of communication vessels is called the circle of Willis.

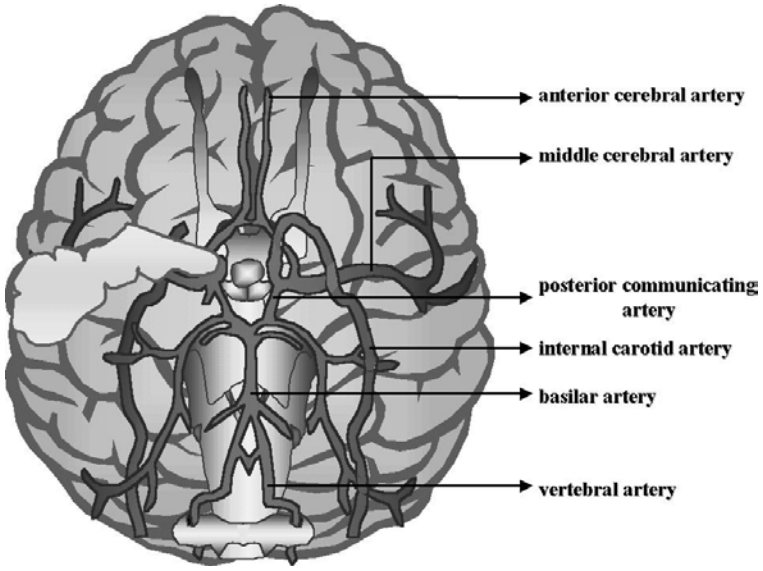

Figure 2.12 – Distribution of the extra and intracranial arteries

The circle of Willis (and the arteries that compose it) is considered one of the anatomically most variable parts of the human circulation.

The peripheral resistance of the major cerebral arteries as well as their share in the cerebral blood supply are quite variable due to the high variability of their diameter [Zwan *et. al*, 1993].

Table 2.1 shows average values of the MCA, reported in three published works.

Reference	Number of subjects	Diameter
[Jain, 1964]	610	0.3 to 0.5cm
[Zwan *et. al*, 1993]	63	2.7mm
[Serrador *et al.*, 2000]	n. a.	2.51±0.2mm for women 2.54±0.25mm for men

Table 2.1 – Studies on the MCA diameter

The average length of the MCA was estimated to be 1.6 cm [Jain, 1964].

The velocities observed for blood in MCA vary according to the age of the subject. Krejza and colleagues reported that, on the average, the peak velocity would be

ranged from 54 to 166 cm s^{-1}, the mean velocity from 33 to 133 cm s^{-1} and the velocity at the end diastole from 21 to 77 cm s^{-1} [Krejza *et al.*, 1998].

2.4.2 BLOOD COMPOSITION

Doppler ultrasound blood diagnosis highly depends on blood composition. Cardiovascular diseases can be revealed from the movement of blood particles, and embolic events can be characterized from the comparative behaviour between normal blood flow (from now on referred as just blood for simplicity) and blood with travelling emboli. To understand the information obtained from blood, it is important to review the nature of blood, its movement, and its behaviour as a scatterer of ultrasound waves.

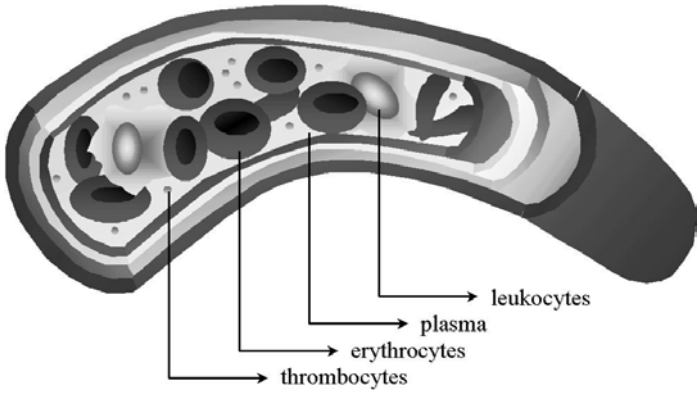

Figure 2.13 – Blood composition

The main blood components (see Figure 2.13) are cells and the solution where the cells are contained, named plasma. The cells are of different kind: white cells (leukocytes), responsible for protecting the body from invader organisms (the number of the white cells is bigger when there is an infection), red blood cells (erythrocytes) which transport the oxygen through the body, and platelets (thrombocytes) that along with some other plasma substances prevent uncontrolled lost of blood when a vessel injury occurs. Plasma is composed of 90% of water and several salts, glucose, cholesterol, proteins, etc.

Table 2.2 shows some characteristics of the blood cells.

Cell	Concentration (particles/mm^3)	Dimensions (μm)	Total of blood volume (%)
Erythrocytes	5×10^6	7.2×2.2	45
Leukocytes	5×10^3	9-25	~0.8
Thrombocytes	2.5×10^5	2-3	~0.2

Table 2.2 – Blood cells [Evans, McDicken, 2000]

2.4.3 TYPES OF BLOOD FLOWS

Blood flow within closed vessels can be classified as laminar and turbulent flow. Laminar or streamline flow is characterized by the blood cells movement along smooth paths in layers with every layer sliding smoothly over its neighbour. A velocity increase can turn laminar into disturbed flow, making the movement of blood particles to become irregular, with eventual formation of vortices. In the limit, the flow may become turbulent. In this case, the cells in the fluid start to take irregular and erratic paths, and the velocities vary continuously both in magnitude and in direction [Evans, McDicken, 2000].

Additionally, the pulsatile nature of blood due to the intermittent pumping of the heart together with the viscoelastic properties of the arterial walls, lead to the propagation of both pressure and velocity along the arterial system, following a finite pulse velocity.

The behaviour of blood as a scatterer is strongly conditioned by the wavelength of the emitted ultrasound being much bigger than the dimension of a red blood cell. Blood is composed by small aggregates of red blood cells and the volume of those aggregates is a random variable with probability density function depending on the shear rate.

The backscattering cross-section of a single erythrocyte can be defined by,

$$BCS_b = \frac{Vol_c^2 \pi^2}{\lambda^4}\left[\frac{\beta_e - \beta_p}{\beta_p} + \frac{3(\rho_e - \rho_p)}{2\rho_e + \rho_p}\right] \tag{2.6}$$

where Vol_c is the average volume of one erythrocyte, λ the ultrasound wavelength, $\beta_e = 3.41\times10^{-10}\,\mathrm{m^2N^{-3}}$ and $\beta_p = 4.09\times10^{-10}\,\mathrm{m^2N^{-3}}$ are, respectively, the adiabatic

compressibility of the erythrocytes and plasma, and finally, $\rho_e = 1.091 \times 10^3$ kgm^{-3} and $\rho_p = 1.021 \times 10^3$ kgm^{-3} are the densities of blood and plasma [Evans, McDicken, 2000].

According to this, the backscattering coefficient for blood is given by

$$\Phi_{bs} = BCS_b \frac{H_{ae} W_{pack}}{V_c} \left(\mu_\upsilon + \sigma_\upsilon^2 \right), \tag{2.7}$$

where H_{ae} is the haematocrit, υ a measure of the size of the aggregate scattering unit (with μ_υ and σ_υ being the mean and the standard deviation of the scattering size distribution), and W_{pack} the packing factor associated to a particular aggregate size distribution [Evans, McDicken, 2000].

Table 2.3 shows some properties of blood related to its interaction with the ultrasound waves.

Property	Definition	Value
Density	Mass for each unity of volume	1.05g/ml
Viscosity	Moving fluid's resistance to flow	0.035 kg m^{-1} s^{-1}
Kinematics Viscosity	Viscosity for unity of density	0.033 cm^2 s^{-1}
Velocity of sound	Sound velocity while crossing the fluid	1.57 mm/μs
Acoustic impedance	Measures fluids restraint to sound waves propagation	1.6×10^6 kg m^{-2} s^{-1}
Attenuation	Signal's intensity decreasing while passing through a fluid	0.21dB cm^{-1}MHz^{-1}

Table 2.3 – Blood Properties.

2.5 DOPPLER SIGNALS PROCESSING

The Doppler signal is formed out of biological events and technical conditions associated to the instrumentation. However, the information contained in the signal is not clear until proper signal processing techniques are applied to it.

The correct understanding and interpretation of the contents of the signals returned by the Doppler instrumentation, and the extraction of the information through spectral analysis are treated in this section.

2.5.1 CHARACTERISATION OF THE BLOOD FLOW SIGNAL

The background Doppler signal, obtained by the transducer, is a time domain signal. The real part of the signal presents a form similar to the signal represented in Figure 2.7, where each time index contains the information about the average scattering from one insonation.

The direct flow (flow towards the probe) in the pulsed Doppler ultrasound signal $x_D(t)$, can be described by its phase and quadrature components, respectively $x_F(t)$ and $x_Q(t)$, as:

$$x_D(t) = x_F(t) + jx_Q(t). \tag{2.8}$$

Doppler ultrasound signals are random signal as their specific values may have occurred in any order [Challis, Kitney, 1991a] [Proakis, Manolakis, 1988].

The Doppler signal represented by equation (2.8) can also be classified as a wide sense stationary process (WSS), as its non-stationary nature can be ignored in small enough slices of the signal. In that case, the signal can be regarded as a stationary complex Gaussian process, completely characterised by its covariance function $c_{xx}(t_1\ t_2)$.

The covariance function corresponds to the difference between the autocorrelation function (ACF) $r_{xx}(t_1\ t_2)$ of the process $x_D(t)$ for the time instants t_1 and t_2, and the squared modulus of the mean values (μ_x) of the process for the same times t_1 and t_2.

The mean value μ_x of a WSS process is constant and its ACF depends on the lag τ considered.

The covariance function is

$$\begin{aligned} c_{xx}(\tau) &= r_{xx}(\tau) - |\mu_x|^2 \\ \tau &= t_{i+1} - t_i \end{aligned} \tag{2.9}$$

and its value for zero lag corresponds to the variance σ_x^2 of the process,

$$\sigma_x^2 = c_{xx}(0) = r_{xx}(0) - \mu_x{}^2 \tag{2.10}$$

As the signal $x_D(t)$ is a Gaussian WSS process with zero mean [Mo, Cobbold, 1986], it can be completely statistically determined by the ACF.

For real signals, the power spectrum density[4] (PSD), presents always non-negative real values: for complex processes, $r_{xx}(\tau)=r_{xx}^{*}(\tau)$ ($r_{xx}^{*}(\tau)$ is the conjugate of $r_{xx}(\tau)$); and for real processes, the ACF is a real even function [Kay, 1988].

It is common practice to work with a single realisation of the random process, and from there, although the ACF is unknown, it is possible to determine the temporal average of the realisation.

As the signal $x_D(t)$ is an ergodic signal on the first and second moments, it is possible to substitute the temporal averages by sample means, and take the ACF temporal mean $r'_{xx}(\tau)$ (instead of the sampled ACF mean $r_{xx}(\tau)$) from a window with length N,

$$\begin{aligned} r_{xx}(\tau) &= \lim_{N\to\infty} r'_{xx}(\tau) \\ &= \lim_{N\to\infty} \frac{1}{N}\int_{-N/2}^{N/2} x_D(t+\tau)x_D^{*}(t)dt \end{aligned} . \tag{2.11}$$

The Fourier transform (FT) of $r_{xx}(\tau)$ is [Kay, Marple, 1981],

$$\begin{aligned} \hat{P}(f) &= \int_{-N/2}^{N/2} r_{xx}(\tau)e^{-j2\pi f t}dt \\ &= \frac{1}{N}\left|\int_{-T/2}^{T/2} x_D(t)e^{-j2\pi f t}dt\right|^2 \end{aligned} . \tag{2.12}$$

When N gets near to infinity, the true PSD $P(f)$ is achieved,

$$\mathrm{P}(f) = \lim_{N\to\infty} \mathcal{E}\left[\hat{P}(f)\right], \tag{2.13}$$

where $\mathcal{E}[\bullet]$ is the expected value operator.

Let $x_D(n)$ be the sample version of the signal $x_D(t)$, obtained at a determined sampling frequency f_s. If the random process is bounded in the range $[-T_s/2, T_s/2]$, where T_s is the sampling period, the autocorrelation sequence (ACS) with respect to $x_D(n)$ is given by

$$r_{xx}(\tau) = \mathcal{E}\left[x_D(n+\tau)\,x_D{}^{*}(n)\right], \tag{2.14}$$

and its Fourier transform produces the PSD

$$P(f) = \sum_{k=-\infty}^{\infty} r_{xx}(\tau)e^{-j2\pi k f/f_s} . \tag{2.15}$$

[4] Power distribution along the frequency.

The PSD of a random process can be determined by the direct method, calculating the PSD through the application of the FT directly to the signal $x_D(n)$; or by an indirect method, determining FT of the signal's ACS [Kay, 1988].

2.5.2 SPECTRAL CHARACTERIZATION

When a blood vessel is insonated for Doppler ultrasound diagnosis, the ultrasound waves collide with several blood particles (mainly the red blood cells) travelling in the vessel and, from each one of those particles, an echo is returned.

In a normal situation, the flow will be laminar with parabolic profile of velocities. The blood particles will be moving approximately in the same direction and the range of velocities recorded at each time will not be very wide.

The Doppler frequencies (2.2) that are related to the echoes returned for each transmitted ultrasound beam, will be contained in the range $[mf, Mf]$, where mf and Mf are respectively the minimum and maximum registered Doppler frequencies. The mean frequency fm can be obtained by the weighted average of the observed frequencies.

For each time t, the echo of each wave can be represented as shown in Figure 2.14.

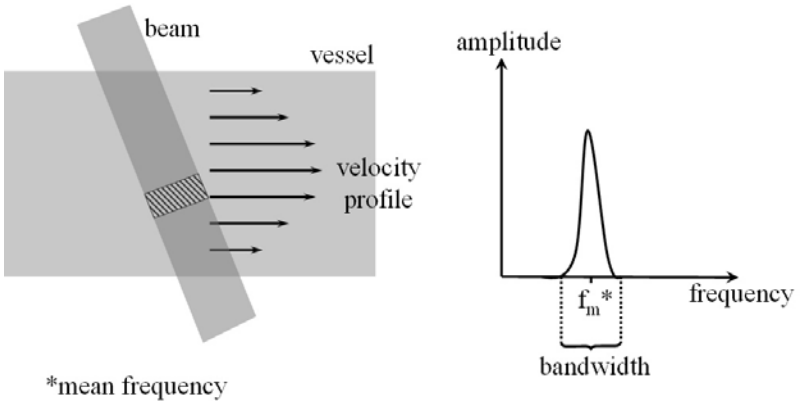

Figure 2.14 – Doppler frequency spectrum

The representation of the observed frequencies for each time *t* under consecutive insonations of the vessel will produce a graphic like the one presented in Figure 2.15.

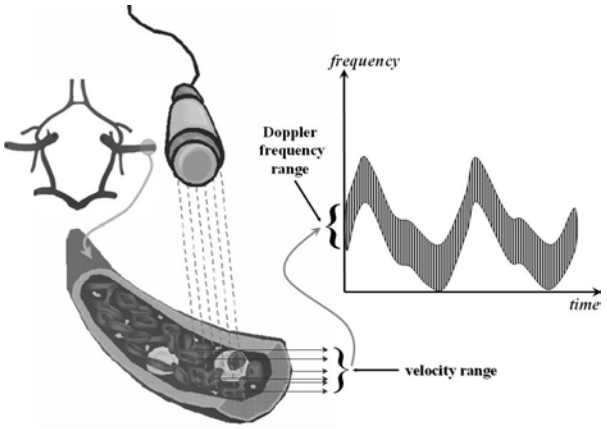

Figure 2.15 – Time-frequency representation of Doppler spectrum

The analysis of the Doppler signal can be simplified if the signal is represented in the frequency domain.

The time-frequency representation of the MCA signal in Figure 2.7, is shown in Figure 2.16.

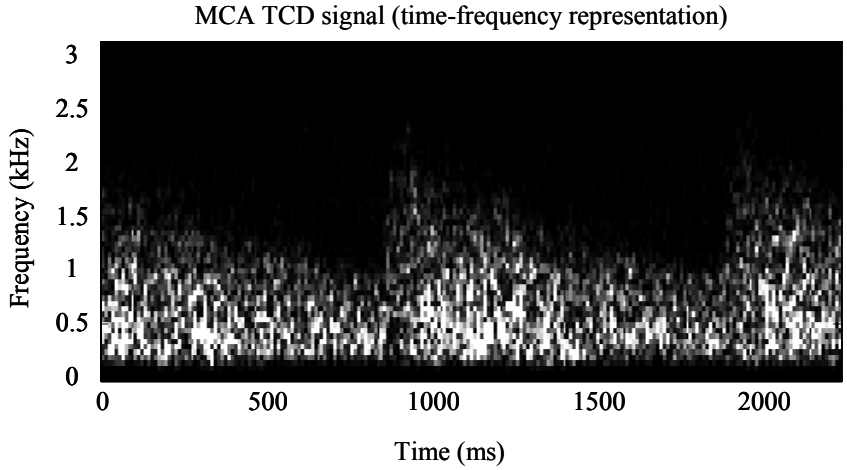

Figure 2.16 – Time frequency representation of an MCA TCD signal.

Transforming a signal from time to the frequency domain is usually done using discrete Fourier transform (DFT), typically applying a widely employed algorithm known as Fast Fourier Transform (FFT). The main problem is that the DFT is suitable for application to stationary signals, but not to cyclostationary signals like the Doppler ultrasound blood flow signal.

However, successive DFTs can be applied to time sequences of the signal with stationary properties. In this case, the determination of the squared amplitude of the resulting signal, the PSD, yields the true spectrum. This method is designated the Spectrogram or STFT.

The blood flow Doppler signal is considered stationary for periods from 10 to 20 ms, which will lead to a frequency resolution no higher than 50 to 100Hz [Evans, McDicken, 2000]. The application of the FFT to truncated segments of the signal corresponds to successive multiplications of the time-domain signal by sequential rectangular windows with finite dimension. As result, the PSD may become affected by distortion and spread of energy to the side lobes, due to the signal's truncation.

This effect can be reduced when other windows than the rectangular are employed, enabling a progressive decrease of the amplitude at the extremes of the data segment. Nevertheless, sometimes it is still necessary to enlarge the main lobe of the window, maintaining a trade-off between the non-stationary assumption and the frequency resolution.

Blood flow Doppler signals spectra present Gaussian probability density function due to the large number of red blood cells that contribute to the signal echoes [Fish, 1991]. The variance of the spectral estimation for a random Gaussian process is given by [Evans, McDicken, 2000] [Challis, Kitney, 1991b],

$$\sigma^2_{P'(\omega)} = P(\omega)^2\left[1+\left(\frac{\sin(\omega N)}{N\sin(\omega)}\right)^2\right] \tag{2.16}$$

where $P(\omega)$ and $P'(\omega)$ are respectively the true and estimated PSD, N the number of points to which the FFT is applied, and ω the angular frequency.

Due to the nature of the signal, for large N, it is common practice to apply the Bartlett procedure to reduce the estimated PSD variance. The Bartlett procedure consists on dividing N into K sequences, each one with N' elements, in order to have,

$$\sigma^2_{P'(\omega)} = \frac{1}{K}P(\omega)^2\left[1+\left(\frac{\sin(\omega N')}{N'\sin(\omega)}\right)^2\right], \tag{2.17}$$

which, for $N \to \infty$, will lead to

$$\sigma^2_{P'(\omega)} = \frac{1}{K}P(\omega)^2. \tag{2.18}$$

If the value of N is not large enough, the reduced spectral resolution may become troublesome. Because of the ergodic nature of the Doppler signal, a possible solution is to use K cardiac cycles instead of K segments of N.

The variance can be reduced even more, if the windows used with the FFT are not consecutive but overlapped [Welch, 1967].

Improvement of the accuracy of the PSD produced by conventional methods, can lead to more accurate diagnosis and interpretation of the Doppler signal. Alternative spectral estimators can be found among parametric methods or time-frequency distributions.

Parametric methods, suitable for use on stationary signals, are based on priori knowledge of the signal characteristics or on assumptions on the process that generates the signal. Usually it is possible to select a model that performs a good approximation to the real process.

In general, better spectral estimations are obtained with these methods, when compared to the estimations obtained by the application of conventional methods. Higher spectral accuracy and frequency resolution are obtained when the spectral estimates are based on a model whose parameters are computed from the available clinical data.

These methods involve three main steps: the selection of the method that better fits the available data set, the estimation of the model parameters, and the spectrum estimation.

Ruano [Ruano, 1992] studied the performance of parametric spectral estimators applied to common carotid artery Doppler blood flow signals. This study reported that it was possible to improve the spectral accuracy, when FFT is replaced by parametric methods, on the estimation of small stationary segments of the signal. This study also identified the fourth order Autoregressive Modified Covariance (ARMC) as a suitable choice for this application, since it presented a good trade-off between the accuracy of the estimation and the computational burden.

Time-Frequency Distribution (TFD) methods describe the signal's frequency variations with time, mapping the traditional one-dimensional time domain function into a bi-dimensional time and frequency domain function. These methods allow the localization of the signal's energy both in time and in frequency without constraining the data segments' lengths to stationary properties [Cohen, 1989].

Results of the performance of some Cohen's class TFD methods when compared with the STFT[5], applied to Doppler signals from common carotid artery [Cardoso et al., 1996a], recommend the use of CWD.

[5] Also a Cohen's class distribution.

Comparisons between parametric methods and TFD applied to Doppler blood flow signals were also reported. Results obtained for femoral artery [Guo *et al*., 1994], common carotid artery [Wang, Fish, 1996] and exit of the aortic valve (aorta) [Leiria *et al.*, 1999] suggest that TFD methods produce more accurate spectral estimations. These studies also confirmed that the parametric methods are preferred to the classical ones.

However, any chosen method must run in real-time, for clinical and research applications. Thus, it is necessary to verify, for each method, that the real-time implementation is possible and that it does not change the accuracy of the estimator.

Studies on the analysis of the performance of the ARMC and CWD algorithms on homogeneous and heterogeneous parallel processing architectures can be found in [Madeira *et al*., 1999a] [Cardoso *et al*., 1996b] [Madeira *et al*., 1999b]. The diversity of results leads to the conclusion that the algorithms' execution times are a function of the processor velocity and of several other factors, as the processing architecture used [Tokhi, Hossain, 1995]. Therefore, even if the best statistical benefit is obtained by the use of a particular algorithm, if the implementation architecture does not allow a real-time execution, that particular algorithm may have to be excluded from practical applications.

2.6 EMBOLIC EVENTS

Disorders related to embolic occurrence are among the important causes of death. Because microemboli can frequently be found during carotid endarterectomy or cardiac surgery, TCD diagnosis became an important tool to prevent strokes associated with arterial fibrillation and in patients with prosthetic heart valves.

The use of TCD technology allows the localisation of the embolic source, the identification of patients with higher risk of stroke occurrence or recurrence, the monitoring of therapy effectiveness and the monitoring of cardiac and carotid surgery [Dietler, 2001].

Embolic diagnosis requirements are not limited to the detection and measurement of emboli. It is necessary to be capable of separating artefacts (patient movements, tissue vibration, etc) from real circulating emboli, distinguishing the nature of emboli (gaseous, particulate or fat), differentiating between different types of solid emboli, and evaluating microemboli size.

This section includes an introduction to embolic events, a discussion on the importance of emboli characterization emboli and a description of the Doppler signals containing emboli records.

2.6.1 STROKE AND EMBOLI

The most typical types of strokes are hemorrhagic strokes that occur with vascular lesions rupture (what leaves the blood free to involve the cerebral tissue around the injury), and ischemic[6] strokes that are derived by an obstruction of the bigger arteries from the cerebral circulation [Hademenos, 1997].

Ischemic strokes are obstructions mainly produced by arteriosclerosis, embolus, thrombus, haemorrhage, or vasospasms. Arteriosclerosis is a pathologic process characterised by yellowish cholesterol plaques, lipids and cellular detritus located on arterial walls. As the plaques are formed, the walls become thick, fibrotic and calcified, and the lumen gets narrower, decreasing the blood flow supplied to the tissues. While allowing platelet aggregation, the plaques of arteriosclerosis may be contributing to the formation of emboli or thrombi. An embolus is a solid, liquid, or gaseous intravascular mass that is released and flows with blood, to a region distant from its original localization. A thrombus is a blood clot (an aggregate composed of platelets and fibrin) formed to face an atherosclerotic lesion or an injury in a vessel.

Most emboli are derived from thrombus and are called thromboemboli. Some other rare emboli are originated by: bone or haematopoietic medulla fragments, atheromatous detritus from atherosclerotic plaques, fat little drops, tumour fragments, and organism's foreign bodies and air or nitrogen bubbles [EstudMed.com, 2001].

Embolism is classified according to the place of occlusion or the nature of the embolic material as pulmonary, systemic, infusion (emboli caused by amniotic liquid), gaseous or fat.

Pulmonary embolism is a frequent cause of death, and is generally consequence of thromboses that begin on the large and deep veins of the inferior members. Depending on their size, these emboli can produce occlusions of the pulmonary artery's

[6] Ischemia is defined as the decrease of blood supply to a tissue, what is a reversible condition. However if that problem is not corrected it will lead to the tissue death by anoxia (lack of oxygen).

smaller branches. This class of embolism hardly penetrates the brain circulation unless for interatrial or interventricular defects.

Systemic emboli travel through the arterial circulation and can start by intracardiac thrombus (the most common), ulcerated atherosclerotic plaques, aortic aneurysm, valve prosthesis or paradoxical emboli, in some cases, may have unidentified origin. Most of these emboli result in infarction, and the most frequent regions of lodgement are the legs, the brain, the viscera, or the superior extremities. The arteries where emboli get fixed and the size of the emboli can be used to define the dangerousness of the embolic occurrence. The occlusion of MCA by a small embolus might lead to death in a few days or even in a few hours.

Infusion provoked embolism occurs with parturition or immediately after parturition. These rare events occur by infusion of the amniotic liquid in the mother's circulation, and frequently lead to the mother's death.

Gaseous emboli are air or gas bubbles that obstruct the vascular flow due to lesions in the tissues (barotraumas). The air might arise from parturition or abortion, pneumothorax[7], pulmonary lesions or breaks in the thorax wall. Air bubbles behave like physical masses and generally go to the brain or lungs. Gas bubbles, usually come from exposition to sudden changes of the atmospheric pressure, and eventually can lead to problems on the cerebral vessels and result on coma or death.

Fat emboli are small drops of fat that arise from fractures of the large bones (fat medullas) and infrequently from burns or trauma to the soft parts. Usually, they are not lethal, but the formation of fat micro-aggregates might lead to pulmonary or cerebral occlusion [Hademenos, 1997].

2.6.2 EMBOLIC SIGNALS CHARACTERIZATION

Emboli are often identified as high intensity transient signal, and their detection, through TCD, depends on the power returned from emboli being higher than the one returned from the background blood flow. The effective power of the ESs cannot be accurately measured, as the attenuation by the tissues between the transducer and the embolus is not known. The estimated power of the background signal, which suffers similar attenuation, is typically used as a basis of comparison [Evans, 1999].

[7] Rupture or accidental penetration on a big artery or vein.

Figure 2.17 shows an excerpt of an MCA signal obtained with TCD.

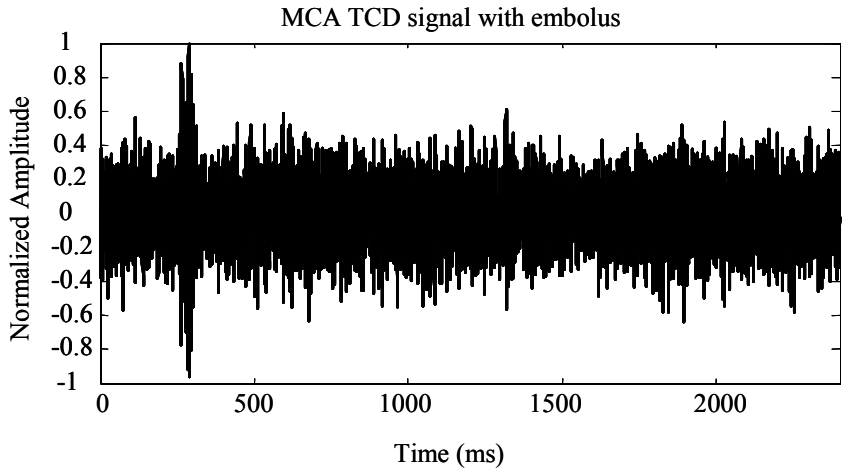

Figure 2.17 – Excerpt of an MCA TCD signal with an embolus.

The time-frequency representation of the MCA signal in Figure 2.17, is shown in Figure 2.18.

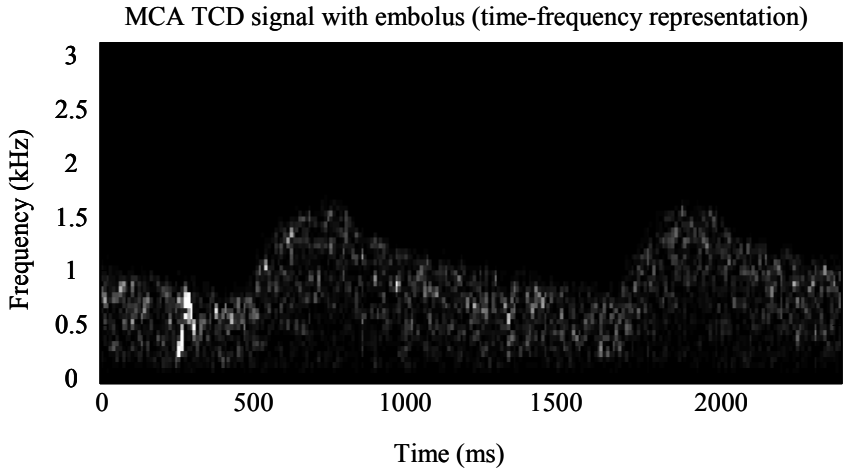

Figure 2.18 – Time frequency representation of an MCA TCD signal

ESs are usually described as amplitude modulated sine waves, sometimes also containing frequency modulation. Emboli duration frequently varies between 2 and 100ms and their powers range from 3dB to more than 60dB above the power of the background signal. Within the proper dynamic range of the bidirectional instrumentation, the signal should be unidirectional within the Doppler spectrum. Depending on the equipment used and on the velocity of the emboli, the ESs can be identified as a snap, a chirp or a moan on an audible output [Consensus, 1995] [Evans, 2003].

Detection of embolic events can be thought as a statistical process, on which an occurrence with a small size and power has less probability of being detected.

Most embolic detection systems are based on subjective decisions made by experienced technicians, which can lead to some mistakes.

Automatic detection systems are not simple, and must consider factors like: the determination of ratio between the power backscattered by the embolus and the power of the remaining signal; the detection threshold (measured in decibels) chosen to classify an event as being or not an emboli; the position in the cardiac cycle at which the event occurs; the size of the sample volume; spectral estimation method used and time and frequency resolutions achieved; the dynamic range of the instrumentation (in decibels); the transmitted ultrasound frequency (in megahertz); the filter settings in kilohertz (high pass filters should suppress low frequencies from arterial wall oscillations); and the recording time [Ringelstein *et al.*, 1998], [Ringelstein, Droste, 1999].

There is still no consensus on the best way to compute the backscattered power ratio, and different equipment may use different approaches. The determination of the embolic Doppler power can be estimated from the peak intensity measurement or from averaged intensity over a defined period and frequency frame. The power of the background signal can be obtained from the mean intensity observed in the area where the embolus was found, but in other cardiac cycles; from the frames following the embolus; or from the whole sweep including signal free areas. These measurements also depend on the frequency scale settings, which are broader for increased PRF values.

The detection threshold usually recommended for emboli detection ranges from 2 to 9 dB. Lower thresholds may originate false-positives identifications and higher thresholds reduce the sensitivity. The detection thresholds might be defined by the range of spontaneous intensity fluctuations within the Doppler signals of normal controls, or by intra-patients fluctuations on case-by-case basis during emboli free periods of the background spectrum.

Emboli have higher probability to be missed during systole than during diastole, mainly because velocities are higher in systole, and thus, emboli can only be seen for a shorter period. Furthermore, the systole corresponds to the passage of a higher amount of blood in the artery, what might increase the risk of confusing the power of emboli with the power of background blood.

The width of the ultrasound beam and the cross section of the sample volume vary with the insonation depth. Although the skull can badly distort the beam, TCD probes allow large enough sample volume cross sectional diameters (around 6 mm). The drawback is that higher sample volumes have more blood particles surrounding the embolus, which causes inefficient detection of emboli. Axial volume lengths from 3 to 10 mm are commonly used in practice.

Spectral estimators based on FT cannot deal with the very short durations of some embolic events, due to the trade-off between time and frequency resolutions. Furthermore, the multiplication of the signal by non-rectangular sliding windows, although reducing spectral leakage, may also reduce the spectral resolution. Solutions to these problems are the overlapping of the windows or the use of alternative methods as the Wigner analysis [Smith *et al.*, 1997], wavelet analysis [Krongold *et al.*, 1999] [Aydin *et al.*, 1999], or even time-domain processing [Müller *et al.*, 1998], [Smith *et al.*, 1998]. It is still worth to mention two other works on this subject, one reporting the comparison between several spectral estimation methods including the STFT [Roy *et al.*, 2000] and another suggesting the optimal parameters to use on STFT [Aydin, Markus, 2000].

The dynamic range of the signals is defined by the highest and the lowest levels of the power received by the targets. Conventional Doppler units are designed for blood flow analysis; thus, usually the dynamic range expected does not exceed 25 to 30dB. However, ESs may reach much higher values, producing overloading, and clipping of the waveform. The resulting spectral display is called embolus overload artefact, and is characterized by noise spikes occupying most, if not all, the spectral display. To overcome this problem Smith et al. suggested the use of two channels, one for the normal forward display and measurements of the blood flow signal, and the other containing the attenuated signal appropriate for the analysis of emboli [Smith *et. al*, 1994].

It is generally agreed that the transmitted ultrasound frequency for intracranial devices should be 2 MHz. Higher frequencies will reduce the sensitivity, and lower frequencies will reduce the Signal to Noise Ratio (SNR) instead of improving emboli detection [Cullinane, Markus, 2001].

Distinguishing between embolic events and artefacts due to patient or transducer movement, or even to surgical manipulation or diathermy, is one of the problems of the embolic analysis [Evans, 1999].

Higher powers or lengths greater than the ones to be expected from emboli might indicate the presence of an artefact. Considering that almost all sources of artefact produce power increases simultaneously in forward and reverse channels, the observation of both the channels can help on the identification of artefacts, as, unless the system overloads, emboli will only register power in one channel. Finally, as ESs usually has a narrow bandwidth and artefacts wide bandwidths, the recognition of the sound of emboli can be an additional criterion for artefact rejection [Evans, 2003].

A more complex method is the multigated or multidepth technique, which consists of tracing the embolus at two or more depths in the same artery. A transient increase in Doppler power, due to an embolic event, is expected to present a time delay in adjacent gates, because of the finite propagation of the embolus along the artery. Artefacts, on the contrary, will appear simultaneously at all depths. Problems of this system are mainly due to low signal's power or emboli only appearing in one channel [Devuyst *et al.*, 2001], [Smith *et al.*, 1997].

A variant of the multigated technique, where one of the sample volumes is placed outside the vessel and any event producing increase of power in both channels is considered an artefact, can be used to improve the results [Georgiadis *et al*., 2000].

The classification of emboli according to its nature is critical for solid emboli being potentially more dangerous than the gaseous one.

It is known that the power returned by a gaseous embolic event is higher than that returned by approximately equal sized solid embolus (by two or three orders of magnitude). In addition, there is an overlap between the backscattered cross section of large particulate emboli and small gaseous emboli; and unlike solid emboli, the backscattered cross section of gaseous emboli increase monotonically with size [Evans, 1999].

Most methods reported to determine the microembolic composition are based on this knowledge. Published studies include power-based methods, duration of ES and estimation of the apparent axial length of the emboli [Fan *et al.*, 2001] [Smith *et al.*, 1998] [Cullinane *et al.*, 2000] [Moehring, Kleppler, 1994].

2.7 CONCLUDING REMARKS

In this chapter, a review of the main points related to Doppler ultrasound instrumentation and the acquisition of signals containing important information on the

blood flow behaviour was accomplished. Therefore, an overview of ultrasound's theory, Doppler effect, and Doppler ultrasound main systems was included. The TCD was also referred.

The circulatory system was briefly described, and the main events of the heart that induce the blood flow behaviour were mentioned. Blood vessels were described, with a special attention to the MCA, and blood was characterized as a scatterer.

The mathematical characterization and an overview of some methods for estimating the Doppler signals were also included.

The characterization of emboli as a source of disease, the description of the Doppler signals containing information on embolic events, and methods of interpreting that information, were also considered in this chapter.

3 SIGNAL SIMULATION

3.1 INTRODUCTION

The analysis of the performance of different spectral estimators cannot be held without a reliable reference, which could be used as a guide for the evaluation of the results. Simulated signals can be used as a reference of the expected spectral representation of Doppler blood flow signals.

This chapter is concerned with the simulation of MCA embolic free ultrasound signals, includes a discussion of the motives for using simulated signals and an overview of some published Doppler blood flow simulators. A simulator to use on the current application is pointed out, together with the requirements for its implementation. At the end of the chapter, the performance evaluation of this simulator is presented.

The simulator selected is fed with Doppler signal spectral waveforms that will be characterized later in the chapter. Some methodologies reported in bibliography for estimating the spectral parameters variation are reviewed. The specific requirements of the MCA blood flow signals and the simulator lead to the proposal of a new method presented here. Finally, the performance assessment of the new method is also reported.

Figure 3.1 shows a general scheme of how the methods and signals used in this chapter are related.

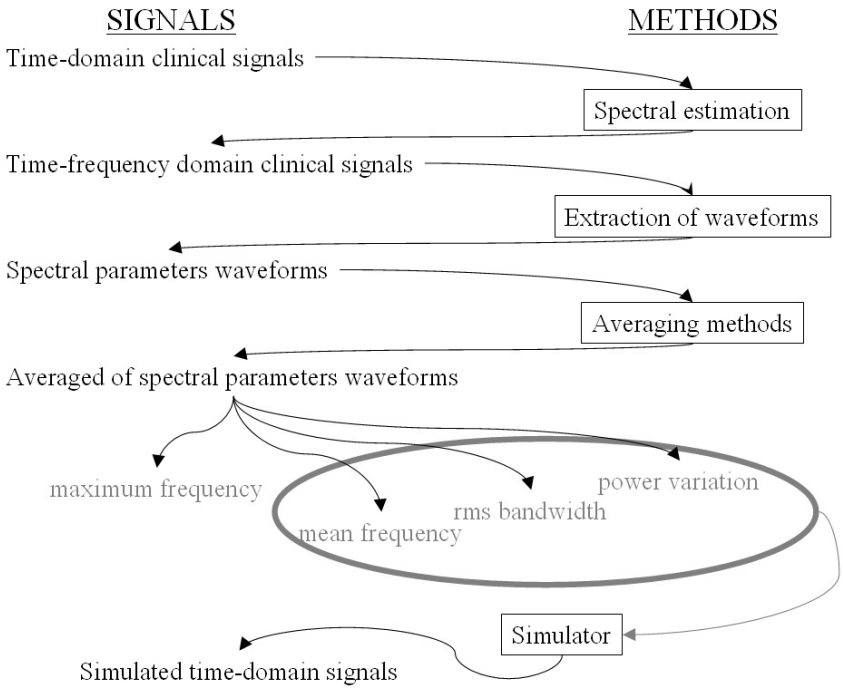

Figure 3.1 – Methods and signals used in this chapter.

3.2 BLOOD FLOW SIGNAL SIMULATION METHODS

Most of the work reported in this thesis was performed with simulated Doppler ultrasound blood flow signals. From the several methods of simulating Doppler signals suggested in literature, the ones considered more adequate for this work are described and discussed. A particular simulator, proposed by Wang and Fish (WF), is identified, according to the requirements of the MCA blood flow signal.

3.2.1 THE IMPORTANCE OF SIMULATING SIGNALS

To identify embolic events in blood flow, it is necessary to know in advance the expected behaviour of embolic free blood flow. This involves knowledge of the particularities of the time-frequency representation of MCA blood flow.

A spectral estimator's skill to produce an accurate time-frequency representation of the signal can only be evaluated when it is possible to distinguish among the features due to the signal from the ones caused by the estimation procedure. That discrimination is not easy mainly due to the variability of clinical Doppler ultrasound blood flow

signals. This variability is caused by physiologic factors (such as heart rate variability, respiration and ventricular contraction and filling) and physical phenomena (related to the properties of the instrumentation and ultrasound) [Kitney, Giddens, 1983]. Therefore, simulated signals with well-known characteristics and controlled behaviour are advantageous for analysing the quality of distinct spectral estimation techniques and methods.

3.2.2 BRIEF REVIEW OF SOME SIMULATION METHODS

There are various Doppler ultrasound signals simulators available in bibliography. It is convenient to review the characteristics of some of those simulators before choosing one of them for using in this work.

In 1986, van Leeuwn and colleagues suggested the simulation of the power spectrum density and its posterior transformation into the time domain by an inverse FFT to obtain an approximation to Doppler blood flow signals [Leeuwn et al., 1986]. In the same year, Mo and Cobbold proposed a model based on the sum of a large number of sinusoids with appropriate amplitude and phases [Mo, Cobbold, 1986]. In 1988, two other simulators were proposed. One of them was based on the assumption that the signal could be represented through a frequency-modulated sine wave weighted by a time stochastic function [Talhami, Kitney, 1988], and the other suggested that a time-domain Doppler signal could be generated through a Finite Impulse Response (FIR) filter with coefficients obtained from clinical data [Kristoffersen, Angelsen, 1988]. During the year after, Mo and Cobbold improved their simulator by allowing it to generate non-stationary signals [Mo, Cobbold, 1989], and, in 1990, Jones and Giddens proposed a method to generate time-domain signals considering the amplitude and phase of the signal as functions of the sample volume shape [Jones, Giddens, 1990]. Two years later, this model was improved to allow the estimation of pulsatile and non-steady flow [Wendling et al, 1992]. In that same year, Mo and Cobbold proposed a new method for modelling the backscattered signal from blood that combines the particle[8] with the continuum[9] approaches [Mo, Cobbold, 1992]. Latter on, in 1996, Wang and Fish presented a simulator that generates the signal using a filter with a time-varying

[8] All the small elemental volumes within the sample volume contribute to generate the Doppler signal.

[9] The contribution from each elemental volume is function of the random fluctuations in local hematocrit.

impulse response [Wang, Fish, 1996], and, in that year, an improvement for the Mo and Cobbold method was also presented, introducing a packing factor for explaining the changes in backscattered power on different flow conditions [Bascom, Cobbold, 1996]. In 1996, another model was still proposed, considering the signal dependence on the sample volume shape and time-varying velocity field [Bastos et al., 1996]. Finally, in 2003, Schlaikjer's team introduced a method for incorporating relevant features like the motion in the surrounding tissue on the signals simulation [Schlaikjer *et al.*, 2003].

After analysing more deeply some of those simulators, it was decided to use the simulator proposed by Wang and Fish. That choice was based on two criteria: the adequacy of the simulator to MCA signals and its skill for generating a large number of simulated signals in a short computational time.

3.2.3 WANG AND FISH SIMULATOR

A Doppler signal can be described as

$$x_D(t) = r_{gauss}(t)e^{j\Phi(t)}, \tag{3.1}$$

where the time-varying frequency shift is described by the exponential term, the deterministic phase is given by

$$\Phi(t) = 2\pi \int fm(t)dt + C\,; \tag{3.2}$$

$r_{gauss}(t)$ is a random Gaussian variable, centred at the zero frequency, fm is the mean frequency of the Doppler signal.

The random part of the signal is the output of a linear filter excited by a Gaussian random process. This way, the power spectral density of $r_{gauss}(t)$ is proportional to the filter frequency response.

As time-varying bandwidths are involved, $r_{gauss}(t)$ must be a time-varying random Gaussian process and the filter has to vary with time. The system that generates $r_{gauss}(t)$ is

$$r_{gauss}(t) = \int r_n(t-\varsigma)h(\varsigma,t)d\varsigma\,. \tag{3.3}$$

where $h(t,\tau)$ is a time varying filter and $r_n(t)$ the white Gaussian noise.

Considering the power spectral density of $r_{gauss}(t)$ as

$$P(f,t)=\frac{p(t)}{\sqrt{2\pi b_f(t)}}e^{-\frac{f^2}{2b_f^2(t)}}, \tag{3.4}$$

Wang and Fish developed the following Gaussian filter,

$$h(t,\varsigma)=\text{const.}\sqrt{\frac{p(t)}{b_t(t)}}e^{-\frac{\varsigma^2}{2b_t^2(t)}} \tag{3.5}$$

assuming $p(t)$ as the Doppler signal's power variation over time and $b_t(t)$ as the filter bandwidth, which is related to the signal root mean square (rms) bandwidth $b_f(t)$ by

$$b_t(t)=\frac{1}{2\sqrt{2}\pi b_f(t)}. \tag{3.6}$$

3.3 CHARACTERIZATION OF THE SIGNALS SPECTRAL PARAMETERS

The WF simulator employs as inputs waveforms representing the behaviour of some relevant spectral parameters that characterize the Doppler signal. Those spectral parameters are the mean frequency, the rms bandwidth, and the power variation over time. The maximum frequency is another relevant parameter that, although not required for simulation, describes important characteristics of blood flow signals.

Because of a certain degree of randomness, it is not possible to know the true values of the spectral parameters over time, but they can be estimated from clinical data.

The characterization of Doppler blood flow signals spectra and the review of some methods that can be used to compute the deterministic inputs of the simulator will be described below.

3.3.1 CHARACTERIZATION OF THE DOPPLER SPECTRUM

Time-frequency representation helps observing and drawing conclusions on signals spectral content over time. Blood cells velocities, flow turbulence or the variation of blood cells passing at each time, are just some of the issues that are made easier when time domain Doppler blood flow signals are mapped into the time-frequency domain.

When clinical evaluation of blood flow is required, or when some particular features of the blood signal are under analysis it is common to extract that information from the spectral waveforms (see Annex A).

Four of the most significant clinical parameters that can be extracted from the time-frequency spectrum are the power variation over time, the maximum frequency, the mean frequency, and the rms bandwidth.

3.3.1.1 Power variation over time

The signal power contains information about the particles that are scattering the ultrasound waves back to the transducer at each time instant. The nature and the amount of scatters in the sample volume are some of the deductions that can be obtained analysing the power of the signal.

The power waveform can be computed from each time slice, to which an FT was applied, in the course of a STFT process. The spectral density associated with a time instant can be written as

$$X(k)=\sum_{n=0}^{N-1} x_w(n) e^{-j2\pi kn\Delta T} \tag{3.7}$$

n and k represent respectively the discrete time and frequency, $x_w(n)$ results from the application of a window function to the signal $x(n)$, and ΔT is the time period being processed.

The corresponding power density spectrum is [Jensen, 1996]

$$P(k)=\frac{1}{N}\left|X(k)\right|^2 . \tag{3.8}$$

The factor $1/N$ in the previous expression ensures that the power spectrum is an average value over the slice of time observed (not a function of the window size).

If the window function applied to the signal is rectangular, given by

$$w(n)=\begin{cases} 1 & 0 \le n \le N-1 \\ 0 & otherwise \end{cases}, \tag{3.9}$$

the expression (3.8) will represent a good approximation of the PSD. However, if the window function does not present unitary power density spectrum, it is necessary to introduce the power density of the window as

$$E_N = \frac{1}{N}\sum_{n=0}^{N-1} w^2(n), \tag{3.10}$$

thus,

$$P(k)=\frac{1}{NE_N}|X(k)|^2. \tag{3.11}$$

Accordingly, the power density at each time instant n is

$$P(n,k)=\frac{1}{NE_N}|X(n,k)|^2 \tag{3.12}$$

and the power variation over time is

$$p(n)=\sum_{k=0}^{N-1}P(n,k). \tag{3.13}$$

3.3.1.2 Maximum frequency

The maximum frequency envelope is directly proportional to the maximum velocity reached by the blood flow cells at each time, as stated by the Doppler equation (2.2).

Several maximum frequency processors are suggested in literature. Among them, the Modified Geometric Method (MGM) was chosen for this work since it is considered suitable for general-purpose software, totally automatic and robust [Evans, McDicken, 2000],

To compute the MGM, it is necessary to define, for each time bin, the curve of the integrated Doppler power spectrum. The function corresponding to the discrete version of that curve is

$$\Gamma(n,k)=\sum_{i=f_L}^{k}\hat{P}(n,i), \tag{3.14}$$

where f_L is a low frequency below which the noise can no longer be assumed to be white Gaussian.

For each time n, considering that $k_{\max}(n)$ is the maximum frequency registered, it is possible to draw a straight line $C(n,k)$ connecting the maximum and the minimum of curve $\Gamma(n,k)$,

$$C(n,k)=k\frac{\Gamma(n,k_{\max}(n))-\Gamma(n,f_L)}{k_{\max}(n)-f_L}+\frac{k_{\max}(n)\Gamma(n,f_L)-\Gamma(n,k_{\max}(n))f_L}{k_{\max}(n)-f_L}. \tag{3.15}$$

Thus, the vertical distances between $\Gamma(n,k)$ and $C(n,k)$ are given by

$$d(n,k)=|\Gamma(n,k)-C(n,k)|, \tag{3.16}$$

and the maximum frequency waveform is formed by the frequencies corresponding to the maximum of $d(n,k)$ for each time (Figure 3.2),

$$[f_{MAX}(n): d(n, f_{MAX}(n))] = \max(d(n,k)) \tag{3.17}$$

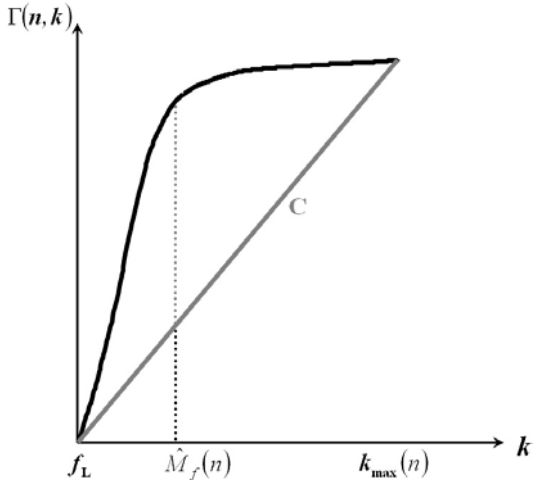

Figure 3.2 – Modified Geometric Method for time *n*.

3.3.1.3 Mean frequency

The spectral mean frequency is proportional to the mean velocity of the blood in the vessel. For each time instant, the mean frequency is given by the average of the frequencies weighted by the correspondent spectral intensity,

$$\widehat{f}_m(n) = \frac{\sum_{k=0}^{N-1} f(n,k)P(n,k)}{\sum_{k=0}^{N-1} P(n,k)}. \tag{3.18}$$

3.3.1.4 Bandwidth

The bandwidth is proportional to the flow turbulence observed in the sample volume. Generally, the bandwidth can be defined as the width of the spectral density, but for many applications, it is common to use the rms bandwidth,

$$\widehat{b}_f(n) = \sqrt{\frac{\sum_{k=0}^{N-1}\left[\widehat{f}_m(n) - f(n,k)\right]^2 P(n,k)}{\sum_{k=0}^{N-1} P(n,k)}}. \tag{3.19}$$

The rms bandwidth corresponds to the standard deviation of the blood spectrum density function, a Gaussian function, obtained by normalizing the area of the spectral density to unity [Gardner, 1990].

3.3.2 AVERAGE WAVEFORMS

To feed the blood flow simulator, some spectral parameters may be reliably obtained from clinical signals to enable a more realistic simulation of blood flow.

When a sufficient amount of data[10] representing blood flow information from different subjects is available, then sufficient information of the four relevant spectral parameters (maximum and mean frequencies, rms bandwidth and power variation) can be extracted from each cardiac cycle time-frequency representation. Representative waveforms can be obtained by averaging all the clinical waveforms for each spectral parameter.

Due to the characteristics of blood flow signals, the averaging process involves more than a simple averaging operation. The duration of a heartbeat is not constant even if it is observed for the same person in consecutive cycles. The factors influencing the waveforms' variation are not uniformly distributed over the cycle. These contributions affect essentially the diastole slice of time; the systole duration is usually fairly constant[11] [Kitney, Giddens, 1983]. Some methods proposed in bibliography, to average spectral waveforms from Doppler blood flow signals, will be analysed next.

3.3.2.1 Delimiting the cardiac cycle

As the average waveforms required have the duration of one heartbeat, and the clinical signals contain more than one cardiac cycle, the first action to take is to delimit the cardiac cycles in the signals.

The usual procedure is to identify the same feature point on every cardiac cycle, and take that point as the start of the cycle. This can be done collecting an electrocardiogram (ECG) signal together with the Doppler signal.

---

[10] By sufficient amount of data should be understood at least 30 cardiac cycles from at least 30 subjects.

[11] Unless in the case of tachycardia occurrence

Consider the ECG signal obtained with a standard lead configuration and represented in Figure 3.3.

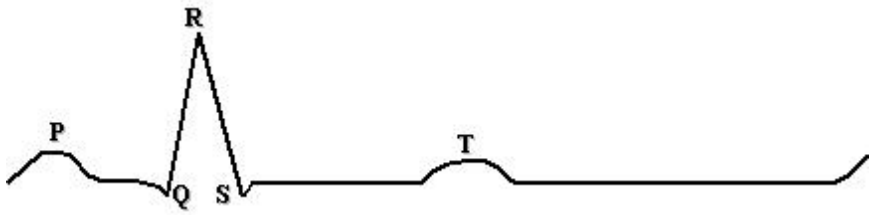

Figure 3.3 – ECG over a cardiac cycle

The R wave in the picture, which is assumed to be the start of the systole, seems to be the easiest point to identify in the cycle. Thus, the identification of all the R waves in the ECG provides a mean to flag the frontier between consecutive cardiac cycles. One of the methods to identify the start of the systoles is to compute the ECG first derivative and flag the R wave through the zero crossing points. The spectral waveforms can be split at the positions flagged on the ECG [Holdsworth *et al.*, 1999].

This method although suitable for working with most signals from healthy subjects, may present some problems with atypical signals.

The main disadvantage of this approach is the dependence on a signal other than the Doppler signal. In that sense, the Pulse-Foot-Seeking algorithm (PFS) [Evans, 1988] provides a more efficient way to delimit the cardiac cycle, as it operates on the maximum frequency waveform of the Doppler signal.

The implementation of the PFS is schematised in Figure 3.4.

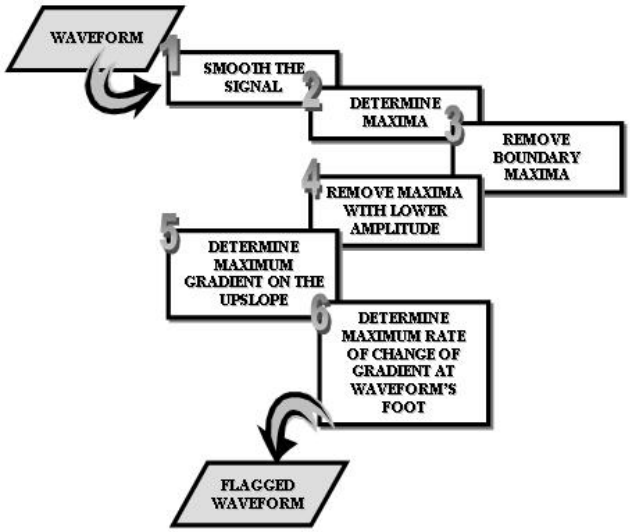

Figure 3.4 – PFS algorithm schematic representation

Assuming that the first manifestations of each cardiac cycle appear from the beginning of the systolic upslope, the strategy is to detect and flag that point in the maximum frequency envelope.

The first thing to do is to smooth the maximum frequency waveform, with a five-point Moving Average (MA), to simplify the analysis of the signal. The next step is to split the smoothed signal into segments of $N1$ points.

Empirical studies reported that $N1$ depends on the heart rate and sampling frequency [Evans, 1988]. Table 3.1 presents the estimates of $N1$ for neonatal cerebral arteries.

Case	Heart rate Window (cycles/second)	*N1* value (number of points)	Approximate capture window (cycles/second)
A	Normal	$375\times f_s$	64-144
B	Low	$750\times f_s$	32-72

Table 3.1 – Choice of the capture window to be used on PFS algorithm (values considered for neonatal blood flow in cerebral arteries [Evans, 1988])

The next step is to locate the maxima of the smoothed signal that can be the true local or boundary maxima. Boundary maxima that are adjacent to higher values on near segments can be removed comparing any maxima in segments boundary with the signal's height on the other side of the boundary. If any segment still has more than one maximum flagged, the untrue maxima can be removed searching any maxima located less than $\pm N1$ bins far from each other, and eliminating the ones with lower amplitude.

Working backwards from the true maxima towards the beginning of the cycles, the next step is to find the maximum on each upslope of the signal's gradient. The gradient can be computed from a simple (-2, -1, 0, 1, 2) weighting algorithm, and the maxima are searched within the $187.5\times f_s$ points before the last flags.

Using the second differential of the smoothed signal, also computed from a (-2, -1, 0, 1, 2) weighting algorithm, the foot of each waveform corresponds to the maximum in the $100\times f_s$ points previous to the first differential maxima.

To reduce the effect of noise on further processing, a simple (1-2-1) low pass filter can still be applied to the maximum frequency envelope [Evans, 1988].

3.3.2.2 Averaging the waveforms

One of the published methods, for averaging maximum frequency waveforms, was developed envisaging the characterization of blood flow in the common carotid artery [Holdsworth *et al.*, 1999]. As it is based on the waveforms main features, it will be identified in this thesis as Waveform Main Features Averaging (WFA).

After identifying the start of the cardiac cycles from the ECG signal, the first step is to flag some characteristic features on the maximum velocity waveform. Additional points are also flagged at fixed intervals on the waveforms. Table 3.2 shows the features identified for carotid artery signals [Holdsworth *et al.*, 1999].

FEATURE POINTS DESCRIPTION	
Over one cardiac cycle	**Other information**
GENERAL	Number of cardiac cycles of each signal
Average of maximum velocity	Diameter of left artery
Maximum acceleration	Diameter of right artery
Averaged velocity between maximum and minimum diastolic velocities (V_{HM})	Average diameter of left and right arteries
Cycle duration	
Time during early systole during which the velocity is lower or equal to V_{HM} value	
Time period during which velocity is higher or equal to V_{HM} value	
VELOCITY VALUES	
Minimum diastolic velocity	
Velocity at point of maximum acceleration	
Maximum systolic velocity	
Minimum velocity in diastolic notch	
TIME VALUES	
Time of diastolic minimum velocity	
Time of maximum acceleration	
Time of maximum systolic velocity	
Time of minimum velocity in diastolic notch	

Table 3.2 – Description of the feature points for common carotid artery's maximum velocity waveform [Holdsworth *et al.*, 1999].

A synthetic waveform can be built by averaging each feature and additional points from all the available maximum frequency waveforms. The points in the new waveform are then interpolated with cubic spline fitting. Linear extrapolation is also applied to the late diastolic region to include cycles longer than the average.

Mean velocity waveforms for pulsatile blood flow, consistent with the observed maximum velocity waveform, assuming Womersley flow, can be calculated by invoking Womersley's analytic solution for velocity profiles under pulsatile conditions [Evans, 1992].

Another method for averaging maximum frequency waveforms is the Phase Shift Algorithm (PSA) [Kitney, Giddens, 1983].

The following expression represents a maximum frequency waveform during a cardiac cycle, which has been computed out of an ensemble average

$$u(t) = U(t) + u'(t), \tag{3.20}$$

where $U(t)$ and $u'(t)$ are respectively the deterministic and random components of the waveform $u(t)$. The deterministic component corresponds to the underlying ensemble average, built from several cardiac cycles. The random component depends on several physical and physiological random factors.

Assuming that, in general, all the cycles start with the same ECG, that T is the period of the waveform and N_c is the number of the cycles available, the ensemble average can be written as

$$U(t) = \lim_{N_c \to \infty} \frac{1}{N_c} \sum_{n=0}^{N-1} u(t + nT), \qquad 0 \le t \le T\,. \tag{3.21}$$

Thus, for a big enough N_c, the random part of the signal can be almost vanished from the result, while any features appearing in the same position on every cycle remain in $U(t)$.

To implement the method, it is necessary to overcome problems like heart rate variability, other "physiological" variations (due to respiration, ventricular contraction and filling, etc.), or the diastole length variability. The differences among the cardiac cycles may have undesirable effects as smoothing or vanishing important features of the waveforms.

After cutting the maximum frequency signals into cardiac cycles using the ECG, the new signals are stored in different data blocks. Without further processing, those

blocks probably contain slight phase variations due to physiological variability and triggering errors.

The PSA is an iterative process that starts by averaging all the cycles to obtain an ensemble average. Every cycle in the average is time shifted according to the lag corresponding to the maximum correlation between the particular cycle and the average. The shifted signals are used to compute a new ensemble average. The process is repeated until a desired convergence criterion is satisfied. The following expressions symbolize the PSA algorithm:

$$U^{i}(t)=\frac{1}{N_c}\sum_{n=0}^{N_c-1}u^{(i,n)}(t) \tag{3.22}$$

$$r_{uU}^{(i,n)}(\tau)=\mathcal{E}\left[u^{(i,n)}(t)U^{i}(t+\tau)\right]\Rightarrow \tau^{*(i,n)} \tag{3.23}$$

$$u^{(i+1,n)}(t)=u^{(i+1,n)}\left(t+\tau^{*(i,n)}\right) \tag{3.24}$$

where, in this case, n denotes an individual waveform, i identifies the current iteration. $r_{uU}(\tau)$ is the result of the cross correlation for lag τ, and τ^{*} is the lag that maximizes $r_{uU}(\tau)$. $\mathcal{E}[\bullet]$ is the expected value operator.

3.4 PROPOSED AVERAGING ALGORITHMS

The averaging methods described above have been developed envisaging the characterization of the maximum frequency waveforms on carotid artery. However, the current goal is to determine average of the four spectral parameters extracted from MCA signals. The revision of the methods for adaptation to the new aims led to the redefinition of the feature and additional points in the WFA and to the development of a new PSA algorithm aiming an efficient computational calculus of the deterministic spectral parameters variation over time.

3.4.1 ADAPTED WAVEFORM MAIN FEATURES AVERAGING

As blood flow behaves differently in carotid artery and MCA, the corresponding maximum frequency waveforms also present different characteristics. The redefinition of MCA main feature points was conducted by visual analysis of several maximum frequency waveforms extracted from clinical signals (an example in Figure 3.5), and the resulting features are presented in Table 3.3.

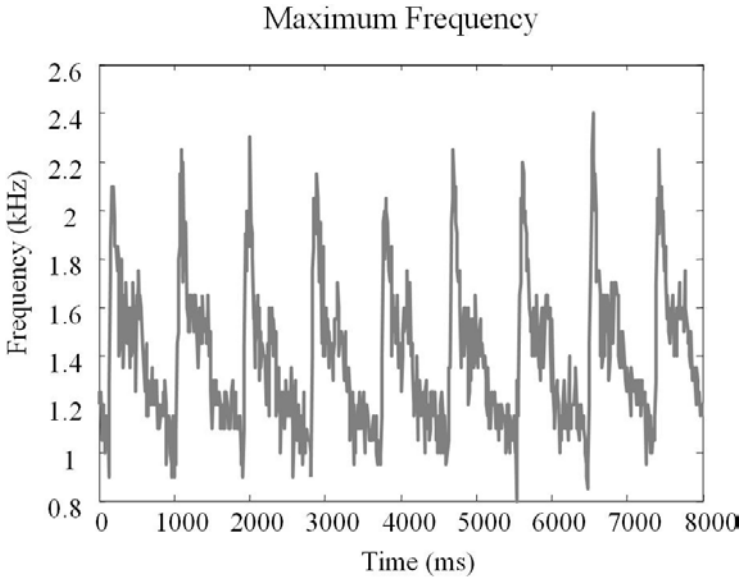

Figure 3.5 – MCA maximum frequency waveform extracted from clinical data.

As the mean frequency and rms bandwidth variation roughly follow the behaviour of the maximum frequency, the same feature points can be used to average those waveforms.

FEATURE POINTS DESCRIPTION		
For each cycle	Amplitude values	Time values
Pulse-foot	Amplitude at pulse-foot occurrence	Time at pulse-foot occurrence
	Maximum systolic	Time at maximum systolic
	Maximum amplitude after maximum systolic	Time at maximum value after maximum systolic
	Minimum amplitude between maxima	Time at minimum value between maxima
Maximum deceleration between maxima	Amplitude at maximum deceleration between maxima	Time at maximum deceleration between maxima
Maximum acceleration during systolic rise	Amplitude at maximum acceleration on systolic rise	Time at maximum acceleration on systolic rise

Table 3.3 – Description of the feature points for middle cerebral artery spectral parameters waveform when clinical data is considered.

As the original WFA algorithm, additional points are also used on the adapted version. However, in this case, a fixed number of points are placed between any two consecutive feature points, and after the last feature point.

After averaging the frequency points and the time points, the signal is interpolated to build the reference waveform.

3.4.2 NEW PHASE SHIFT AVERAGING ALGORITHM: SEQUENTIAL PHASE SHIFT AVERAGING

The original PSA algorithm is an iterative algorithm depending on a subjective convergence criterion.

Remember that $\tau^{*(i,n)}$ is the lag that maximizes the correlation between the n^{th} waveform in the clinical signal and the $(n-1)^{th}$ average, for the i^{th} iteration. The ideal convergence criterion should be

$$\sum_{n=0}^{N-1} \tau^{*(i,n)} = 0 \tag{3.25}$$

to guarantee that all the waveforms are, as much as possible, in phase with the average. However, the waveforms that are set in phase with the average at any time can become displaced on the next iteration. On one of the tests done to study this method, the convergence criterion was not accomplished; and on the others, several iterations were required to satisfy the condition (3.25) [Leiria *et al.*, 2004].

The reformulated PSA algorithm, described next, aims to overcome the lack of convergence identified in the original PSA.

In this new approach, one of the cycles is taken as reference for phase shifting. Each one of the remaining waveforms is cross-correlated with the reference, is shifted according to the lag corresponding to the maximum correlation, and then it is added to the reference. The final ensemble average is the resulting sum of all the waveforms divided by N_c.

To improve the efficiency of the process, the reference waveform is updated at each step, with the sum of the most recently shifted waveform; and the cross-correlation is performed over the normalized gradient of the waveforms.

According to this new formulation, a computationally fast sequential algorithm substitutes the previous iterative process, and the convergence criterion (3.25) is always

satisfied. For that reason, the new method was called Sequential Phase Shift Averaging (SPS).

The sequence of mathematical expressions for the new SPS algorithm is

$$r_{Su}^{n}(\tau)=\mathcal{E}\left[\left(\frac{\partial\left(S_n(t)/\max\left(S_n(t)\right)\right)}{\partial t}\right)\left(\frac{\partial\left(u_n(t+\tau)/\max\left(u_n(t)\right)\right)}{\partial t}\right)\right]\Rightarrow\tau_n^{*} \quad (3.26)$$

$$S_n(t)=S_{n-1}(t)+u_n\left(t+\tau_n^{*}\right) \quad (3.27)$$

$$U(t)=S_{N_c}(t)/N_c \quad (3.28)$$

assuming the same nomenclature as in Section 3.3.2.2. $S_n(t)$ is the sum of the $n+1$ already shifted waveforms.

3.5 IMPLEMENTATION OF THE AVERAGING METHODS

For this study, the Medical Physics Department of the University of Leicester in United Kingdom kindly provided clinical signals from MCA obtained with TCD instrumentation.

This section follows with the description of those clinical signals and the choices made to transform them into the time-frequency domain. The computational implementation of the methods, and the details of several decisions required to proceed with that implementation, will also be described.

Matlab Version 6 Release 13 was used to implement the work described in this chapter, including the computational tools used for the analysis of the results.

Figure 3.6 shows a schematic representation of the relationship between the methods of averaging and the methods of delimiting the cardiac cycles studied in this work.

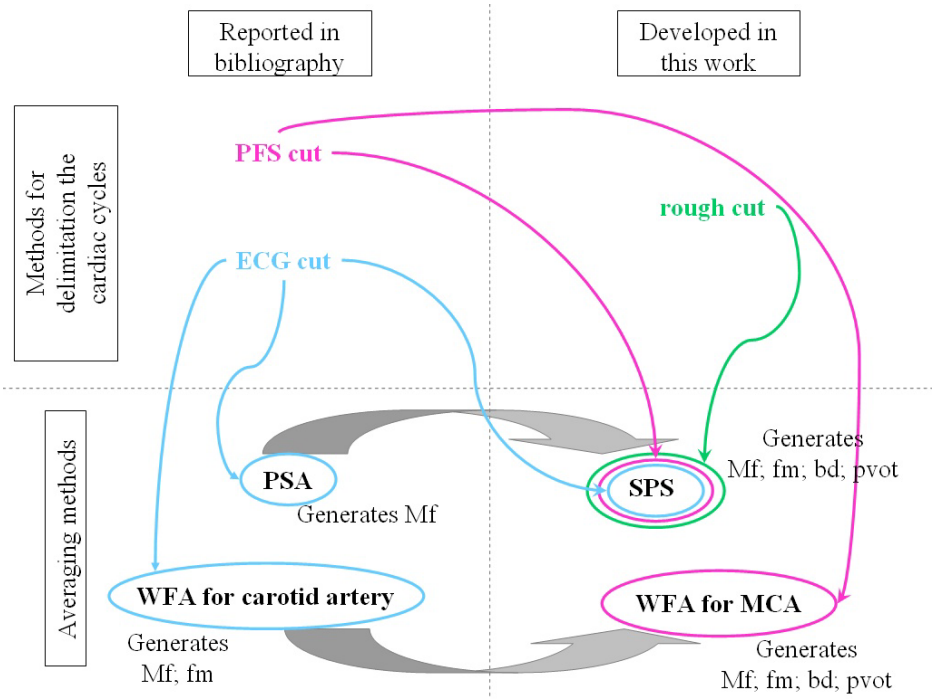

Figure 3.6 – Averaging methods and methods for delimitating the signals studied in this work.

3.5.1 CLINICAL SIGNALS

Some of the signals provided by the University of Leicester are free of embolic events. These signals, taken from eight different healthy adults, include 240 complete heartbeats. For each of the examined individuals Doppler and ECG signals were simultaneously collected and stored on the same data file.

The Doppler data were obtained with a probe of two Megahertz, directed with an angle between 0º and 30º, and a 12.5 kHz sampling frequency was used.

Details of the heart rate of these signals are presented in Table 3.4.

File ID	Approximate Maximum heart rate (min^{-1})	Approximate Minimum heart rate (min^{-1})	Approximate Mean heart rate (min^{-1})	Number of complete cycles	Case
FILE1	64.44	74.30	68.52	30	B
FILE2	85.59	101.75	92.51	38	A
FILE3	55.50	60.11	58.24	28	B
FILE4	44.19	68.36	53.54	23	B
FILE5	62.09	68.85	65.11	38	B
FILE6	66.43	72.21	69.79	30	A
FILE7	45.05	59.72	53.45	24	B
FILE8	50.37	67.95	57.50	29	B

Table 3.4 – Heart rates of the clinical signals

The column "Case" establishes the relationship between the characteristics of the signals and the choice of the capture window defined in Table 3.1. Notice that the signals used to determine the values in Table 3.4 were obtained from adults, and thus Cases A and B do not correspond to the normal and low heart rate definition (defined for neonates) used in Table 3.1.

3.5.2 TIME-FREQUENCY REPRESENTATION

At this stage, Doppler signals spectral representation was obtained through the classical method, the STFT. The window function used was the Hanning window (as it was reported) to reduce the undesirable signal loss of energy to the side lobes, as already discussed in the last chapter [Guo *et al*., 1994] [Cardoso *et al*., 1996a] [Leiria *et al.*, 1999].

Doppler blood flow signals are usually considered stationary for periods lower than 10–20ms [Evans, McDicken, 2000]. To fulfil these requirements, 20ms windows were tested on the MCA clinical signals. The variations of the spectral parameters (maximum frequency, mean frequency, rms bandwidth, and power variation over time) obtained were too irregular, leading to inaccurate identification of the feature points. For that reason, the results reported in this chapter were derived using 40ms windows with

50% of overlap. Preliminary tests showed that, this window-overlap pair of values allows a time resolution short enough not to loose truly important features of the signal, and long enough to avoid the previously mentioned inaccuracy. These STFT parameters were used in this study despite from the published stationarity limits not being respected with such window length.

Figure 3.7 shows the result of the application of the STFT, with the chosen parameters, to a segment of one of the clinical data files.

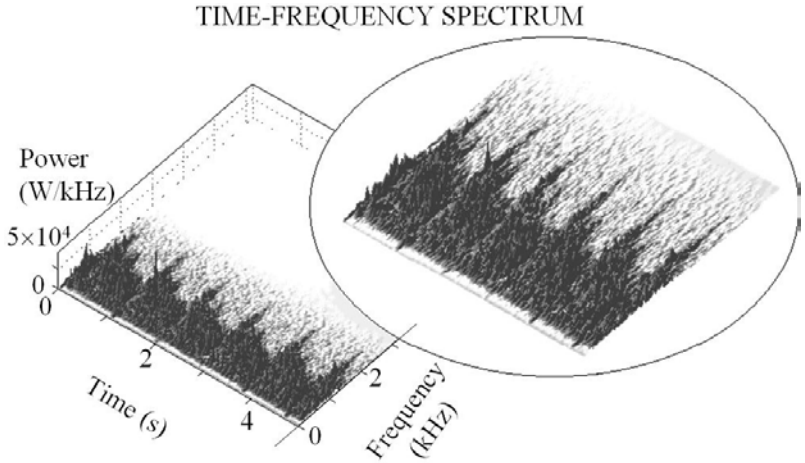

Figure 3.7 – Time-frequency representation of a denoised MCA Doppler blood flow signal. The significant part of the spectrum is shown in detail.

The waveforms to be cut and averaged are extracted from the denoised[12] time-frequency spectrum. The waveforms extracted from the spectrum in Figure 3.7, are shown in Figure 3.8.

[12] Through a soft-thresholding function from Matlab

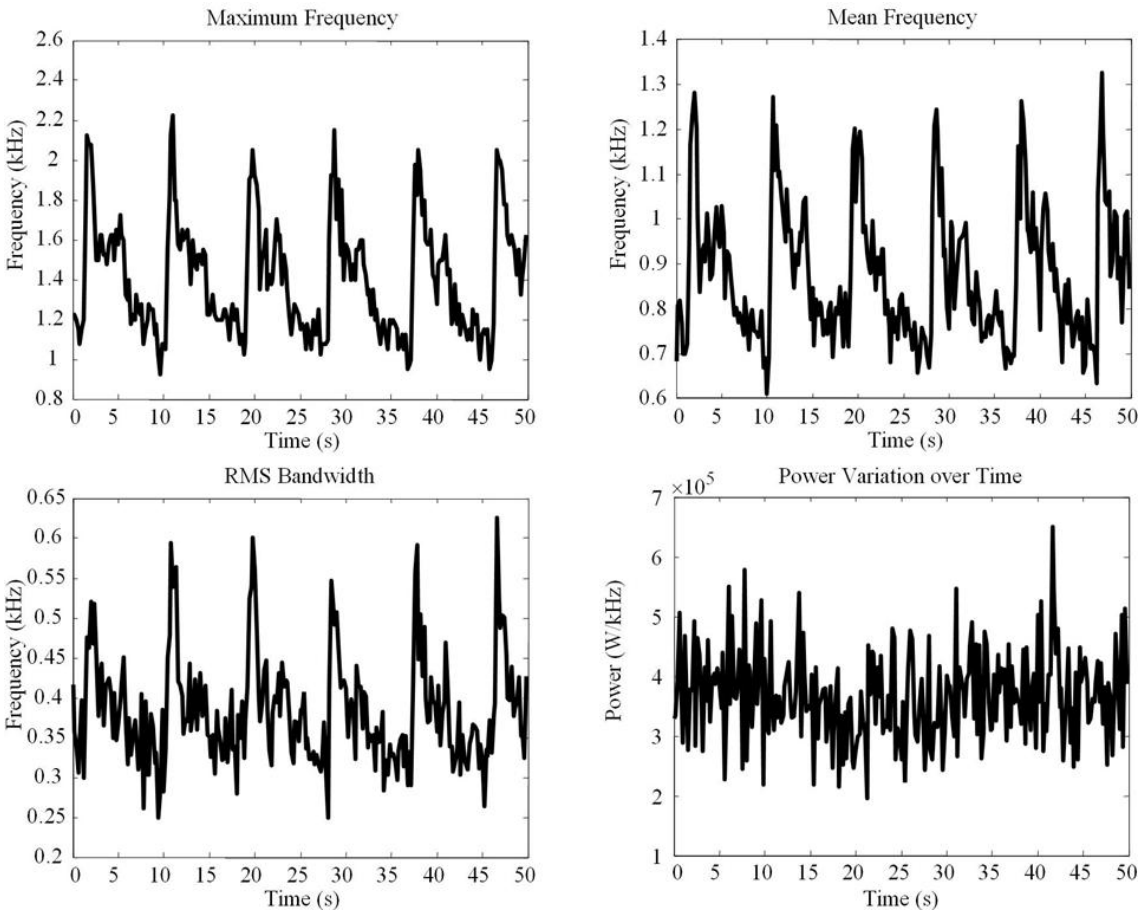

Figure 3.8 – Spectral parameters waveforms taken out of a MCA Doppler signal

To be noticed from Figure 3.8, that the power variation over time does not follow the shape of the other curves.

3.5.3 SIGNALS DIVISION INTO CARDIAC CYCLES

Each of the eight embolic-free signals contains at least 23 complete cardiac cycles. The delimitation of all the cardiac cycles in the signals must be clearly identified before averaging.

The implementation of the two algorithms already described (ECG and PFS) and the suggestion of a new algorithm (rough-cut) to cut the signals are summarized next.

All these recursive algorithms require the input of the initial values of various parameters. These values are adjusted until a proper delimitation of the cycles in the signals is achieved.

3.5.3.1 Delimitation using electrocardiograms

The theory associated with this method has been described in Section 3.3.2.1.

The ECG signals in the files do not correspond to a standard lead. Figure 3.9 shows a fraction of one of the signals.

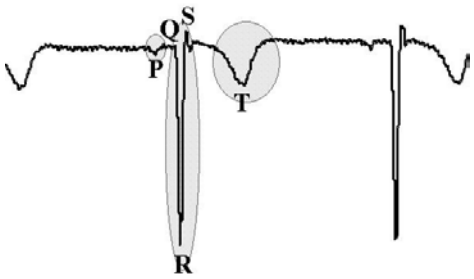

Figure 3.9 – Typical appearance of the clinical ECG signals.

Nevertheless, the identification of the cycles can be done as described in 3.3.2.1, as the R wave is still the most prominent feature of the ECG.

To improve the efficiency of the algorithm, the first differential of the ECG was submitted to a previous segmentation based on the PFS method. Thus, the gradient is divided into sections, each one containing $N1$ points calculated according to the heart rate. The local maxima are detected and flagged on the gradients. Any spurious maxima can be removed as described for the PFS algorithm, in Section 3.3.2.1.

The minima found between any maxima and the $M2$ bins before it, are also flagged. The R waves are identified as the zeros between maxima and minima. Transferring the location of the R waves to the Doppler signal identifies the start of the cardiac cycles in the spectral waveforms.

Each cardiac cycle can be stored in a different file. However, in the current application, the signals are maintained unbroken, and the flags are saved separately.

The initial values of some parameters of the algorithm, have to be defined before execution. These parameters are the length of the segments ($N1$), the upper limit of the range where spurious maxima can be found ($M1$), the amplitude below which any flagged maxima is excluded (rf), and the lower limit of the range where minima can be found ($M2$).

Although there are not enough cycles in the signals to allow generalization, empirical trials with the available data, lead to the choice of the initial values presented in Table 3.5.

Parameter	Value
N1	see Table 3.1
M1	*N*/2
rf	0.95
M2	187.5×f_s

Table 3.5 – Values of the parameters to use on the ECG signals division (first approach)

According to Table 3.1, Table 3.4 and Table 3.5, the parameters used to run the ECG division of the clinical signals are presented in Table 3.6. The automatic classification was submitted to visual inspection, and in some cases, a manual correction was required.

	N1/f_s	*M1*/f_s	*rf*	*M2*/f_s
FILE1	750	375	0.95	187.5
FILE2	375	187.5	0.95	187.5
FILE3	750	375	0.95	187.5
FILE4	750	375	0.95	187.5
FILE5	600	300	0.95	187.5
FILE6	375	187.5	0.95	187.5
FILE7	750	375	0.95	187.5
FILE8	750	375	0.95	187.5

Table 3.6 – Parameters used to divide ECG on each file

Figure 3.10 depicts the steps of the algorithm to delimit the cycles using the ECG signal.

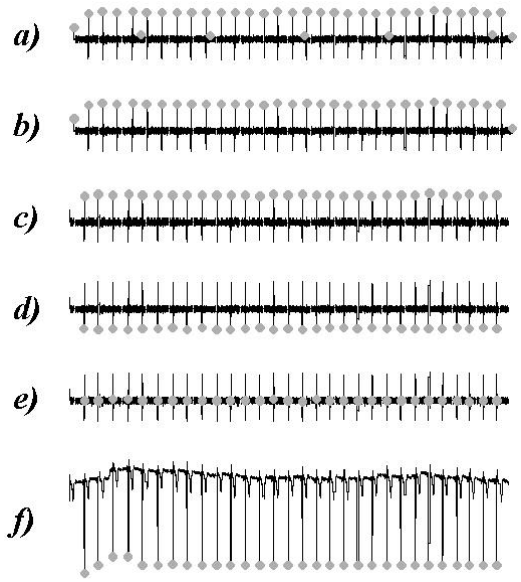

Figure 3.10 – ECG division by R wave: *a)* Maximum of each segment of length *N1*; *b)* After removal of extra flags (using *M1*); *c)* Final removal of the remaining extra flags (using *rf*); *d)* Minima before maxima (using *M2*); *e)* Zero-crossing; *f)* R wave flagged in the ECG signal

3.5.3.2 Pulse Foot Seeking

The theory of this method was given in Section 3.3.2.1.

The implementation of the PFS was done following the algorithm schematised in Figure 3.4. The initial values required for running the algorithm are defined in Table 3.7.

Parameter	Value	Description
N1	see Table 3.1	Length of the segments
M1	*N*/2	Upper limit for removing boundary flags
rf	0.95	Amplitude below which extra flags are removed
M2	187.5*f_s	Lower limit for finding the maxima of first gradient
M3	100*f_s	Lower limit for finding the pulse-foot of the waves

Table 3.7 – Description and first approach to the values of the parameters to be used in the PFS

According to Table 3.1, Table 3.4 and Table 3.7, the parameters for each clinical file are presented in Table 3.8. The *rf* parameter was adjusted according to the amplitude of the signals maximum frequency, and in some cases the other parameters were adjusted by the user.

	$N1/f_s$	$M1/f_s$	rf	$M2/f_s$	$M3/f_s$
FILE1	750	375	0.8	187.5	100
FILE2	375	187.5	0.95	187.5	100
FILE3	750	375	0.95	187.5	100
FILE4	750	375	0.8	187.5	100
FILE5	600	300	0.8	187.5	100
FILE6	375	187.5	0.95	187.5	100
FILE7	750	375	0.8	187.5	100
FILE8	750	375	0.8	187.5	100

Table 3.8 – Parameters used to find pulse-foot of the cycles on each file

Figure 3.11 shows the process of finding the pulse-foot on some cycles contained in one of the data files. The waveform used was the maximum frequency.

Figure 3.11 – Cycles identification by PFS. *a)* Original maximum frequency waveform; *b)* Maximum of each segment, after the moving average, defined by *N1*; *c)* After removal of extra flags (using *M*1); *d)* Final removal of the remaining extra flags (using *rf*); *e)* Maxima of the first gradient (using *M2*); *e)* Maximum rate of change of the gradient (using *M*3); *f)* Pulse-foot flagged on the moving average of the maximum frequency waveform.

3.5.3.3 Rough cut of the signal

As the delimitation of the signals involves the later phase shifting of the cycles, there is no need for an accurate determination of the beginning and end of each

heartbeat. A satisfactory solution can be reached if the flags are set before the start of each cardiac cycle and if between any two flags there is one and only one systolic peak.

The algorithm developed in this work to achieve this solution consists of multiplying the waveform by sliding rectangular windows. Each cardiac cycle in the waveform can be defined as

$$u_n(t) = x(t)w(t + nM1), \tag{3.29}$$

where $x(t)$ is a signal containing several cycles and $w(t)$ is a rectangular window. $M1$ is the length of the window, and must be larger than the average length of the cardiac cycle.

Overlapping of the windows may be necessary due to the variability of the duration of the cardiac cycle.

After several trials, the initial window length was settled as the nearest integer to $(60/hbr) \times f_s \times 1000$, where hbr is a theoretical heart rate, and the starting overlap 0%. For $hbr = 70$ cycles/min, the initial values of the parameters are shown in Table 3.9

Parameter	Value
Window length	$857.1 \times f_s$
Step	$857.1 \times f_s$

Table 3.9 – First approach to initial values of the parameters for rough division of spectral waveforms.

Table 3.11 presents the parameters after being adjusted by the user.

	Window length/f_s	**Step/f_s**
FILE1	1200	860
FILE2	860	640
FILE3	1400	1020
FILE4	1240	1120
FILE5	1060	940
FILE6	860	860
FILE7	1260	1120
FILE8	1100	1040

Table 3.10 – Parameters used for the rough division of the signals from each file.

The division of one of the maximum frequency of one of the signals is displayed in Figure 3.12.

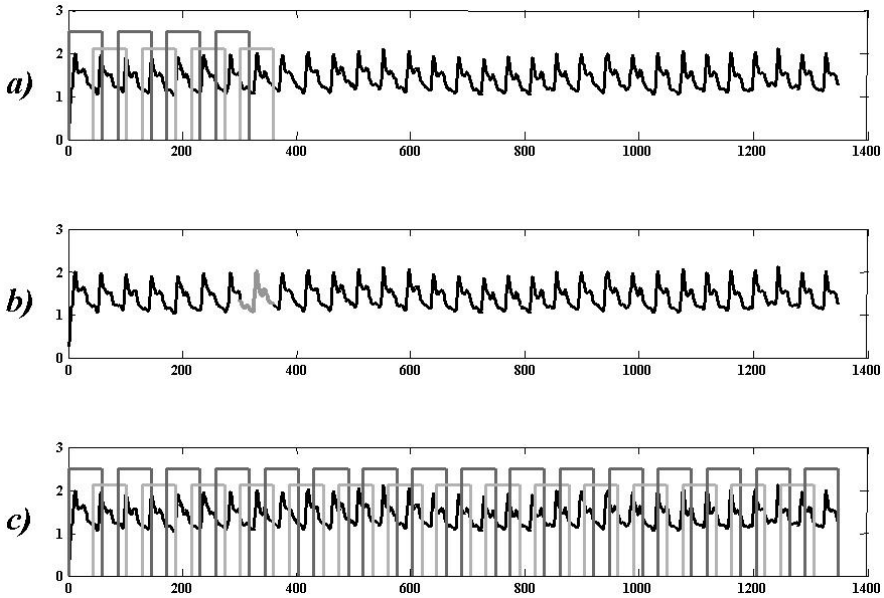

Figure 3.12 – Rough identification of the cardiac cycles. *a)* the process of delimitation of the cycles; *b)* the portion of the file that will be in the current segment appears distinguished; *c)* all the cycles within the file delimited by the windows.

3.5.4 ADAPTED WAVEFORM MAIN FEATURES AVERAGING

The theory of this method is given is Section 3.3.2.2.

As the start of the cardiac cycles and the systolic peaks are required, the WFA algorithm can use PFS to determine these two feature points. For that reason, the ECG is not necessary in this implementation.

The next step is to find two maxima in the signal gradient. One located in the range between the $M3$ and $M3+M4$ points after the systolic peak and another within the next $M5$ bins. The minima located between the two maxima are flagged. Next, the first differential of maximum frequency (the acceleration of the blood flow) is computed. The maximum acceleration between any pulse-foot and systolic maximum, and the minimum acceleration between any systolic maximum and minimum (found before) are marked. A pre-determined number of additional points are then placed and equally spaced between any two consecutive feature points, and between the last feature point and the start of the next cycle.

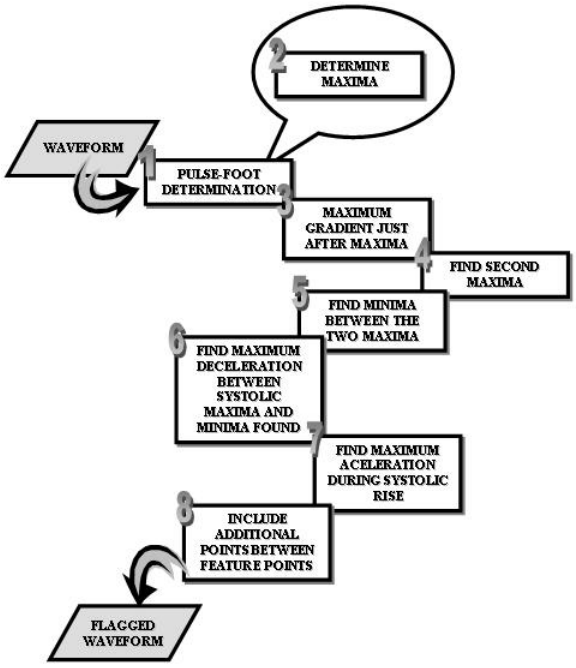

Figure 3.13 – Schematic representation of the WFA algorithm

The choice of the parameters is an iterative process. Table 3.11 shows the parameters used in this method along with their initial values.

FEATURE POINTS		
Feature points	Identification	Values
Pulse-foot	See Table 3.7	See Table 3.7
Systolic peak		
Maximum gradient after systolic peak	*M3*	0
	M4	350*f_s
Maximum value after systolic peak	*M5*	*N1*/2
Additional points	Between pulse foot and systolic peak	160*f_s points
	Between systolic peak and minimum after it	120*f_s points
	Between second maximum and end	200*f_s points

Table 3.11 – Parameters used to determine feature points

The values found for parameters according to the files are presented in Table 3.12.

	$N1/f_s$	$M1/f_s$	$M2/f_s$	rf	$M3/f_s$	$M4/f_s$	$M5/f_s$
FILE1	See Table 3.8				0	350	100
FILE2					150	150	100
FILE3					150	200	100
FILE4					150	200	200
FILE5					0	350	100
FILE6					150	200	150
FILE7					150	200	150
FILE8					200	150	100

Table 3.12 – Values used to determine the feature points

Figure 3.14 shows a portion of a file containing four cycles with the feature points flagged on it.

Figure 3.14 – Maximum frequency waveform with feature points

For each feature or additional point, the time and amplitude of its occurrence is obtained from the average of all the cycles.

The final average waveform results from the interpolation of all the average points sorted in ascending time order of occurrence.

For the current implementation, the number of points added by interpolation was such that the sample frequency of the resulting signal became 1kHz (one point per milisecond).

One of the problems with the implementation of the WFA algorithm was related to the synchronization of the four final spectral waveforms. The features of the three frequency parameters (maximum and minimum frequency and rms bandwidth) occur at different times. The differences between the initial point positions of the waveforms (given by the pulse foot) are particularly undesirable when it is required to establish a common start of the cardiac cycle. Additionally, as the power variation over time does not follow the shape of the other waveforms, it is not possible to determine its feature points as described in Table 3.11, and often it is difficult to determine unequivocally some of the feature points on the bandwidth curve (existence of false-positives).

After some experiments, it was decided to apply this method only to maximum frequency waveforms. The determination of the other three spectral waveforms is computed by averaging values at time points define by the feature points from the corresponding maximum frequency waveforms. The time values are taken from the feature and the additional points on the maximum frequency and the new amplitudes are the values that the different spectral parameters assume for each time.

Figure 3.15 shows the averaged waveforms obtained with the WFA, together with the clinical signals that were used to generate them. The waveforms in the figures are normalized to its mean value.

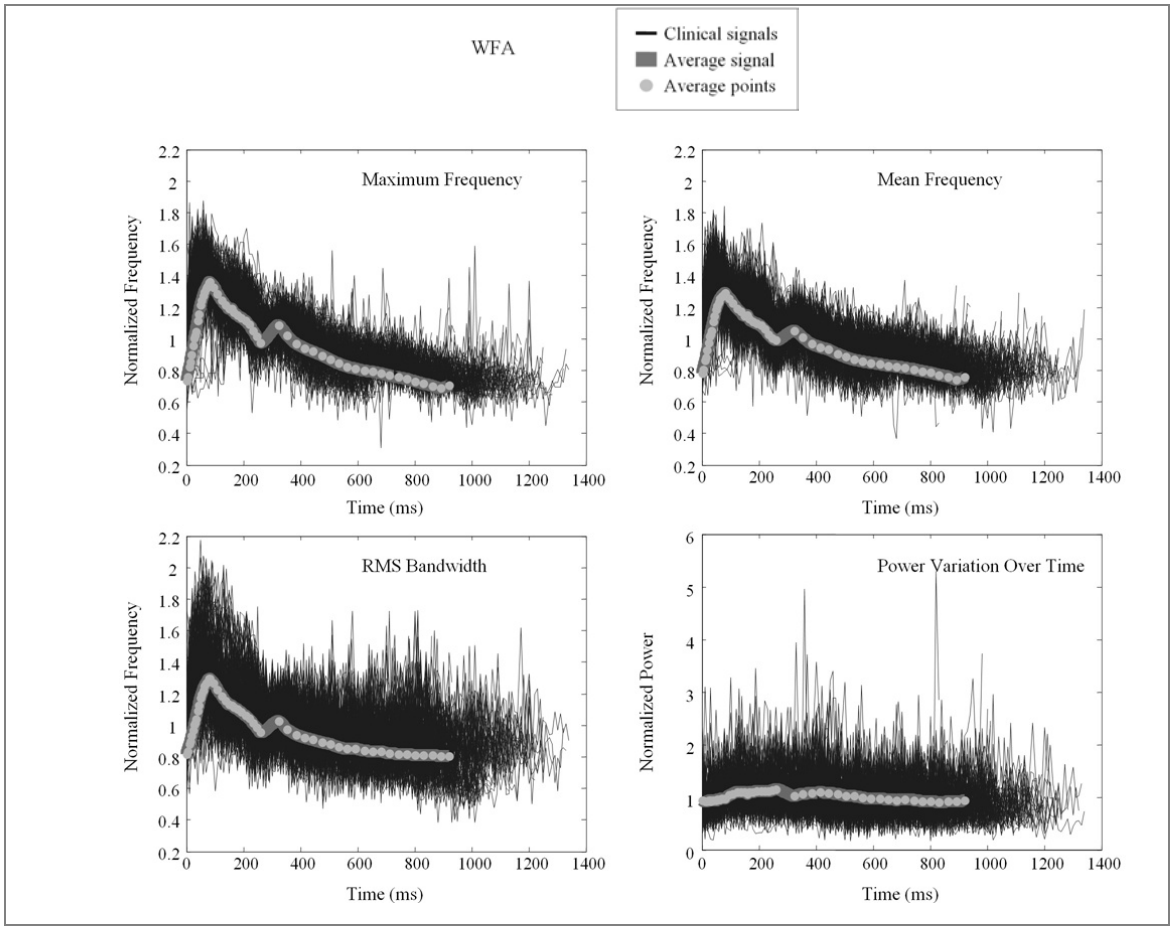

Figure 3.15 – Average signals representing the maximum frequency, mean frequency, rms bandwidth and power variation, generated with the WFA. Clinical waveforms, feature points, and additional points are also represented.

3.5.5 SEQUENTIAL PHASE SHIFT AVERAGING

The SPS (Section 3.4.2) was implemented to work on the maximum frequency waveform. The other spectral waveforms are determined according to the results obtained from the maximum frequency.

The possibility of separating the cardiac cycles in the signals, by any of the three methods described in Section 3.3.2.1, was considered.

The program developed to run this algorithm allows the user to choose the reference cycle to start the process. The normalized maximum frequency gradient of each segment is compared with the normalized gradient of the reference signal, shifted if needed, and added to it. All the other spectral waveforms are shifted according to the maximum frequency and included in the respective sums. After each maximum frequency shift operation, the maximum frequency sum becomes the new reference signal, and the process continues until the last segment from the last file is contained in the sum. The four final sums, divided by the number of clinical cycles used, will give the four average waveforms.

The original PSA was prepared to determine the average behaviour of the maximum frequency during systole and early diastole. The current application requires the estimation of all the events in the cycle. To simulate the end of the cardiac cycle, another point, with the same amplitude of the pulse foot feature and time corresponding to the average duration of the heartbeats, is added to the waveforms.

The resulting averages are interpolated to present values at each millisecond.

Figure 3.16 to Figure 3.18 show the average waveforms obtained with the SPS, considering the three different ways to divide the cardiac cycles (ECG, PFS and rough cut).

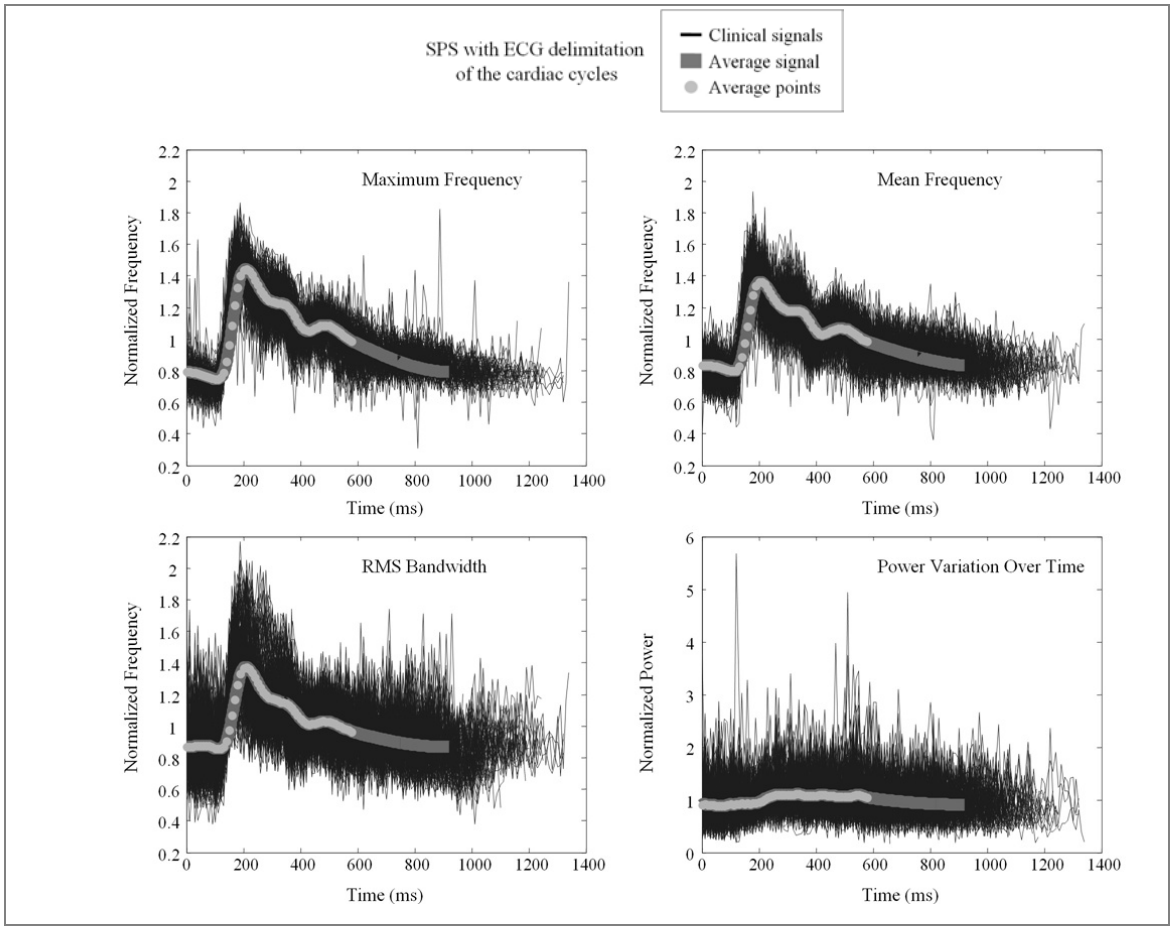

Figure 3.16 – Average signals representing the maximum frequency, mean frequency, rms bandwidth and power variation, generated with the SPS and the ECG. Clinical waveforms, feature points, and additional points are also represented.

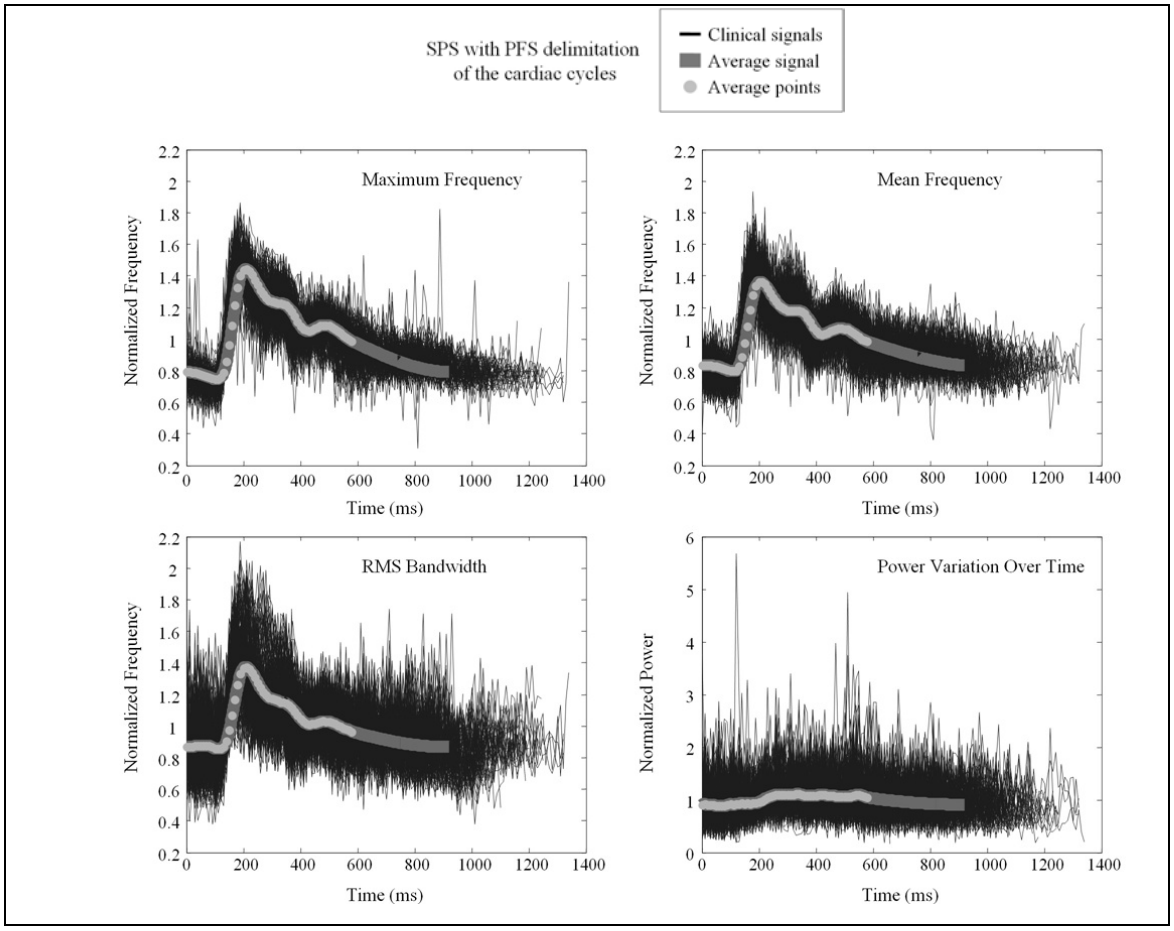

Figure 3.17 – Average signals representing the maximum frequency, mean frequency, rms bandwidth and power variation, generated with the SPS and the PFS. Clinical waveforms, feature points, and additional points are also represented.

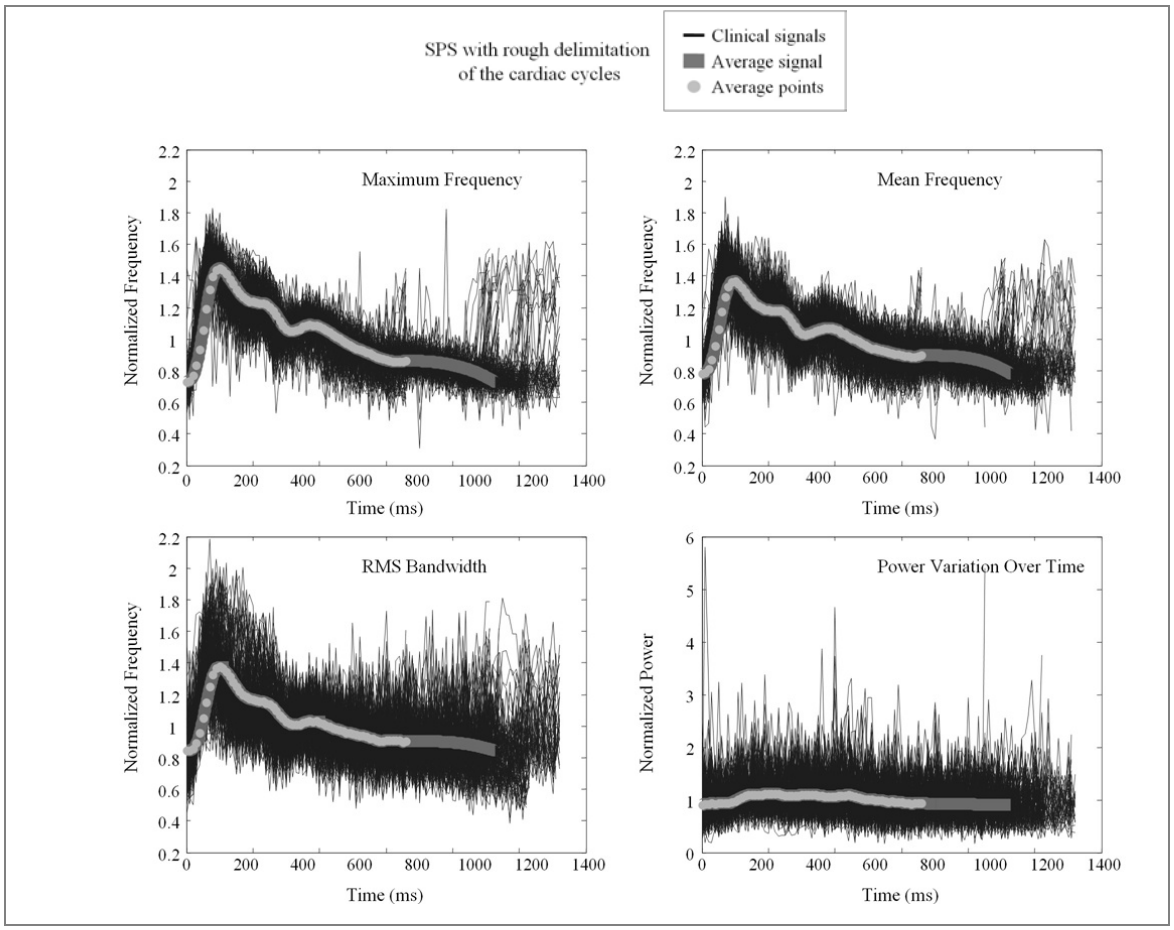

Figure 3.18 – Average signals representing the maximum frequency, mean frequency, rms bandwidth and power variation, generated with the SPS having the signals been roughly cut. Clinical waveforms, feature points, and additional points are also represented.

3.6 RESULTS

Although the SPS method seems to be simpler and faster than the adapted WFA, and that the rough cut of the signal seems to be the easiest way to delimit the cardiac cycle, it is necessary to evaluate the performance of the methods before deciding which method will be used to generate the average waveforms that will feed the simulator.

A quantitative evaluation of the methods may be based on the measurement of the deviations observed between the final average and the clinical signals that were used to generate that average.

The Root Mean Square Error (RMSE) measures how closely each waveform matches the original data. It is defined as,

$$\mathrm{RMSE} = \sqrt{\mathrm{bias}^2 + \sigma_u^2}\ . \tag{3.30}$$

The bias is the actual measure of accuracy. It corresponds to the distance between the average value of all the measurements and the true value, and is given by,

$$\text{bias} = \frac{1}{N}\sum_{n=0}^{N-1}\mathcal{E}[\hat{u}(n)-u(n)]. \tag{3.31}$$

The variance is a measure of the data dispersion around the average point [Gardner, 1990], and can be obtained by

$$\sigma_u^2 = \frac{1}{N}\sum_{n=0}^{N-1}\mathcal{E}\left[\hat{u}(n)-\bar{\hat{u}}(n)\right]^2. \tag{3.32}$$

In the above expressions, $u(n)$ is the true value, $\hat{u}(n)$ the estimated value, and $\bar{\hat{u}}(n)$ the mean estimated value of the samples of the signal $u(n)$ at time n.

Another important measurement of error is the standard deviation around a central point, being given by,

$$\sigma_u = \sqrt{\sigma_u^2} \tag{3.33}$$

This section reports the results obtained from the tests carried out to compare the obtained average waveforms with the waveforms from the original clinical signals. Results concerning the extraction of clinical variables and indexes extracted from the waveforms (see Annex A) are also described in this section.

Another set of tests concerning the SPS is also reported here. These tests were performed to identify which of the cutting methods was more precise with respect to the cut of the signals, and what is the true importance of phase shifting.

The computation for all spectral parameters was performed over normalized parameters, for each cycle, where the normalization is obtained regarding the mean value of the respective parameter. Unless otherwise stated, the normalized power will be considered for the rest of the thesis, as the true power values depend on other factors than only the backscattering coefficient.

Quite often, the errors (i.e., the relationship between the error and the corresponding spectral waveform value) will be presented as percentage values.

Finally, all the clinical waveforms are smoothed before being processed, since for some of the tests, a prior identification of particular feature points is required. Additionally, to correctly identify the features on the bandwidth waveforms, smoothed signals are required.

3.6.1 ADAPTED WAVEFORM MAIN FEATURES AVERAGING

Figure 3.19 presents the errors obtained while using the adapted WFA, between the four average waveforms and the corresponding clinical waveforms used to generate them. The errors were computed for every time bin.

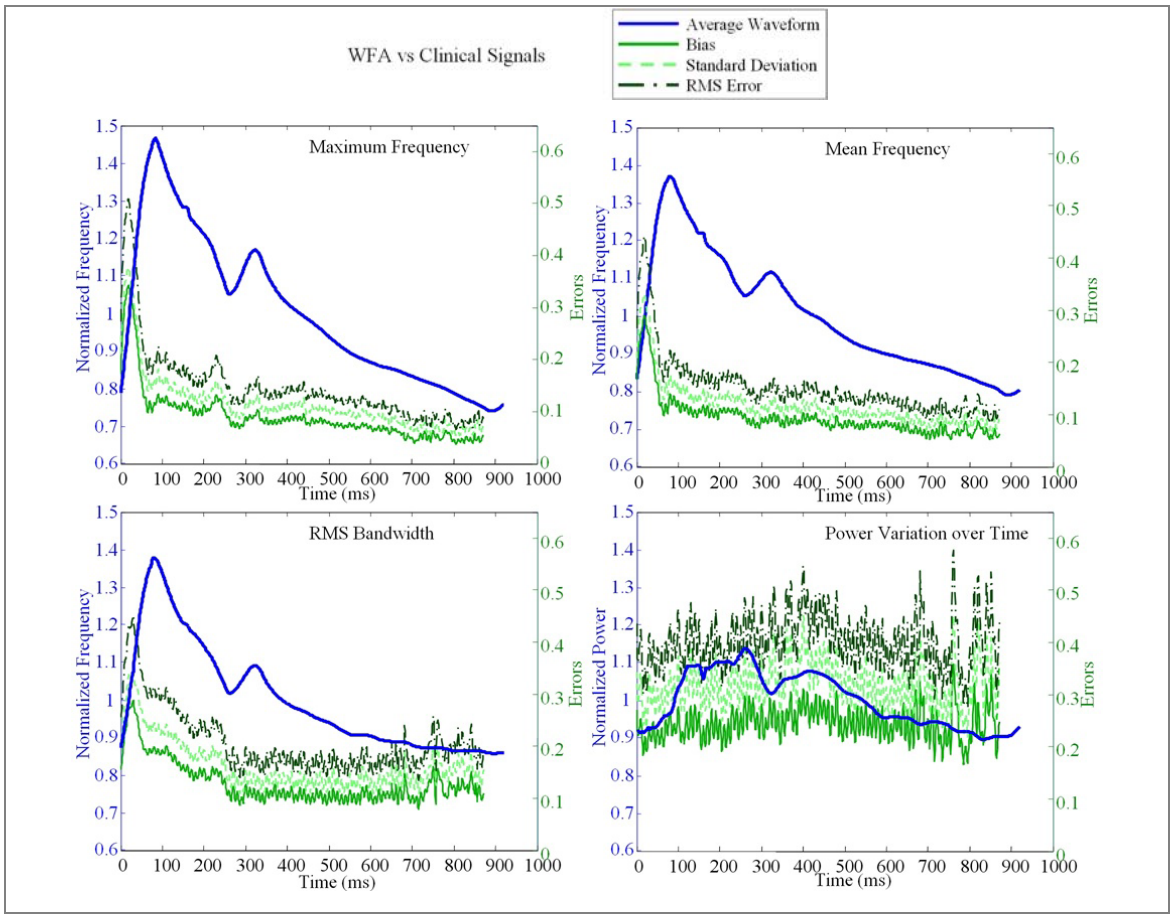

Figure 3.19 – Adapted WFA method: average waveforms errors versus clinical waveforms. Note that the left hand scale refers to the average waveforms and the right hand scale to the errors.

The main errors of the frequency waveforms are localised on the systolic rise, and seem to be gradually decreasing towards the end of the cycle. There are, however, some local maximum errors just before and after the diastolic notch occurrence, and at the end of the curves.

The errors from the power waveform are distributed along the cardiac cycle, although there are some error peaks occurring during the last part of the signal.

Table 3.13 shows the minimum, maximum, and average percentage of errors obtained for all the waveforms.

The time column in the next table and the followings corresponds to the precise time where the percentage error has been measured.

		Maximum Frequency		Mean Frequency		RMS Bandwidth		Normalized Power	
		%Error	Time (ms)	%Error	Time (ms)	%Error	Time (ms)	%Error	Time (ms)
Bias	Minimum	4.80	706	5.97	705	8.35	345	17.36	205
	Maximum	35.69	16	29.51	18	27.53	19	38.87	761
	Mean	8.82		9.32		12.78		24.35	
Std	Minimum	6.93	806	8.19	696	10.53	345	22.63	206
	Maximum	39.29	17	33.76	18	33.80	19	49.22	821
	Mean	11.25		11.68		16.15		31.78	
RMSE	Minimum	8.45	806	10.24	695	13.44	345	28.58	205
	Maximum	53.08	17	44.83	18	43.60	19	62.41	761
	Mean	14.30		14.95		20.59		40.05	

Table 3.13 – Adapted WFA: Minimum, maximum and mean percentage errors between the average and clinical waveforms, and their time of occurrence.

Table 3.13 confirms that, for the three frequency parameters, the most serious errors occur during the first part of the cardiac cycle. This is probably due to the rapid rate of frequency change observed in systole. In addition, in the last part of the cycle no feature point could be identified, so, for all the spectral waveforms, the average at the end of the cycle was only reached through the additional points (see Table 3.11).

Because the higher rate of frequency change is observed in the maximum frequency curve, the higher maximum errors occur on this waveform. As the feature points were taken out from the maximum frequency curve, it was expected that this estimation would present the minimum errors.

Figure 3.20 show the position of the average of some of the feature points taken from the clinical waveforms on the average waveforms. The chosen points are the minimum systolic, peak systolic, diastolic notch and the mean value of the waveforms. These points can be identified visually on the average waveforms and are important to the identification of some common diseases of the cardiovascular system.

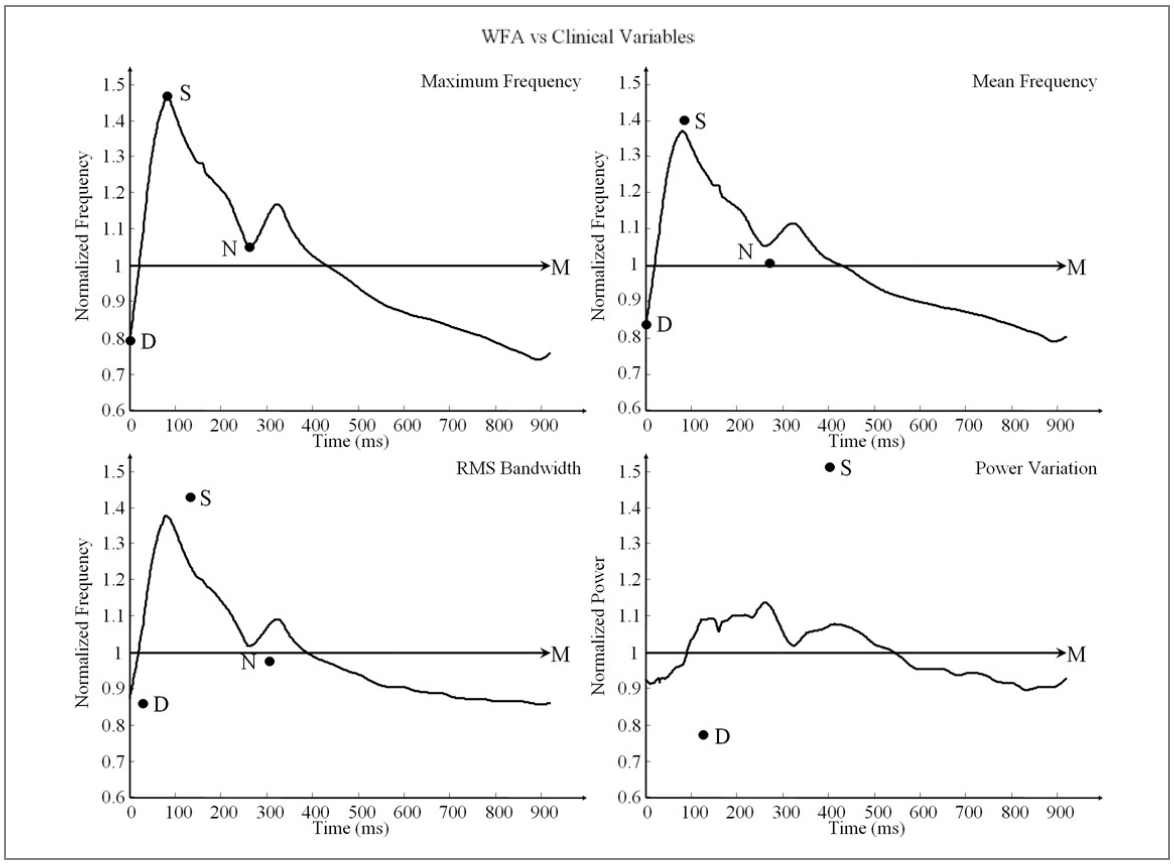

Figure 3.20 – Adapted WFA: some feature points from clinical waveforms versus the average waveforms. The feature points considered are minimum systolic (D), peak systole (S), diastolic notch (N), and mean value (M).

As it was expected, the feature points exactly match the maximum frequency waveform, are close to the average waveform positions for the mean frequency, but present more considerable errors for the rms bandwidth. The feature points do not have any known clinical significance on the power variation waveform; however, the maximum and minimum values are presented to give the idea of the relationship between the values observed in clinical and average curves.

Table 3.14 shows the percentage bias for the clinical variables when the clinical signals are compared to the average waveforms.

% Error	Maximum Frequency	Mean Frequency	RMS Bandwidth	Normalized Power	Weighted Average
Mean Value (M)	0	0	0	0	0
Area under the curve before S (A_1)	8.00	10.69	29.35	N.A.	16.01
Area under the curve after S (A_2)	0.07	0.28	3.47	N.A.	1.27
Systolic Peak (S)	0.04	2.27	3.54	24.82	7.67
Minimum Value (D)	0.45	0.39	1.36	N.A.	0.74
Diastolic Notch (N)	0.02	4.37	3.88	N.A.	2.76

Table 3.14 – Adapted WFA: percentage errors for clinical variables obtained from the comparison of clinical waveforms with average waveforms.

There was no error on the estimation of the mean values of the waveforms. Except for the minimum value, the maximum frequency averaged curve presents a better representation of the clinical variables. Although the rms bandwidth errors are higher than the other frequency waveforms, notice that except for the area before systole those errors do not exceed four percent.

3.6.2 SEQUENTIAL PHASE SHIFT AVERAGING

The same initial reference signal was used for the three variations of the SPS, to avoid unfair comparisons. However, before analysing the performance of the method, it is important to compare the performance of the cut through the ECG and PFS and to study the importance of phase shifting the signals.

3.6.2.1 Analysis of the performance of the cut of the signals

Figure 3.21 shows the shifts performed on each cycle, during the execution of the SPS when the signals were divided through the ECG and through the PFS.

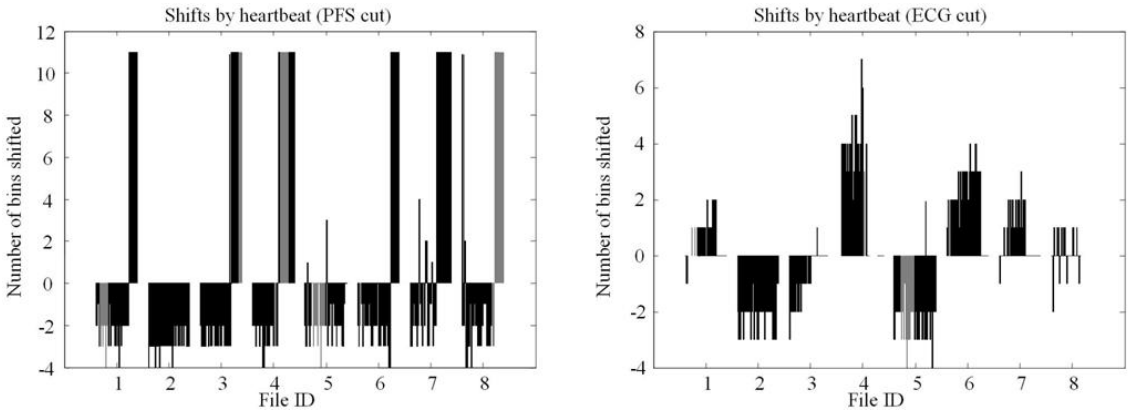

Figure 3.21 – SPS: amount of shift suffered by the cycles (each bin corresponds to 20ms).

In Figure 3.21 File ID identifies each of the eight files of clinical signals (see Table 3.4). Each file contains several cardiac cycles that were shifted. The amount of shift, required for each cardiac cycle in a file, is represented above the File ID.

Looking at the graphs in Figure 3.21, it is clear that the amount of shifts that were introduced by the PFS on each cycle (on the left side) was much higher than the amount of shifts on the signals cut using ECG (on the right). This fact is also due to the reference signal chosen. As the signals cut through the PFS algorithm start with pulse-foot of the maximum frequency waveform, the reference cycle was chosen in order to start a little before that event. This way all the cycles had to be shifted, at least by the duration of the additional points at the end of the signal, to make sure that the average waveform would also include the occurrences immediately before the pulse-foot.

At first sight, it looks like the signals from the ECG cut present a more irregular behaviour although that conclusion might be conditioned by the difference between the graph scales and because of the choice of the reference signal, meaning that this method could be other than the one leading to a minor amount of shifts.

Figure 3.22 shows the results that would have been obtained if the ideal reference waveform were chosen.

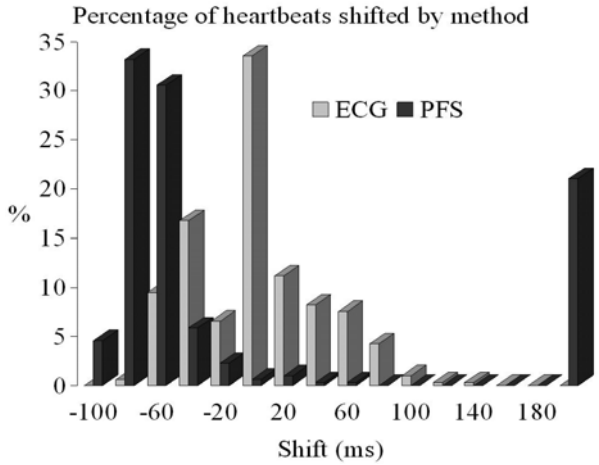

Figure 3.22 – Percentage of heartbeats shifted by amount of shift for each method

The first conclusion is that cutting with the PFS results on a more inaccurate division. Notice that there are cases of phase differences of 200ms (140ms is the maximum for ECG cut), and around 68% of the shifts are performed for more than 60ms left. On the average, the cycles cut with PFS suffer shifts of 9.7ms left (corresponding to 0.49 bins), and the ones cut with ECG suffer shifts of 1ms right (corresponding to 0.05 bins)

Nevertheless, on both cases, the majority of the cycles have to suffer shifts, so, shifting the cycles is an indispensable procedure for obtaining an average waveform.

3.6.2.2 Analysis of the importance of phase shifting the cycles

To better understand the importance of shifting, Figure 3.23, Figure 3.24, Table 3.15 and Table 3.16 show the comparison of the final averages with and without shifting the cycles.

The waveforms obtained for each parameter are not exactly coincident with the non-shifted versions of the same waves. Unexpectedly, for all the spectral parameters, the average based on the ECG divisions is more dependent on the phase shifts, given the results showed in Figure 3.22.

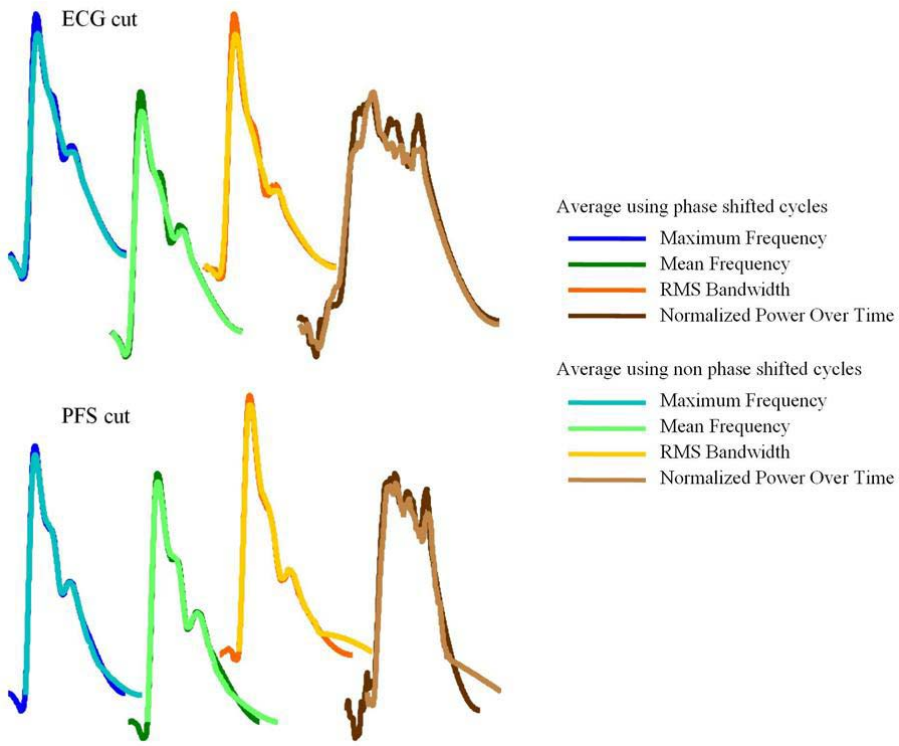

Figure 3.23 – Comparison of the average waveforms when the signals are set in-phase and when are used directly from cut. Signals cut through the ECG on the top and through the PFS on the bottom.

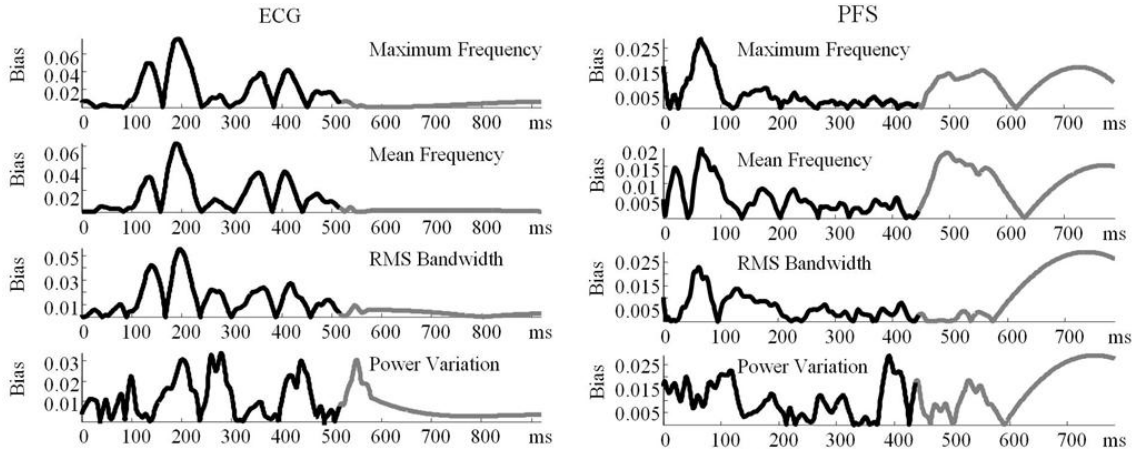

Figure 3.24 – Comparison of the average waveforms when the signals are set in-phase and when are used directly from cut. Signals cut through the ECG on the right and through the PFS on the left.

Figure 3.23 shows that the feature points of the ECG are smoother than the non-shifted signals. As the amplitudes of the waveforms obtained with the two phase-shift approaches are similar, this behaviour can only be understood if the errors are related to the characteristics of the reference signal. However, some tests performed with different reference signals were not conclusive, since the PFS seems to present results that are

always more accurate. The possible explanation is the influence of the first points before the systolic rise, as they are present in the ECG clinical cycles but the PFS based approach does not have to deal with them. Detailed observation of Figure 3.24 seems to support this conclusion, since ECG based averages present low bias values at early systole.

A curious observation is that the ECG based average is more accurate at the end of the cycle, contrarily to what happens with the PFS based average. This has nothing to do with the phase shifting, but instead with the additional point placed at the end of the cycles, after averaging. Because the cycles from non-shifted PFS start later than the shifted ones (see Figure 3.23) the frequency (or the normalized power) considered for the last point is considerably different, what does not happen on the ECG derived cycles.

During the rest of the cycle, the PFS versions are much closer to each other than the ECG ones. On both cases, it seems probable that some features are lost or masked, or even overvalued with the non-shifting approaches.

ECG	Maximum Frequency (kHz)	Mean Frequency (kHz)	RMS Bandwidth (kHz)	Normalized Power
Maximum Error	0.0766	0.0624	0.0561	0.0339
Mean Error	0.0126	0.0095	0.0104	0.0094
Minimum Error	0	0	0	0

Table 3.15 – ECG based delimitation: bias between average waveforms when built with signals set in-phase and with signals obtained directly from cut (signals with expanded cycles).

PFS	Maximum Frequency (kHz)	Mean Frequency (kHz)	RMS Bandwidth (kHz)	Normalized Power
Maximum Error	0.0291	0.0201	0.0292	0.0287
Mean Error	0.0082	0.0079	0.0093	0.0125
Minimum Error	0	0	0	0

Table 3.16 – PFS based delimitation: bias between average waveforms when built with signals set in-phase and with signals obtained directly from cut (signals with expanded cycles).

3.6.2.3 Electrocardiogram delimitation

Figure 3.25 shows the errors between the average waveforms obtained with the SPS for cycles delimited through ECG, and the clinical signals used to generate them.

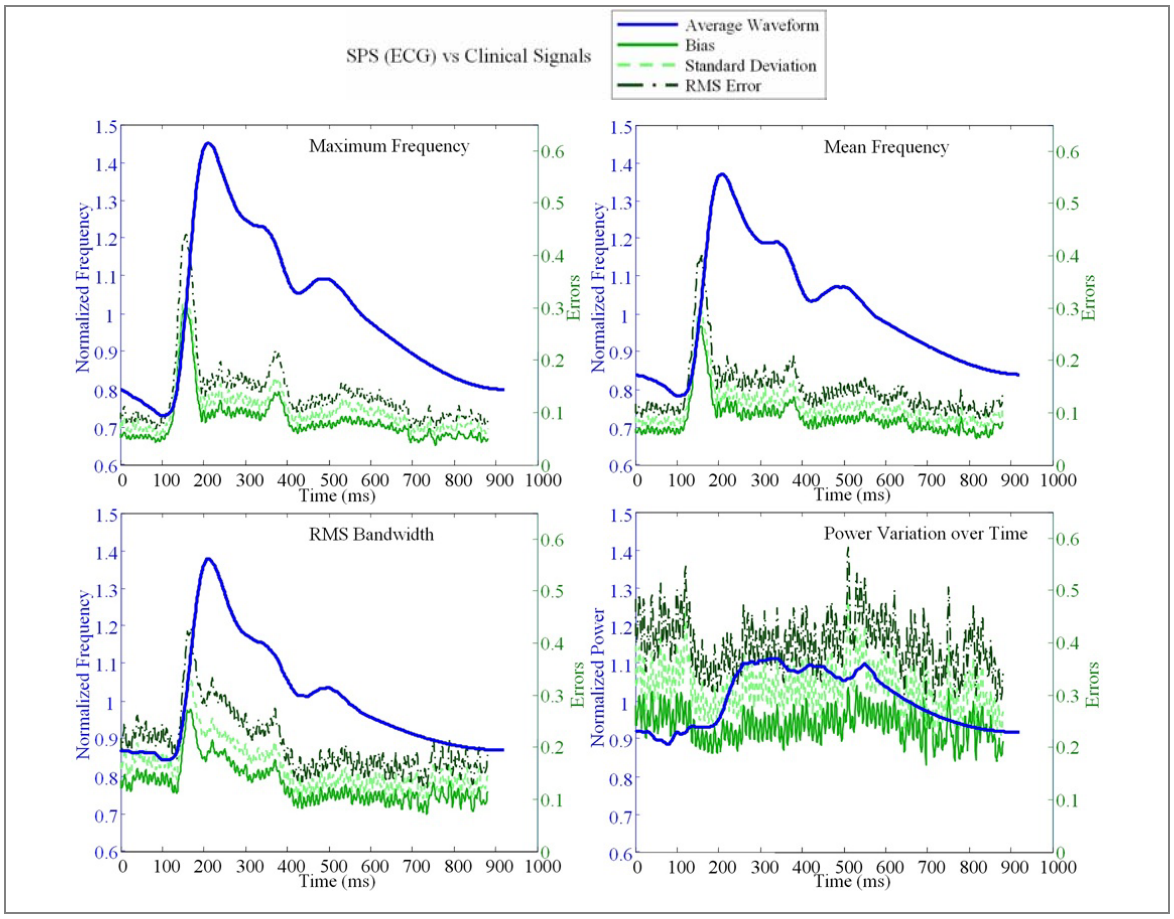

Figure 3.25 – SPS method with ECG delimitation: average waveforms errors versus clinical waveforms.

The apparent almost random behaviour of the clinical signals power variation, leads to a mean RMSE of almost 40%, but the mean bias between the clinical signals and the average waveform stays near 24%.

The errors distribution is similar to the one obtained with the adapted WFA. There are no other truly relevant observations from the figures, although from Table 3.17, which presents the percentage errors, it is worth to verify that the rms bandwidth and the mean frequency present lower maximum errors than the maximum frequency. This was not expected, as the signals were set in-phase through the maximum frequency waveform. However, the higher amplitude of the maximum frequency waveform may justify that.

		Maximum Frequency		Mean Frequency		RMS Bandwidth		Normalized Power	
		%Error	Time (ms)	%Error	Time (ms)	%Error	Time (ms)	%Error	Time (ms)
Bias	Minimum	4.38	755	5.93	817	7.84	735	17.15	696
	Maximum	31.30	149	27.18	149	26.12	159	33.78	40
	Mean	8.35		8.97		12.81		24.20	
Std	Minimum	6.40	695	8.15	665	10.35	425	23.12	645
	Maximum	33.24	149	30.46	149	31.21	159	50.81	120
	Mean	10.45		11.21		16.09		31.52	
RMSE	Minimum	7.86	755	10.31	825	13.24	436	29.59	355
	Maximum	45.66	149	40.82	149	40.70	159	59.72	120
	Mean	13.38		14.36		20.57		39.75	

Table 3.17 – SPS method with ECG delimitation: Minimum, maximum and mean percentage errors between the average and clinical waveforms, and their time of occurrence.

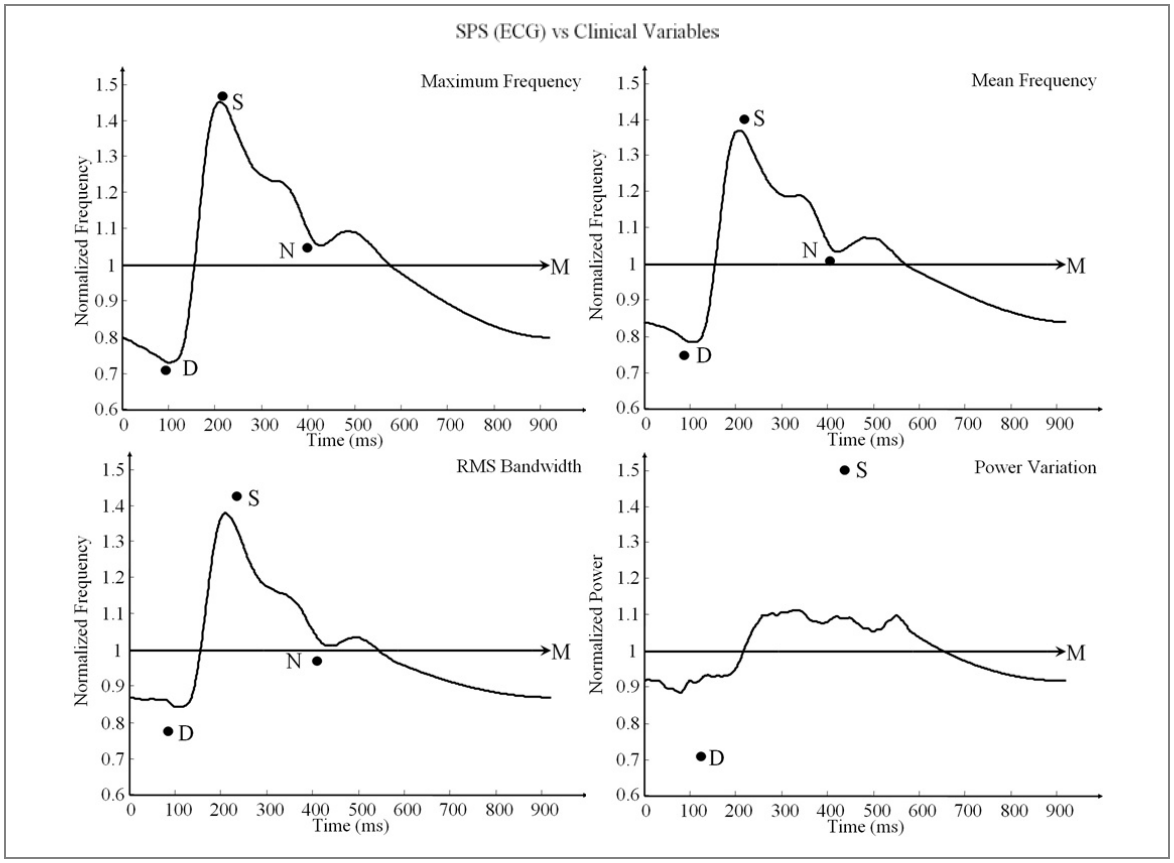

Figure 3.26 – SPS method with ECG delimitation: some feature points from clinical waveforms versus the average waveforms. The feature points considered are minimum systolic (D), peak systole (S), diastolic notch (N), and mean value (M).

As expected, the maximum frequency shows lower errors than the other spectral parameters for all the clinical variables (Figure 3.26 and Table 3.18). The rms bandwidth shows the worst results if the power is not considered.

% Error	Maximum Frequency	Mean Frequency	RMS Bandwidth	Normalized Power	Weighted Average
Mean Value (M)	0	0	0	0	0
Area under the curve before S (A_1)	16.00	21.06	29.83	N.A.	22.30
Area under the curve after S (A_2)	1.43	2.52	4.85	N.A.	2.93
Systolic Peak (S)	1.08	2.37	3.40	25.88	8.18
Minimum Value (D)	2.89	4.33	8.16	N.A.	5.13
Diastolic Notch (N)	2.03	3.19	4.08	N.A.	3.10

Table 3.18 – SPS method with ECG delimitation: percentage errors for clinical variables obtained from the comparison of clinical waveforms with average waveforms.

3.6.2.4 Pulse Foot Seeking delimitation

The results obtained using the SPS, considering that the cycles were divided through the PFS algorithm, are described in Figure 3.27, Figure 3.28, Table 3.19 and Table 3.20. The conclusions to be taken are similar to the ones taken with the ECG cut approach.

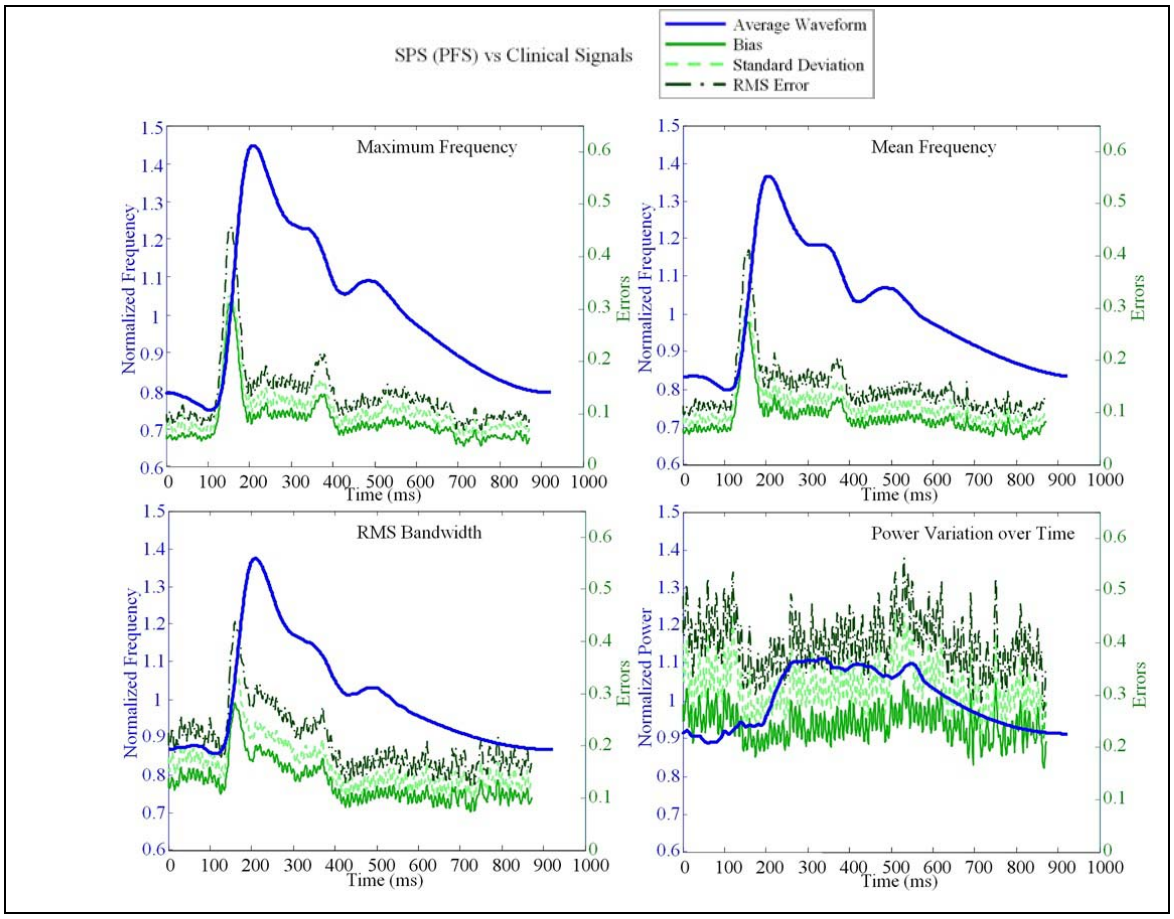

Figure 3.27 – SPS method with PFS delimitation: average waveforms errors versus clinical waveforms.

		Maximum Frequency		Mean Frequency		RMS Bandwidth		Normalized Power	
		%Error	Time (ms)	%Error	Time (ms)	%Error	Time (ms)	%Error	Time (ms)
Bias	Minimum	4.47	714	5.63	817	8.08	425	17.06	696
	Maximum	32.58	149	27.87	149	26.91	159	35.17	60
	Mean	8.50		9.04		12.81		24.31	
Std	Minimum	6.47	696	8.07	817	10.00	425	23.03	716
	Maximum	34.31	149	31.02	149	32.05	159	49.31	120
	Mean	10.61		11.29		16.07		31.74	
RMSE	Minimum	7.97	715	9.84	817	12.86	425	29.61	866
	Maximum	47.31	149	41.70	149	41.85	159	58.98	60
	Mean	13.60		14.47		20.56		39.99	

Table 3.19 – SPS method with PFS delimitation: Minimum, maximum and mean percentage errors between the average and clinical waveforms, and their time of occurrence.

% Error	Maximum Frequency	Mean Frequency	RMS Bandwidth	Normalized Power	Weighted Average
Mean Value (M)	0	0	0	0	0
Area under the curve before S (A_1)	14.38	28.86	38.82	N.A.	27.35
Area under the curve after S (A_2)	1.39	4.06	6.74	N.A.	4.07
Systolic Peak (S)	1.40	2.66	3.75	26.11	8.48
Minimum Value (D)	5.27	6.06	9.39	N.A.	6.91
Diastolic Notch (N)	1.51	2.81	4.26	N.A.	2.86

Table 3.20 – SPS method with PFS delimitation: percentage errors for clinical variables obtained from the comparison of clinical waveforms with average waveforms.

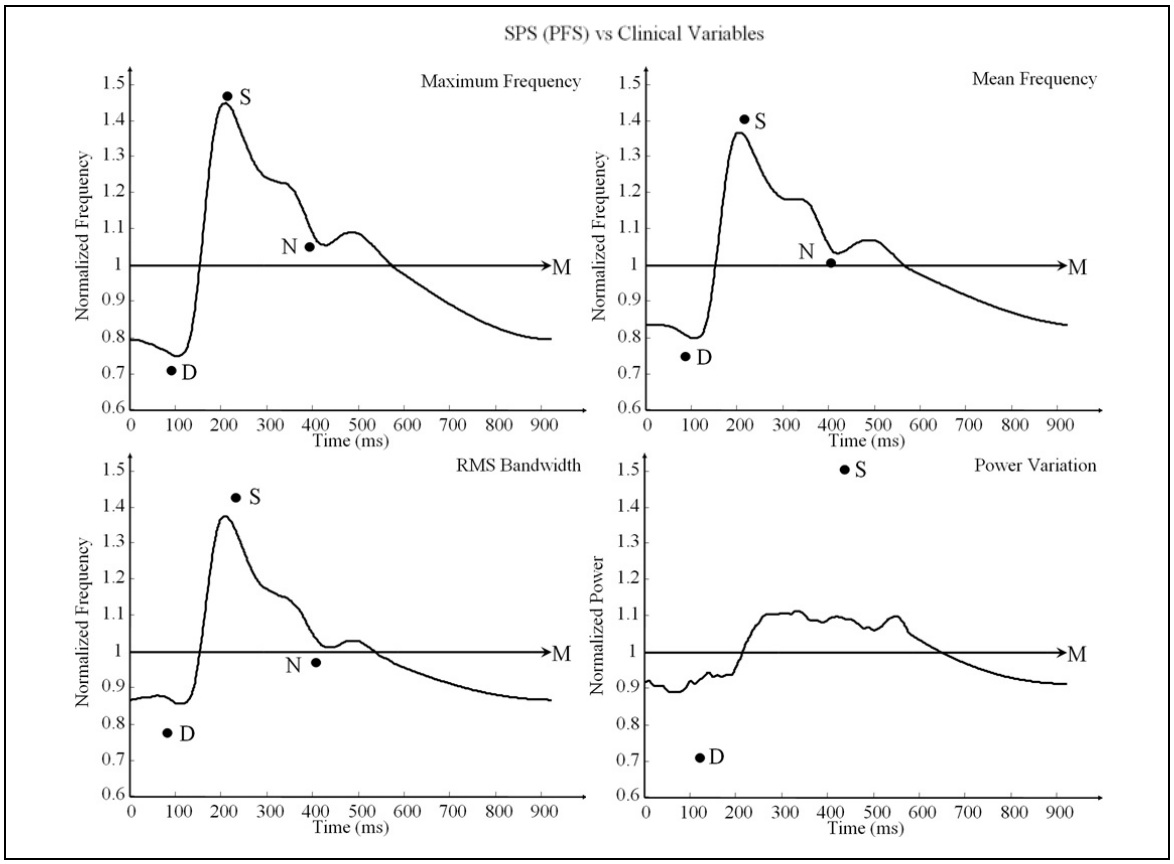

Figure 3.28 – SPS method with PFS delimitation: some feature points from clinical waveforms versus the average waveforms. The feature points considered are minimum systolic (D), peak systole (S), diastolic notch (N), and mean value (M).

3.6.2.5 Rough delimitation

The last SPS approach is characterised by the rough delimitation of the cardiac cycles.

The main evidence observed in Figure 3.29 and Table 3.21, is the huge increase of errors observed on the late diastole. This is due to the additional point placed at the end of the cycle, which seems to have a significant consequence for this method.

Although the reference signal includes the early systolic events, some of the other cycles do not include early systolic events. The irregular heart beat lengths of some signals restrains the choice of other window lengths or overlapping. Because this average signal starts later than the two other SPS alternatives, the disparity between the effective length of the average waveforms and those calculated from the mean heart rate is greater.

The behaviour of the errors in the rest of the cycle is similar to the remaining approaches, as showed in Figure 3.29, Figure 3.30, Table 3.21 and Table 3.22.

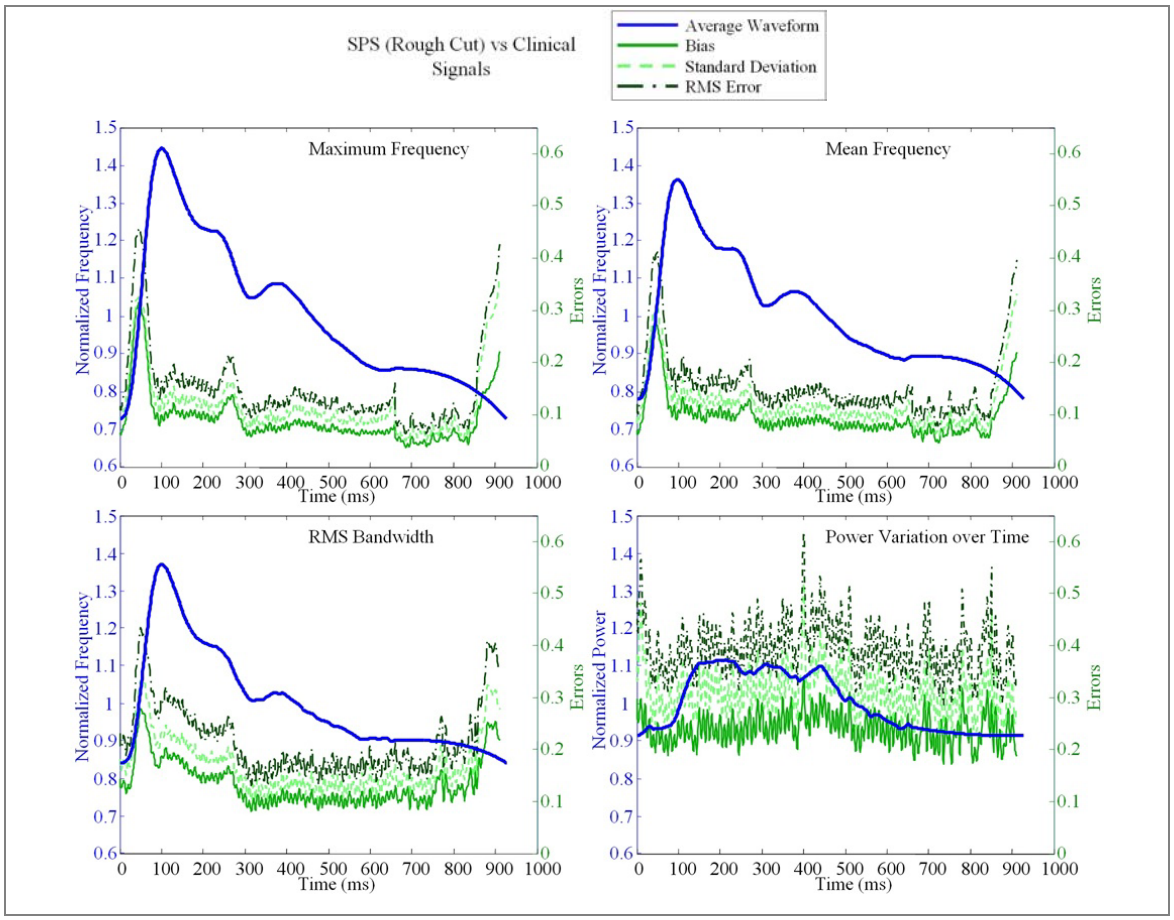

Figure 3.29 – SPS method with rough delimitation: average waveforms errors versus clinical waveforms.

		Maximum Frequency		Mean Frequency		RMS Bandwidth		Normalized Power	
		%Error	Time (ms)	%Error	Time (ms)	%Error	Time (ms)	%Error	Time (ms)
Bias	Minimum	4.32	686	5.21	723	8.08	315	17.33	245
	Maximum	33.00	39	28.69	39	29.50	900	34.56	781
	Mean	9.27		9.73		13.46		24.03	
Std	Minimum	5.80	736	6.60	724	10.07	315	22.95	245
	Maximum	48.67	911	41.35	911	37.29	882	52.40	10
	Mean	12.20		12.44		16.96		31.31	
RMSE	Minimum	7.33	686	8.41	724	12.92	315	28.76	245
	Maximum	56.94	911	49.60	911	47.22	882	61.58	10
	Mean	15.35		15.80		21.66		39.48	

Table 3.21 – SPS method with rough delimitation: Minimum, maximum and mean percentage errors between the average and clinical waveforms, and their time of occurrence.

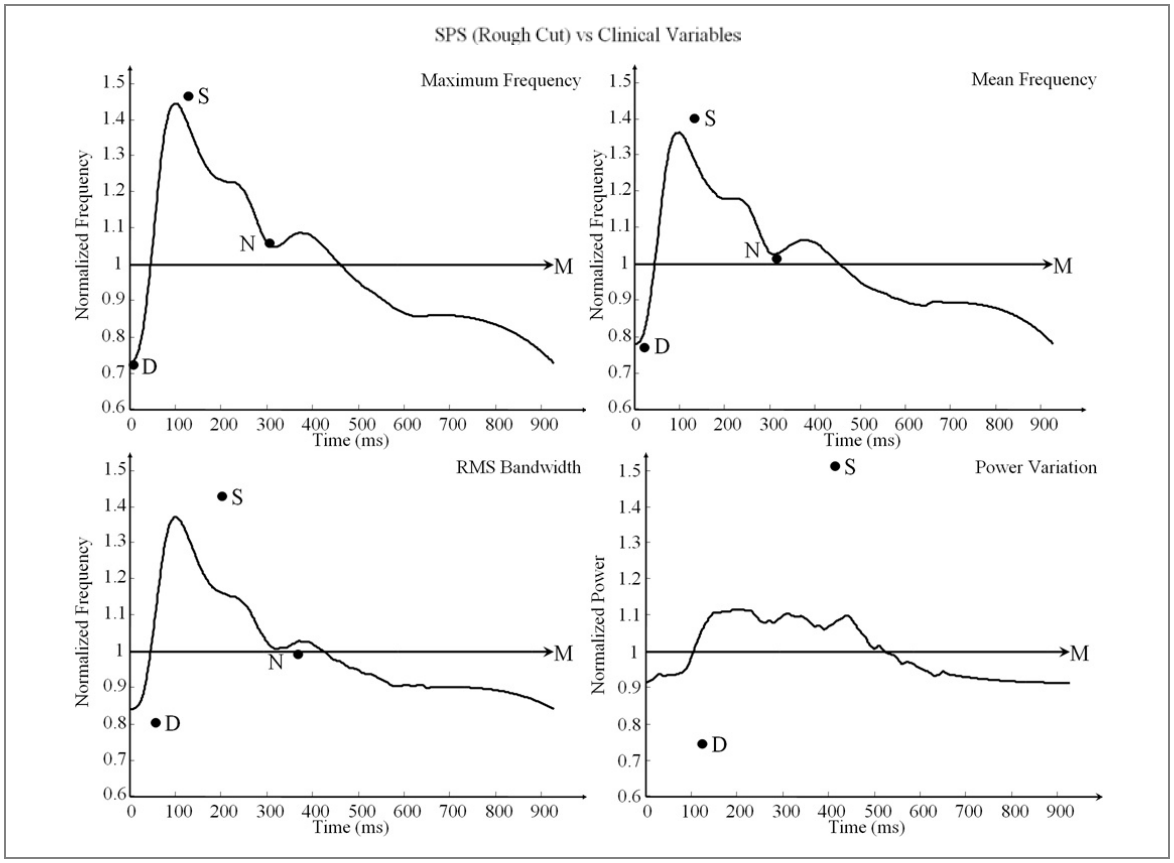

Figure 3.30 – SPS method with rough delimitation: some feature points from clinical waveforms versus the average waveforms. The feature points considered are minimum systolic (D), peak systole (S), diastolic notch (N), and mean value (M).

% Error	Maximum Frequency	Mean Frequency	RMS Bandwidth	Normalized Power	Weighted Average
Mean Value (M)	0	0	0	0	0
Area under the curve before S (A_1)	23.22	17.52	35.10	N.A.	25.28
Area under the curve after S (A_2)	2.17	0.97	5.34	N.A.	2.83
Systolic Peak (S)	1.48	2.97	4.03	26.20	8.67
Minimum Value (D)	0.59	1.13	4.21	N.A.	1.98
Diastolic Notch (N)	0.14	1.56	9.65	N.A.	3.78

Table 3.22 – SPS method with rough delimitation: percentage errors for clinical variables obtained from the comparison of clinical waveforms with average waveforms.

Except for the diastolic notch on the bandwidth variation signal, which presents a 10% of error probably due to its erroneous time identification (see Figure 3.30), there are no evidences that this method presents a different performance in comparison with the others when clinical variables are required.

3.6.3 COMPARISON BETWEEN METHODS

Figure 3.31 shows the RMSE normalized to the mean value for each spectral parameter, obtained from the application of the four approaches considered for averaging clinical waveforms.

The general poor performance of the WFA when compared with the SPS method is clear in the figure. The results from the SPS with the signals roughly cut are slightly worse than those obtained with the ECG and PFS approaches. In fact, no significant difference was expected from these results if the same reference waveform has been used, as evidence Table 3.17, Table 3.19 and Table 3.21. The minimum errors observed for all the spectral parameters are quite close for the three variations.

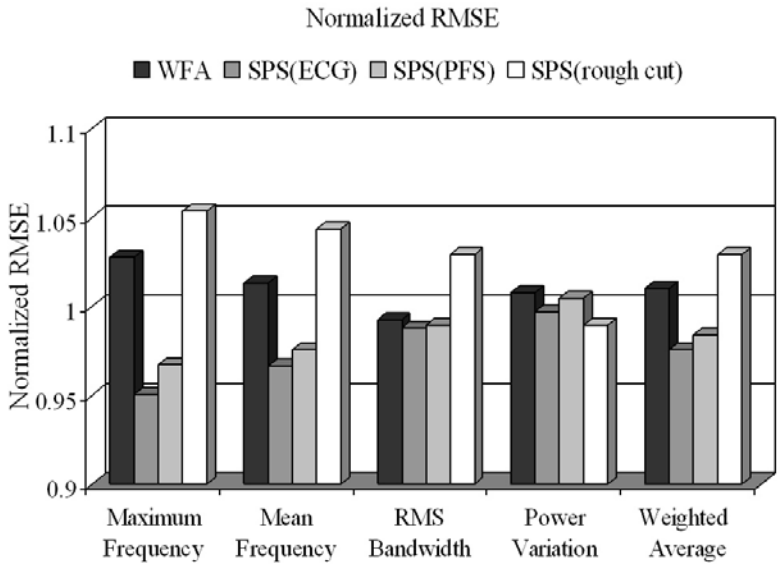

Figure 3.31 – RMSE normalized to the average for all methods and obtained when comparing the average waveforms with the waveforms from clinical signals.

Figure 3.32 shows the percentage of bias found while comparing the clinical variables on the average waveforms and on the clinical signals.

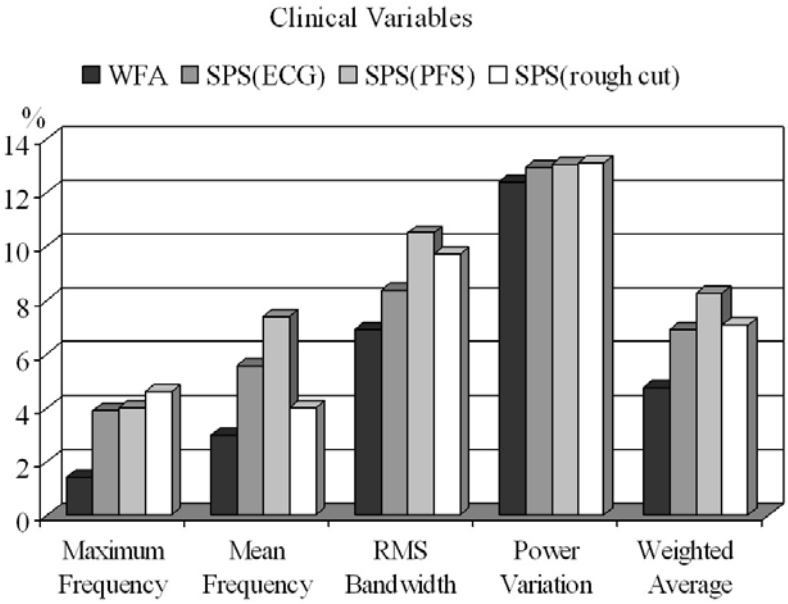

Figure 3.32 – Percentage bias for clinical variables obtained when comparing the average waveforms with the waveforms from clinical signals.

The more accurate results are obtained from WFA, as expected. However, the three SPS approaches do not present similar results. The PFS delimitation presents the highest errors, followed by the ECG cut, except for the power variation.

These results may affect important characteristics of the signals that are frequently used for diagnosis. These characteristics can be quantified using some

clinical indicators (see Annex A). To exemplify, the average of some clinical indexes was used to determine the percentage bias obtained by comparing the average waveforms with the clinical signals. The clinical indexes were not computed from the power variation as might be seen by the behaviour of the power variation waveform. This way, the adequacy of the waveforms, obtained from the averaging methods, to represent the Pulsatility Index, the Pourcelot's Resistance Index, acceleration and the Spectral Broadening Index and the results are shown, respectively, in Figure 3.33, Figure 3.34, Figure 3.35 and Figure 3.36.

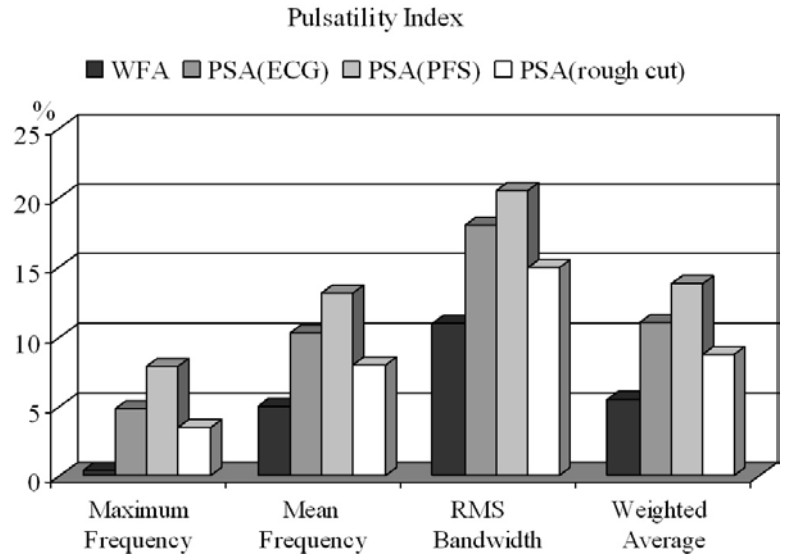

Figure 3.33 – Percentage bias observed from the comparison between the average waveforms and the waveforms from clinical signals for the Pulsatility Index.

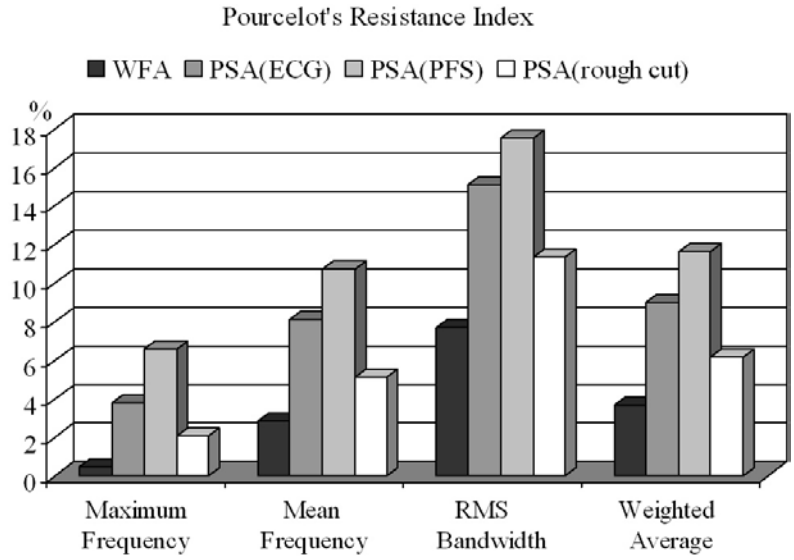

Figure 3.34– Percentage bias observed from the comparison between the average waveforms and the waveforms from clinical signals for the Pourcelot's Resistance Index.

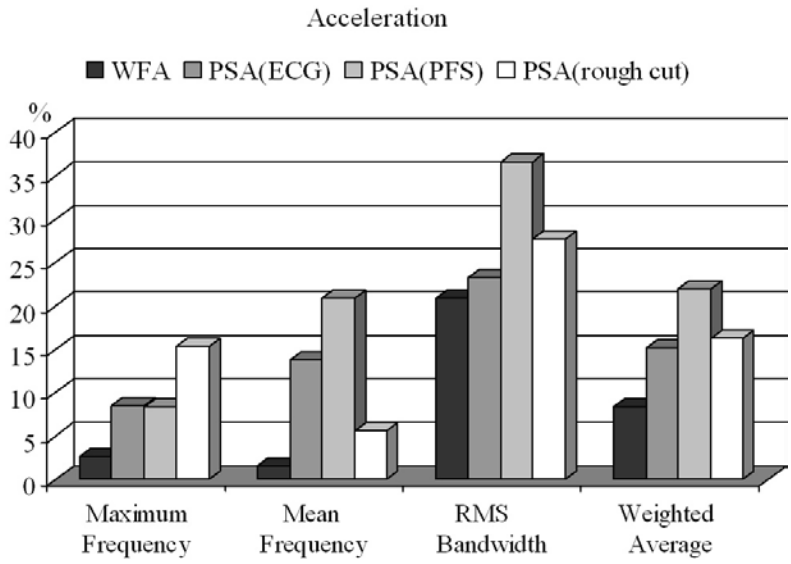

Figure 3.35 – Percentage bias observed from the comparison between the average waveforms and the waveforms from clinical signals for the acceleration.

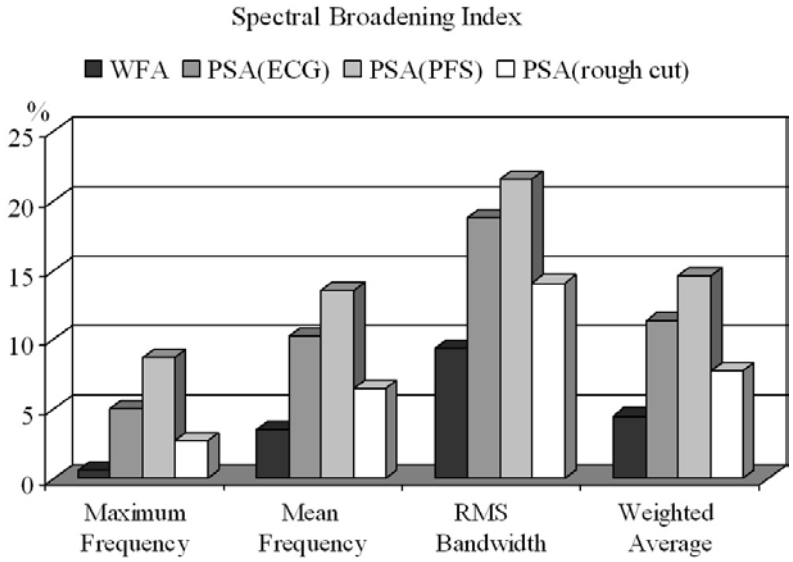

Figure 3.36– Percentage bias observed from the comparison between the average waveforms and the waveforms from clinical signals for the Spectral Broadening Index.

From the previous graphs, it can be observed that, in general, the maximum frequency average waveform maintains the average characteristics of the clinical waveforms. The errors obtained with the estimation of the four clinical indexes considered through the averaged spectral parameters are higher for the rms bandwidth. For all the cases, the WFA is the method that produces the lower differences between the indexes of the average and the averaged indexes. The SPS with rough-cut is the next more accurate method. The waveforms obtained with SPS with ECG present a slight better performance than the ones obtained with the PFS.

The main conclusion of this study is that the selection of the averaging method should depend on the application. If the average signals are to be used for the analysis of vascular diseases, the WFA is the best method; otherwise, the SPS with ECG or PFS should be chosen.

For the work described in this thesis, the average signals will be used for simulating ESs; one of the SPS approaches will be used. Although the errors obtained with the ECG cut are slightly lower than the ones obtained with the PFS cut, the PFS approach will be preferred since it does not depend on ECG signals.

3.6.4 SIMULATED SIGNALS

The average waveforms obtained from the SPS with PFS delimitation of cycles were computed for use in the generation of simulated signals.

To analyse the performance of the simulator, average spectral waveforms, non-smoothed and non-normalized, will be used.

The first step of the simulation process is the determination of the filter from equation (3.4). Figure 3.37 show the filter modulated with the average rms bandwidth and power variation waveforms.

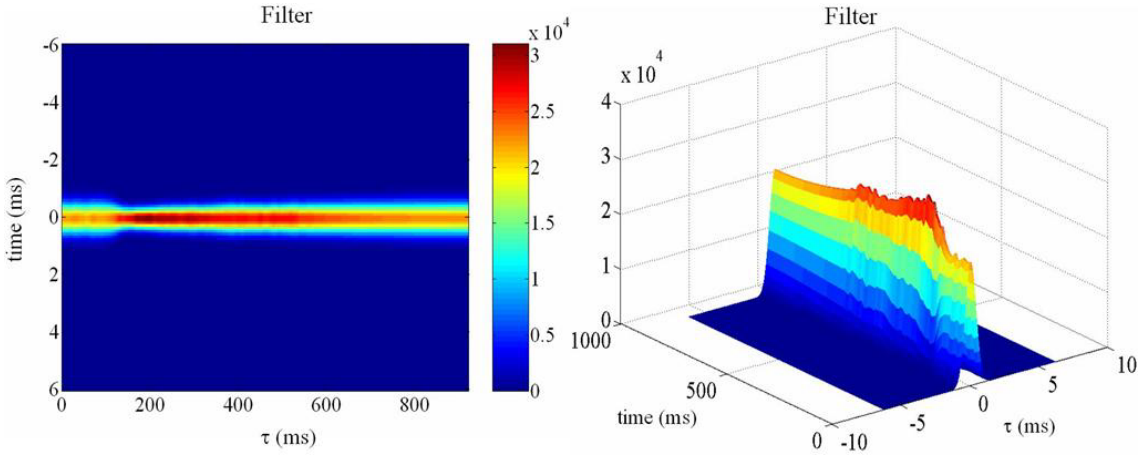

Figure 3.37 – Filter modulated with the average waveforms.

Figure 3.38 shows the display of the spectral estimation of three clinical cardiac cycles randomly chosen, and of three simulated signals.

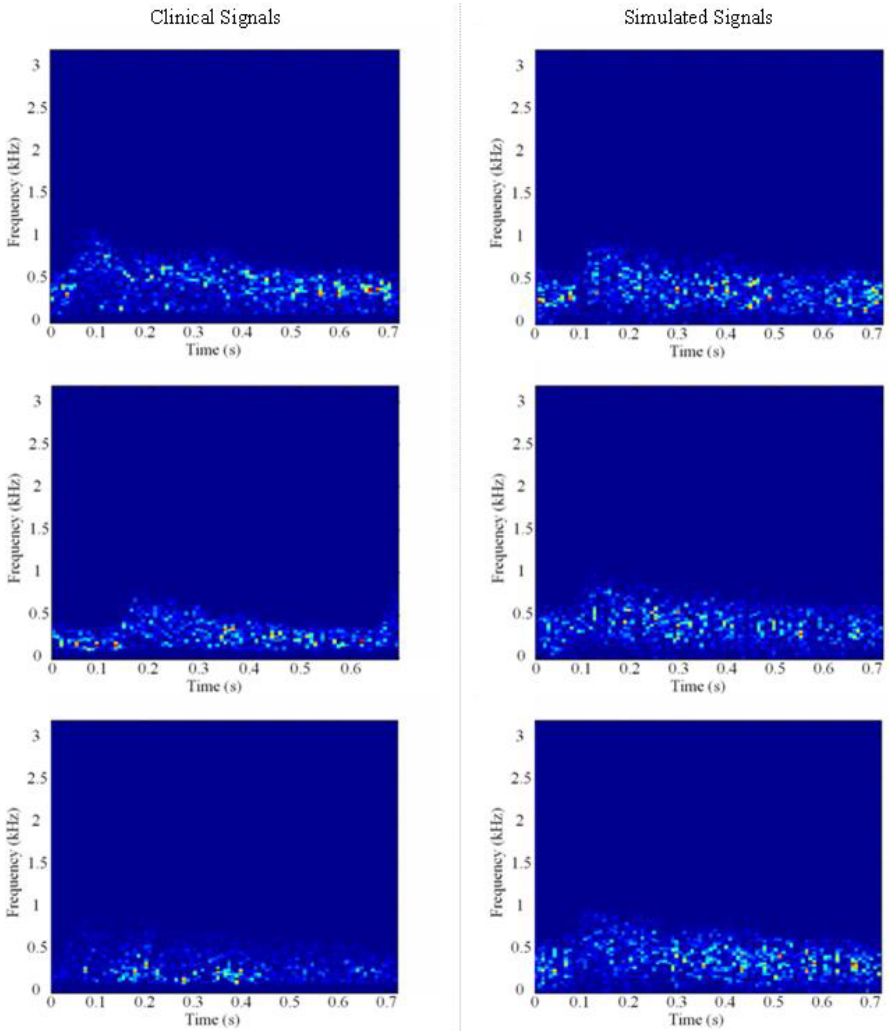

Figure 3.38 – Spectral representation of three clinical cardiac cycles and three simulated signals (both randomly selected).

Figure 3.39, Figure 3.40 and Table 3.23 show the results from the comparison between the average waveforms (considering 100 simulated signals) and the reference waveforms.

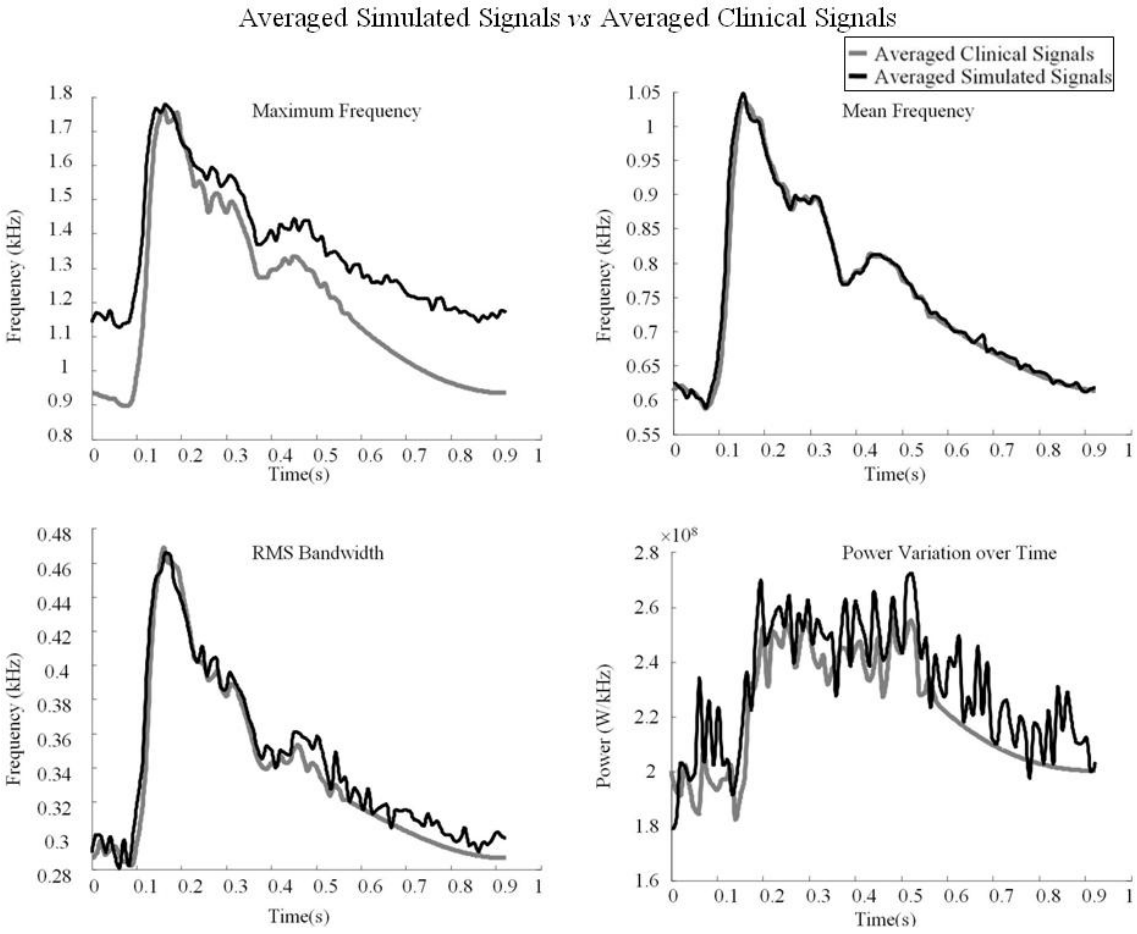

Figure 3.39 – Representation of the reference waveforms against the average waveforms from 100 simulated signals.

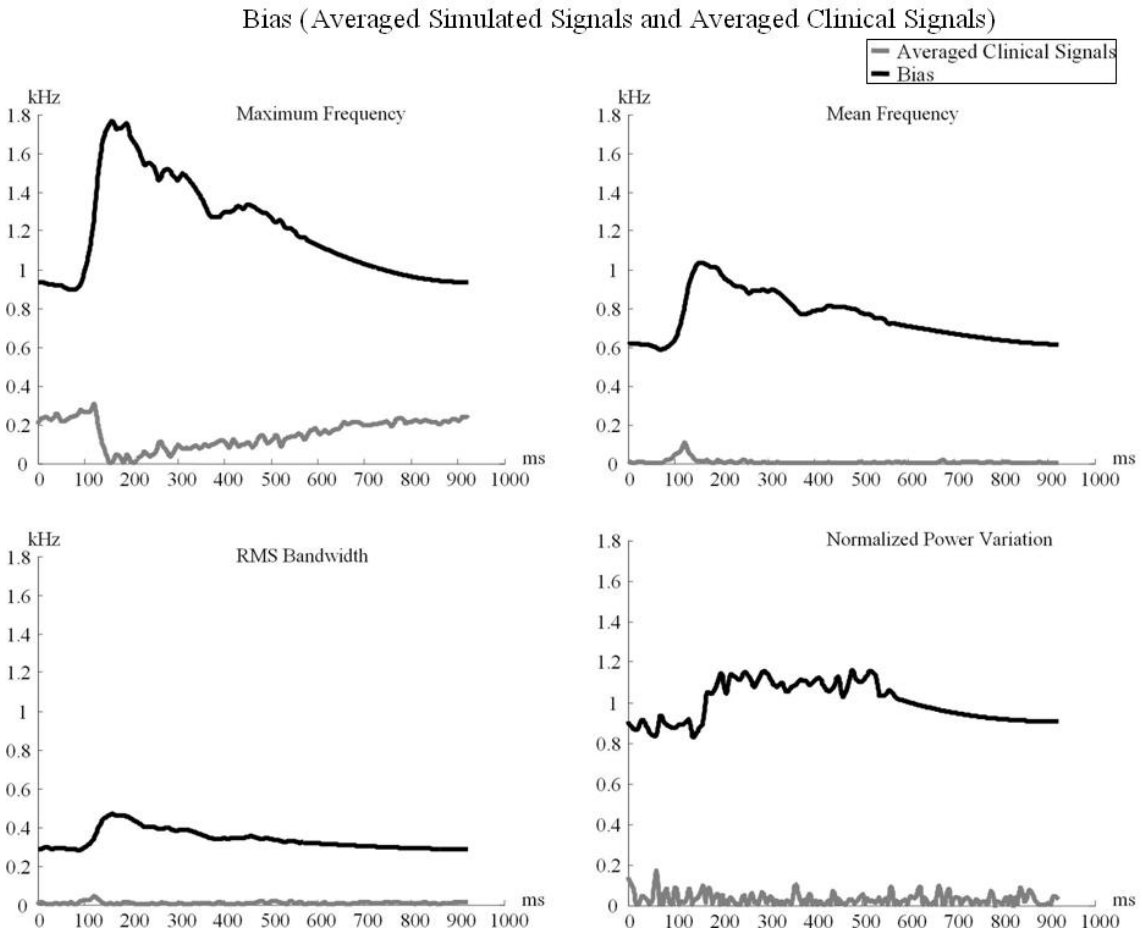

Figure 3.40 – Bias achieved while comparing the reference waveforms with the average waveforms from 100 simulated signals.

The most problematic waveform is the maximum frequency. Some studies were attempted in order to solve this problem, however until now it has not been possible to do so without ruining the performance of the other spectral parameters. The solution can be related to the extraction of the maximum frequency envelope. It was decided to postpone this study for another work, as it would lead to further investigation on the maximum frequency estimation. The maximum frequency, not being one of the inputs for simulation, is another issue that requires some improvement and that may be the origin of the problem.

The mean frequency from the simulated signals presents very good adjustment, which is mainly due to the mean frequency being related to the deterministic part of the signal (expression (3.1) of the Doppler signal).

The rms bandwidth and the power variation over time are also quite close to the expected values.

		Maximum Frequency		Mean Frequency		RMS Bandwidth		Normalized Power	
		%Error	Time (ms)	%Error	Time (ms)	%Error	Time (ms)	%Error	Time (ms)
Bias	Minimum	0	746	0	356	0	226	0	226
	Maximum	29.73	158	13.17	121	12.82	121	20.55	121
	Mean	14.33		0.99		2.63		3.30	

Table 3.23 – Minimum, maximum and mean percentage errors for the average waveforms from 100 simulated signals relatively to the reference waveforms.

3.7 CONCLUDING REMARKS

This chapter was dedicated to the simulation of MCA embolic-free blood flow Doppler ultrasound signals.

Firstly an overview of some published Doppler ultrasound signals simulators was given. Among them, the WF simulator was the one chosen to be used in this work.

The WF was described. As the simulator requires the input of deterministic mean frequency, rms bandwidth and power variation waveforms, the methods of achieving those waves were then addressed.

As extracting and averaging the corresponding spectral parameters from several cardiac cycles can estimate each deterministic waveform, a significant part of this chapter was concerned to the analysis, development, and implementation of averaging methods. In particular, two methods reported in literature were adapted and modified to fit the requirements of this work. Their computational efficiency has been improved.

The evaluation of the averaging methods considering general errors and errors of the estimation of clinically relevant variables together with the characteristics of the methods, led to the choice of the SPS and the use of the PFS algorithm to delimit the cardiac cycles in the clinical Doppler signals.

The application of the reference waveforms from the SPS to the simulator indicated that, although the estimated maximum frequency from the simulated signals

presents more deviations than was expected, the other three parameters seem to follow very closely the behaviour of the clinical signals.

4 SPECTRAL ANALYSIS

4.1 INTRODUCTION

The time-frequency domain representation of blood flow Doppler signals is a widely used technique to analyse the behaviour of the blood stream and its relationship with eventual disorders on the circulatory system.

ESs are the mixture of blood flow signals and emboli signals. As, in this study, the main goal is the correct characterization of the emboli signals, the blood flow signal can be understood as a background signal.

Spectral analysis of emboli and spectral analysis of background blood have different requirements, and depend on distinct relevant parameters. Usually, analysis of blood flow requires accurate estimation of mean frequency and rms bandwidth, and the study of emboli requires accurate estimation of mean frequency and power variation over time.

The spectral estimator that will be used in this work must allow an accurate estimation of, at least, the three mentioned spectral parameters, and if possible, emphasize the emboli signal above the background signal.

This chapter describes only the background signal. It is understood as a good spectral estimator the method that avoids undesirable artefacts which could corrupt the spectrum and interfere with the emboli signals detection.

Traditionally, the STFT is the spectral estimator used to obtain the time-frequency representation of signals, but other methods have been described as enhancing the quality of the estimation. Previous studies reported the STMC and the

Discrete CWD (DCWD) as good alternatives to the conventional method, when applied to arterial blood flow Doppler signals [Cardoso *et al.*, 1996a] [Wang, Fish, 1996], [Leiria, 2000]. To start with, and taking advantage of those studies, the STMC and the DCWD will be considered as possible good estimators of the mean frequency and rms bandwidth, and eventually of the power variation, of MCA signals.

To evaluate that assumption, the performance of those methods on the estimation of the three spectral parameters, will be compared with the performance of the STFT. Additionally, the accuracy on the estimation of the maximum frequency will also be analysed, for reasons that will be explored in Chapter 6.

The evaluation of the spectral estimators will also include an analysis of the influence of the several parameters of the spectral methods on the accuracy of the estimators. This study of the methods' parameters, aims the establishment of rules of tuning of the spectral estimators to ease future work on this field.

The description and characterization of the spectral estimation methods will precede the report of their evaluation.

Figure 4.1 shows the relationship between the methods and signals used in this chapter.

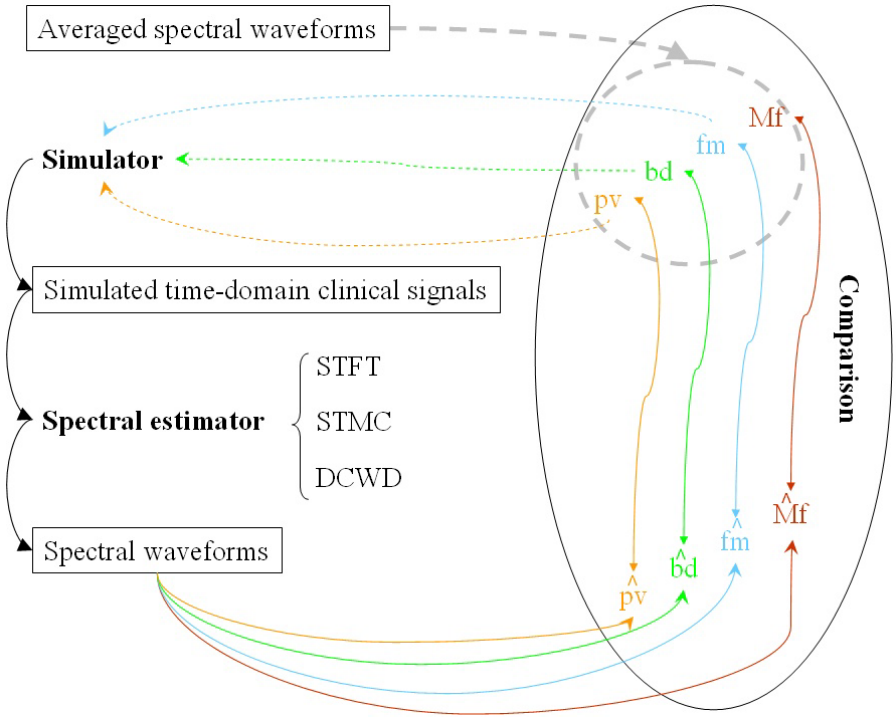

Figure 4.1 – Methods and signals used in this chapter.

4.2 TIME-FREQUENCY ANALYSIS

Fourier analysis is an important tool for determining the frequencies in a signal. The main limitation is its inadequacy to deal with most non-stationary signals, as it is not able to distinguish the times at which each frequency occurs.

However, some non-stationary signals can still be characterized both in time and in frequency domains through the concepts of instantaneous frequency and group delay [Cohen, 1996a].

A time domain non-stationary signal can be expressed as

$$x(t) = x_R(t) + jx_I(t) = A(t)e^{j\varphi(t)}, \tag{4.1}$$

where $x_R(t)$ and $x_I(t)$ are respectively the real and complex components, $A(t)$ is the amplitude and $\varphi(t)$ is the phase of the signal.

When $x(t)$ is transformed into the frequency domain, it becomes

$$X(\omega) = B(\omega)e^{j\psi(\omega)}, \tag{4.2}$$

where $B(\omega)$ and $\psi(\omega)$ are respectively the amplitude and the phase of $X(\omega)$.

The time-frequency characterization of the signal can be obtained by analysing the instantaneous frequency of $x(t)$, or the frequency occurring at each time,

$$\omega_i(t) = \frac{1}{2\pi}\frac{d\varphi(t)}{dt}. \tag{4.3}$$

and the group delay of $x(t)$, or the time of each frequency occurrence,

$$t_g(\omega) = -\frac{d\psi(t)}{dt}. \tag{4.4}$$

However, if more than one frequency occurs at the same time, the concept of instantaneous frequency[13] is not applicable; and if more than one-time occurrences are observed for the same frequency, the concept of group delay[14] is not applicable.

The need for studying general non-stationary signals led to the development of other time-frequency estimators capable of describing a signal's density of energy in time and frequency simultaneously. This will allow knowing which frequencies are present in the signal and when they occur [Cohen, 1989].

[13] The result becomes an average of the frequencies instead of a single frequency for each time.

[14] The result becomes an average of the times instead of a single time for each frequency.

4.3 CONVENTIONAL METHODS

The PSD of a random process can be determined by the direct or by the indirect method. The direct method applies the FT directly to the signal, while the indirect method applies the FT to the signal ACS [Kay, 1988]. Conventional methods are based on the direct method.

4.3.1 FOURIER TRANSFORM

Any signal can be represented by a sum of sinusoids with different frequencies,

$$x(t) = \frac{1}{2\pi}\int_{-\infty}^{+\infty} X(\omega) e^{j\omega t} d\omega \,. \tag{4.5}$$

Therefore, any signal can be understood as the linear superposition of several other simpler waveforms $e^{j\omega t}$ characterized by the angular frequency ω. The contribution of each waveform to the signal is specified by coefficient

$$X(\omega) = \int_{-\infty}^{+\infty} x(t) e^{-j\omega t} dt \tag{4.6}$$

called spectrum or FT of the signal $x(t)$.

4.3.2 PERIODOGRAM

According to the direct method, the PSD of discrete time signal $x(n)$ can be computed though the periodogram

$$\hat{P}(k) = \frac{1}{N}\left| \sum_{n=0}^{N-1} x(n) e^{-\frac{j2\pi kn}{N}} \right|^2 = \frac{1}{N}\left| X(k) \right|^2 \quad , \tag{4.7}$$

where $X(k)$ is the FT of the discrete signal $x(n)$ and N is the length of the signal. [Challis, Kitney, 1991a].

The periodogram is not a consistent estimator of the PSD, as its variance does not decrease with the increase of the data segment. However, the Bartlet or the Welch versions of the periodogram can reduce the variance with the application of sample averaging techniques. Dividing the data set into non-overlapped data segments, estimating the periodogram for all the subsets, and averaging the resulting periodograms to obtain the signal spectrum, enables the computation of the Bartlet periodogram. The Welch method, allows overlapping the segments, and consists of applying a window

function to each subset before calculating the estimated periodograms; the estimated spectrum is obtained from the average of the modified periodograms.

4.3.3 SHORT TIME FOURIER TRANSFORM

The STFT can be interpreted as an adaptation of the Welch periodogram to non-stationary signals. The modified periodograms are not averaged like in the Welsh method but represented side by side on the time axis. The schematised process is represented in Figure 4.2.

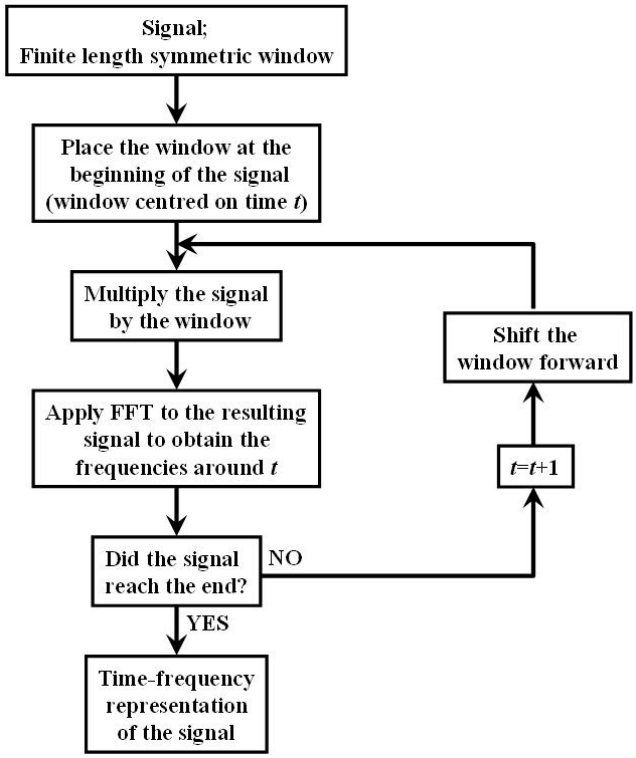

Figure 4.2 – STFT

In the discrete formulation, the STFT, can be represented as

$$STFT(n,k)=\left|\sum_{k=0}^{N-1}x(n)w(n)e^{-\frac{j2k\pi}{N}}\right|^2, \tag{4.8}$$

where n and k are respectively the discrete time and frequency indexes, $x(n)$ is the time domain Doppler signal, $w(n)$ a symmetric sliding window function centred on n, and N is the number of points of the window.

The length of the windows must be such that a set of stationary signals is obtained from the multiplication of the signal by the windows.

4.3.4 DRAWBACKS

The major drawback results from the application of windows to the signal, already discussed in Section 1.4.2.2. The non-stationarity of the signals constrains frequency resolution, as the length of the segments should be narrow enough to guarantee their stationarity properties; and the time-resolution is limited by result of the windows' FT.

Additionally, the frequency resolution can be strongly affected when the method is applied to non-stationary signals. The frequency resolution obtained with the application of FFT to data segments depends on the size of the segments. For segments of N seconds, $1/N$ Hz is the best frequency resolution that is possible to obtain. However, the length of the segments also determines the time-resolution.

Therefore, the optimal time-frequency resolution is function of the best trade-off between the time and the frequency resolution.

4.4 PARAMETRIC METHODS

Spectral estimation methods based on parametric models have been suggested to improve the performance achieved by conventional methods.

Frequency analysis by parametric methods includes the choice of the model, the estimation of the model parameters, and the identification of the solution of the theoretical PSD expression from estimated parameters.

The models considered in this work, are time series, or rational transfer functions. Those can be Autoregressive (AR), Moving Average (MA) or Autoregressive Moving Average (ARMA) models [Marple, 1989].

Unlike the conventional methods, parametric methods do not assume that the non-available data, or the data points that fall outside of the window, are null. This prevents them to be affected by the limitations associated with the windowing of the signal.

4.4.1 AUTOREGRESSIVE, MOVING AVERAGE AND AUTOREGRESSIVE MOVING AVERAGE

The ARMA is a time series model that fits many discrete random processes found in nature, and may by be expressed by the system:

$$\begin{aligned} x(n) &= -\sum_{m=1}^{p} a(m)x(n-m) + \sum_{m=0}^{q} b(m)v(n-m) \\ &= \sum_{m=0}^{\infty} h(m)v(n-m) \end{aligned} \tag{4.9}$$

where $h(n)$ is a linear causal[15] filter with complex coefficients, $v(n)$ an input function that generates a white noise sequence and $x(n)$ the system's output.

This system is characterised by the rational transfer function,

$$H(z) = \frac{X(z)}{V(z)} = \frac{B(z)}{A(z)} \tag{4.10}$$

where $H(z)$, $V(z)$ and $X(z)$ are respectively the z transform of $h(k)$, $v(n)$ e $x(n)$. In the above equation, $A(z)$ corresponds to

$$A(z) = \sum_{m=0}^{p} a(m)z^{-m}\ , \tag{4.11}$$

and represents the z transform of the model's autoregressive branch. $B(z)$ is given by

$$B(z) = \sum_{m=0}^{q} b(m)v(n-m), \tag{4.12}$$

which is the z transform of the moving average branch of the model. In (4.11) and (4.12) $a(m)$ and $b(m)$ are respectively the AR and MA models' parameters, and p and q are respectively the number of poles and zeros of the filter. When all the zeros of $A(z)$ can be found within the unit circle of the z-plane, the stability of the filter $H(z)$ is guaranteed.

Assuming $a(0) = 1$, without loss of generality, the filter (4.10) becomes,

$$H(z) = \frac{\sum_{m=0}^{q} b(m)z^{-m}}{1 + \sum_{m=1}^{p} a(m)z^{-m}}\ . \tag{4.13}$$

[15] $h(m) = 0$ if $k < 0$

When the system is fed with a white noise process with variance σ_v^2, the PSD of the system's output is

$$P_{ARMA}(f)=\sigma_v^2\left|\frac{B(z)}{A(z)}\right|^2\Bigg|_{z=e^{j2\pi f_n}}=\sigma_v^2\left|\frac{\sum_{m=0}^{q}b(m)e^{-j2\pi mf_n}}{\sum_{m=0}^{p}a(m)e^{-j2\pi mf_n}}\right|^2. \tag{4.14}$$

where $f_n=f/f_s$ is the frequency normalized by the sampling frequency ($f_n\in[-1/2,1/2]$).

If the filter has p poles and no zeros, it is an AR model (AR(p)), and the spectrum of the signal will present peaks. Assuming $b(0)=1$, without loss of generality, the transfer function becomes

$$H(z)=\frac{1}{1+\sum_{m=1}^{p}a(m)z^{-m}} \tag{4.15}$$

as $q=0$.

If the filter has q zeros and no poles, it is a MA model (MA(q)). The spectrum will present valleys, and the transfer function is

$$H(z)=\sum_{m=0}^{q}b(m)z^{-m}. \tag{4.16}$$

If the filter has p poles and q zeros, it is an ARMA (ARMA(p,q)), and the spectrum will contain peaks and valleys [Marple, 1989].

The model and the order of the model (p and/or q) must be carefully chosen. Low order models leads to lower frequency resolution and high order models are statistically unstable and show spurious spectral peaks [Kay, 1988].

The estimation of the ARMA parameters is obtained from their relationship with $r_{xx}(m)$ (the ACS of the process $x(n)$) given by [Marple, 1987],

$$r_{xx}(m)=\begin{cases} r_{xx}^*(-m) & m<0 \\ -\sum_{i=1}^{p}a(i)r_{xx}(m-i)+\sigma_v^2\sum_{i=m}^{q}b(i)h^*(i-m) & 0\le m\le q \\ -\sum_{i=1}^{p}a(i)r_{xx}(m-i) & m>q \end{cases}. \tag{4.17}$$

.

Equivalent expressions can be obtained for an AR process, if q is set to zero,

$$r_{xx}(m)=\begin{cases} r_{xx}^{*}(-m) & m<0 \\ -\sum_{i=1}^{p} a(i) r_{xx}(m-i)+\sigma_v^2 & m=0 \\ -\sum_{i=1}^{p} a(i) r_{xx}(m-i) & m>q \end{cases}, \tag{4.18}$$

or, in the matrix from,

$$\begin{bmatrix} r_{xx}(0) & r_{xx}(-1) & \cdots & r_{xx}(-p+1) \\ r_{xx}(1) & r_{xx}(0) & \cdots & r_{xx}(-p+2) \\ \vdots & \vdots & \cdots & \vdots \\ r_{xx}(p-1) & r_{xx}(p-2) & \cdots & r_{xx}(0) \end{bmatrix} \begin{bmatrix} a(1) \\ a(2) \\ \vdots \\ a(p) \end{bmatrix} = -\begin{bmatrix} r_{xx}(1) \\ r_{xx}(2) \\ \vdots \\ r_{xx}(p) \end{bmatrix}. \tag{4.19}$$

The $p \times p$ matrix in (4.19) is designated the autocorrelation matrix R_{xx}. This is a Hermitian[16], Toeplitz[17], and positive semidefinite matrix [Marple, 1987].

The properties of R_{xx} allow its resolution by computationally efficient methods such as the Levinson algorithm [Marple, 1987].

Equivalently, equations (4.17) can be adapted to a MA(q) process. Making $p=0$ and $h(m)=b(m)$ for $1 \le m \le q$, the relation becomes

$$r_{xx}(m)=\begin{cases} r_{xx}^{*}(-m) & m<0 \\ \sigma_v^2 \sum_{i=m}^{q} b(i) h^{*}(i-m) & 0 \le m \le q \\ 0 & m>q \end{cases}. \tag{4.20}$$

The unknown input sequence $u(n)$ induces nonlinearities in (4.17) and (4.20). However, any ARMA or MA (or AR) process can be uniquely represented by an AR (or MA) of infinite order [Kay, 1988].

Usually an AR process is chosen because the complexity of the algorithm is lower than that required for processing an ARMA or MA process [Marple, 1987].

For all the cases, the optimal parameters are the ones that minimize the mean squared error ρ,

$$\rho = \mathcal{E}\left[\left| x(n)-\hat{x}(n) \right|^2 \right] = \left\| x(n)-\hat{x}(n) \right\| \tag{4.21}$$

---

[16] $[R_{xx}]^H = R_{xx}$

[17] The elements along any diagonal are equal.

where $\hat{x}(n)$ is the estimate of the data sequence for a parametric model, and $\|\bullet\|$ is the Euclidian norm of a vector [Marple, 1989].

4.4.2 ESTIMATION OF THE AUTOREGRESSIVE PARAMETERS

The process of estimating the AR parameters can be identified with the linear prediction theory.

Let $x(n)$ be an AR(p) process. The estimation of the forward linear prediction of $x(n)$ based on the p previous data records is given by [Kay, Marple, 1981]

$$\hat{x}^f(n) = -\sum_{m=1}^{p} a^f(m)x(n-m), \tag{4.22}$$

where $\{a^f(1), a^f(2),\ldots,a^f(p)\}$ are the forward linear prediction coefficients and f denotes the forward prediction.

The forward linear prediction error (4.23), or its squared equivalent, the mean squared forward linear prediction error (4.24), measures the accuracy of the estimation.

$$e^f(n) = x(n) - \hat{x}^f(n). \tag{4.23}$$

$$\mathcal{E}\left[\left|e^f(n)\right|^2\right] = \mathcal{E}\left[\left|x(n) - x^f(n)\right|^2\right] = \rho^f \tag{4.24}$$

The measure ρ^f is also called the power of the forward linear prediction error [Marple, 1987].

Considering $r_{xx}(-m) = r_{xx}^*(m)$ and assuming that $x(n)$ is a WSS process, the vector $a^f(m)$ that minimizes ρ^f is given by the solution of the following system [Marple, 1987],

$$\begin{bmatrix} r_{xx}(0) & r_{xx}(1) & \cdots & r_{xx}(p) \\ r_{xx}(1) & r_{xx}(0) & \cdots & r_{xx}(p-1) \\ \vdots & \vdots & \cdots & \vdots \\ r_{xx}(p) & r_{xx}(p-1) & \cdots & r_{xx}(0) \end{bmatrix} \begin{bmatrix} 1 \\ a^f(1) \\ \vdots \\ a^f(p) \end{bmatrix} = \begin{bmatrix} \rho^f \\ 0 \\ \vdots \\ 0 \end{bmatrix} \tag{4.25}$$

This process can be compared with (4.19).

The backward linear prediction estimate, or the estimate of the process $x(n)$ using the p last samples, is defined by,

$$\hat{x}^b(n) = -\sum_{m=1}^{p} a^b(n)x(n+m), \tag{4.26}$$

where $\{a^b(1), a^b(2),\ldots,a^b(p)\}$ are the backward linear prediction coefficients and b stands for backward prediction.

Backward linear prediction errors are determined through

$$e^b(n) = x(n-m) - \hat{x}^b(n-m) \tag{4.27}$$

and the power of the backward prediction errors through

$$\rho^b = \mathcal{E}\left[\,\left|\, e^b(n)\right|^2\right] \tag{4.28}$$

The $a^b(m)$ sequence that minimizes ρ^b is achieved by the solution of the system [Marple, 1987]

$$\begin{bmatrix} r_{xx}(0) & r_{xx}^*(1) & \cdots & r_{xx}^*(0) \\ r_{xx}(1) & r_{xx}(0) & \cdots & r_{xx}^*(p-1) \\ \vdots & \vdots & \ddots & \vdots \\ r_{xx}(p) & r_{xx}(p-1) & \cdots & r_{xx}(0) \end{bmatrix} \begin{bmatrix} a^b(p) \\ \vdots \\ a^b(1) \\ 1 \end{bmatrix} = \begin{bmatrix} 0 \\ 0 \\ \vdots \\ \rho^b \end{bmatrix} \tag{4.29}$$

From (4.25) and (4.29) it is proved that [Marple, 1987],

$$1 \le m \le p \Rightarrow \begin{cases} \rho^b = \rho^f \\ a^b(m) = \left(a^f(m)\right)^* \end{cases} \tag{4.30}$$

Equations (4.25) and (4.29) can be solved through the Levinson algorithm [Kay, 1988].

4.4.3 AUTOREGRESSIVE MODIFIED COVARIANCE METHOD

Considering the forward linear prediction estimate of an AR(p) process as

$$\hat{x}(n) = -\sum_{m=1}^{p} a(m)x(n-m), \tag{4.31}$$

from (4.30) the backward linear prediction estimate becomes

$$\hat{x}(n) = -\sum_{m=1}^{p} a^*(m)x(n-m). \tag{4.32}$$

For both estimates, the minimum prediction error is given by the white noise variance [Marple, 1987].

The modified covariance method (ARMC) uses all the available samples for estimating the parameters through the minimization of the arithmetic average of the forward and backward prediction errors

$$\hat{\rho} = \frac{1}{2}\left(\hat{\rho}^f + \hat{\rho}^b\right). \tag{4.33}$$

where

$$\hat{\rho}^f = \frac{1}{N-p}\sum_{n=p}^{N-1}\left|x(n)+\sum_{m=1}^{p}a(m)x(n-m)\right|^2 \tag{4.34}$$

and

$$\hat{\rho}^b = \frac{1}{N-p}\sum_{n=0}^{N-1-p}\left|x(n)+\sum_{m=1}^{p}a^*(m)x(n+m)\right|^2 . \tag{4.35}$$

The development of the expression that minimizes $\hat{\rho}$ with $a(m)$, after some simplifications, leads to [Marple, 1987]

$$\begin{bmatrix} c_{xx}(1,1) & c_{xx}(1,2) & \cdots & c_{xx}(1,p) \\ c_{xx}(2,1) & c_{xx}(2,2) & \cdots & c_{xx}(2,p) \\ \vdots & \vdots & \ddots & \vdots \\ c_{xx}(p,1) & c_{xx}(p,2) & \cdots & c_{xx}(p,p) \end{bmatrix}\begin{bmatrix} \hat{a}(1) \\ \hat{a}(2) \\ \vdots \\ \hat{a}(p) \end{bmatrix} = -\begin{bmatrix} c_{xx}(1,0) \\ c_{xx}(2,0) \\ \vdots \\ c_{xx}(p,0) \end{bmatrix} \tag{4.36}$$

where the $p \times p$ matrix, called the covariance matrix, is Hermitian and positive definite [Marple, 1987]. The elements of the matrix are obtained from

$$c_{xx}(i,j) = \frac{1}{2(N-p)}\left(\sum_{n=p}^{N-1}x^*(n-i)x(n-j)+\sum_{n=0}^{N-1-p}x(n+i)x^*(n+j)\right). \tag{4.37}$$

The determination of the estimated parameters is the solution of the system (4.36), which can be achieved with the Cholesky decomposition [Kay, 1988] [Marple, 1987].

The white noise estimate is computed from

$$\hat{\sigma}_v^2 = \hat{\rho}_{\min} = c_{xx}(0,0)+\sum_{m=1}^{p}\hat{a}(m)\,c_{xx}(0,m). \tag{4.38}$$

Finally, the power spectrum can be determined from

$$\hat{P}(f_n) = \frac{\hat{\sigma}_v^2}{\left|1+\hat{a}(1)e^{-j2\pi f_n}+\ldots+\hat{a}(p)e^{-j2\pi f_n p}\right|}. \tag{4.39}$$

4.4.4 "*SHORT TIME MODIFIED COVARIANCE*"

Parametric methods, as conventional methods, are prepared to deal with stationary signals. To obtain proper time-frequency spectra, an algorithm similar to the one used for STFT must be adopted. This approach, the STMC, is schematised in Figure 4.3.

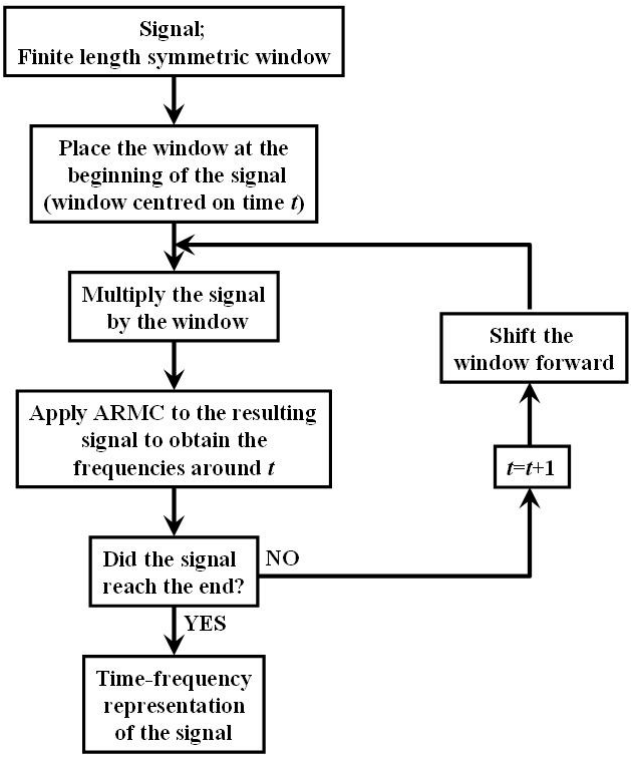

Figure 4.3 – STMC

4.4.5 DRAWBACKS

Although the parametric methods present improved frequency resolution, they still use window functions and suffer from the consequences already discussed.

4.5 COHEN'S CLASS METHODS

The main goal of the time-frequency analysis is to obtain information about the total amount of energy for unit of time and for unit of frequency [Cohen, 1989].

The fractional energy of the signal $x(t)$ in the time cell Δt for the instant of time t is,

$$\Delta E = |x(t)|^2 \Delta t \tag{4.40}$$

and the fractional energy in the frequency cell $\Delta\omega$ at frequency ω is

$$\Delta E = |X(\omega)|^2 \Delta\omega \tag{4.41}$$

where $X(\omega)$ is the frequency representation of $x(t)$. The function of joint density, $P(t,\omega)$, must be such that

$$\Delta E = P(t,\omega)\Delta t\Delta\omega\,. \tag{4.42}$$

This function represents the fractional energy in the time-frequency cell $\Delta t\Delta\omega$ at time t and frequency ω.

Ideally, the time marginal (4.43) and the frequency marginal (4.44) conditions should be achieved,

$$\int_{-\infty}^{+\infty} P(t,\omega)d\omega = |x(t)|^2 \tag{4.43}$$

$$\int_{-\infty}^{+\infty} P(t,\omega)dt = |X(\omega)|^2 \tag{4.44}$$

These conditions guarantee that the sum of the energy distribution for all the frequencies occurring at a given time is equivalent to the instantaneous power[18], and the sum of the energy distribution for all the times at which a given frequency occurs is equivalent to the energy density spectrum [Cohen, 1995]. The total energy of the distribution is

$$E = \int_{-\infty}^{+\infty} |x(t)|^2\, dt = \int_{-\infty}^{+\infty} |X(\omega)| d\omega\,, \tag{4.45}$$

and must satisfy

$$E = \int_{-\infty-\infty}^{+\infty+\infty} P(t,\omega)d\omega dt\,. \tag{4.46}$$

The method of the characteristic function operator is a consistent method to deduct time-frequency distributions. According to it, the distributions can be characterized by an auxiliary function, called the kernel, and the restrictions imposed on the kernel will establish the properties of the distribution.

Distributions generated by this criterion are usually classified as general Cohen's class distributions.

Any joint time-frequency distribution can be expressed according to

$$\mathrm{TFD}(t,\omega) = \int_{-\infty}^{+\infty}\int_{-\infty}^{+\infty}\int_{-\infty}^{+\infty} x\left(\mu+\frac{\tau}{2}\right)x^*\left(\mu-\frac{\tau}{2}\right)\phi(\xi,\tau)\,e^{(j\xi\mu - j\tau\omega - j\xi t)}d\mu\, d\tau\, d\xi\,, \tag{4.47}$$

where $x(t)$ is the time domain signal, $x^*(t)$ the complex conjugate of $x(t)$, ξ the frequency lag, τ the time lag. $\phi(\xi,\tau)$ is the kernel function that characterizes each one of the Cohen's class time-frequency distributions.

[18] Energy per unit of time

Recalling the indirect method for computing the PSD, and generalizing it to the time-frequency domain, the result is

$$\mathrm{TFD}(t,\omega)=\int_{-\infty}^{+\infty} R'_x(t,\tau)\,e^{-j\tau\omega}d\tau\,, \tag{4.48}$$

where $R'_x(t,\tau)$ is the generalized time-indexed autocorrelation function.

Comparing (4.47) with (4.48) leads to

$$\mathrm{R}'_x(t,\tau)=\int_{-\infty}^{+\infty}\int_{-\infty}^{+\infty} x\left(\mu+\frac{\tau}{2}\right)x^*\left(\mu-\frac{\tau}{2}\right)\phi(\xi,\tau)\,e^{j\xi(\mu-t)}d\mu\,d\xi\,. \tag{4.49}$$

The instantaneous autocorrelation function of $x(t)$ can be identified in (4.49) as being

$$\mathrm{R}_x(t,\tau)=x\left(\mu+\frac{\tau}{2}\right)x^*\left(\mu-\frac{\tau}{2}\right). \tag{4.50}$$

Defining the autocorrelation domain kernel as the FT of the kernel

$$\Psi(t,\tau)=\int_{-\infty}^{+\infty}\phi(\xi,\tau)\,e^{-j\xi t}\,d\xi\,, \tag{4.51}$$

then expression (4.49) can be rewritten as

$$\mathrm{R}'_x(t,\tau)=\int_{-\infty}^{+\infty}\mathrm{R}_x(\mu,\tau)\,\Psi(t-\mu,\tau)\,d\mu\,. \tag{4.52}$$

The scheme in Figure 4.4 shows the basic processing for the determination of the spectrum of a non-stationary signal $x(t)$ through the Cohen's class time-frequency distributions.

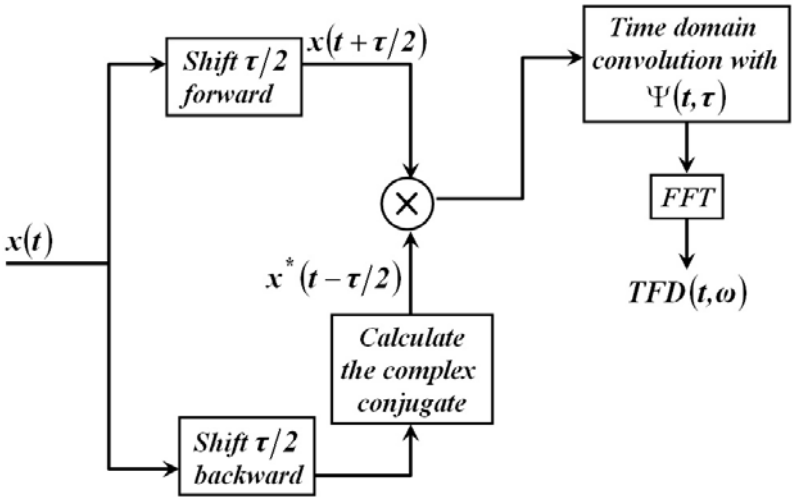

Figure 4.4 – Scheme for determining the time-frequency spectrum, using the concept of time-frequency distribution [Forsberg *et al.*, 1999].

Table 4.1 summarizes the desirable properties of the time-frequency distributions and the correspondent kernel restrictions.

Property	Distribution	Kernel
Non negativity	$\mathrm{TFD}(t,\omega)\geq 0$	$\phi(\xi,\tau)$ is the ambiguity[19] function of other function $w(t)$
Real-valued	$\mathrm{TFD}(t,\omega)=\mathrm{TFD}^{*}(t,\omega)$	$\phi(\xi,\tau)=\phi^{*}(-\xi,-\tau)$
Time shift	$x(t)\rightarrow x(t-t_0)\Rightarrow$ $\mathrm{TFD}(t,\omega)\rightarrow \mathrm{TFD}^{*}(t-t_0,\omega)$	$\phi(\xi,\tau)$ does not depend on t
Frequency shift	$x(t)\rightarrow x(t)e^{j\omega_0 t}\Rightarrow$ $\mathrm{TFD}(t,\omega)\rightarrow \mathrm{TFD}^{*}(t,\omega-\omega_0)$	$\phi(\xi,\tau)$ does not depend on ω
Time marginal	$\int_{-\infty}^{+\infty}\mathrm{TFD}(t,\omega)d\omega=\lvert x(t)\rvert^2$	$\phi(\xi,0)=1$ for any ξ
Frequency marginal	$\int_{-\infty}^{+\infty}\mathrm{TFD}(t,\omega)dt=\lvert X(\omega)\rvert^2$	$\phi(0,\tau)=1$ for any τ
Instantaneous frequency	$\frac{\int_{-\infty}^{+\infty}\omega\mathrm{TFD}(t,\omega)d\omega}{\int_{-\infty}^{+\infty}\mathrm{TFD}(t,\omega)d\omega}=\omega_i(t)$	$\phi(0,\tau)=1$ for any τ $\left.\frac{\partial\phi(\xi,\tau)}{\partial\xi}\right\rvert_{\xi=0}=0$ for any τ
Group delay	$\frac{\int_{-\infty}^{+\infty}t\mathrm{TFD}(t,\omega)dt}{\int_{-\infty}^{+\infty}\mathrm{TFD}(t,\omega)dt}=t_g(\omega)$	$\phi(\xi,0)=1$ for any ξ $\left.\frac{\partial\phi(\xi,\tau)}{\partial\tau}\right\rvert_{\tau=0}=0$ for any ξ
Time support	$x(t)=0$ if $\lvert t\rvert>T\Rightarrow$ $\mathrm{TFD}(t,\omega)=0$ if $\lvert t\rvert>T$	$\int_{-\infty}^{+\infty}\phi(\xi,\tau)e^{-j\xi\tau}d\theta=0$ if $\lvert\tau\rvert<2\lvert t\rvert$
Frequency support	$X(\omega)=0$ if $\lvert\omega\rvert>\Omega\Rightarrow$ $\mathrm{TFD}(t,\omega)=0$ if $\lvert\omega\rvert>\Omega$	$\int_{-\infty}^{+\infty}\phi(\xi,\tau)e^{-j\omega\tau}d\tau=0$ if $\lvert\xi\rvert<2\lvert\omega\rvert$

Table 4.1 – Some desirable properties of the time-frequency distributions and the corresponding kernel restrictions [Jeong,Williams,1992a].

[19] $A(\xi,\tau)$ is the ambiguity function of $w(t)$ if $A(\xi,\tau)=\frac{1}{2\pi}\int_{+\infty}^{-\infty}w^{*}\left(t-\frac{1}{2}\tau\right)w\left(t+\frac{1}{2}\tau\right)e^{j\xi\tau}dt$

4.5.1 SHORT TIME FOURIER TRANSFORM AS A COHEN'S CLASS METHOD

Considering the STFT of $x(t)$ as discussed before, the windowed signal $x_w(t,\tau)$ can be defined for each time t as

$$x_w(t,\tau)=\begin{cases} x(t)w(\tau) & t-\tau/2<t<t+\tau/2 \\ 0 & t<t-\tau/2 \wedge t>t+\tau/2 \end{cases} \tag{4.53}$$

where $w(t)$ is a window function with length τ, with the characteristics already described.

The time-frequency spectrum of $x_w(t,\tau)$ will be

$$X_w(t,\omega)=\int_{-\infty}^{+\infty} x(\tau)w(\tau-t)e^{-j\omega\tau}d\tau\,, \tag{4.54}$$

and its PSD, STFT or spectrogram is

$$STFT(t,\omega)=|X_w(t,\omega)|^2=\left|\int_{-\infty}^{+\infty} e^{-j\omega\tau}x(\tau)w(\tau-t)d\tau\right|^2. \tag{4.55}$$

It can be proved that the STFT fits in the Cohen's class of time-frequency distributions with the kernel [Cohen, 1989]

$$\phi(\xi,\tau)=\int_{-\infty}^{+\infty} w^*\left(y-\frac{\tau}{2}\right)w\left(y+\frac{\tau}{2}\right)e^{-j\xi y}dy\,. \tag{4.56}$$

However, the spectrogram does not satisfy the marginal conditions, and it is not certain that the distribution becomes null when the signal is zero. Among the properties of Table 4.1, only the first four are properties of the STFT.

4.5.2 CHOI-WILLIAMS

Multi-component signals are the result of the sum of several components. The time-frequency representation of these signals can present cross-terms that compromise the correct interpretation of the signal [Choi, Williams, 1989]. The bilinear nature of the distributions sometimes causes the occurrence of non-zero values where it should be null. These spurious cross-terms arise between the auto-terms [Jeong, Williams, 1992b].

In 1989, Choi and Williams suggested a new time-frequency distribution that they called the exponential distribution, and has been referenced in bibliography as the

Choi-Williams distribution (CWD). This method has shown good results in diminishing the cross-terms effect [Choi, Williams, 1989].

The kernel of the CWD is

$$\phi(\xi,\tau) = e^{-\xi^2\tau^2/\sigma} \tag{4.57}$$

where $\sigma > 0$ is a scaling factor that reflects the compromise between the auto-terms frequency resolution and the suppression of the cross-terms.

Higher values of σ will improve the auto-term resolution but increase the cross-term interference. Values of $\sigma > 1$ are advised for signals with sudden changes in frequency or amplitude. The choice of an optimal value for this parameter should be within the range $[0.1, 10]$ [Choi, Williams, 1989].

Expression (4.57) shows that CWD satisfies the marginal conditions as

$$\phi(\xi,0) = \phi(0,\tau) = 1. \tag{4.58}$$

The real-valued, time and frequency shifts, instantaneous frequency and group delay properties are also satisfied [Choi,Williams, 1989].

This distribution can be reached by substituting (4.57) into (4.48),

$$\mathrm{CWD}(t,\omega) = \int_{-\infty}^{+\infty} e^{-j\tau\omega} \int_{-\infty}^{+\infty} \frac{1}{\sqrt{4\pi\tau^2/\sigma}}\, e^{-\frac{(\mu-\tau)^2}{4\tau^2/\sigma}} x\left(\mu+\frac{\tau}{2}\right) x^*\left(\mu-\frac{\tau}{2}\right) d\mu\, d\tau, \tag{4.59}$$

being its discrete version [Choi, Williams, 1989]

$$\mathrm{DCWD}(n,\theta) = 2\sum_{\tau=-\infty}^{+\infty} e^{-j\theta\tau} \sum_{\mu=-\infty}^{+\infty} \frac{1}{\sqrt{4\pi\tau^2/\sigma}}\, e^{-\frac{(\mu-n)^2}{4\pi\tau^2/\sigma}} x(\mu+\tau) x^*(\mu-\tau). \tag{4.60}$$

When the signal contains several samples, its implementation requires the use of weighting windows. These windows, $w_N(\tau)$ and $w_M(\mu)$ will slide along the time axis according to the sums in (4.60):

$$\mathrm{DCWD}(n,\theta) = 2\sum_{\tau=-\infty}^{+\infty} w_N(\tau) e^{-j\theta\tau} \sum_{\mu=-\infty}^{+\infty} w_M(\mu) \frac{1}{\sqrt{4\pi\tau^2/\sigma}}\, e^{-\frac{(\mu-n)^2}{4\pi\tau^2/\sigma}} x(\mu+\tau) x^*(\mu-\tau). \tag{4.61}$$

The use of analytical signals is advised for the computation of (4.61) [Cohen, 1995] [Choi,Williams,1989]. The analytical signal can be obtained from the original signal by doubling its positive frequencies and removing the negative.

The window $w_N(\tau)$ in (4.61) should be symmetric with non-zero values within the range $-N/2 \le \tau \le N/2$. The size and shape of $w_N(\tau)$ establishes the frequency resolution of the distribution. Practical experiments indicate that lower values of N

correspond to worst auto-terms frequency resolution but also to a lower interference of the cross-terms [Choi, Williams, 1989].

The window $w_M(\mu)$ is usually a rectangular window set to unity for $-M/2 \le \mu \le M/2$. The parameter M defines the range from which the time index autocorrelation function is estimated.

The good performance of the CWD depends on the correct identification of the parameters σ, M and N. If the overlapping of $w_N(\tau)$ windows is considered, then the percentage of overlapping is another parameter to be studied.

4.5.3 DRAWBACKS

Most known time-frequency distributions do not respect all the demands listed in Table 4.1. Furthermore, most of the methods derived to deduct that kind of distributions cannot be considered consistent methods [Cohen, 1995], [Cohen, 1996b].

The major limitation is the non-existence of a comprehensible and complete theory on this subject. However many techniques and ideas that have been used, have been shown to be powerful and to agree with the intuition [Cohen, 1995]. Those techniques have been successfully applied in practice due to their improved time and frequency resolution.

Another limitation of some of those methods, namely of the DCWD, is the increase of computational burden involved on its implementation, when compared to the STFT or even the STMC.

4.6 SIMULATED SIGNALS SPECTRAL ESTIMATON

This section reports a set of tests conducted to study the performance behaviour of the STFT, STMC, and DCWD, when applied to MCA blood flow signals.

The relationship between the spectral estimators, the spectral parameters, and the parameters of the methods, were studied on 100 simulated signals. The WF simulator generated these signals with non-normalized averages computed from the SPS method with PFS delimitation of the cardiac cycles.

As clinical signals obtained from the TCD are corrupted with noise, the simulated signals were also used to generate signals with 20dB[20] and 10dB[21] of SNR. For this effect, additive white noise was considered so that constant spectral density was obtained.

All the results reported in this chapter represent the average of the 100 signals.

The spectral estimators were first implemented and tested on Matlab Version 6 Release 13, but due to the large number of tests were substituted by optimised programs developed in C language [Ruano *et al.*, 2003], [Moura, 2004].

To avoid overweighting the spectral parameters with higher values, all the errors are presented normalized to the mean of the respective reference signal, unless otherwise stated. The power variation over time is always considered normalized to its mean.

As it is intended to analyse how close the estimated signals can get to the true value, it was decided to evaluate the methods based only on the bias.

For all spectral estimations, rectangular windows were used. The test of other window functions would cause an unmanageable increase in the number of tests at this stage.

To relate the parameters of the methods with the estimation errors, the results were compared through the correlation coefficients given by,

$$r = \frac{\sum_{i=1}^{N}\left(bias_i - \overline{bias}\right)\left(u_i - \overline{u}\right)}{\sqrt{\sum_{i=1}^{N}\left(bias_i - \overline{bias}\right)^2 \sum_{i=1}^{N}\left(u_i - \overline{u}\right)^2}} \tag{4.62}$$

where $bias$ stands for the bias between the average of the estimated curves and the true curves, and u the value of the spectral curve under analysis.

4.6.1 SHORT TIME FOURIER TRANSFORM

To analyse the performance of the STFT it was chosen to consider windows of 11 different lengths, equally spaced between 60 and 560 bins. This corresponds to blood flow signal segments between 4.8ms and 44.8ms. Although 4.8ms is much lower than

[20] Typical of commercial Doppler systems in near optimal conditions.

[21] Corresponding to a noisy system

the 20ms usually advised, the unknown behaviour of the methods on the power variation over time and maximum frequency encouraged its use.

Ten different levels of overlap, from 0 to 90%, were used for each window. In total, 90 combinations of parameters were tested on each of the 300 simulated signals (signals with and without noise).

Figure 4.5 and Figure 4.6 show the correlation coefficients between the parameters and the averaged bias obtained with the application of STFT to simulated signals with ∞dB, 20dB and 10dB of SNR, for estimating the maximum and minimum frequency, rms bandwidth and power variation over time curves.

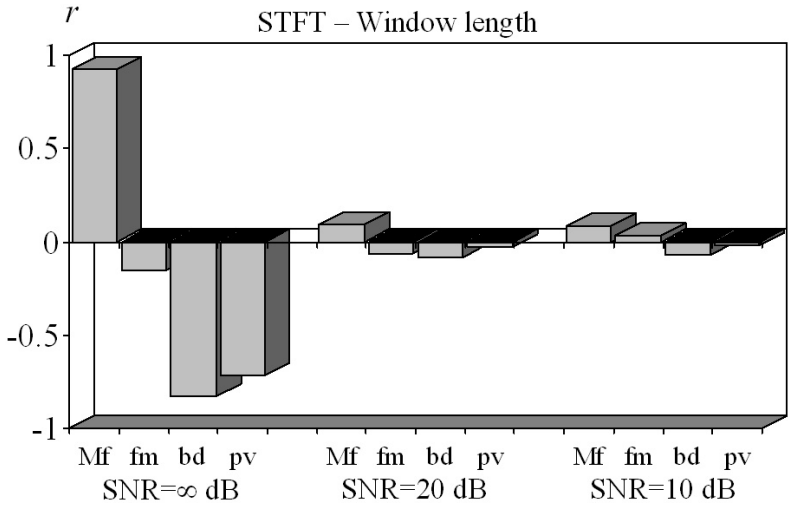

Figure 4.5 – Correlation coefficients between the window length and the averaged bias obtained with the application of STFT to estimate the four spectral parameters. The results were obtained using simulated signals with and without noise.

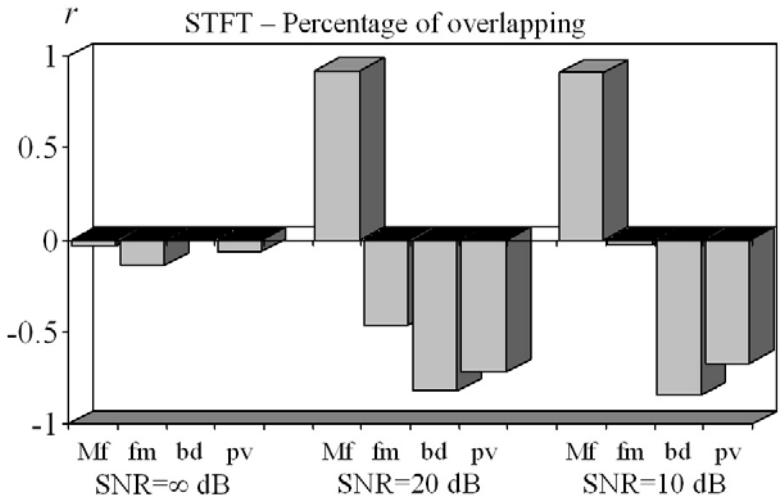

Figure 4.6 – Correlation coefficients between the percentage of windows overlap and the averaged bias obtained with the application of STFT to estimate the four spectral parameters. The results were obtained using simulated signals with and without noise.

The main conclusion from the figures is that the errors in estimates of noisy signals strongly depend on the choice of the amount of windows overlapping. On the contrary, the errors in estimates of signals with no noise depend mostly on the size of the window. However, for a good estimation of the mean frequency, the overlapping should not be disregarded on signals without noise and the window length should not be disregarded on very noisy signals.

The analysis of the results also led to the conclusion that on average, for signals with no noise, the lower errors of the estimates of maximum frequency correspond to lower window lengths, and of power variation to higher window lengths. The errors of the mean frequency estimates from non noisy signals decreases with the increase of window length until around the 260 bins, and from there, increase for larger windows. The estimates of the other spectral parameters show lower errors for larger windows. The analysis of the behaviour of overlapping is inconclusive, as it depends on the window chosen.

The estimates of maximum frequency for signals with 20dB of SNR, presents lower errors for lower windows overlapping. On the contrary, the estimates of rms bandwidth and power variation present lower errors for higher overlap. The errors of mean frequency estimates decrease until around 50% of windows overlap and increase from there onwards.

Finally, the estimates of signals with 10dB of noise present increased errors for the maximum frequency parameter and increased errors for the overlap issue. Mean frequency estimation errors do not start to increase before 30% of overlapping, and power variation estimation errors just decrease until 60% of windows overlap. The estimates of bandwidth present more accurate results for higher percentage of overlapping. Figures illustrating the previous conclusions are included in Annex B.

Table 4.2 shows the minimum and the highest errors obtained for the estimation of the four spectral parameters on noisy and non-noisy conditions.

	SNR=∞	SNR=20dB	SNR=10dB
Maximum Frequency	[0.1394 0.1895]	[0.1427 0.1904]	[0.1396 0.1905]
Mean Frequency	[0.0159 0.0331]	[0.0454 0.0666]	[0.2968 0.3070]
RMS Bandwidth	[0.0635 0.4666]	[0.3737 0.6909]	[1.7600 1.8642]
Power Variation	[0.0234 0.0555]	[0.0235 0.0550]	[0.0247 0.0513]

Table 4.2 – Ranges where the errors obtained from the STFT estimation can be found.

The analysis of Table 4.2, shows that as was expected the errors increase with the noise. However, the estimation of power variation seems to be immune to noise, and the estimation of the rms bandwidth is the one that suffers most from the effect of noise. In general, the STFT can be considered a good estimator of the power.

Table 4.3 presents the optimal parameters of the STFT for signals without noise, and for signals with SNR of 20dB and 10dB. These parameters correspond to the minimum estimation errors presented in Table 4.2.

	SNR=∞		SNR=20dB		SNR=10dB	
	Win. L. (bin)	Overlap (%)	Win. L. (bin)	Overlap (%)	Win. L. (bin)	Overlap (%)
Maximum Frequency	60	30	60	40	60	40
Mean Frequency	260	40	310	90	210	30
RMS Bandwidth	510	20	560	30	560	10
Power Variation	510	90	510	90	360	80
All Parameters Equally Weighted	510	20	510	20	110	0

Table 4.3 – STFT optimal parameters for three levels of SNR (Win L. represents the window length in terms of discrete bins).

4.6.2 "*SHORT TIME MODIFIED COVARIANCE*"

The battery of tests considered for the STMC included the same values for window length and overlapping and all the model orders between 1 and 10.

For the higher order of the models, there were some problems with the determination of spectra corresponding to small windows. Two averages for order 6, 10 averages for order 7, 8 and 9, and 11 averages for order 10 were not included since these cases contained at least one spectrum that could not be determined, due to ill conditioning of the matrix on the Cholesky decomposition. The reasons for these errors were associated with the proximity between the number of points in the window and the order of the model, and were found to depend on the nature of the data [Kay, 1988]. This problem could be overcome with an alternative to the Cholesky decomposition. Due to the inconvenient computational burden involved in that substitution, it was decided to ignore the averages with problems and proceed with the analysis with the rest of the data. Furthermore, none of the noisy signals suffered from this effect.

Figure 4.7, Figure 4.8 and Figure 4.9 show the correlation coefficients between the parameters and the averaged bias obtained with the application of STMC to simulated signals.

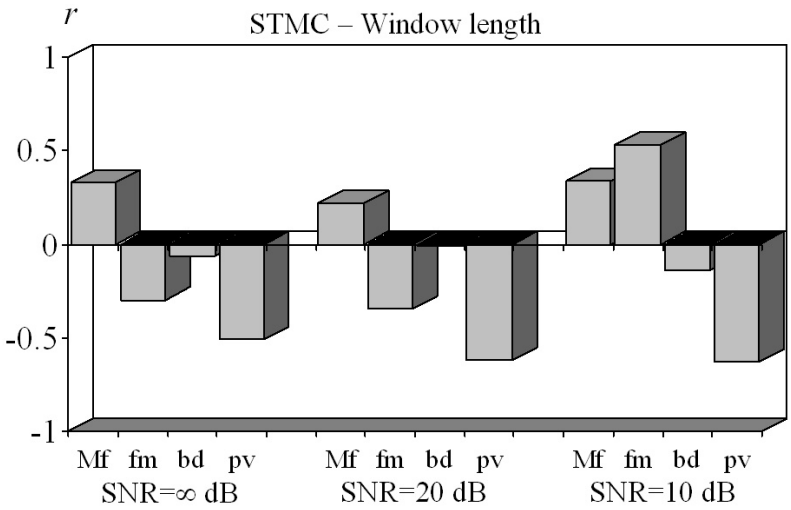

Figure 4.7 – Correlation coefficients between the window length and the averaged bias obtained with the application of STMC to estimate the four spectral parameters. The results were obtained using simulated signals with and without noise.

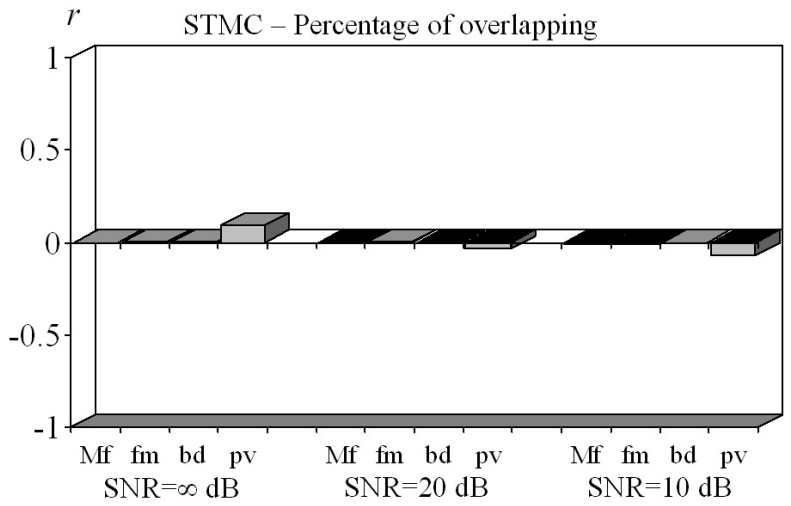

Figure 4.8 – Correlation coefficients between the percentage of windows overlap and the averaged bias obtained with the application of STMC to estimate the four spectral parameters. The results were obtained using simulated signals with and without noise.

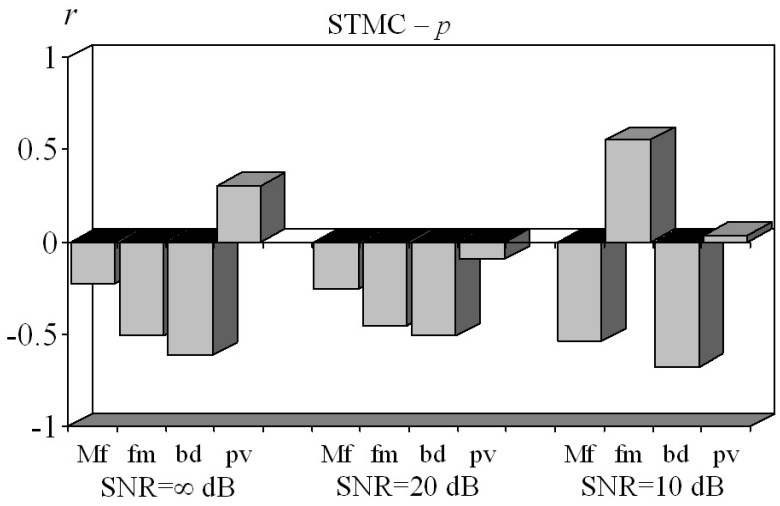

Figure 4.9 – Correlation coefficients between the order of the autoregressive model and the averaged bias obtained with the application of STMC to estimate the four spectral parameters. The results were obtained using simulated signals with and without noise.

By observation of the previous graphs, we may conclude that the percentage of segment overlapping is now the parameter with least influence on the bias. The only exception is the estimation of the power variation of very noisy signals. The influence of the choice of p and N on the accuracy of the estimation must be analysed for each situation. However, it is noticeable that the model order strongly affects the bandwidth estimation and has little importance on the power estimation. The window length should be carefully chosen when power estimation is required. For all other situations, p and N are equally relevant for the accuracy of the results.

Other conclusions can be made from the observation of the behaviour of the STMC according to the spectral parameters, to the parameters of the methods and, to the noise present on the signals (see figures in Annex B). For signals with no noise, the errors obtained from the estimation of the maximum frequency show that, in general, lower errors are related to shorter windows. Mean frequency estimation errors tend to decrease until the window length reaches 260 bins, and slightly increase for larger windows. However, the higher errors occur for shorter windows. As, in the case of the estimates of mean frequency, the order of the model is a significant parameter, it is also possible to determine that the higher errors occur for order 1. The higher errors of the bandwidth estimation occur for shorter window lengths and small orders of the model, and the errors of power variation estimation, decrease with the increase of window length.

Signals with 20dB of SNR tend to present more accurate maximum frequency estimations with windows with 110 bins length, upon which the increase of the window length increases the errors. The order of the model shows increasingly better results until the order 4, and from there the errors tend to grow. However, the lowest error in maximum frequency estimation is reached with order 6. The mean frequency estimates errors are higher for model orders lower than 3. The rms bandwidth estimated errors tend to decrease with the increase of the window length, and present very high values for the order 1 of the model. The errors of estimation of power variation decrease with the increase of the window length.

Signals with 10dB of SNR present higher estimation errors for window lengths of 60 bins and lower for 110 bins. From that size, the errors increase with the window length. The increase of the order of the model makes the estimation errors decrease until order 8. The estimation of mean frequency benefits from lower window lengths and model order. The bandwidth estimation accuracy gets higher with the length of the window applied and increases with the increase of the model order until order 5. Finally, the bandwidth estimation errors decrease until 260 bins of window length.

The ranges of the estimation errors obtained with the STMC are presented in Table 4.4.

	SNR=∞	SNR=20dB	SNR=10dB
Maximum Frequency	[0.0553 0.3292]	[0.0404 0.2595]	[0.0463 0.2351]
Mean Frequency	[0.0094 0.3846]	[0.0124 0.3355]	[0.0694 0.2791]
RMS Bandwidth	[0.0163 2.0368]	[0.2567 2.1074]	[1.7579 2.6400]
Power Variation	[0.0229 0.4402]	[0.0229 0.1179]	[0.0229 0.0620]

Table 4.4 – Ranges where the errors obtained from the STMC estimation can be found.

The minimum errors obtained with the STMC for the estimation of bandwidth correspond to a very good performance for signals without noise. For some reason the presence of noise seems to help with the estimation of the maximum frequency and power. This may be due to the attenuation of noise, as these results were obtained from the average of 100 signals. Other factors that can explain these results are the errors in the simulation of the maximum frequency waveform or the almost random nature of the power variation waveforms. Notice however that the maximum errors obtained for the estimation of the other parameters are not proportional to the increase of noise.

The optimal parameters for the signals with and without noise are shown in Table 4.5.

	SNR=∞			SNR=20dB			SNR=10dB		
	p	Win. L. (bin)	Overl. (%)	p	Win. L. (bin)	Overl. (%)	p	Win. L. (bin)	Overl. (%)
Maximum Frequency	5	60	40	6	110	0	8	110	10
Mean Frequency	2	260	30	3	260	30	2	60	40
RMS Bandwidth	6	210	10	3	110	60	5	560	10
Power Variation	3	510	90	7	460	80	2	260	50
All Parameters Equally Weighted	10	360	20	3	260	50	8	110	0

Table 4.5 – STMC optimal parameters for three levels of SNR (Win L. represents the window length in terms of discrete bins).

4.6.3 DISCRETE CHOI-WILLIAMS DISTRIBUTION

The set of parameters selected to study the DCWD were the same lengths of window that were considered for the other methods. The same percentage of overlapping with the exception of 0% was also considered. The hypothesis of non-overlapping was ignored because the *C* programs were not coded to deal with this situation. The values tested for M were 10, 20, 30, 40 and 50, and for the σ values employed were 0.1, 1, 3, 5, 7 and 9.

Figure 4.10, Figure 4.11, Figure 4.12 and Figure 4.13 show the correlation coefficients between the DCWD parameters and the averaged bias obtained for estimating simulated signals spectral parameters.

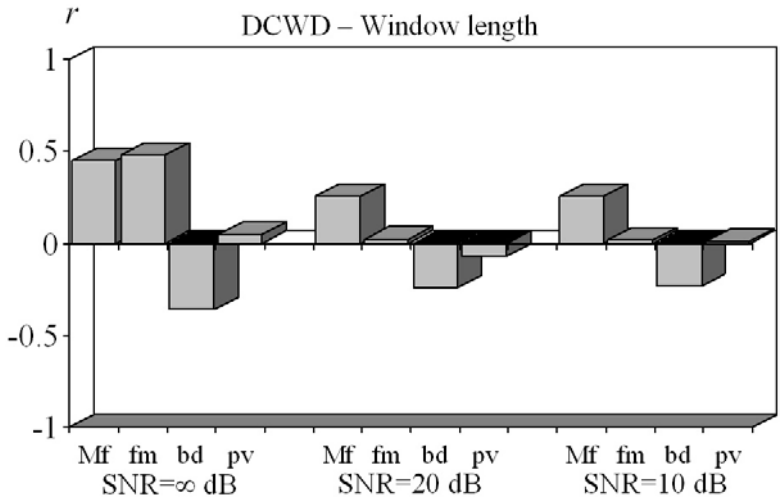

Figure 4.10 – Correlation coefficients between the windows length and the averaged bias obtained with the application of DCWD to estimate the four spectral parameters. The results were obtained using simulated signals with and without noise.

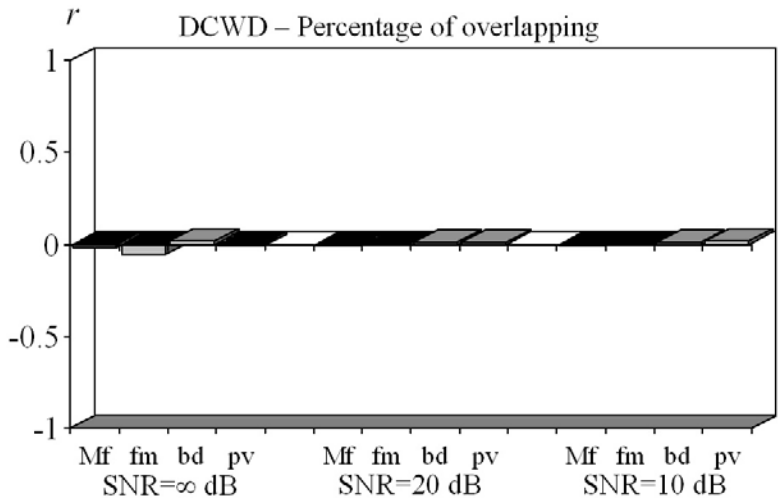

Figure 4.11 – Correlation coefficients between the percentage of windows overlap and the averaged bias obtained with the application of DCWD to estimate the four spectral parameters. The results were obtained using simulated signals with and without noise.

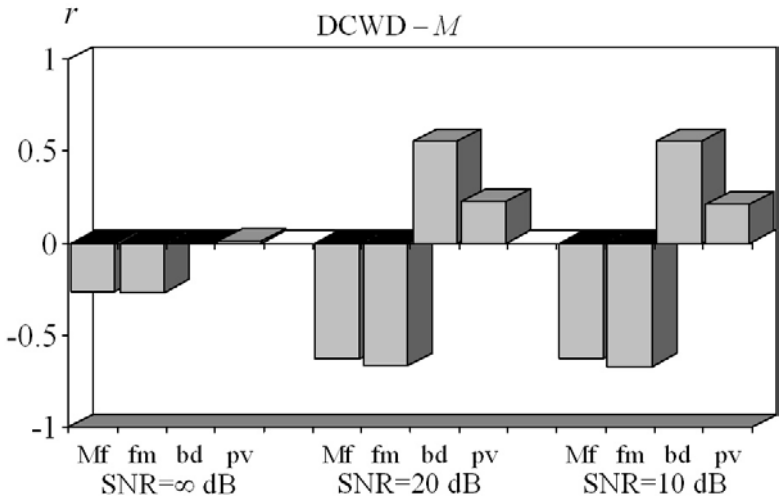

Figure 4.12 – Correlation coefficients between the range from which the time index autocorrelation function is computed and the averaged bias obtained with the application of DCWD to estimate the four spectral parameters. The results were obtained using simulated signals with and without noise.

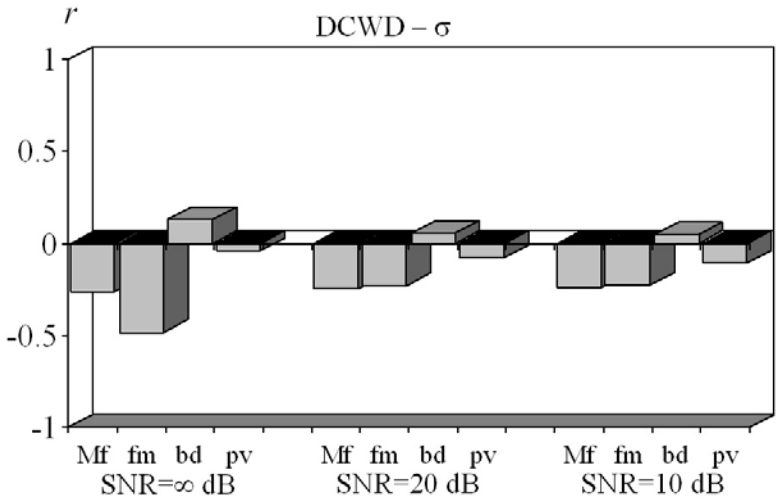

Figure 4.13 – Correlation coefficients between the scaling factor and the averaged bias obtained with the application of DCWD to estimate the four spectral parameters. The results were obtained using simulated signals with and without noise.

The previous graphs illustrate that the percentage of overlapping is the least important parameter. For signals without noise, the window length is the more relevant parameter, but for noisy signals, M becomes the parameter with most influence.

A more detailed analysis (see Annex B), shows that as more parameters are involved, the more difficult is to predict the behaviour of the errors obtained with each parameter regardless the other parameters. However, for signals without noise, the maximum and minimum errors of the estimates of maximum frequency occur for $M = 10$, the minimum errors for $\sigma = 3$, and finally the errors increase with the

increase of the window length. The mean frequency estimation errors decrease with the increase of M and σ. The lowest errors for bandwidth estimation occur for $M = 20$ and $\sigma = 0.1$. The maximum and minimum errors of power variation estimation occur for window lengths of 560 bins and 10% of window overlapping.

Signals with 20dB of SNR present lower maximum frequency estimation errors for higher values of M and σ. Lowest errors on the estimation of mean frequency are obtained with larger M values. The bandwidth estimates show the highest errors for $M = 50$ and the lowest errors for $\sigma = 0.1$. The estimates of power variation benefit from the application of higher window lengths and low percentages of overlapping.

The lowest errors for maximum frequency estimation for signals with 10dB of SNR are obtained with higher M and σ values. High values of M are also advised for mean frequency estimation, while very low values of σ are not advised. Rms bandwidth estimation benefits from the usage of low σ values and gets worst when higher values of M are used. The lower errors of estimates of power variation over time can be found with 10% of window overlapping.

The ranges of the errors obtained with the DCWD are presented in Table 4.6.

	SNR=∞	SNR=20dB	SNR=10dB
Maximum Frequency	[0.3900 0.6488]	[0.2765 0.6484]	[0.2765 0.6504]
Mean Frequency	[0.1561 0.2179]	[0.0607 0.2177]	[0. 0607 0.2209]
RMS Bandwidth	[0.0440 0.1880]	[0.0440 0.7011]	[0.0454 0.7011]
Power Variation	[0.6577 1.4718]	[0.6073 1.5914]	[0.6774 1.5914]

Table 4.6 – Ranges where the errors obtained from the DCWD estimation can be found.

The DCWD seems to be a good estimator for noisy signals. The smoothing kernel of the Choi-Williams distribution can explain this. Notice that although, in general, the maximum errors increase with noise, the minimum errors tend to be maintained regardless the noise condition.

Table 4.7 shows the best parameters for the use of DCWD on all kinds of signals.

	SNR=∞				SNR=20dB				SNR=10dB			
	M (bin)	σ	Win. L. (bin)	Overl. (%)	M (bin)	σ	Win. L. (bin)	Overl. (%)	M (bin)	σ	Win. L. (bin)	Overl. (%)
Maximum Frequency	10	3	60	50	50	9	510	20	50	9	510	20
Mean Frequency	50	9	410	10	50	3	310	20	50	3	310	20
RMS Bandwidth	20	0.1	460	20	20	0.1	460	20	20	0.1	460	20
Power Variation	40	7	560	10	40	5	560	10	30	7	460	10
All Parameters Equally Weighted	20	7	460	10	50	9	560	30	50	9	560	30

Table 4.7 – DCWD optimal parameters for three levels of SNR (Win L. represents the window length in terms of discrete bins).

4.6.4 COMPARISON BETWEEN THE METHODS

After having analysed the performance of all the methods individually, it is necessary to compare them.

Figure 4.14 shows the normalized errors obtained with the best results of the three methods on the estimation of all the spectral parameters.

From the graph, the immediate conclusion is that, except for the bandwidth, the DCWD is the worst estimator of blood flow in the MCA. However, this could also be due to the simulated signals having been generated based on the STFT. The performance on the estimation of the power is similar for the STFT and the STMC. For the rest of the cases, the STMC presents better results than the STFT.

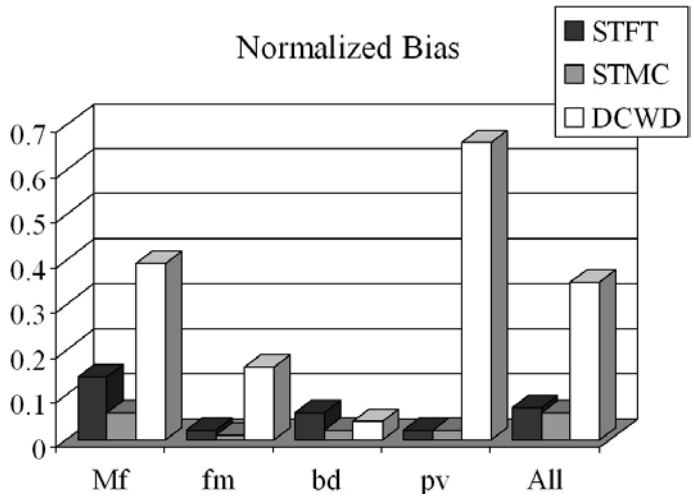

Figure 4.14 – Most favourable bias obtained with the estimation of the four spectral parameters with the three estimators. In the graph, Mf stands for maximum frequency, fm for mean frequency, bd for rms bandwidth and pv for power variation over time, and All for considering all parameters equally relevant for the assessment of the method.

Figure 4.15 shows the comparative performance (normalized bias) of the spectral estimators for all the spectral parameters on the three SNR conditions.

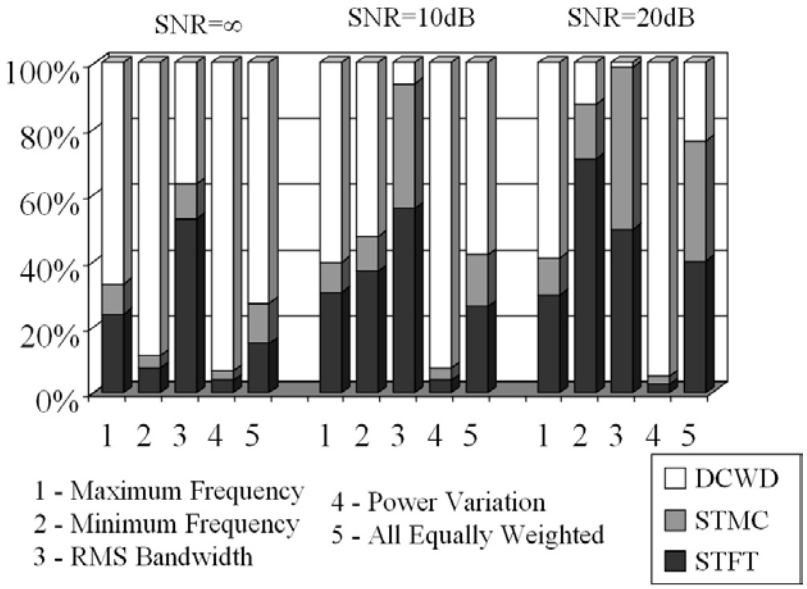

Figure 4.15 – Performance of the spectral estimation methods with the different spectral parameters for three levels of SNR. The smaller the percentage of bias, the better the estimation.

From the previous graph, it is noticeable that as the noise increases, the performance of the STFT worsens in general. On the contrary, the performance of the DCWD improves very much on the estimation of mean frequency and rms bandwidth, although it is always a bad estimator of the maximum frequency and power. When

embolic analysis is demanded, the DCWD can be excluded, because of its poor performance with respect to power estimation.

The STMC presents slightly better averaged results compared with the STFT while estimating power, but the analysis of individual cycles advises its exclusion due to the presence of spurious power peaks that could be taken as emboli. Furthermore, Figure 4.16 shows that when maximum frequency and power variation are the most relevant parameters, and except for unrealistic noiseless conditions, the STFT is the most accurate estimator. For reasons to be described in Chapter 6, this combination of parameters will be the most relevant for detecting emboli. Although the good estimation of mean frequency and power (relevant for emboli characterization) suggests the use of STMC, the differences between the performance of STFT and STMC are not drastically significant.

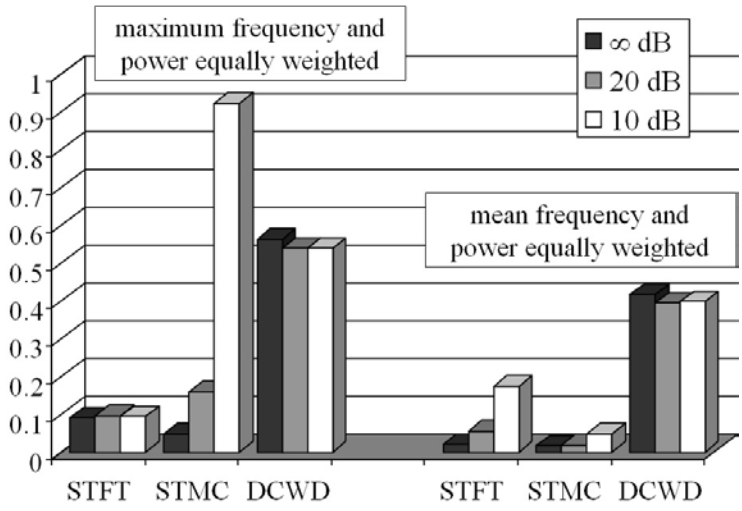

Figure 4.16 – Performance of the estimators when a good estimation of the maximum frequency and power variation or of the mean frequency and power variation is required.

The results obtained support the use of the STFT in the rest of this work, leaving the search of a better time-frequency estimator for future work.

4.7 CONCLUDING REMARKS

This chapter started with the discussion of the importance of using time-frequency analysis, and the description of three spectral estimation methods that have proven to be adequate for the treatment of Doppler ultrasound signals.

A detailed analysis of the behaviour of such estimators when applied to signals without emboli was also made in this chapter. The conclusions indicate that when

accurate power estimation is required, STMC and DCWD are not good alternatives to the STFT. Other applications, such as the search for stenosis could however benefit from the use of such estimators, as it depends on the accurate estimation of mean frequency and rms bandwidth.

Other methods of calculating the time-frequency representation of Doppler signals, considering that the maximum frequency and the power also have important information for medical applications, should be an issue for future work.

Other important results taken from the studies presented in this chapter were the establishment of a hierarchy of influences on the performance for the parameters of all the methods considered. This will be an important feature for future studies of applications of these methods. In this way, when the optimal parameters of the STFT are required, the choice must start with the window length. For the STMC, providing that $p > 1$, the choice must start with the window length, followed by the order of the model, and finally by the percentage of overlap. If the mean frequency is the main spectral parameter, probably the choice should start at p and be followed by the window length.

The analysis of the hierarchy of the parameters is more complex when DCWD is to be applied. For the maximum and minimum frequency waveform estimates, providing that $M > 20$ and $\sigma > 20$, the window length parameter is the most important. After having chosen the length of the window σ, M and overlapping should be chosen in this order. If the estimation of bandwidth is required, σ and M should be chosen before the window length and the overlap. Finally, the spectral power estimation accuracy depends mainly on the window length and overlap, and it is not clear what the influence of other parameters is.

Future work should include an analysis of the parameters with intermediate values not studied in this work.

5 SPECTRAL ANALYSIS OF SIMULATED EMBOLIC SIGNALS

5.1 INTRODUCTION

Time-frequency representations of Doppler signals allow an easy to interpret display, and the observation of the spectral parameters is a simple way of studying signal behaviour. However, several authors have expressed their preference for time-domain processing when embolic analysis is required [Smith *et. al.*, 1998] [Evans, 2003].

Embolic analysis mostly relies on the observation of the increased power in the Doppler signal during the passage of emboli through the sample volume. Other features, like the duration or the velocities associated to such occurrences, can also be analysed to distinguish embolic events from artefacts or to characterise emboli.

This chapter addresses the evaluation of time-frequency and time-domain analysis when the study of embolic events is required, based on the analysis of simulated embolic signals. It includes the description of the simulation process, the report of the tests performed, and the results obtained.

This chapter also includes a study on the optimal conditions to analyse embolic events when signal processing is employed.

Figure 5.1 shows the main methods and signals used in this chapter.

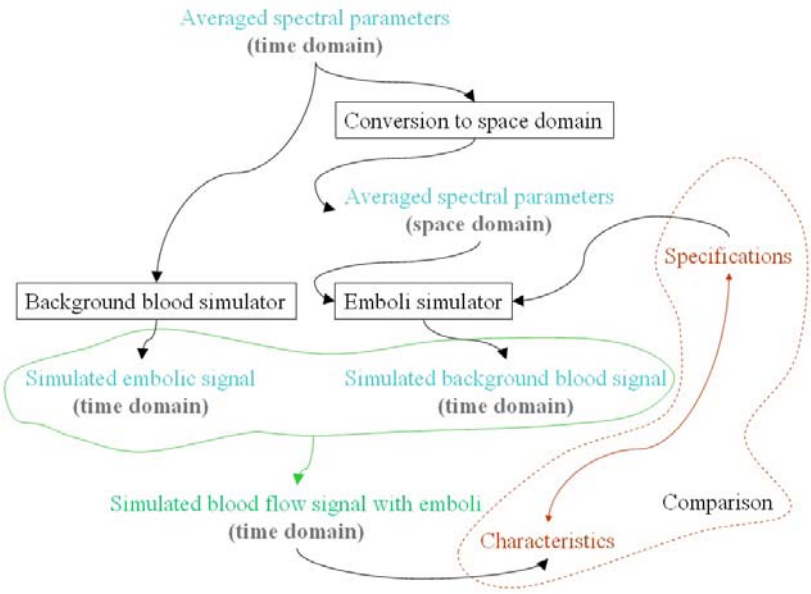

Figure 5.1 – Main methods and signals used in this chapter.

5.2 ANALYSIS OF EMBOLIC SIGNALS

There are at least three important features that can be used to characterize embolic events, the power returned from an emboli, the velocity of travel and the sample length over which it can be detected [Smith *et. al.*, 1998] [Evans, 2003].

A proper observation of those properties is deeply related with many other factors. Some of those factors can be mathematically manipulated, as the choice or tuning of the signal processing techniques, but others depend on the conditions under which the Doppler signal was recorded.

Included in the last group of factors are the relationship between the power returned by the background signal and the power returned from the embolus, and the duration of ESs.

Information on the power ratio and the velocity are contained in the time domain signal and must be regarded when simulation of emboli is required.

The relationship between the Doppler power scattered from blood and emboli depend mainly on the characteristics of the embolic event. Nevertheless, this ratio is influenced by the amount of blood in the Doppler sample volume.

The only dimension of the sample volume size that can be manipulated is the axial sample volume length, as the others depend on the dimensions of the artery.

The volume of blood included in the sample volume can be estimated from

$$Vol_b = A_{vl}\pi r_v^2 \tag{5.1}$$

where A_{vl} is the axial sample volume length of the probe and r_v the radius of the artery.

Large A_{vl} values produce large sample volume sizes that will reach a larger number of blood cells, and the total power scattered by blood will be higher. If an embolus is present, its power tends to be masked by the higher power of the surrounding blood, making the detection more difficult.

The time during which the effects of emboli are observable also depends on the axial length of the sample volume. The emboli will return significant signal over a great range of depths if the sample volume is large.

In addition, the velocity of an embolus defines the number of time bins that contain that embolus. From now on, the time bins containing an embolus will be referred to as positive bins. If the embolus is moving fast, it will be present in fewer time bins and in contrast, when the embolus is travelling slowly, there will be more positive bins.

Expressions relating the sample volume size, the velocity, the observable duration of emboli and detectable power can be studied by simple mathematical formulation. However, the randomness associated with biological signals requires a deeper study on the impact of the sample volume size on the probability of detecting and characterizing embolic events.

Taking into account the above-mentioned factors, several scenarios must be studied and the results analysed to identify the conditions of embolic detection when signal processing techniques are applied.

5.2.1 MEASURED EMBOLIC POWER

For reasons of clearness, the developments reported in this thesis were built under the assumptions that the power backscattered by 1mm^3 of blood has an arbitrary value K, the insonation is uniform, the power backscattered by the blood does not present significant variations over the cardiac cycle, and the high-pass filters do not remove significant amount of that power.

In these conditions, the power returned by each sample without emboli, may be computed as

$$P_B = K\pi r_v^2 A_{vl}\,. \tag{5.2}$$

The detection of emboli is usually achieved by comparing the power during the embolic occurrence with the power of blood without emboli. The Measured Embolic Power (MEP) is commonly used as an indicator to evaluate that comparison, being given by

$$\mathrm{MEP} = 10\log_{10}\left(\frac{P_E + P_B}{P_B}\right), \tag{5.3}$$

where P_E stands for the power backscattered by the embolus.

There are several approaches to measure P_E and P_B [Markus *et. al*, 1997]. Assuming that each cycle do not contain more than one embolus, in this work, $P_E + P_B$ can be achieved either from the mean power of the samples or from the maximum power within the record of the embolus, and P_B is found by the average power computed for the rest of the cycle.

Combining (5.2) and (5.3), the MEP becomes

$$\mathrm{MEP} = 10\log_{10}\left(\frac{K\pi r^2 A_{vl} + P_E}{K\pi r^2 A_{vl}}\right). \tag{5.4}$$

To simplify the analysis, the quantity L will be defined as the ratio between the power backscattered by the embolus and the power backscattered per unit of sample volume length,

$$L = \frac{P_E}{K\pi r^2}. \tag{5.5}$$

Figure 5.2 shows that lower axial sample volume lengths correspond to higher MEPs, and that this effect gets more evident for emboli backscattering higher powers.

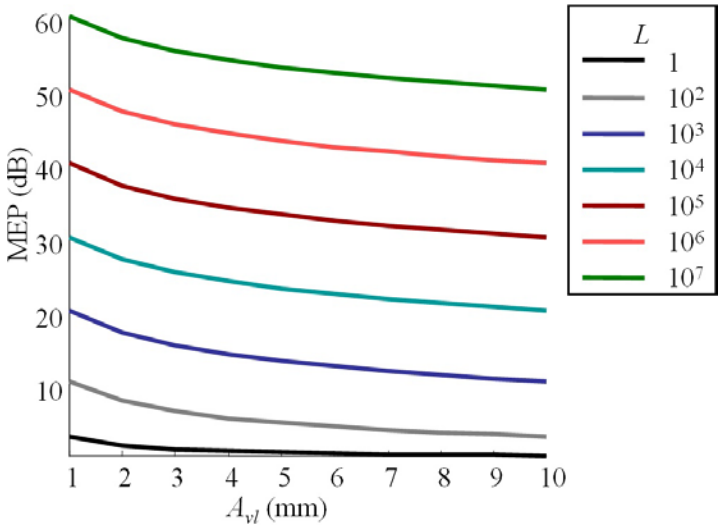

Figure 5.2 – Impact of A_{vl} on MEP, for several values of L.

5.2.2 EMBOLUS DURATION

The duration of the ES and velocity of the embolus are relevant parameters for embolic analysis. The duration of an ES can be observed directly.

The determination of the velocity depends on whether the signal is analysed in time or in the time-frequency domain. In either situation, the velocity is obtained from the frequency of the ES.

For time domain processing, the ES mean frequency can be computed from the number of complete half cycles in the portion of the signal showing embolic evidence. The ES frequency is then,

$$f_E = \frac{N_{hc}}{2D_E} \tag{5.6}$$

where f_E is the mean frequency of the ES, N_{hc} is the number of complete half cycles and D_E is the embolic time duration.

For time-frequency domain processing, the frequency of the ES can be extracted directly from the signal. The frequency corresponding to the embolic event should be observed in the centre of the ES.

The Doppler equation (2.2) establishes the relationship between the velocity of the scatterers and the frequency of the echoes received.

The sample volume length (SVL), is a measure frequently used, and is given by

$$SVL = D_E v_E , \tag{5.7}$$

where v_E is the velocity of the embolus. SVL can be interpreted as the estimate of the axial length over which the embolus is detected.

The observable duration of an embolic event depends on the velocity of the embolus and on the axial sample volume length. This relationship can be examined assuming a constant embolic velocity.

The observable duration of emboli can be computed through

$$D_E = \frac{(M + m - 1)}{v_E} \quad \text{for} \quad \begin{matrix} M = \max(A_{vl}, S_E) \\ m = \min(A_{vl}, S_E) \end{matrix} \tag{5.8}$$

where S_E is the effective axial length of the embolus, and should be interpreted as the effective embolic length scattered by the blood cells and detected by the ultrasound.

Notice that emboli with $S_E \geq A_{vl}$ never return their complete power.

Equation (5.8) illustrates that highest sample volumes maintain a longer track of the signal[22]. This effect and the relationship between the sample volume length and the observed duration of the emboli are shown in Figure 5.3. The graphics were created from (5.8) considering a constant velocity of $v_E = 0.2\text{ms}^{-1}$ and emboli with effective lengths of $S_E = 1\text{mm}$, $S_E = 5\text{mm}$, and $S_E = 10\text{mm}$. The effective sizes of the emboli were chosen to provide the observation of extreme cases.

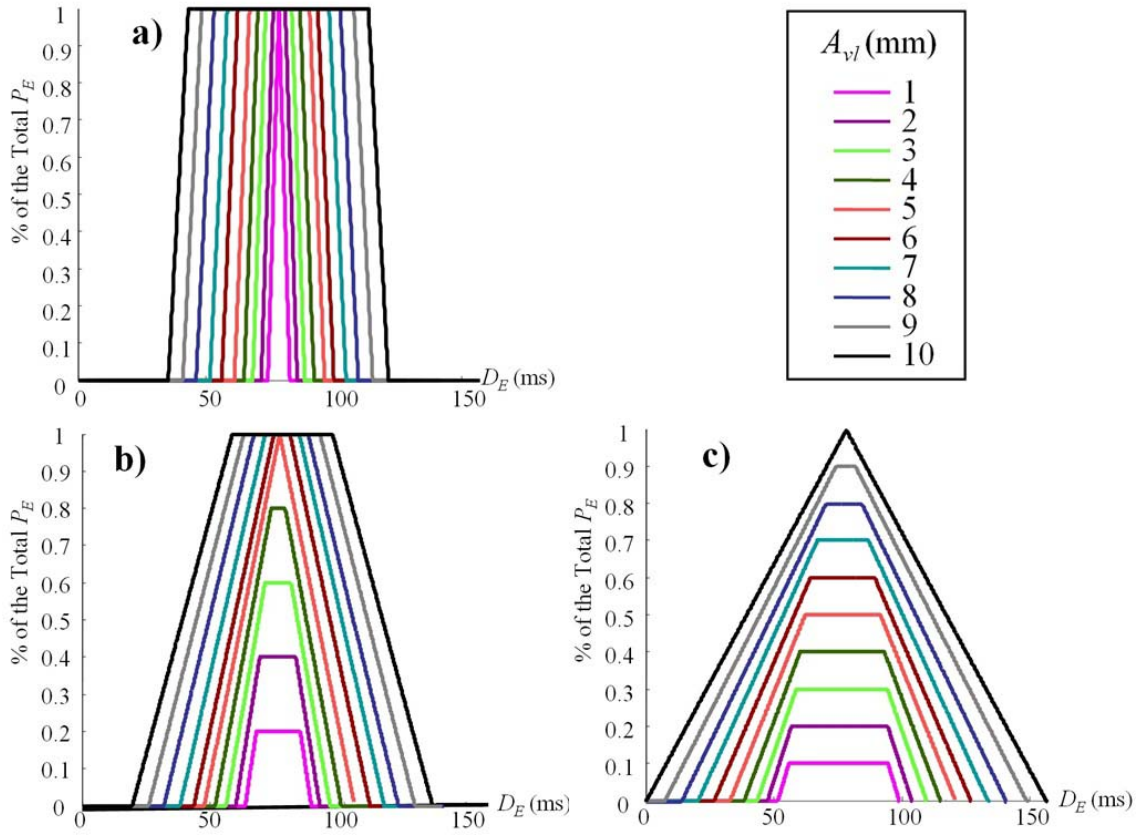

Figure 5.3 – Variation of the embolic time duration with the embolic power, for a constant velocity and emboli lengths of a) S_E=1mm, a) S_E=5mm, and a) S_E=10mm.

The time during which the complete power of emboli can be seen is given by the sensitivity function

$$D_E = \frac{(M - m + 1)}{v_E}. \tag{5.9}$$

22 D_E can present small variations according to the embolus position when the first positive beam reaches the embolus.

Notice that the graphs in Figure 5.3 were produced assuming a hypothetic direct relationship between the geometry of the areas backscattered by the embolus and backscattered by the blood cells. This is most probably an unrealistic assumption that will have little consequence on the conclusions that are aimed in the current study. As so, this assumption will be considered for the rest of the thesis. A detailed study on the shape of area backscattered by the emboli according to S_E and the nature of the emboli will be addressed in future works.

The velocity at which the embolus travels is another factor affecting the time during which that embolus is observed, as

$$D_E = v_E / S_E \ . \tag{5.10}$$

The relationship between the three variables, axial sample volume length, velocity of embolus, and embolus time duration is shown in Figure 5.4.

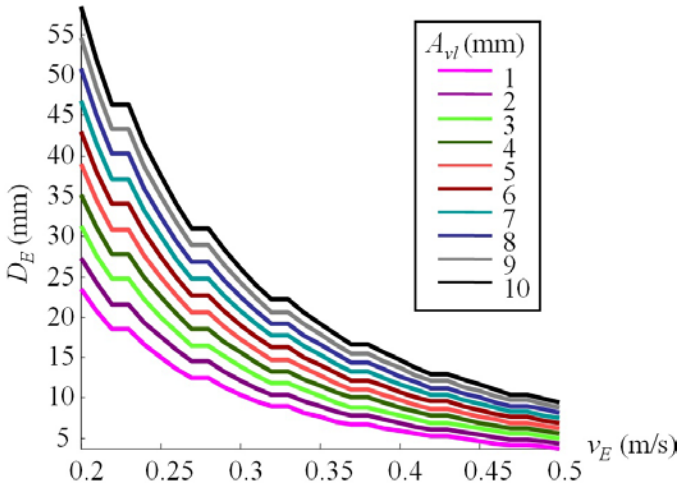

Figure 5.4 – Variation of the time during which an embolus is observable with respect to embolus velocity and the axial sample volume length considered.

5.3 SIMULATION OF EMBOLI

Recalling the waveforms of the spectral parameters studied in Chapter 3 and considering the previous exposition, it is reasonable to assume that the probability of detecting an embolus in the diastole is higher than in the systole. Assuming that the movement of embolic events follows the movement of the blood cells that surround it, then the velocity of emboli will reach higher values in the systole. Moreover, the MEP will be lower in the systole once the power of the background signal is higher.

According to this, the ability to detect an embolus will depend on the part of the cycle during which it travels through the sample volume. Emboli with the same size and nature will seem larger and will backscatter more power in diastole than in systole.

Power variation over time, as being the more relevant waveform, will affect all the results in this chapter. To avoid the increased power in systole masking the conclusions of this chapter, the power waveform will be considered constant all over the cycle. This simplification must however be reconsidered when conclusions are to be drawn. Nevertheless, the variation of the velocities along the cardiac cycle, as well as the effect of the axial sample volume length must be considered for simulating the ESs.

5.3.1 METHODOLOGY

The simulation of ESs involves four main steps: the estimation of the representative clinical averaged waveforms for ESs, the simulation of the time-domain background signal, the simulation of the time-domain embolic event, and the addition of both time signals. For clearness of explanation, from now on the averaged waveforms obtained in Chapter 3 will be identified as reference waveforms.

5.3.1.1 Reference waveforms

Time-domain clinical Doppler signals represent the average of all the ultrasound waves returned from the sample volume at each point in time. Therefore, the reference waveforms used to generate the background signal must reflect that information.

The significant features contained in the time domain signal can be extracted from just some of the samples. The relevant samples, or independent samples, are the ones that contain new information from the blood. The rest of the samples should be able to be obtained from the interpolation of the independent samples.

Treating the reference waveforms as function of independent samples, instead of time, allows the simulation of emboli regardless of the velocity, and considering the effect of the sample volume length on the background signal.

The value of each independent sample of the reference waveforms is a function of the mean velocity of the blood cells in the sample volume at each time,

$$u_s(s_i) = u_s(s_{i-1}) + u\left(\frac{A_{vl}}{v_{i-1}}\right) \tag{5.11}$$

where $u(n)$ is the reference waveform from the spectral parameter on analysis represented as a function of time, $u_s(s_i)$ is the same waveform represented as function of the independent samples, and v_i the mean velocity of the blood at time s_i.

Equation (5.11) represents the waveforms as function of the axial space traversed by the blood.

Figure 5.5 shows the mean frequency and rms bandwidth reference waveforms as a function of the independent samples. The waveforms were computed from (5.11), using the reference waveforms obtained in Chapter 3 (Figure 3.27) and considering $A_{vl} = 1$mm. Note that these are no longer equally spaced in time.

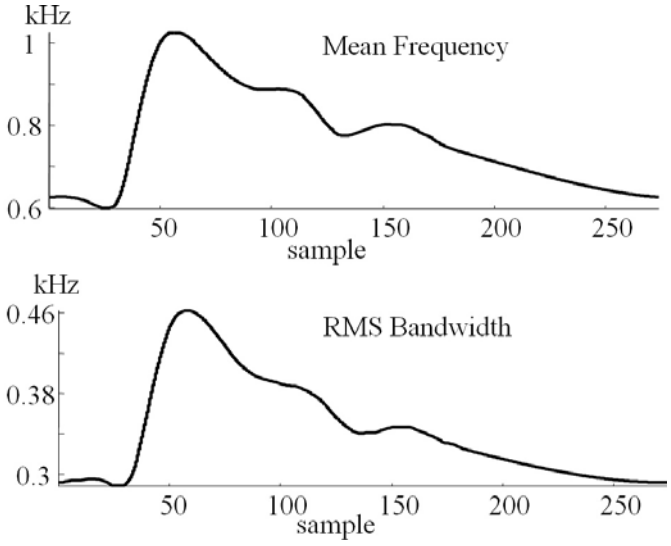

Figure 5.5 – Representation of the independent samples of mean frequency (top) and rms bandwidth (bottom) waveforms.

The power is considered constant over time, becoming a function of only the axial sample volume length.

5.3.1.2 Background blood flow signal

The simulation of the background blood flow has already been discussed in Chapter 3. However, the treatment of reference waveforms, when emboli simulation is required, involves further processing.

To simulate axial sample volume length effects, it is necessary to redraw the reference waveforms considering them a function of the axial space traversed by the blood.

To build the new mean frequency and rms bandwidth reference waveforms, the following adaptation of (5.11) was used,

$$u_s(s_i) = u_s(s_{i-1}) + u\left(\frac{\Delta s}{v_{i-1}}\right) \tag{5.12}$$

where Δs is the axial space resolution required to include small emboli within sample volumes.

The mean frequency and rms bandwidth reference waveforms can be converted back to the time-frequency domain through

$$u(n) = \frac{\sum_{i=nA_{vl}}^{(n+1)A_{vl}} u_s(s_i)}{A_{vl}} \tag{5.13}$$

where n is the discrete time index. The amplitude variation over time can be reconverted through

$$u(n) = \sum_{i=nA_{vl}}^{(n+1)A_{vl}} u_s(s_i). \tag{5.14}$$

Remember the squared amplitude gives the power. The simulated signals were generated according to the algorithm described in Section 3.2.3. It is convenient to preserve the $u_s(s_i)$ values contained in each $u(n)$, as they will be required for emboli simulation.

5.3.1.3 Embolic events

To provide a straightforward analysis of the results, a simple algorithm for simulating embolic events was sought.

ES can be described as short duration amplitude modulated sine waves [Evans, 2003]. One of the doubts that came out was if this amplitude form was determined by the sensitivity function (see Eq. 5.9). In this context, ES were considered amplitude-modulated sine waves with frequencies corresponding to the mean velocity of the blood cells surrounding them. However, the simulator accepts the option of not considering the sine amplitude modulation.

Now the variables required for the simulation are the power backscattered from the embolus, its axial length, and the velocity at which the embolus is flowing. Thus, the computation of the signal of the embolus as function of time can be performed as

$$x_e(n) = A_E w_E(n) y_{FM}(n) y_{AM}(n) \tag{5.15}$$

where A_E is the maximum amplitude of the embolus signal and $w_E(n)$ is a weighting factor indicating the amount of the embolus contained in the sample volume that corresponds to the sample at time *n*. The vector $w_E(n)$ is obtained from the interception of the axial space on the background signal, with the effective axial space position of the emboli, and thus, $w_E(n)$ is given by the sensitivity function.

The function $y_{AM}(n)$ reproduces the amplitude modulation and is given by

$$y_{AM}(n) = \sin(n+\pi)\sin(-n-\pi), \tag{5.16}$$

but can be set to ones if amplitude modulation is not required.

Finally, $y_{FM}(n)$modulates the embolus velocity, and is given by

$$y_{FM}(n) = \cos\left(2\pi f_E\left(n + \frac{n}{f_s}\right)\right) \tag{5.17}$$

where f_E is the mean velocity of blood at the axial centre of the embolus.

5.3.1.4 Simulated embolic signals

To obtain the simulated signal with embolus, the background signal must be added to the ES. The only issue on this process is concerned with the time location of the embolus. The range for which the signals are summed can be obtained by recalling the information on the $p_s(s_i)$elements that are contained on each $p(n)$register.

The resulting signal with embolus can be represented by the expression

$$x(n) = \begin{cases} x_b(n) + x_e(n) & n_i \le n \le n_f \\ x_b(n) & \text{other } n \end{cases} \tag{5.18}$$

where n_i and n_f represent the times of, respectively, the beginning and the end of the embolic register.

Figure 5.6 shows and example of the signals involved in Eq.(5.18).

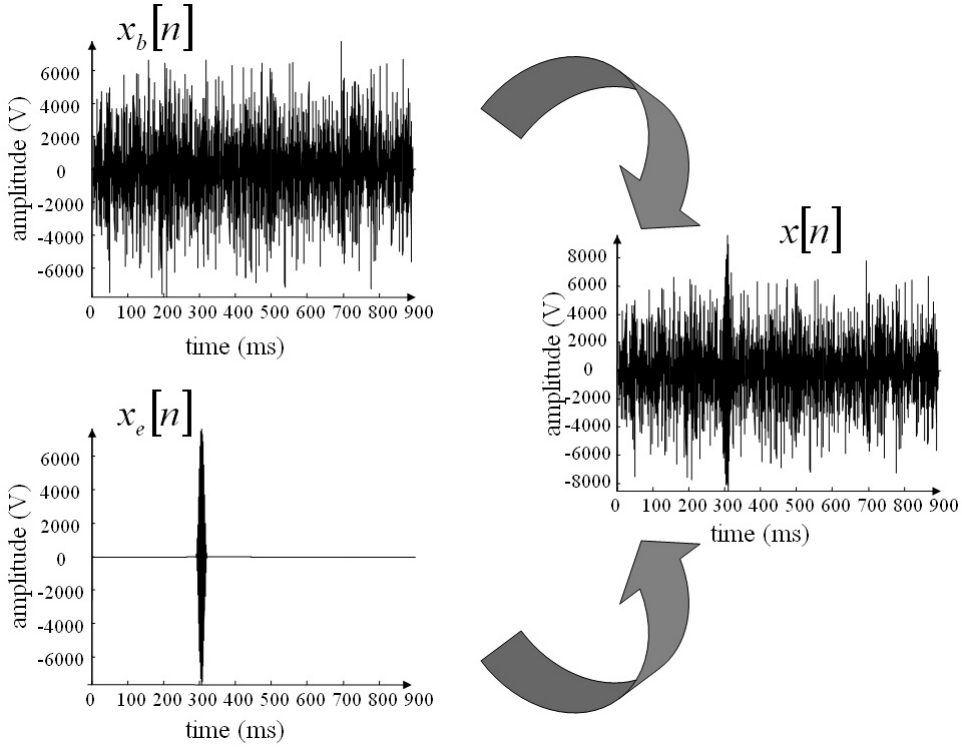

Figure 5.6 – Generation of an MCA Doppler blood flow signal with embolus.

5.4 CASE STUDIES

At this stage, there were several details to be studied. These details included the determination of the parameters of the simulator that correspond to realistic ESs, the effect of the axial sample volume length on the ES, and the decision of whether or not amplitude sine modulation should be used. Nevertheless, the main goal was the comparison of time-domain and time-frequency domain processing

Typical values of the embolic parameters are 0 dB to 65 dB for MEP, 10μs to 160ms for D_E, 2μm to 800μm for embolic diameter and 0.2m/s to 0.5m/s to v_E [Evans, McDicken, 2000] [Evans, 2003].

According to the ES simulator described before, the required input parameters are A_{vl}, L, S_E, the mean velocity of the embolus and position of the emboli in the cardiac cycle.

A first set of tests (see Table 5.1), that will be called first case study, was built with 10 values of A_{vl}. This includes values from 3mm to 1cm, used in other studies involving embolic analysis [Ringelstein *et. al*, 1998], and 1 and 2mm to allow an eventual observation of emboli with lower backscattered power.

The set of L included 20 values between 7320 and 2928000, that were chosen to simulate MEP values, considering the maximum value of $P_E + P_B$, covering the range between 39 and 65dB for $A_{vl} = 1\text{mm}$ and between 29 and 55dB for $A_{vl} = 1\text{cm}$. The L values were chosen to produce equally spaced ES amplitudes between 50000 and 1000000V. Notice that these values should correspond to considerable lower values of MEP when the mean value of $P_E + P_B$ is considered. This set was found to be the one that would lead to an easier visualisation of the effects of the signal processing techniques.

The choice of the group of the S_E values was the most problematic. Although it was not found in literature an estimation of the possible effective lengths observed for emboli, the main feeling was that those values should be very small. For that reason, 20 equally spaced lengths between 10μm and 0.77mm were chosen. Additionally, very small S_E values of 2, 4, 6, and 8μm were also considered. Although higher dimensions could have been used, prior observations pointed out that the current selection was sufficient to show effects that had not yet been reported in scientific articles (as far as known).

Before applying $y_{AM}(n)$ to the signal from the embolus, some tests were done to verify if the amplitude modulation was not a consequence of $w_E(n)$. However, the signals obtained were not exactly similar to the ones that can be found on clinical signals, and so, it was decided to use the amplitude sine modulation.

Figure 5.7 shows a signal with $S_E = 0.77\text{mm}$ simulated with and without sine amplitude modulation.

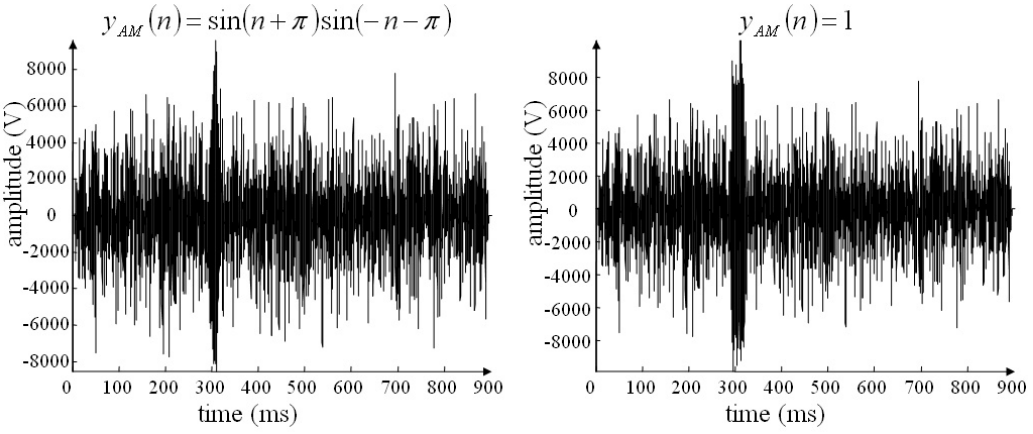

Figure 5.7 – Signal with $S_E = 770\mu\text{m}$ simulated with sine amplitude modulation on the left side, and the same signal without amplitude modulation on the left.

Finally, 7 locations of emboli were considered at critical places of the cardiac cycle, covering locations of acceleration, deceleration, high and low velocities, and feature points of the signal as showed in Figure 5.8. The velocity of each embolus was considered constant and equal to the mean velocity of the background signal at the centre of the embolus. This is purely for simulation.

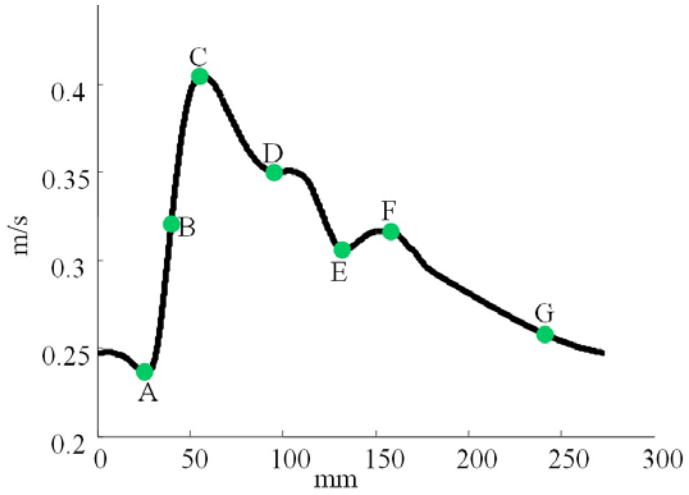

Figure 5.8 – Velocities and localization of emboli.

The letters near each embolus position in Figure 5.8 will be used for identifying the simulated emboli, latter in the text.

Although the simulator allows generating signals with multiple emboli per heartbeat, for this study it was decided to place only one emboli in each cardiac cycle. This allows using more information of the background blood.

Other parameters concerning the simulation are the axial space resolution of 0.001mm used in (5.12), and the time resolution of the time-domain signals that was set to 0.08ms, meaning that a sample containing A_{vl} mm of signal was taken every 0.08ms (see equations (5.13) and (5.14)).

To verify the behaviour of the emboli over the cardiac cycle, all the combinations of those parameters were used to simulate seven emboli placed at different locations on the cardiac cycle. Including embolic free signals, 33610 different scenarios were simulated.

Parameter	Value
A_{vl}	1; 2; 3; 4; 5; 6; 7; 8; 9; and 10mm
L	7,320; 29,280; 65,880; 117,120; 183,000; 263,520; 358,680; 468,480; 592,920; 732,000; 885,720; 1,054,100; 1,237,100; 1,434,700; 1,647,000; 1,873,900; 2,115,500; 2,371,700; 2,642,500 and 2,928,000
S_E	2; 4; 6; and 8μm; and 20 values equally spaced from 10 to 770μm
v_E	0.2367; 0.2583; 0.3062; 0.3165; 0.3209; 0.3504; and 0.4047 ms^{-1}

Table 5.1 – Values used to generate the scenarios of the first case study

Mainly to understand the relationship between $y_{AM}(n)$ and $w_E(n)$ a second case study was developed.

After some preliminary studies, it was verified that the effects of $w_E(n)$ were only observed for values of S_E higher than 1mm (see Figure 5.9). In addition, to produce emboli that could be seen for as long as 80ms, it was necessary to assume values of S_E as big as 10mm. For that reason, a new set of S_E was build with values from 1 to 10mm. The L values in this second case study were chosen to make the MEP (when the mean value of $P_E + P_B$ is considered) vary from 3 to 60dB when $S_E = 5$mm, and $A_{vl} = 10$mm.

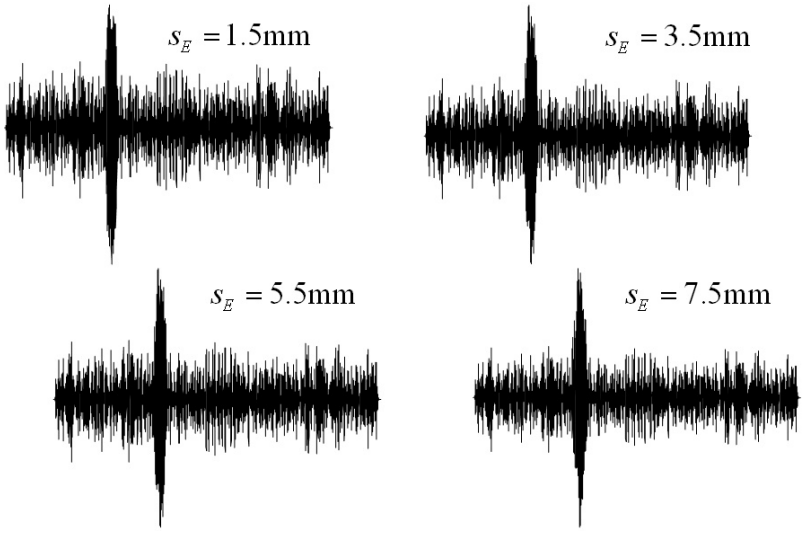

Figure 5.9 – Signals with S_E longer than 1mm, and without sine amplitude modulation.

The mean velocity of the emboli, as well as their position in the cardiac cycle was maintained. The A_{vl} values are the same considered in the first case study. For the

second case study, 14010 different scenarios were simulated, including embolic free signals. Table 5.2 shows the values of the parameters of the simulator used in the second case study.

Parameter	Value
A_{vl}	1; 2; 3; 4; 5; 6; 7; 8; 9; and 10mm
L	112; 373; 913; 2,011; 4,226; 8,680; 17,614; 35,506; 71,292; 142,830; 285,740; 571,150; 1,141,000; 2,278,400; 4,548,700; 9,079,100; 18,120,000; 36,162,000; 72,164,000 and 144,000,000
S_E	1; 2; 3; 4; 5; 6; 7; 8; 9; and 10mm
v_E	0.2367; 0.2583; 0.3062; 0.3165; 0.3209; 0.3504; and 0.4047 ms^{-1}

Table 5.2 – Values used to generate the scenarios of the second case study

All the signals were simulated on Matlab Version 6 Release 13.

Due to the amount of scenarios simulated, and to the consequent amount of computational burden, the results discussed next were produce with only one realisation for each case. For all the cases, the same background blood flow signal was used.

5.5 TIME DOMAIN PROCESSING *VS* SHORT TIME FOURIER TRANSFORM

This section describes some observations made from the application of the STFT and time-domain processing on simulated ESs.

To enable a fair comparison between both techniques, the time-resolution of the STFT was chosen so that relevant information would not be lost. Recalling that the theoretical maximum velocity present on the simulated signals was $0.6973ms^{-1}$, the required step between two FFT's was calculated to be $f_s/0.6973 \approx 18$ bins. To prevent any increase of the maximum velocity due to the random component of the simulated signal, the overlap was taken to be around 88%, corresponding to a step of five bins. This should not have any undesirable effect on the accuracy of the estimator, as noisy environments are not considered in this study and the accuracy of signals without noise weakly depend on the windows overlapping (see Section 4.6.1).

The window used on the STFT was 360 bins length, since this value was the one that better estimated equally weighted power variation over time and mean frequency parameters when high percentage of overlapping is considered.

The version of the STFT used to estimate the spectra of the simulated signals is the same that was used in Chapter4 [Moura, 2004].

5.5.1 FIRST CASE STUDY

The analysis of the results obtained for the first case study is presented in this section. To make the graphical visualisation of the figures in this section easier, the L values in Table 5.1 are coded in the figures according to Table 5.3.

L	Code	L	Code	L	Code	L	Code
7,320	L1	263,520	L6	885,720	L11	1,873,900	L16
29,280	L2	358,680	L7	1,054,100	L12	2,115,500	L17
65,880	L3	468,480	L8	1,237,100	L13	2,371,700	L18
117,120	L4	592,920	L9	1,434,700	L14	2,642,500	L19
183,000	L5	732,000	L10	1,647,000	L15	2,928,000	L20

Table 5.3 – *L* codes for the first case study

5.5.1.1 Time domain processing

The first characteristic analysed from the first case study was the MEP behaviour with the several scenarios simulated. The next graphs show the results of the MEP study. Figure 5.10 shows the MEP estimated for the different simulated effective sample lengths and L. In the same figure, the upper bar represents the expected MEP, that is, the values input into the simulator. The results represented in the graph were computed considering the maximum ES power. This graph was also produced for $A_{vl} = 1\text{mm}$, and for $v_E = 0.2367\text{ms}^{-1}$.

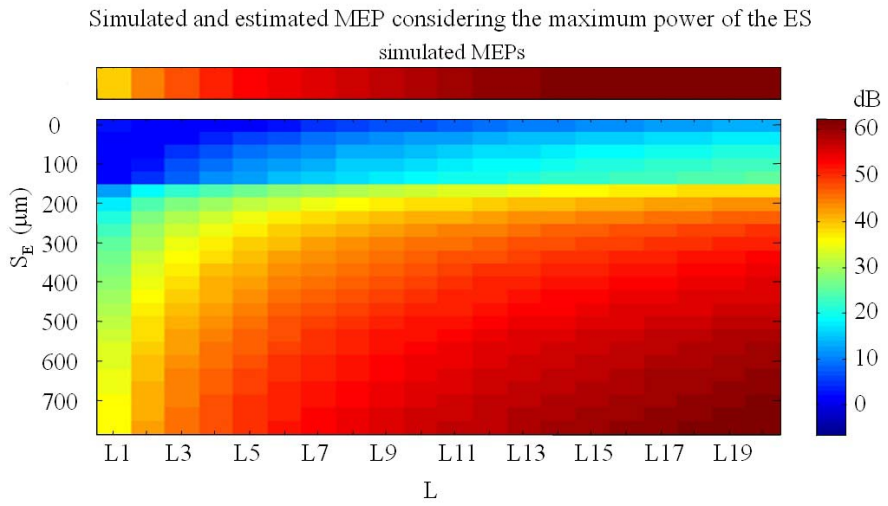

Figure 5.10 – First case study: Estimated MEP (maximum power) obtained with time-domain processing. The upper bar represents the expected MEP values, the right bar represents the colour scales.

The previous graph represents the behaviour of the MEP with the variation of the effective sample length of the emboli, and the influence of the background signal on the characteristics of the ES.

The most obvious feature observed in the graph is that for smaller S_E there seems to be less variability of the MEP than for bigger S_E. Actually, if the ultrasound returned by the embolus corresponds to just a very small part of the total ultrasound beam, even if the power is too high, its contribution to the total power return is very small. Among these, at least the emboli with smaller L values will probably remain undetected. For the same reason as the S_E increases, the powers of the simulated signals become closer to the ones inputted in the simulator.

Figure 5.11 shows the estimated MEP, when the mean power is considered, for the different simulated effective sample lengths and L, $A_{vl} = 1\text{mm}$, for $v_E = 0.24\text{ms}^{-1}$ (embolus located at position A in figure Figure 5.8).

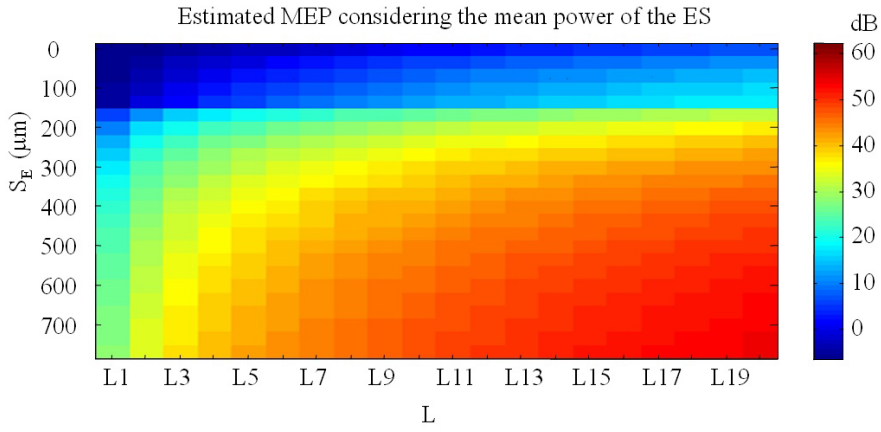

Figure 5.11 – First case study: Estimated MEP (mean power) obtained with time-domain processing. The left bar represents the colour scales.

As expected, the previous figure shows that the estimated power when the mean $P_E + P_B$ of all the positive bins is considered decreases due to the effect of the $w_E(n)$ function.

To analyse the performance of time domain processing in the identification of embolic events, it was necessary to determine a power threshold from which no false ES was detected.

Thresholds of 6, 9, 12, 15, 18, and 21dB were tested. The first threshold not involving false-positives was 15dB for time-domain processing. This way, the next conclusions will be taken under the assumption that only events involving MEPs over 15dB can be considered as emboli.

Figure 5.12 shows the estimated MEP for $A_{vl} = 1\text{mm}$ and for $v_E = 0.24\text{ms}^{-1}$, considering the mentioned threshold for detection.

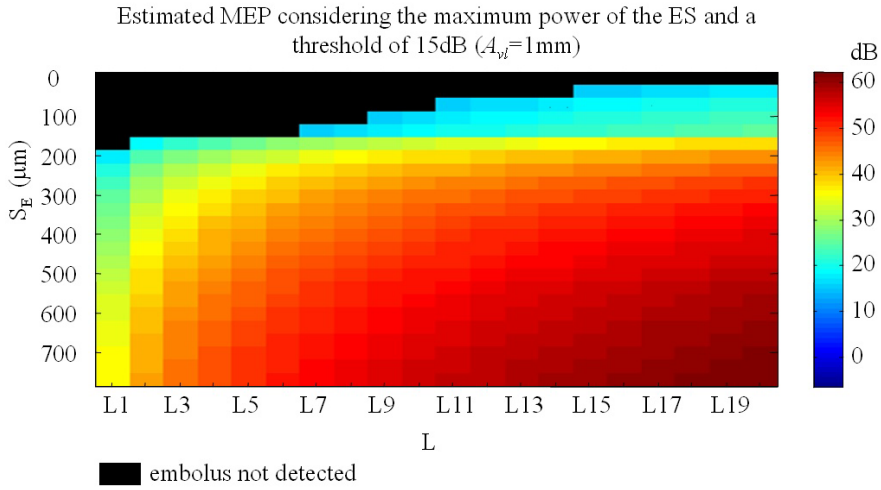

Figure 5.12 – First case study: Estimated MEP (maximum power) obtained with time-domain processing, A_{vl}=1mm, and a threshold for detection of 15dB.

In this case, 59 of the 480 ES whose characteristics are represented in the figure were not detected. As it was expected, the missed emboli correspond to the smaller S_E, and some of them correspond to very high P_E.

As observed in Figure 5.2, MEP decreases with the increase of A_{vl}. Figure 5.13 shows that effect.

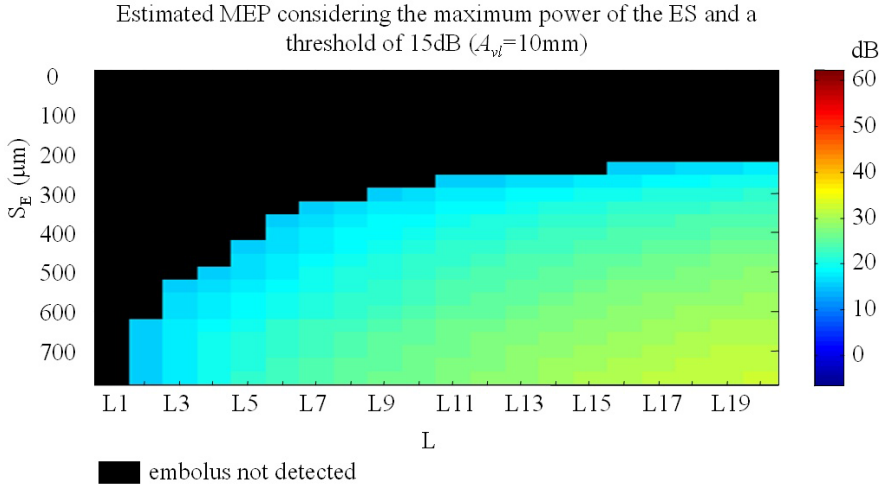

Figure 5.13 – First case study: Estimated MEP (maximum power) obtained with time-domain processing, A_{vl}=10mm, a threshold for detection of 15dB.

The graph corresponds to the different scenarios simulated for emboli identified as A and A_{vl} = 10mm. Comparing Figure 5.12 and Figure 5.13, it can be seen the general decrease of the MEP with the increase of A_{vl}. Even the higher powers, that in Figure 5.12 were located near 60dB, are now close to the 30dB. It also seems much

more difficult to distinguish between emboli with adjacent L values. However, the most significant disadvantage of increasing A_{vl} is the corresponding increased probability of not detecting emboli. In this case, 211 of the 480 simulated emboli were not detected.

Figure 5.14 shows the observed relationship between the number of emboli missed and the increase of A_{vl}, assuming a detection threshold of 15dB. The graph was created considering all the 3360 ES simulated for each A_{vl}.

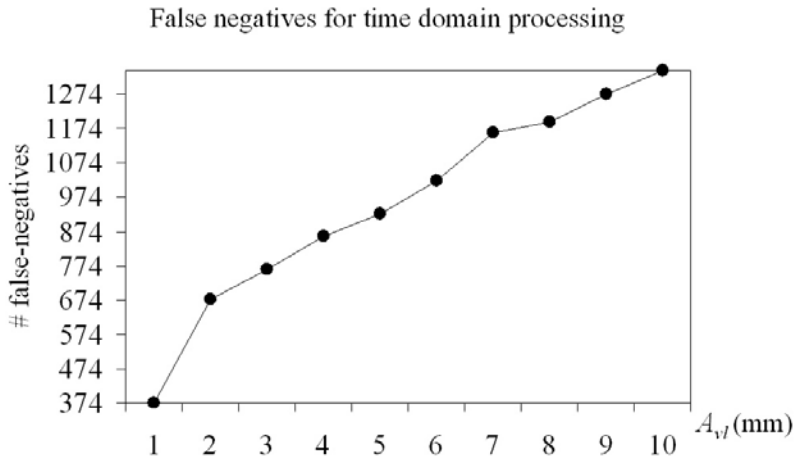

Figure 5.14 – First case study: Total number of false negatives found for the 10 values of A_{vl} using time-domain processing with a threshold for detection of 15dB.

The velocity is a very important parameter as the estimation of the SVL depends on it. The next figures are presented to help on the analysis of the velocities.

In this case, the embolic velocities were estimated according to (5.6) and (2.5).

Figure 5.15 shows the velocity estimated for the signals with emboli, when $A_{vl} = 1$mm, according to Eq. (5.6). The bar on the right represents the velocity scale. The emboli positions (see Figure 5.8) and velocities are also shown in Figure 5.15.

Recall that emboli A and G are the ones with lower velocities. Emboli identified as B is in the area of systolic blood acceleration. C corresponds to the systolic peak, and D, E, and F emboli correspond to locations between the late systole and early diastole.

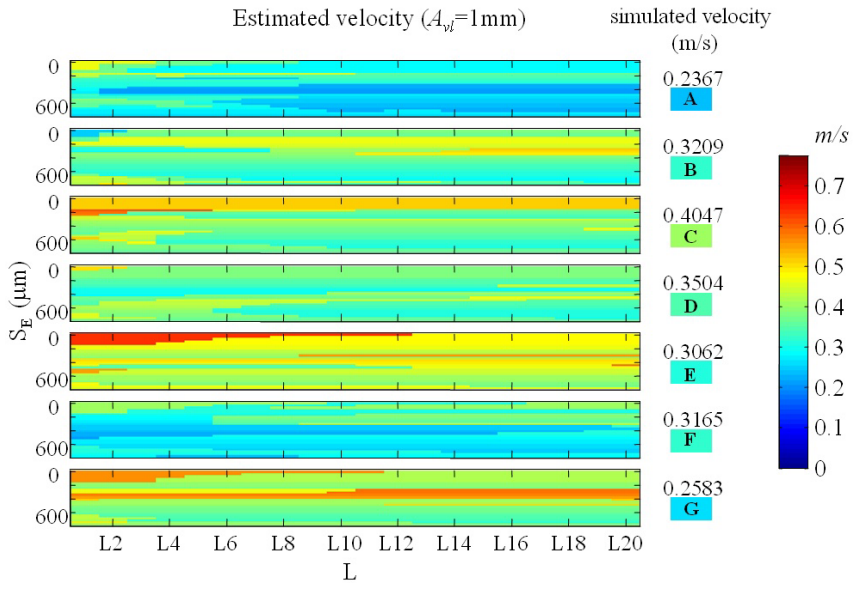

Figure 5.15 – First case study: Estimation of the velocities of the emboli using time-domain analysis for an A_{vl}=1mm.

The variability of the mean frequency spectral parameter, proportional to blood velocity, is responsible for the highly irregular behaviour of the velocity estimation. Smaller S_E and lower L, correspond to an overestimation of the velocity due to the higher influence of the background signal. Emboli placed in position E seem to be the one that suffers more from this effect. Recalling Figure 5.8, position E corresponds to a valley after a period of deceleration and before a period of acceleration, thus corresponds to an area of high variability of velocities. Remember, that in this case, the Doppler signal results from an average of the events from 1mm of blood. Therefore, any variation on the velocities in positive bins, not many in the case of $A_{vl} = 1\text{mm}$, will lead to deviations of the estimated velocity.

When $A_{vl} = 10\text{mm}$ this effect is attenuated, as there are more positive bins involved. This is shown in Figure 5.16.

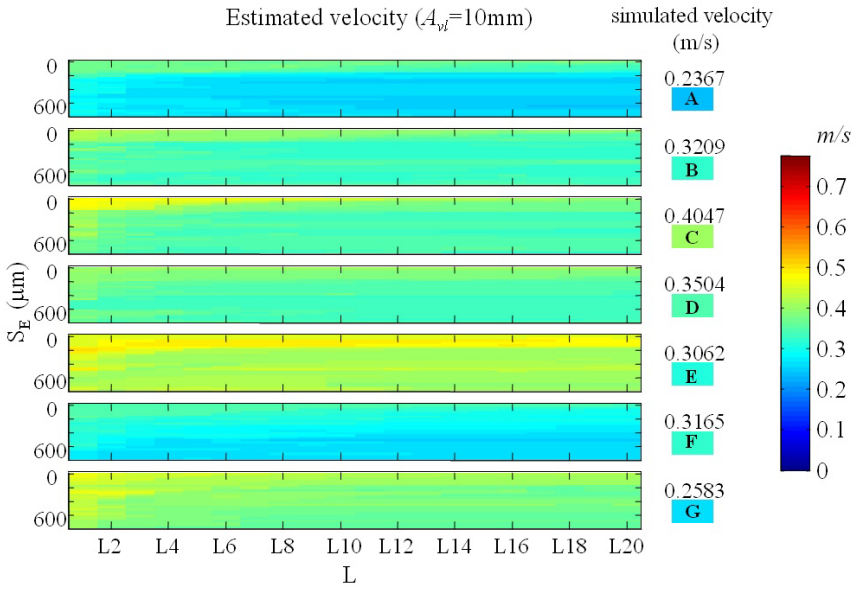

Figure 5.16 – First case study: Estimation of the velocities of the emboli using time-domain analysis for an A_{vl}=10mm.

With $A_{vl} = 10\text{mm}$, it is easier to observe that velocities of emboli in C are mainly underestimated, which was predictable since they were placed on the systolic peak. All the other velocities are mainly overestimated.

Figure 5.17 shows the velocities estimated using $A_{vl} = 1\text{mm}$, and the 15dB detection threshold. As there are less positive bins, when the detection threshold is applied, the velocity of emboli with smaller S_E becomes even more distorted by the background signal.

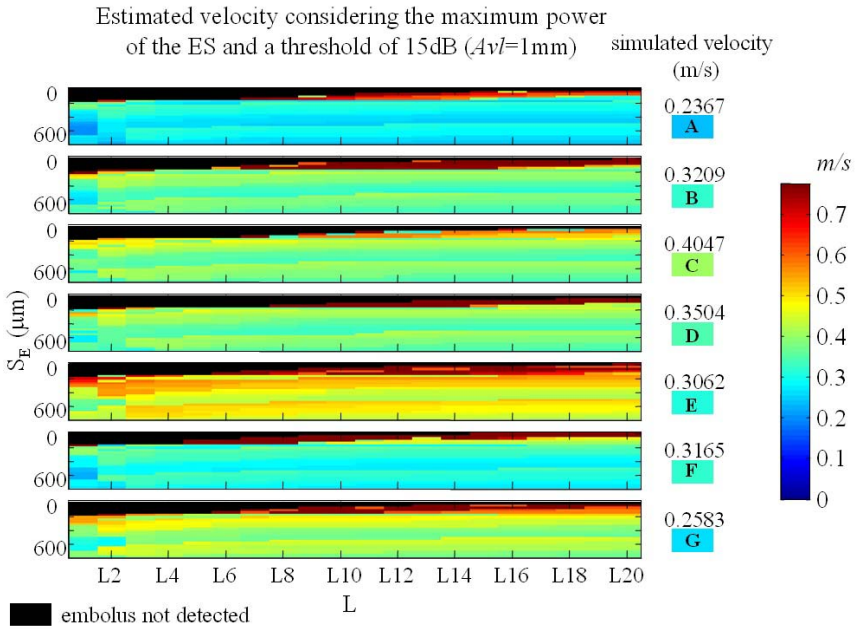

Figure 5.17 – First case study: Estimation of the velocities of the emboli using time-domain analysis for an A_{vl}=1mm, considering a threshold for detection 15dB.

However, the use of $A_{vl} = 10\text{mm}$ with the detection threshold has the opposite effect, as Figure 5.18 shows. As the bins that are neglected are the ones with more influence from blood, most of the estimated velocities are now closer to the simulated embolic velocities. There are however some embolic velocities deeply influenced by the surrounding blood. Those velocities correspond to the lowest L or smaller S_E. Emboli placed at B and E are still the ones presenting more differences between the simulated and the estimates velocities, for the reasons already discussed.

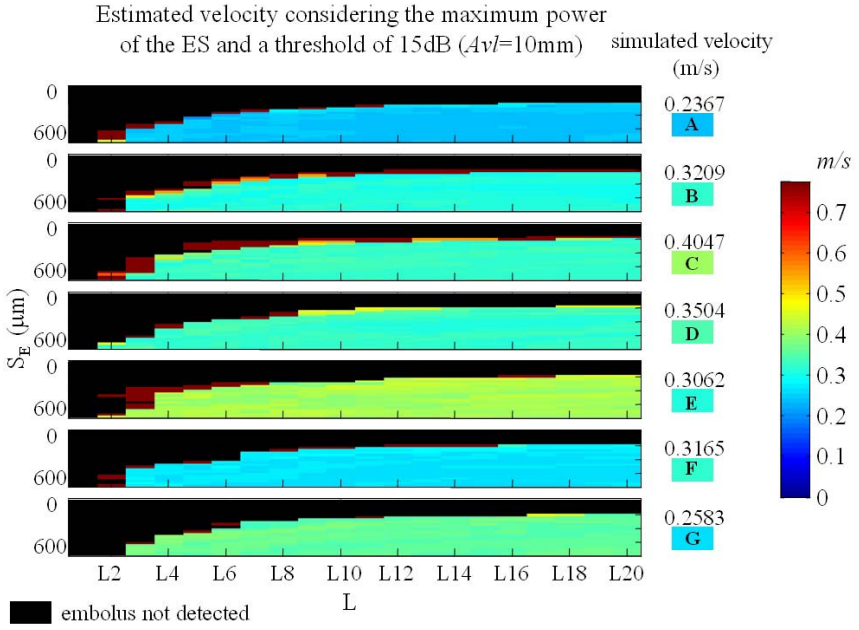

Figure 5.18 – First case study: Estimation of the velocities of the emboli using time-domain analysis for an A_{vl}=10mm, considering a threshold for detection of 15dB.

The last characteristics to be analysed in this study is the SVL of the emboli. As defined in Eq. (5.7), SVL depends on the duration of the ES and on the velocity of the emboli. There are no significant differences between the SVL estimated for several scenarios.

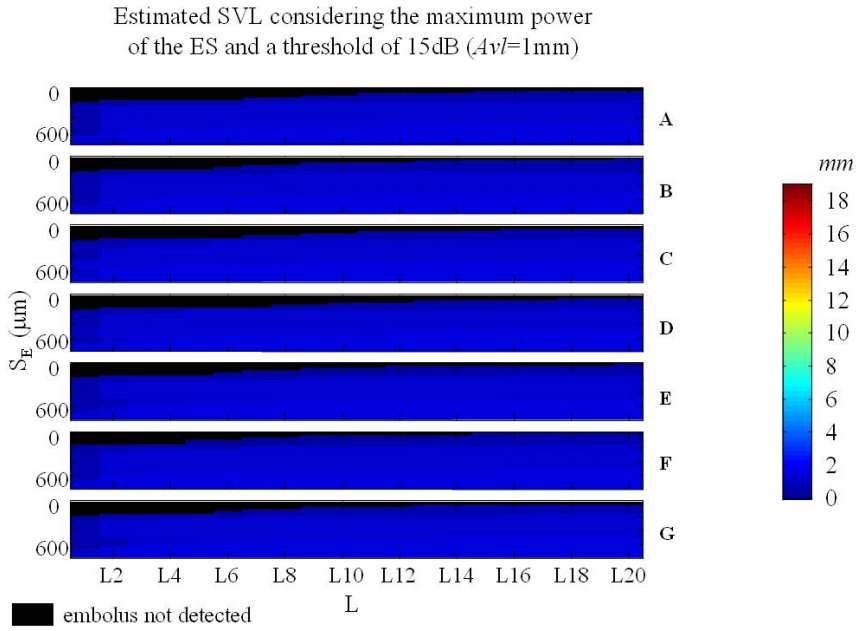

Figure 5.19 – First case study: Estimation of the SVL of the emboli using time-domain analysis for an A_{vl}=1mm, considering a threshold for detection of 15dB.

As expected, when A_{vl} increases the SVL also increases. Actually, with the increase of A_{vl} the duration increases, and the velocity also tends to decrease, as it was previously study. Lower effective embolic axial lengths and powers present lower SVL.

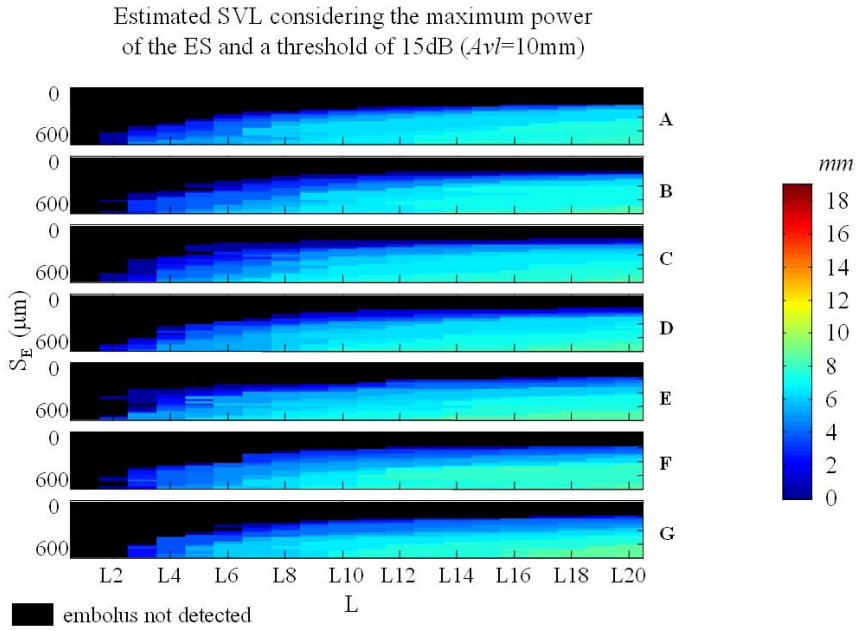

Figure 5.20– First case study: Estimation of the SVL of the emboli using time-domain analysis for an A_{vl}=1mm, considering a threshold for detection of 15dB.

In this context, although there is not a strong connection between the SVL and the S_E, through the joint knowledge of the embolic power and the SVL, and for longer A_{vl}, it is possible to deduct if the effective embolic length is shorter or longer.

5.5.1.2 Short Time Fourier Transform

To observe the effects of the STFT on the estimation of the relevant parameters of the ES, a study similar to the one developed for time-domain processing, was derived to analyse the spectrum of the signals.

Figure 5.21 shows the relationship between the simulated MEP and the estimated MEPs, when the maximum $P_E + P_B$ is used and for $A_{vl} = 1\text{mm}$ and $v_E = 0.24\text{ms}^{-1}$. The same observations made when time-domain processing was applied are still valid for STFT. The main difference is that the MEPs estimated with STFT are significantly lower than the ones obtained from time domain analysis. This is because each time bin in the spectrum obtained with STFT has the contribution of several time bins of the time-domain Doppler signal (in the current case has the contribution of 360 time-domain bins). Thus, the power of the time-domain positive bins will be masked by the power of weaker positive bins or by the power of non-positive bins.

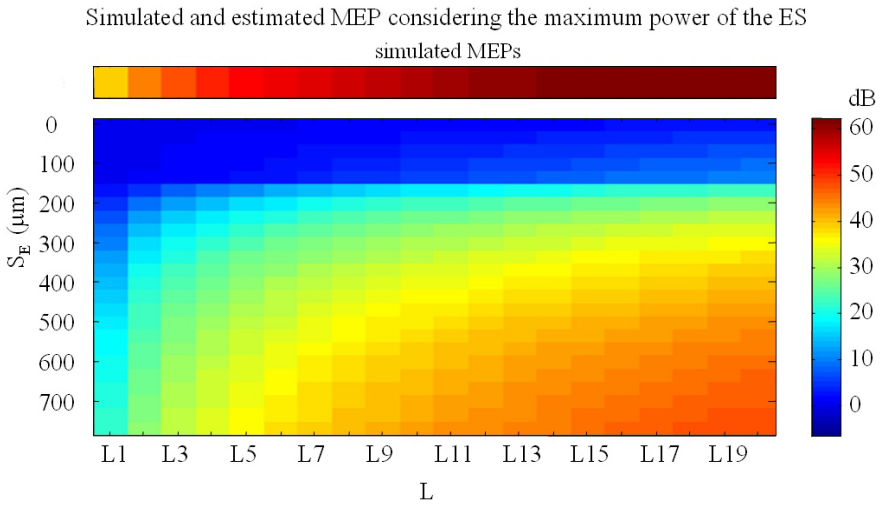

Figure 5.21 – First case study: Estimated MEP (maximum power) obtained with the STFT. The upper bar represents the expected MEP values, the right bar represents the colour scales.

Accordingly, when the mean value of $P_E + P_B$ along the positive bins is used, although the MEP values decrease, the difference is not as evident as it was in time-domain processing. Again, this is because, at each time, the spectra already have the

contribution from adjacent time bins, so the effects discussed for time domain are not so obvious here. Figure 5.22 shows this effect when emboli A is considered.

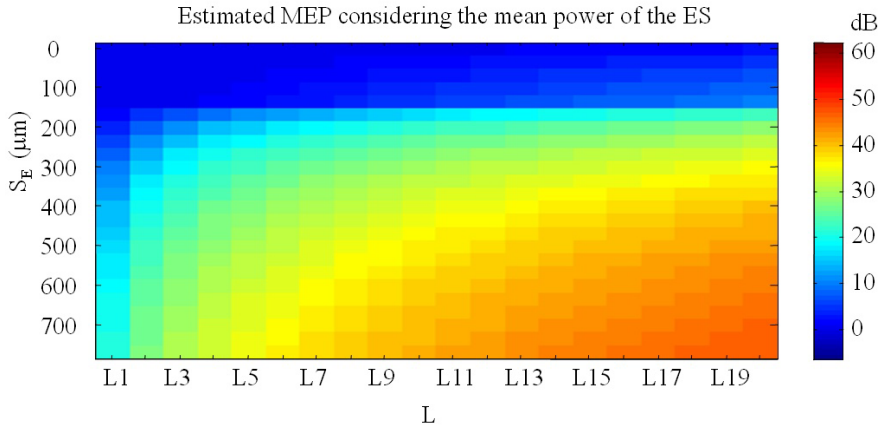

Figure 5.22 – First case study: Estimated MEP (mean power) obtained with the STFT. The left bar represents the colour scales.

To make a realistic interpretation of the effect of the STFT, it is necessary to determine a safe threshold for detection. The tests showed that when that threshold is set to 6dB, there are no false positives.

Figure 5.23 shows the MEPs estimated, for emboli placed in A, when the maximum $P_E + P_B$ of the positive bins and the detection threshold are considered.

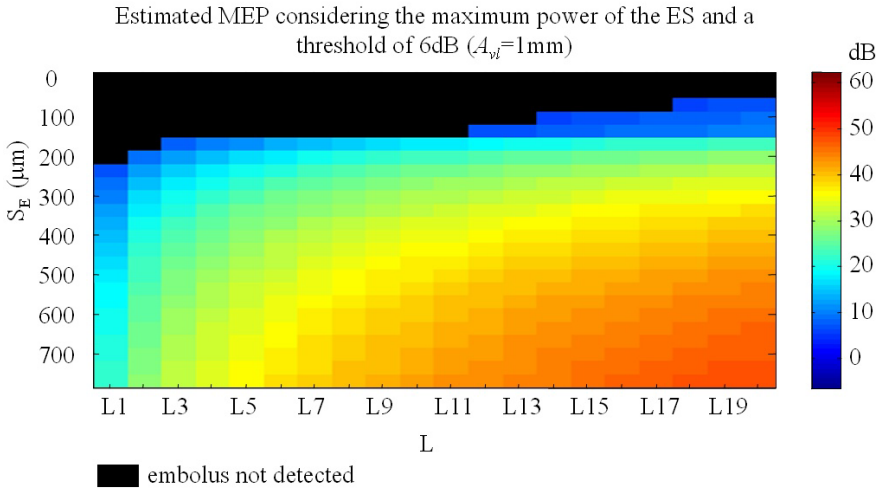

Figure 5.23 – First case study: Estimated MEP (maximum power) obtained with time-domain processing, A_{vl}=1mm, and a threshold for detection of 15dB.

In this case, 84 out of the 480 ES were not identified as emboli, meaning that the probability of losing emboli, in the current conditions, is higher with STFT than it was in time-domain processing.

However, as Figure 5.24 shows, the differences between the performance of STFT and time-domain processing, are not so obvious, when $A_{vl} = 10$mm.

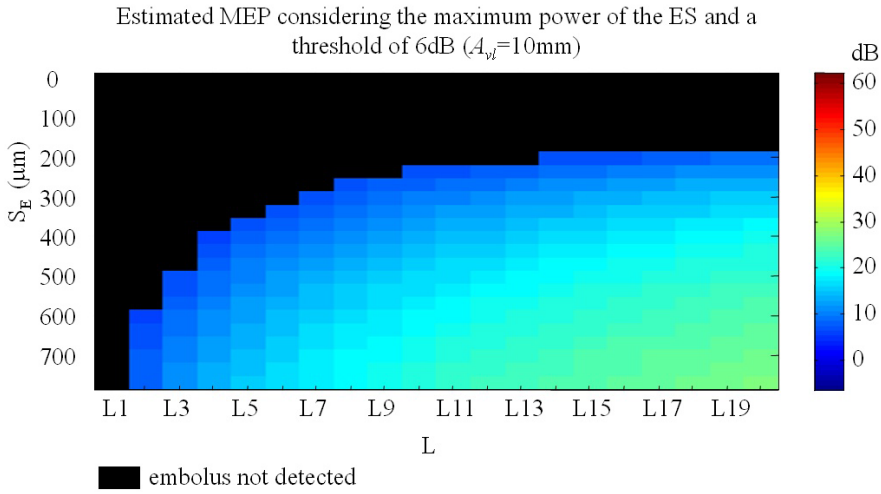

Figure 5.24 – First case study: Estimated MEP (maximum power) obtained with the STFT, A_{vl}=10mm, a threshold for detection of 6dB.

Although the MEPs from STFT are slightly lower than the ones obtained from time-domain processing, in this case, just 185 in 480 simulated ES were not detected; this is less than for time-domain analysis.

The observed relationship between the A_{vl} values and the emboli not detected are shown in Figure 5.25. For each A_{vl}, 3360 were simulated.

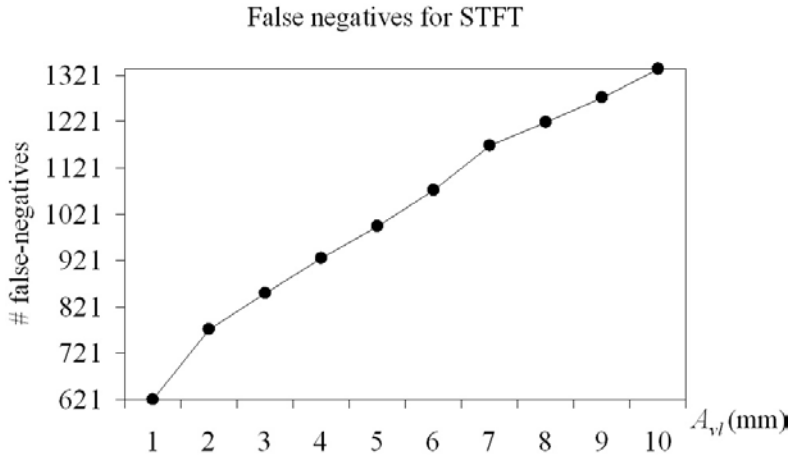

Figure 5.25 – First case study: Total number of false negatives found for the 10 values of A_{vl} using the STFT with a threshold for detection of 6dB.

As expected, as higher is A_{vl}, the higher is the probability of losing emboli. Comparing STFT and time-domain analysis, although the probability of not detecting emboli is higher when STFT is used, that tendency increases with the increase of A_{vl},

and when $A_{vl} = 10$mm, the performance of the STFT is better than the performance of time-domain analysis.

The properties of the STFT are also observable when the velocity of emboli is analysed. Figure 5.26 shows the comparison of simulated and estimated velocities for $A_{vl} = 1$mm.

Embolic velocities were computed from (3.18) and (2.5).

The STFT seems to be more accurate on estimating the embolic velocities than time domain processing. Once again, emboli placed in locations C and E are the ones presenting more deviation from the values of velocities input into the simulator, for the reasons already discussed. Moreover, the estimation of velocities using the STFT does not seem to depend on the power or effective size of the emboli.

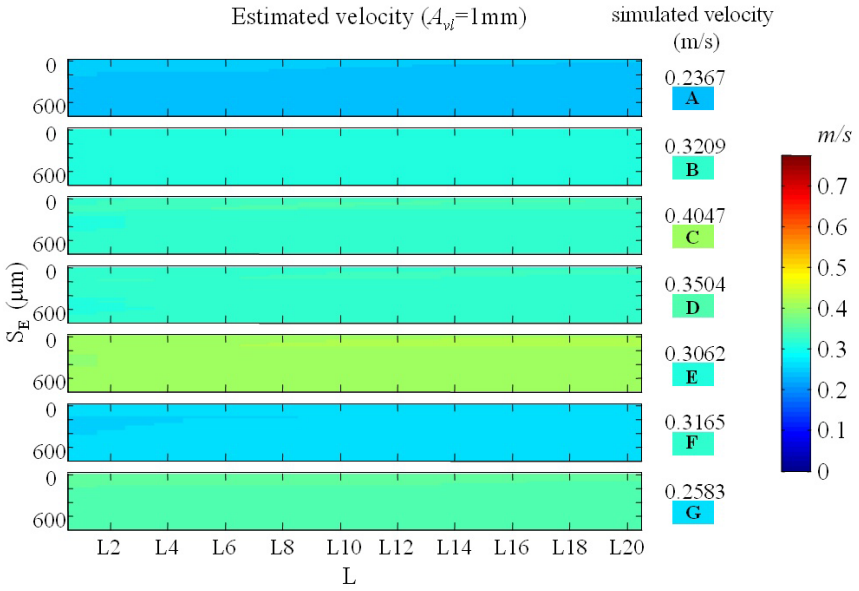

Figure 5.26 – First case study: Estimation of the velocities of the emboli using the STFT for an A_{vl}=1mm.

As expected, Figure 5.27 shows that there is no significant difference on the use of different A_{vl} values.

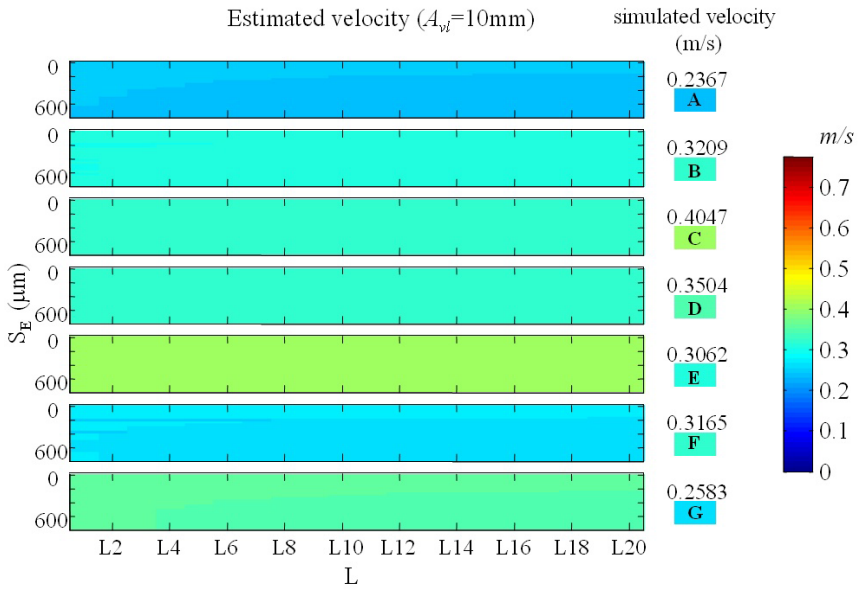

Figure 5.27 – First case study: Estimation of the velocities of the emboli using the STFT for an A_{vl}=10mm.

Similar conclusions are taken when the detection threshold is applied, as can be seen from Figure 5.28 and Figure 5.29.

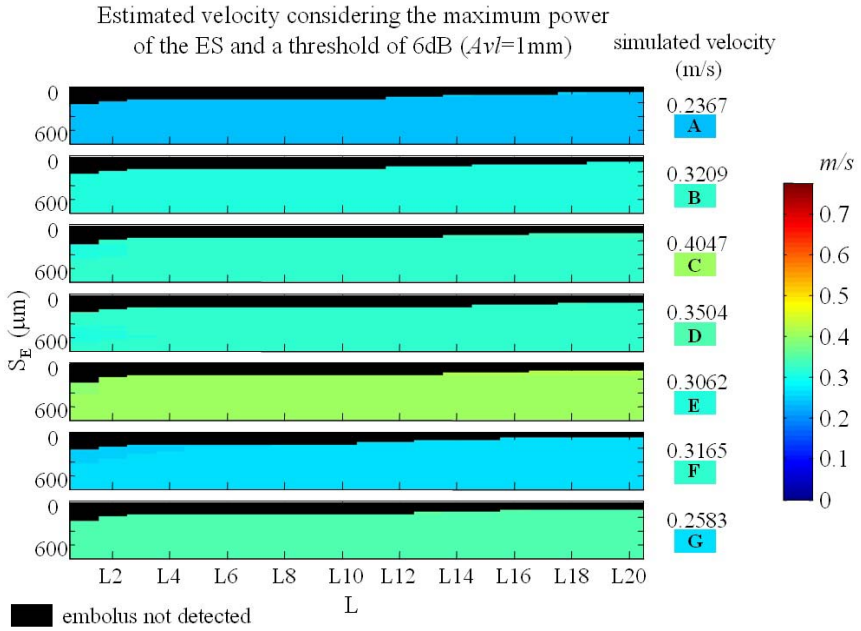

Figure 5.28 – First case study: Estimation of the velocities of the emboli using the STFT for an A_{vl}=1mm, considering a threshold for detection 6dB.

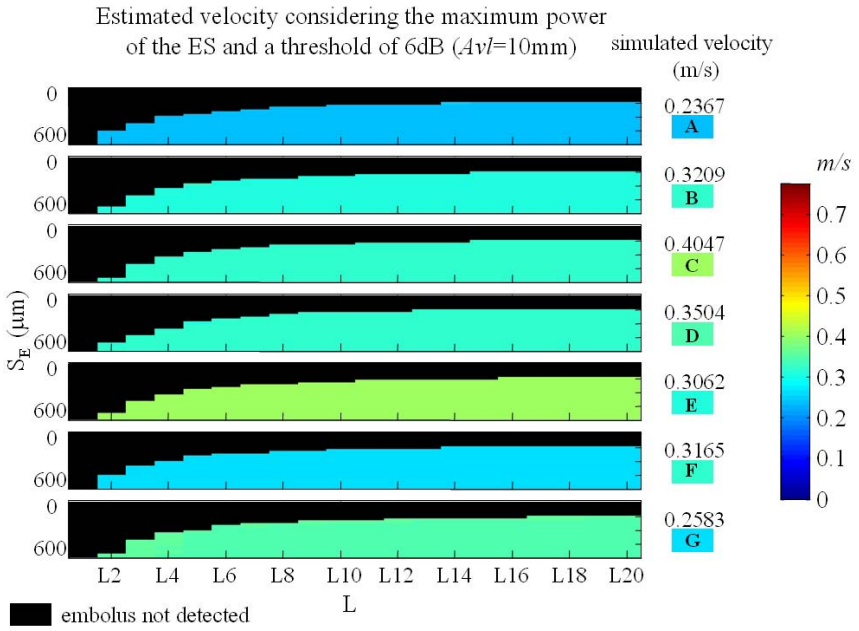

Figure 5.29 – First case study: Estimation of the velocities of the emboli using the STFT for an A_{vl}=10mm, considering a threshold for detection of 6dB.

The behaviour of the STFT on the estimation of the SVL, do not carry any advantage, as the effective length of the emboli cannot be deducted from the SVL. Actually, the SVL seems to depend more on the velocity of the embolus than on the S_E SVL. Remember that the aim of using the SVL as a measure for characterising emboli is to reduce the effects of velocity by multiplying it by the duration of the emboli.

Figure 5.30 and Figure 5.31 represent the estimated SVL using the STFT, for respectively $A_{vl} = 1$mm and $A_{vl} = 10$mm. These graphs were obtained using a detection threshold of 6dB.

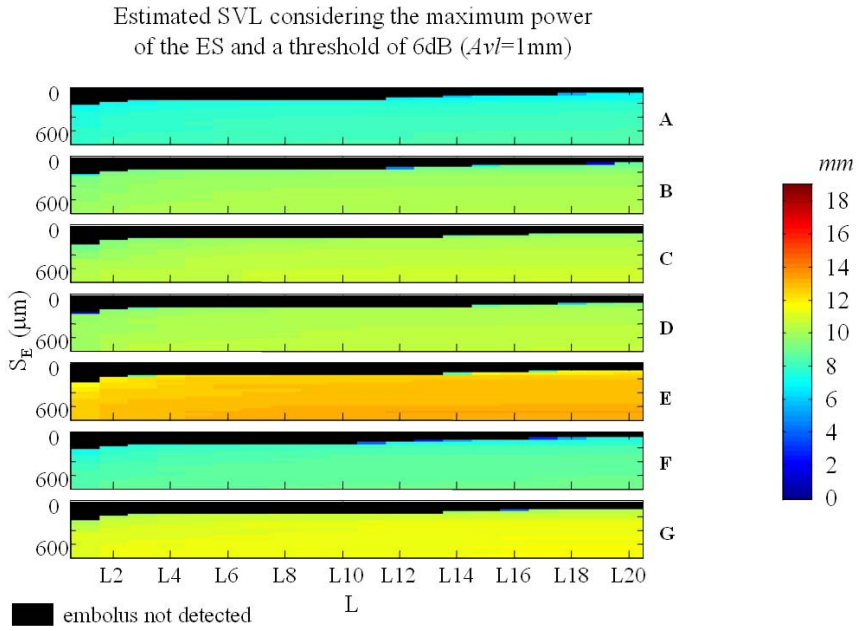

Figure 5.30 – First case study: Estimation of the SVL of the emboli the STFT for an A_{vl}=1mm, considering a threshold for detection of 6dB.

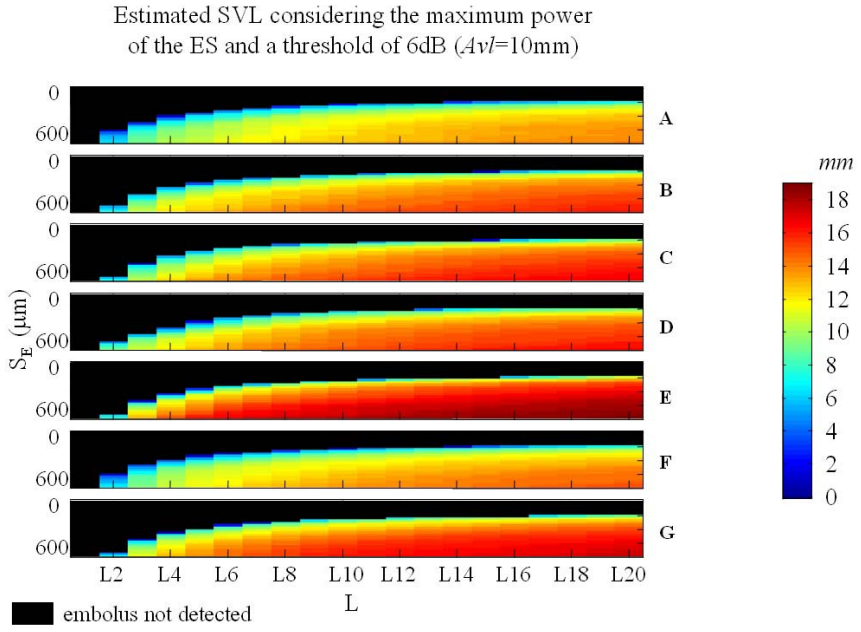

Figure 5.31– First case study: Estimation of the SVL of the emboli using the STFT analysis for an A_{vl}=1mm, considering a threshold for detection of 6dB.

5.5.2 SECOND CASE STUDY

The analysis of the results obtained for the second case study is presented in this section. To make the graphical visualisation, in the figures in this section, the L values in Table 5.1 are coded according to

L	Code	L	Code	L	Code	L	Code
112	L1	8,680	L6	285,740	L11	9,079,100	L16
373	L2	17,614	L7	571,150	L12	18,120,000	L17
913	L3	35,506	L8	1,141,000	L13	36,162,000	L18
2,011	L4	71,292	L9	2,278,400	L14	72,164,000	L19
4,226	L5	142,830	L10	4,548,700	L15	144,000,000	L20

Table 5.4 – *L* codes for the second case study

The study presented next is similar to the one present for the first case study. The main goal of this second case study is to observe if the time-domain and the spectral analysis present any different behaviour if the durations of emboli are considerable longer than the durations studied before.

5.5.2.1 Time domain processing

The graph in Figure 5.32 was generated using $A_{vl} = 1\text{mm}$, $v_E = 0.24\text{ms}^{-1}$, and considering the MEP computed from the maximum of $P_E + P_B$. It shows that the estimated and the simulated MEPs do not present really important differences. Actually, except for very low embolic powers, the simulated and estimated MEPs can be considered practically the same. This is because there are now many positive bins with the complete embolic power contributing to each sample length in the probing process.

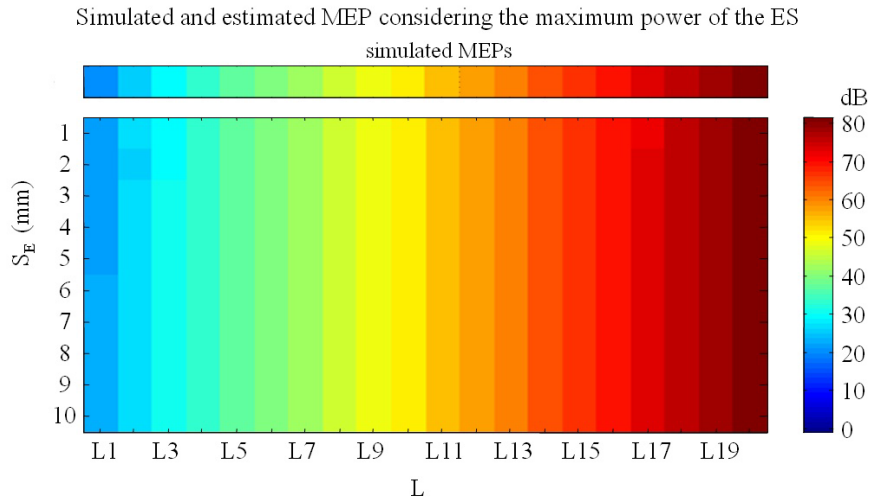

Figure 5.32 – Second case study: Estimated MEP (maximum power) obtained with time-domain processing. The upper bar represents the expected MEP values, the right bar represents the colour scales.

A similar analysis but considering the MEP computed from the mean of $P_E + P_B$ is showed in Figure 5.33. The probability of confounding adjacent MEPs of adjacent L values in the figure is higher in this situation. A difference between the estimation of MEPs from shorter and longer S_E can also be observed in the figure. These differences are not so evident as they were for the shorter S_E values considered in the first case study.

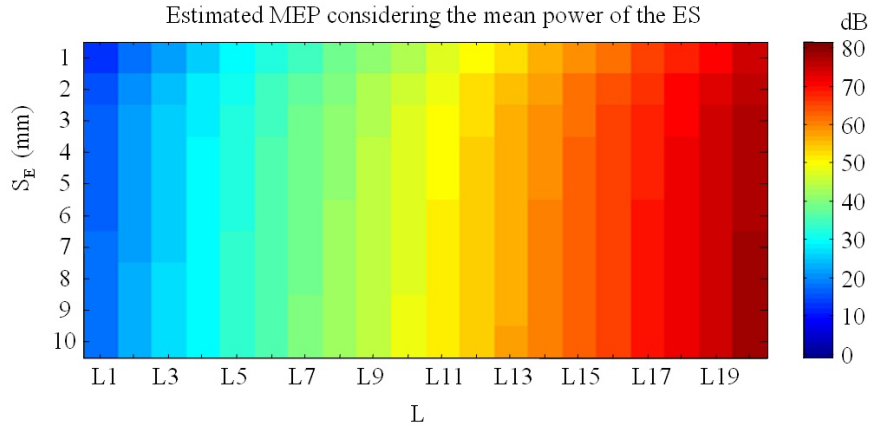

Figure 5.33 – Second case study: Estimated MEP (mean power) obtained with time-domain processing. The left bar represents the colour scales.

A detection threshold of 15dB was also found in this case.

With this threshold, all the emboli simulated for $A_{vl} = 1$mm can still be detected, but other simulated A_{vl} values imply missing emboli.

Figure 5.34 shows the results obtained for $A_{vl} = 10$mm and emboli identified as A, where 17 of the 200 embolic events were not detected. The non-detected emboli correspond to lower power and shorter S_E.

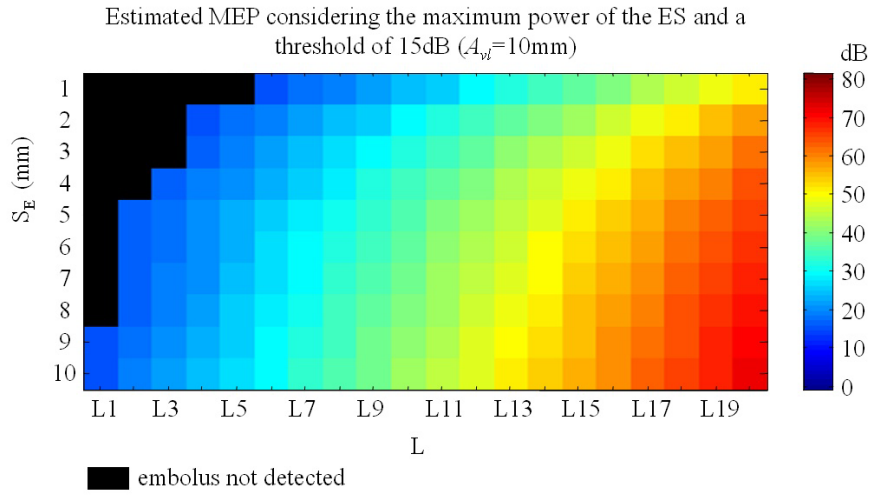

Figure 5.34 – Second case study: Estimated MEP (maximum power) obtained with time-domain processing, A_{vl}=10mm, a threshold for detection of 15dB.

Figure 5.35 shows the number of emboli not detected for each simulated A_{vl} when a detection threshold of 15dB is used. The total number of emboli for each A_{vl} was 1400.

Although the number of false negatives is much less significant than it was in the first case study, there are still many emboli missed mainly for the longer A_{vl}.

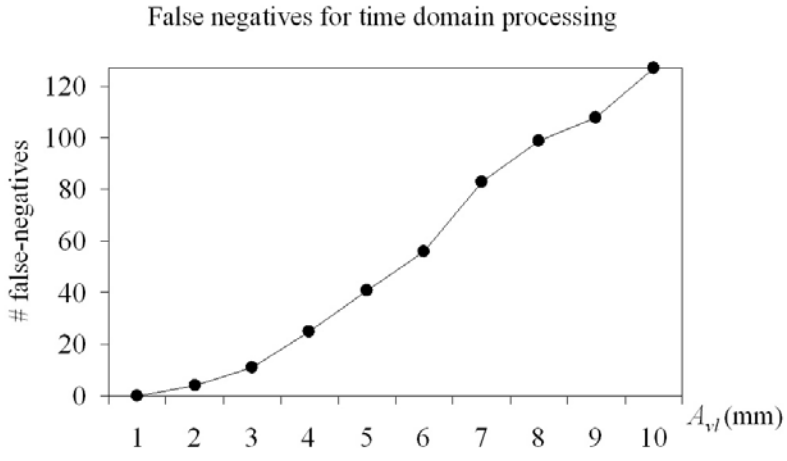

Figure 5.35 – Second case study: Total number of false negatives found for the 10 values of A_{vl} using time-domain processing with a threshold for detection of 15dB. For each A_{vl} the total number of emboli was 1400.

Emboli with this order of S_E present much accurate estimation of velocities. Figure 5.36 shows the estimate velocities for $A_{vl} = 1$mm.

As in the first case study, the velocities were estimated from (5.6) and (2.5).

Comparing these results to the ones obtained in the first case study, it can be concluded (although emboli C and E, are still not well estimated) that the errors are much lower than the ones found in the first case study. In this case, for all the emboli, the estimation of the velocity seems to depend much more on the simulated velocity than on any other factor.

The results presented in Figure 5.37 show that the improvement obtained by increasing A_{vl} is not significant.

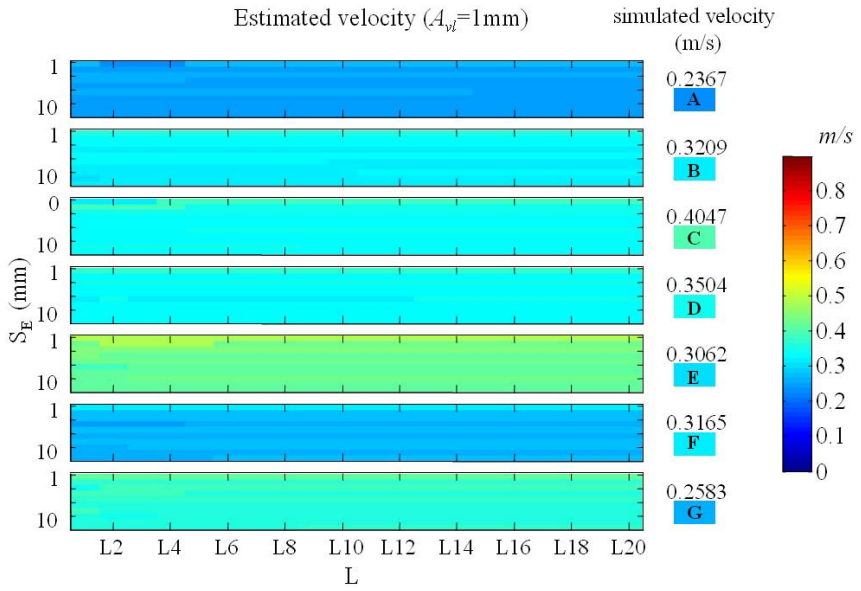

Figure 5.36 – Second case study: Estimation of the velocities of the emboli using time-domain analysis for an A_{vl}=1mm.

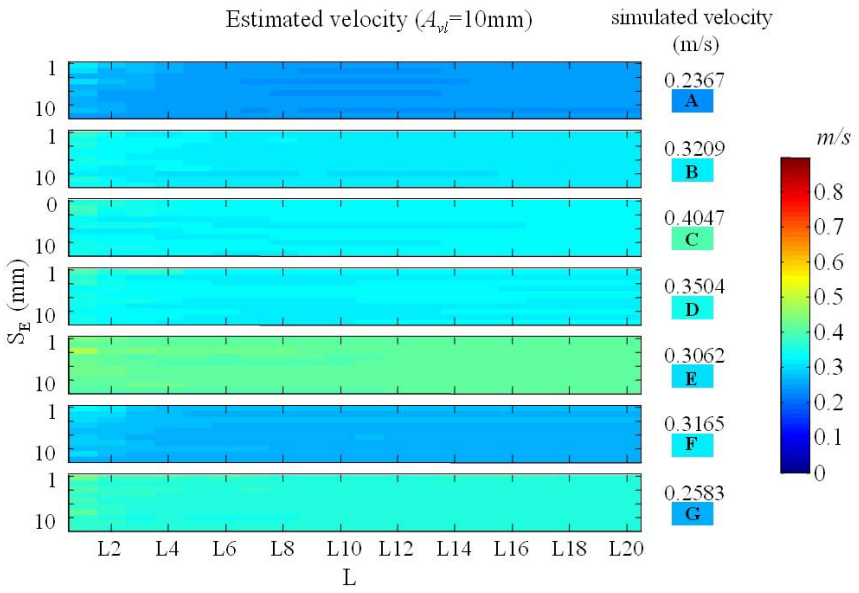

Figure 5.37 – Second case study: Estimation of the velocities of the emboli using time-domain analysis for an A_{vl}=10mm.

The 15dB detection threshold does not have a significant effect on the estimation of the velocity if $A_{vl} = 1$mm, but when the A_{vl} is set to 10mm, the estimation of the velocities of emboli with lower powers and shorter effective length looses accuracy, as Figure 5.38 shows. This is due to the decrease of influence of the positive bins in the ES.

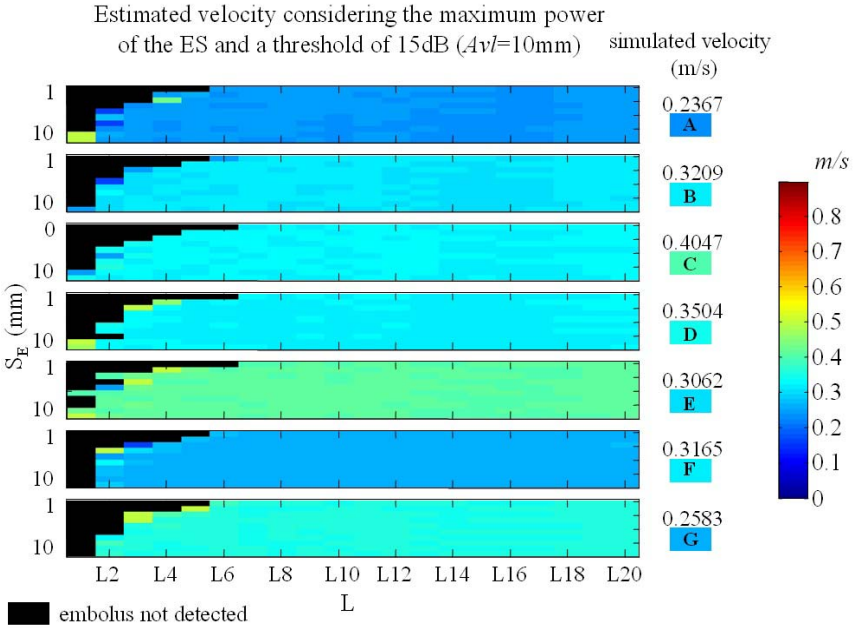

Figure 5.38 – Second case study: Estimation of the velocities of the emboli using time-domain analysis for an A_{vl}=10mm, considering a threshold for detection of 15dB.

The estimation of the SVL when the detection threshold is considered seems to depend much more on the power of the emboli than on the S_E. If the A_{vl} is simulated to be 1mm length (Figure 5.39), than the relationship between S_E and SVL cannot be deducted.

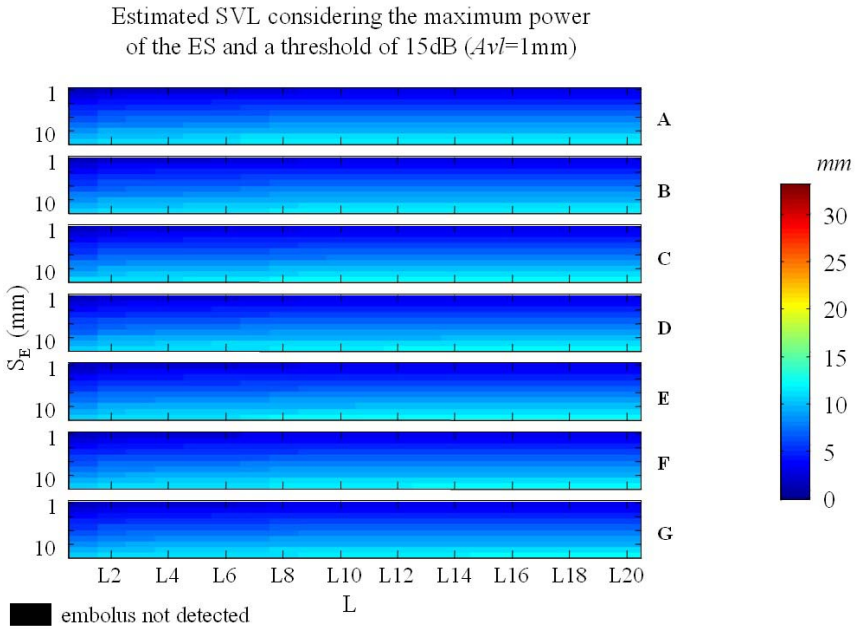

Figure 5.39 – Second case study: Estimation of the SVL of the emboli using time-domain analysis for an A_{vl}=1mm, considering a threshold for detection of 15dB.

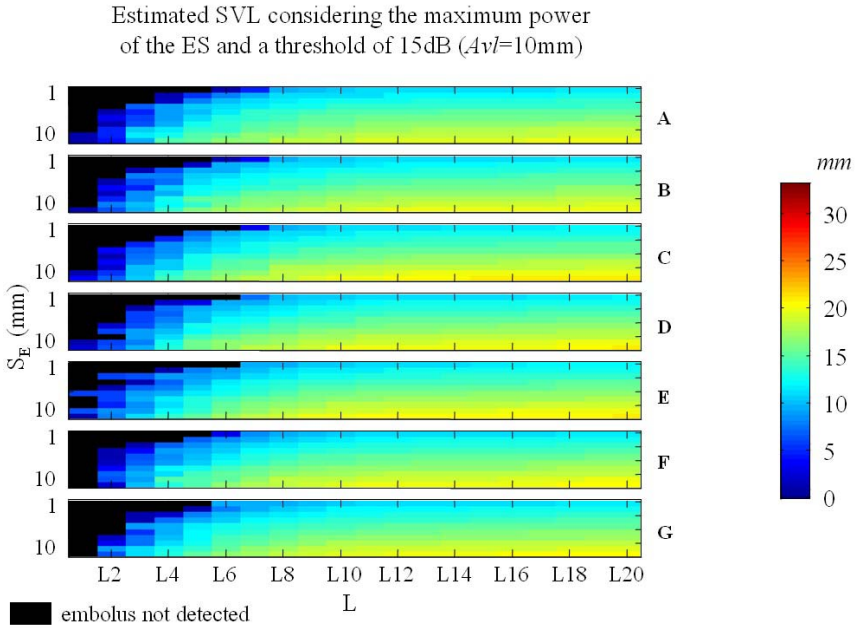

Figure 5.40– Second case study: Estimation of the SVL of the emboli using time-domain analysis for an A_{vl}=1mm, considering a threshold for detection of 15dB.

However, if $A_{vl} = 10\text{mm}$ (Figure 5.40), from the knowledge of L, it is possible to find a rough approximation of the S_E of the embolus.

5.5.2.2 Short Time Fourier Transform

Figure 5.41 shows the estimated and simulated MEPs, computed from the maximum $P_E + P_B$, and obtained from the application of the STFT to the simulated signals with emboli. Although the performance of spectral analysis is not as good as time-domain analysis, the difference between approaches is much less significant than it was in the first case study. This graph was generated using the results obtained for emboli A and $A_{vl} = 1\text{mm}$.

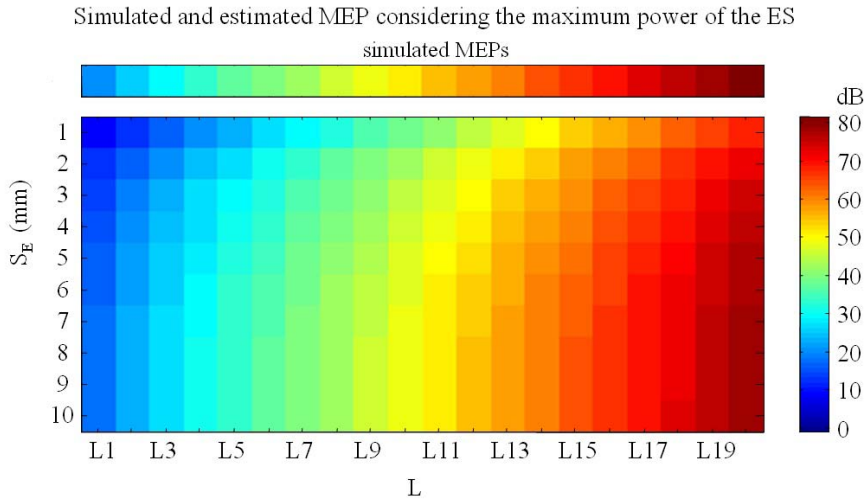

Figure 5.41 – Second case study: Estimated MEP (maximum power) obtained with the STFT. The upper bar represents the expected MEP values, the right bar represents the colour scales.

Because of the characteristics of the STFT discussed before (Section 5.5.1.2), the usage of the mean value of $P_E + P_B$ to compute the MEP (Figure 5.42) does not represent relevant different results from the ones obtained with the maximum value of $P_E + P_B$.

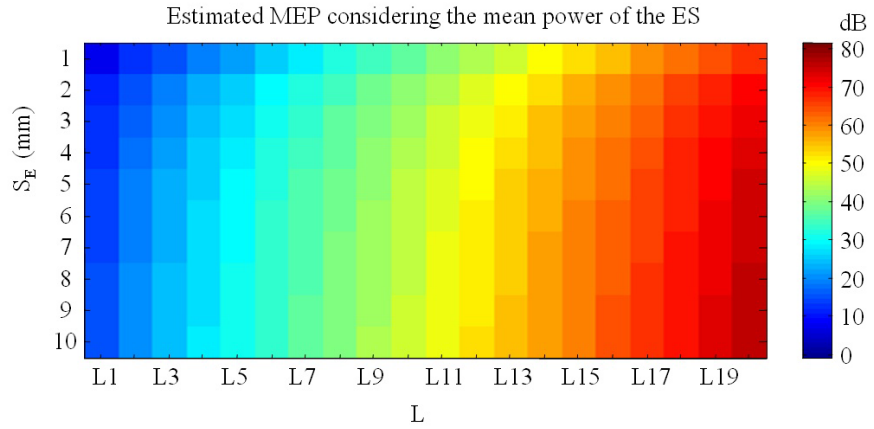

Figure 5.42 – Second case study: Estimated MEP (mean power) obtained with the STFT. The left bar represents the colour scales.

As in the first case study, the detection threshold for the STFT spectra of the simulated signals was 6dB. With this threshold, none of the emboli was missed for $A_{vl} = 1$mm, and 15 emboli were lost for $A_{vl} = 10$mm (see Figure 5.43).

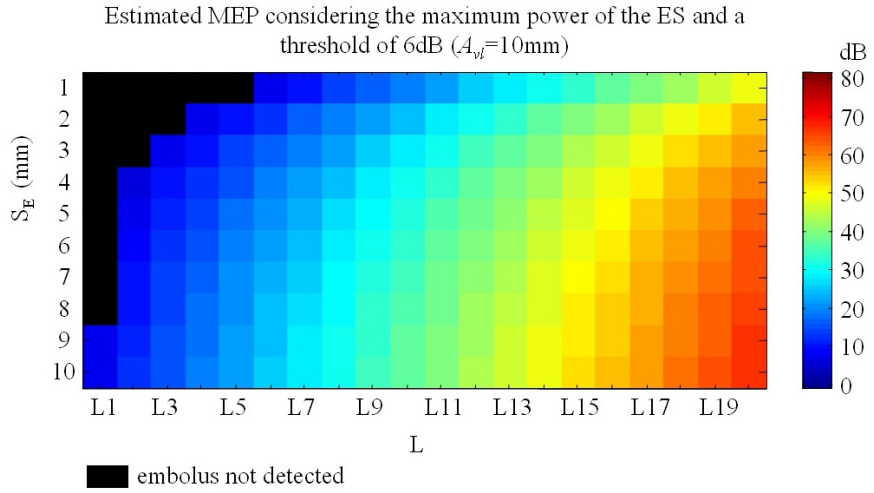

Figure 5.43 – Second case study: Estimated MEP (maximum power) obtained with the STFT, A_{vl}=10mm, a threshold for detection of 6dB.

The increase of false negatives observed with the increase of A_{vl} is represented in the graph in Figure 5.44. The total number of simulated ES for each A_{vl} was 1400.

Notice that from $A_{vl} = 6$mm to $A_{vl} = 10$mm, the performance of the STFT analysis is much better than the time-domain analysis performance.

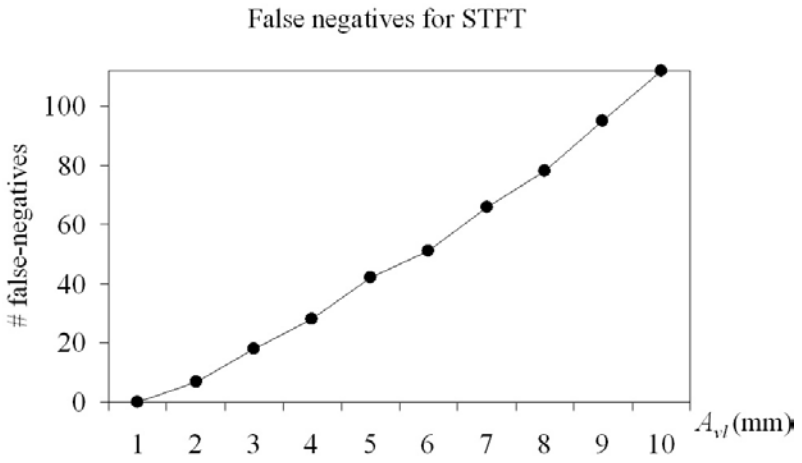

Figure 5.44 – Second case study: Total number of false negatives found for the 10 values of A_{vl} using the STFT with a threshold for detection of 6dB. For each A_{vl} the total number of emboli was 1400.

The same comments made for the analysis of the estimation of velocity when time-domain processing was studied, can be made for the study of the estimation of velocity when the signals were previously transform to the time-frequency domain.

Again, the velocities were estimated from (3.18) and (2.5).

Figure 5.45 and Figure 5.46 represent respectively the estimated velocity when $A_{vl} = 1\text{mm}$ and $A_{vl} = 10\text{mm}$. There are no significant differences between the graphs. Emboli A, B and D still correspond to the more accurate estimations, and emboli C and D correspond to the more biased estimations. In addition, the estimation of velocities depends more on the simulated velocities than on any other factor.

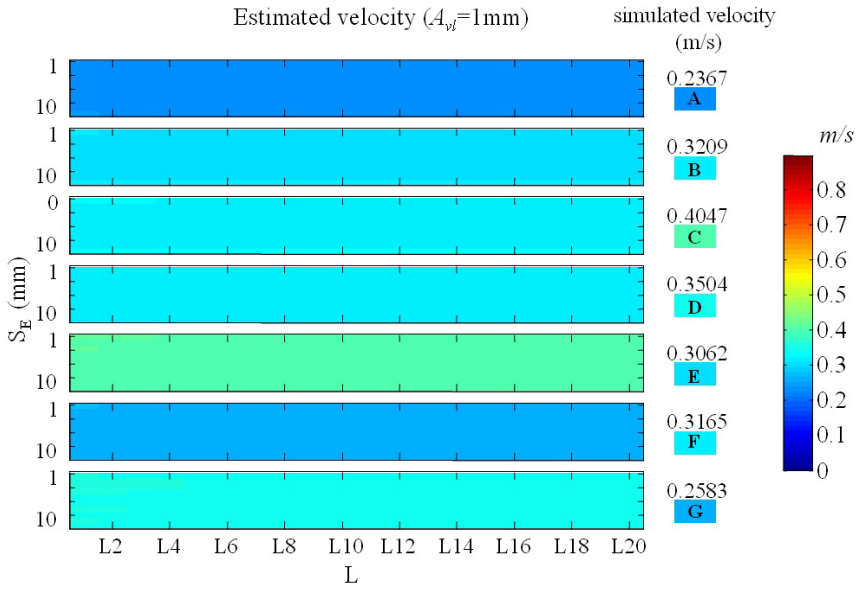

Figure 5.45 – Second case study: Estimation of the velocities of the emboli using the STFT for an A_{vl}=1mm.

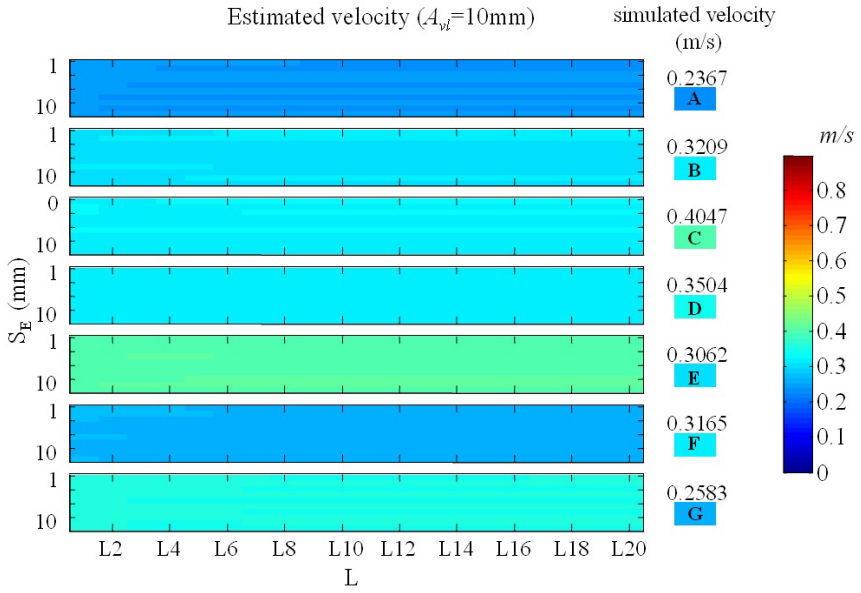

Figure 5.46 – Second case study: Estimation of the velocities of the emboli using the STFT for an A_{vl}=10mm.

When the detection threshold is applied, the estimations obtained do not change behaviour. Although the results obtained for $A_{vl} = 1\text{mm}$ are comparable to the ones verified for time-domain processing, the same cannot be said for $A_{vl} = 10\text{mm}$. Figure 5.47 shows that in this last case, the observed estimated v_E with and without detection estimator are very similar.

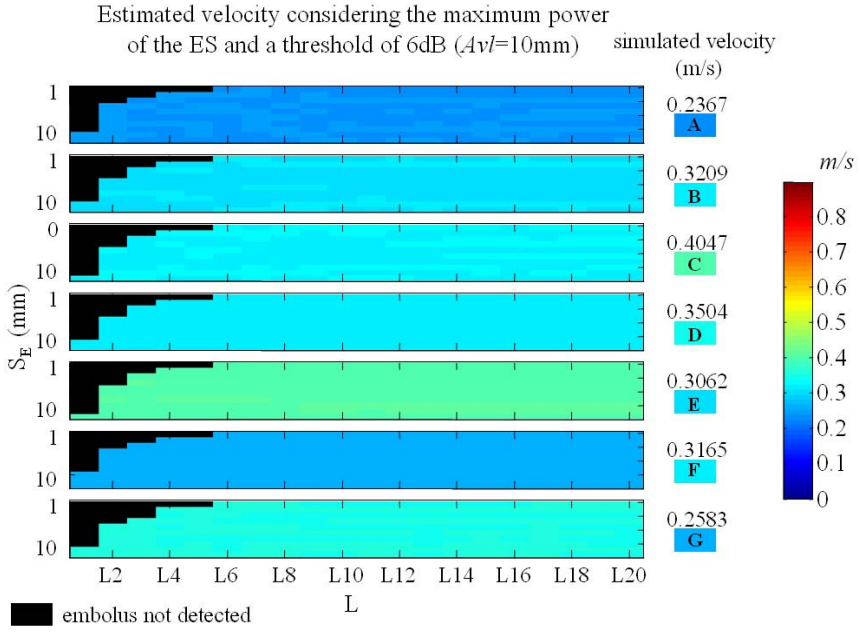

Figure 5.47 – Second case study: Estimation of the velocities of the emboli using the STFT for an A_{vl}=10mm, considering a threshold for detection of 6dB.

Finally, the SVLs estimated using the 6dB detection threshold was found to depend mainly on the power of the ES, but also to depend on the S_E, when $A_{vl} = 1\text{mm}$ (Figure 5.48). Although it is not possible to establish exactly S_E from the SVL, it is possible to find an approximation as long as a previous estimation of L is known.

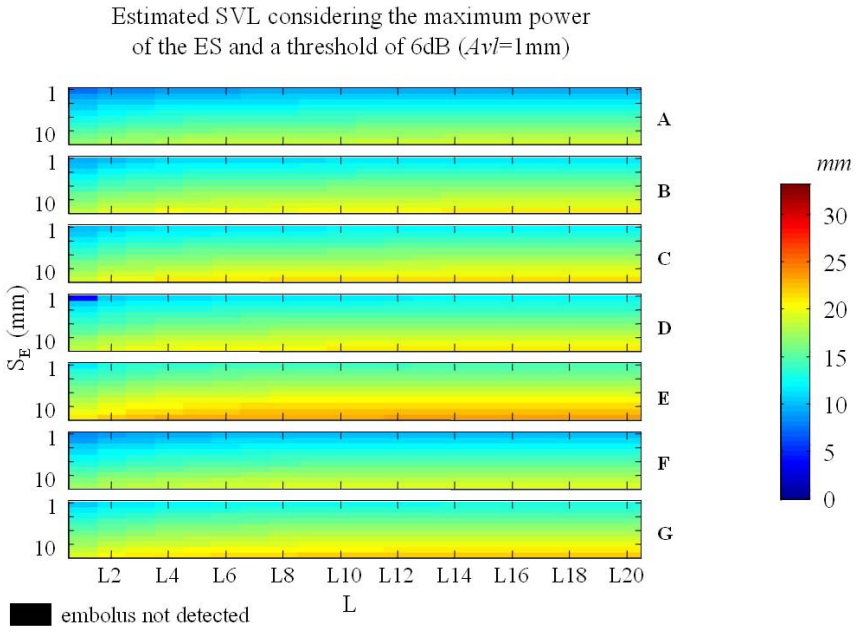

Figure 5.48 – Second case study: Estimation of the SVL of the emboli the STFT for an A_{vl}=1mm, considering a threshold for detection of 6dB.

However the increase of A_{vl} can improve the accuracy of S_E estimation. Figure 5.49 shows the results obtained for $A_{vl} = 10\text{mm}$. Even though it is still required the previous knowledge of the estimated L, the range of values where the true S_E can be found is now much shorter.

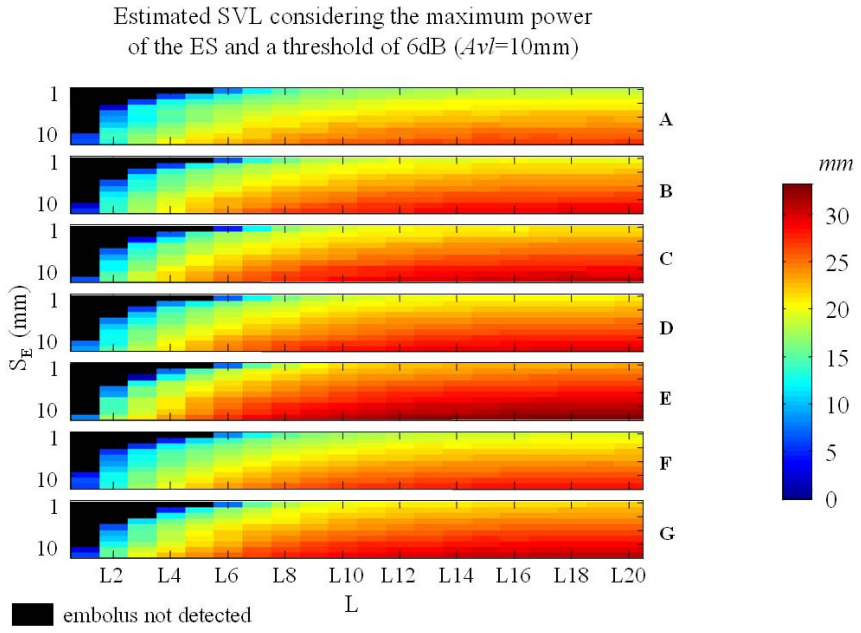

Figure 5.49– Second case study: Estimation of the SVL of the emboli using the STFT analysis for an A_{vl}=1mm, considering a threshold for detection of 6dB.

5.5.3 RESULTS

The tests presented before do not clearly indicate the best method for detecting and characterize emboli, but suggest that the use of time-domain approach may be safer.

The time-domain analysis seems to be a better estimator of the MEP, mainly when lower effective embolic lengths are considered.

Also for smaller values of S_E it seems to be advantage to estimate the velocity of emboli from the time-domain signal.

However, the spectral approach is preferred when SVL is required. The time-domain approach tends to make the SVL depend more on the power of emboli than on the effective length, essentially if smaller A_{vl} are considered.

The choice of A_{vl} was another subject is this study. It was first though that decreasing A_{vl} would be very advantageous. Although in general this conclusion can be maintained, mostly because the signal from emboli becomes more influent on the ES, some remarks must be drawn. Smaller values of A_{vl} correspond to less accurate estimates of the SVL. Although, when a detection threshold is used, time-domain processing allows detecting more embolic signals, when A_{vl} increases the performance

of STFT also increases. For higher A_{vl} the performance of the STFT is even better than the performance of time-domain processing. This is even more evident if longer S_E are involved.

5.6 CONCLUDING REMARKS

In this chapter, a comparative study of the accuracy of spectral analysis and time-domain analysis of ESs was derived.

A theoretical report on the variables that can affect embolic analysis, and a description of the methods typically used to characterise emboli in both approaches were carried out. Based on the main parameters used in that process, the simulator described in Chapter 3 was improved to include the possibility of simulating emboli in the background signal. The process of simulating emboli was explained.

The simulated ESs were used to analyse the performance ability of time-domain processing and STFT to estimate the specific clinical diagnosis parameters. This analysis was derived through two case studies.

The results led to the conclusion that although in terms of power and velocity estimation the time-domain processing can be usefully considered, in terms of accuracy in the determination of the SVL of embolic events, the STFT presents better results.

Moreover, the only way to obtain good performance results was using an overlap of 88% of adjacent segments. This overlap percentage comprises an additional computational load that in a clinical setting could probably be put to better use, such as determination of clinical indicators, statistics, or colour representation.

6 SPACE-FREQUENCY SPECTRAL ESTIMATION

6.1 INTRODUCTION

A new method for spectral representation of Doppler signals is introduced in this chapter. Although this method was specially developed to work with ESs, it could also be useful for other applications.

An explanation of the reasons that led to the search of a new method, and its mathematical formulation are presented here.

At the end of the chapter, the same study performed in Chapter 5 for studying the adequacy of STFT and time-domain processing for treating ESs, is repeated using the new method.

6.2 MOTIVATION

The main advantage of time-frequency estimators is that they allow a dual manipulation of the signals in both time and frequency domains, easing the task of analysis.

The results obtained with the use of STFT (in the last chapter) although not as good as the ones obtained through the time-domain techniques, can be useful. The main drawback is the huge time-resolution required to obtain satisfactory results. The computational burden necessary to achieve such resolution is even less encouraging when real-time processing is required.

In the last chapter, it was possible to know in advance the expected value of the maximum velocity of the signals because simulated signals were being treated. That knowledge, when clinical data is available, requires additional pre-processing and a constant tuning of the time-resolution. Another option would be to consider truly high

values of the velocities that would involve even higher processing times. Any other solution would have to accept lower time-resolution than the one imposed by the higher velocity of the signal, and the consequent loss of information about a possible embolic event.

Furthermore, time and time-frequency processing tend to treat differently emboli travelling in different parts of the cardiac cycle.

An embolus travelling during systole has more chance of being missed than when it is travelling during diastole. Two reasons have been identified to justify this. Figure 3.39 show that the highest velocities and backscattered power occur in the systole. For this reason, during diastole, the register of the emboli will last longer and will have more weight on the power of the Doppler signal. If time-frequency analysis with insufficient time-resolution is used, the probability of losing an embolic occurrence during systole tends to increase significantly.

The spectra in the next three figures were calculated with the STFT, from signals generated as described in Chapter 5. The windows were considered to have 20ms length and the overlapped to be 50%. The axial length for the sampling volume was 10mm.

Figure 6.1 shows the spectrum of the background signal. Notice that the systolic peak occurs around the 200ms. Figure 6.2 shows the same signal with seven emboli. The emboli are 10μm long and backscatter a power corresponding to approximately 6.5dB. Notice that the embolus at 200ms is the one that is seen for a shorter space of time, therefore is the one with the worst estimated power. If the signal had been simulated with a systolic power with higher power, that particular embolus would have been completely masked.

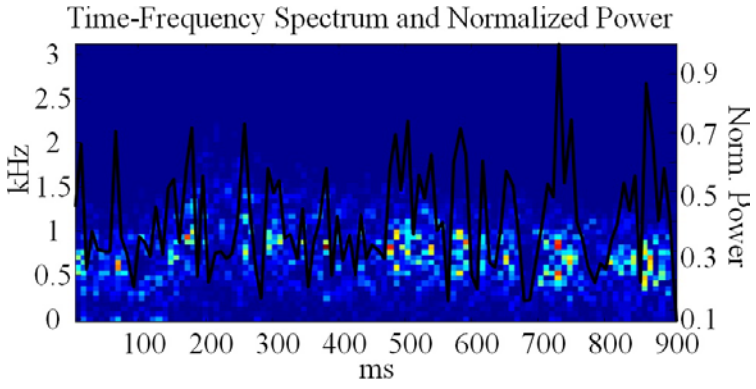

Figure 6.1 – Time Frequency representation of a simulated MCA Doppler signal plotted with the estimated normalized power variation over time. The spectral estimator was STFT with 20ms windows and 50% of overlapping

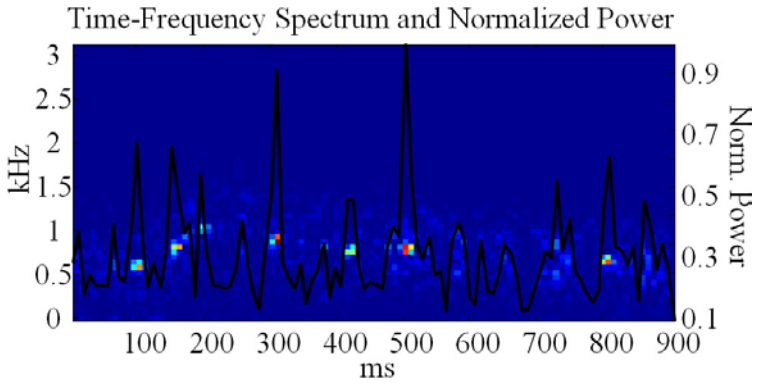

Figure 6.2 – Time-frequency representation of a simulated ES plotted with the estimated normalized power variation over time. The background signal is the same that was represented in Figure 6.1, the seven emboli are localized according to Figure 5.8. The effective axial length of the emboli is 10μm and the MEP is 6.5dB. The sample volume length of the probe was considered to be 1cm.

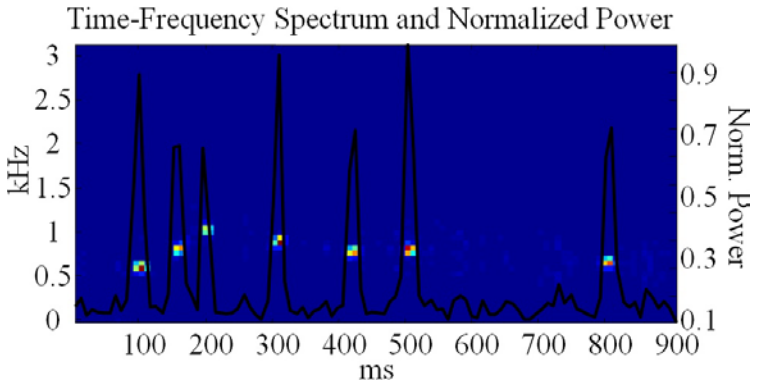

Figure 6.3 – Time-frequency representation of a simulated ES plotted with the estimated normalized power variation over time. The background signal is the same that was represented in Figure 6.1, the seven emboli are localized according to Figure 5.8. The effective axial length of the emboli is 700μm and the MEP is 8dB. The sample volume length of the probe was considered to be 1cm.

Figure 6.3 shows embolus of 700μm effective length and MEP=8dB, to allow a comparison.

Therefore, we may conclude that, both time-domain and time-frequency domain processing will not permit the immediate identification of the embolus at 200ms neither the one at 500ms.

Aiming to overcome these problems, an innovative method of emboli signals' analysis is proposed next, with adaptive characteristics.

6.3 METHODOLOGY

The foundation of this method was already introduced in the last chapter by equation (5.12). It consists on representing the Doppler signal in terms of axial space instead of time, and taking into account the amount of blood cells (scatterers) that are in the sample volume during the each insonation query.

Each bin of the time signal contains information from all the blood cells, and any emboli, in the sample volume. Therefore, after each blood insonation, the next time new information is obtained is when the fastest element of blood leaves the area that is being screened. So, when blood is flowing faster, there will be fewer points in the time-domain signal containing correlated information than when the blood is flowing slower (since the blood scatterers pass quicker through the window of analysis, and therefore less bins containing correlated information are queried by the ultrasound signal). For similar reasons, there is a greater correlation between adjacent bins.

The following expression allows the determination of the next time at which all the scatterers moving with the maximum velocity have been replaced in the sample volume. We will define this as a significant change in information.

$$t_i - t_{i-1} = \frac{A_{vl}}{V(t_{i-1})} \tag{6.1}$$

where t_i and t_{i-1} are two time occurrences between which there is no significant change in information, and $V(t_{i-1})$ is the maximum velocity registered at time t_{i-1}.

To observe this effect consider the synthetic Doppler signal in Figure 6.4, simulated according to [Cardoso, 1988]. This signal has constant bandwidth and power variation over time, and presents higher variations in velocity than MCA, a fact that makes it useful for clarifying this point.

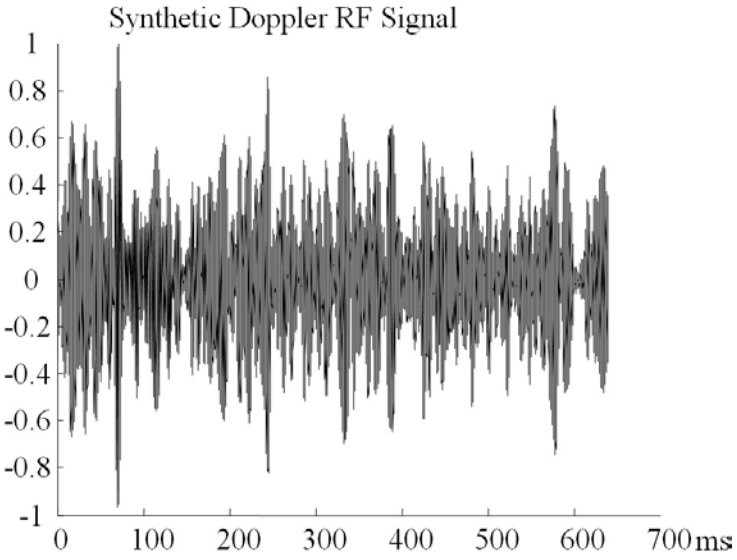

Figure 6.4 – Synthetic signal from carotid artery

Supposing that the probe axial sample volume length is 1mm, adequate temporal overlapping to maintain all the information from the time-domain signal in the time-frequency signal is:

$$\text{overlap} = \frac{100(N-1)}{N}\%\,. \tag{6.2}$$

where N is the length of the window used for spectral estimation.

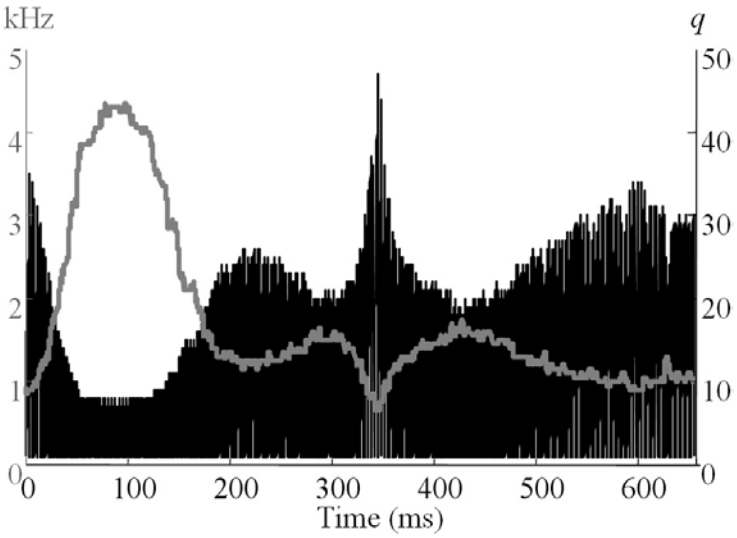

Figure 6.5 – Maximum frequency from a simulated Doppler signal in grey and the number of times that a sample with no significant information is calculated in black (q), when all the points in the time-domain signal are used for spectral estimation

The signal from Figure 6.5 was processed calculating a spectra every 0.08ms. For that purpose, 7943 windows with 20ms were used. The graph shows that at the

point of minimum velocity during diastole, similar information is processed around 47 times. There is no missed information in this case.

To avoid processing redundant information while following the fastest elements within the sample volumes, the overlapping required can be computed using

$$\text{overlap} = \frac{100}{N}\left(N - \frac{V_M / f_s}{A_{vl}} \right)\% \tag{6.3}$$

where V_M is the highest maximum velocity recorded on the signal.

Figure 6.6 shows the synthetic Doppler signal calculated through the STFT. In this case a spectrum was calculated every 2.9ms with windows of 20ms. For these parameters, 215 windows were processed. The results show that there is no redundant information. However, during systole, there are places where 5 samples with relevant information were missed. All over the cycle, important pieces of information are also being skipped. In this case, around 37.5% of the relevant information was not considered.

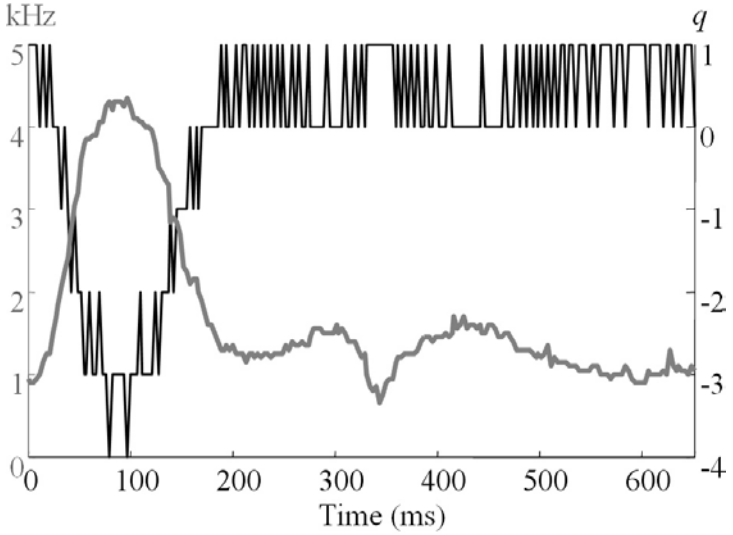

Figure 6.6 – Maximum frequency from a simulated Doppler signal in grey and the number of times that a sample with new information is not calculated in black (*q*), when redundant information is undesired

The other extreme situation would be to guarantee that no information is lost. The percentage of overlap required for the minimum computational burden is

$$\text{overlap} = \frac{100}{N}\left(N - \frac{V_m / f_s}{A_{vl}} \right)\% \,. \tag{6.4}$$

where V_m is the lowest maximum velocity recorded on the signal.

Figure 6.7 shows the result of the application of the percentage of overlap determined by (6.4). To produce that spectrum, 1135 windows of 20ms were required. One FFT was calculated every 0.55ms. Although there is no loss of important information, there is also an overestimation of the spectra on the area of the lowest velocities. In the worst situation, 6 samples in succession with no new information are computed.

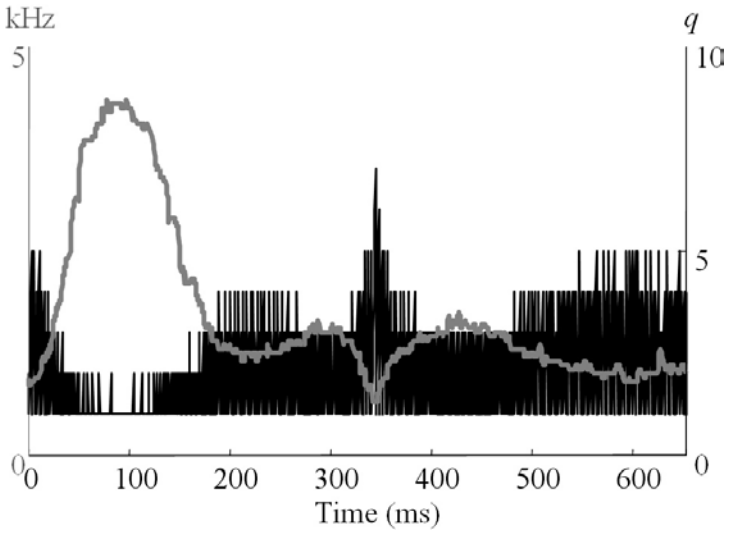

Figure 6.7 – Maximum frequency from a simulated Doppler signal in grey and the number of times that a sample with the same information is calculated in black (*q*), when no significant information is missed

The ideal situation would be to process a sample whenever new information is available. This requires that segment overlapping is determined adaptively, and therefore the determination of the number of times a new spectrum is calculated is controlled by (6.1).

Figure 6.8 shows the result of this approach. There are no missed nor any over calculated samples. Furthermore, the different appearance of the maximum frequency waveform is the result of each group of cells contained in a sample volume being equally treated, despite their velocity.

Figure 6.9 and Figure 6.10 show the display of the STFT representation when respectively adaptive and constant overlapping is used. The size of the window was considered as 20ms for both cases. The overlapping used on the conventional application of the STFT was chosen to obtain the same approximate computational burden of the adaptive overlapping. This way, 430 windows were required to produce the graphic in Figure 6.9 and 442 to produce the graphic in Figure 6.10.

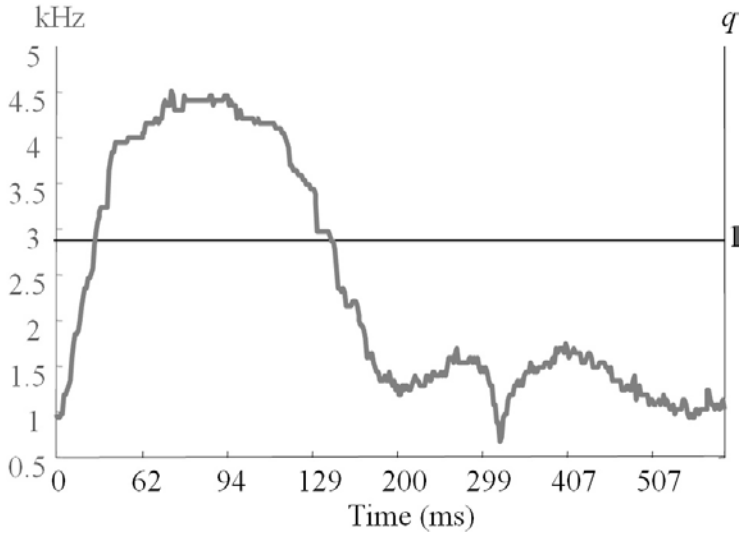

Figure 6.8 – Maximum frequency from a simulated Doppler signal in grey and the number of times that important information is considered (*q*) in black.

The most evident differences between the graphics are around the areas of maximum and minimum velocities. Around the area of systole, an increased resolution is required to allow the analysis of all the elements of the spectrum, in diastole the resolution may be decreased.

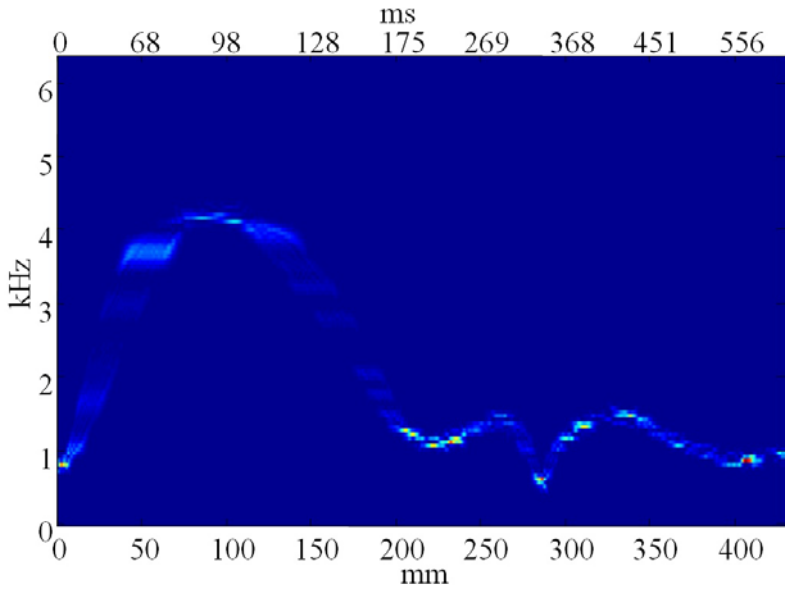

Figure 6.9 – Carotid artery synthetic Doppler signal spectral representation, considering the adaptive overlapping.

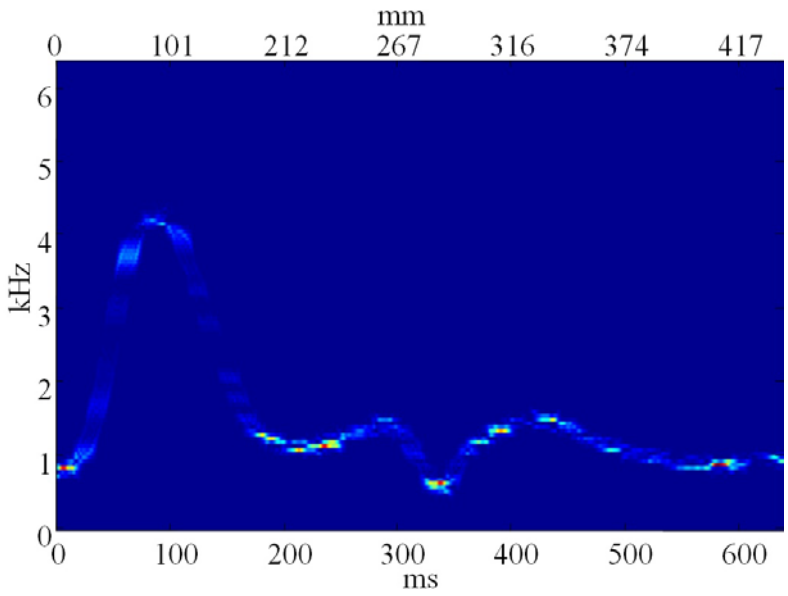

Figure 6.10 – Carotid artery synthetic Doppler signal spectral representation, considering a constant overlapping.

The spectral representation of clinical MCA Doppler signals with and without adaptive overlapping are shown respectively in Figure 6.11 and Figure 6.12. To produce the spectrum with adaptive overlapping, 52 windows were required. The constant overlapping spectrum was calculated with the same number of windows.

The gradient of velocities for these signals is lower than the one presented by the carotid simulated signals used before, therefore the differences are not so evident. Nevertheless, 1% of the samples with relevant information are missing from the spectrum of Figure 6.12.

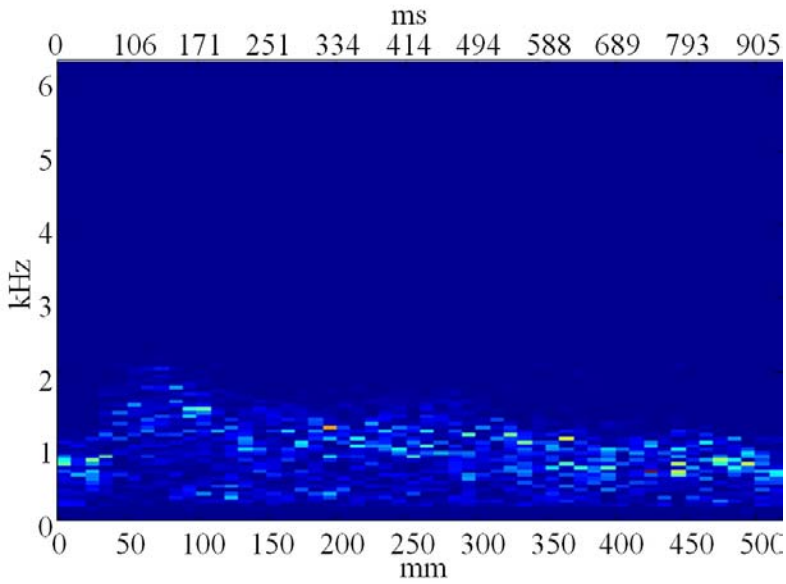

Figure 6.11 – MCA clinical Doppler signal spectral representation, considering the adaptive overlapping

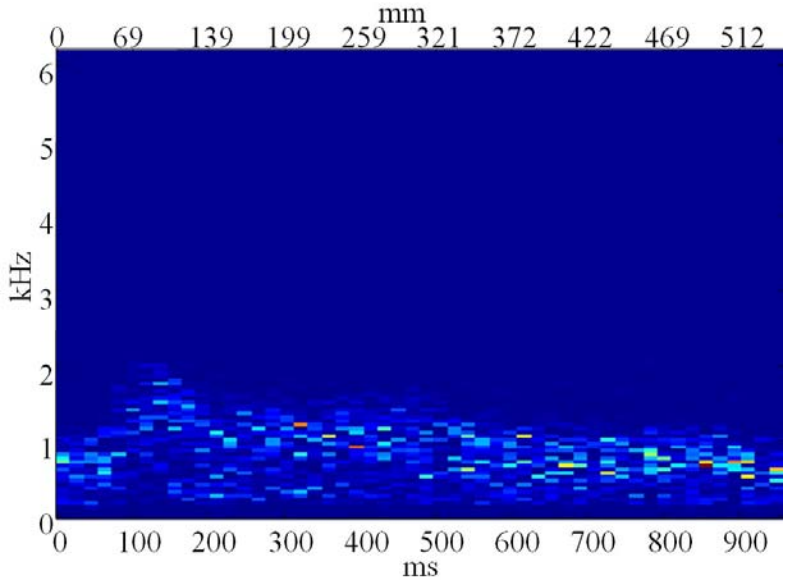

Figure 6.12 – MCA clinical Doppler signal spectral representation, considering a constant overlapping

To guarantee that there is no loss of information when there are rapidly moving scatterers close to the access of the sample volume (due to small variations), or even, for the sake of obtaining a display with better resolution, the resolution of the adaptive overlapping approach (axial space resolution) can be increased.

Figure 6.13 and Figure 6.14 show examples of MCA clinical signals space-frequency estimation, with increased resolution.

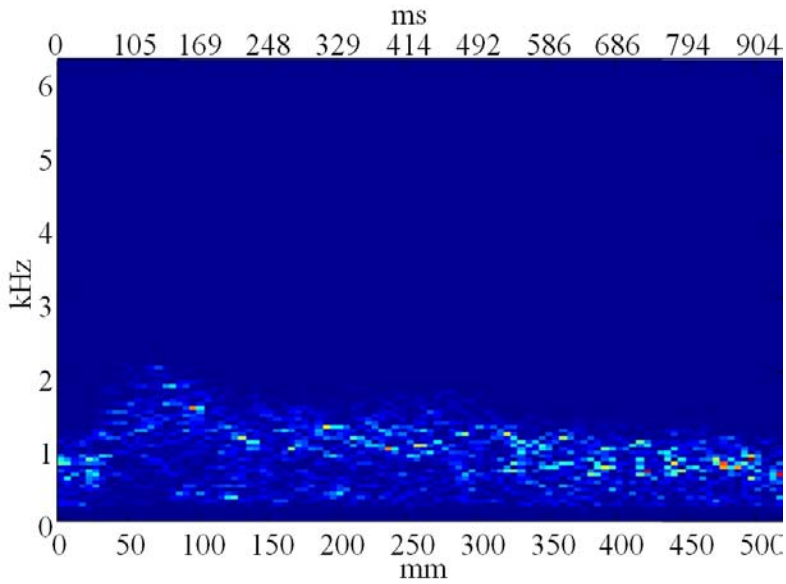

Figure 6.13 – MCA clinical Doppler signal spectral representation, considering the adaptive overlapping and increased spatial resolution (5mm).

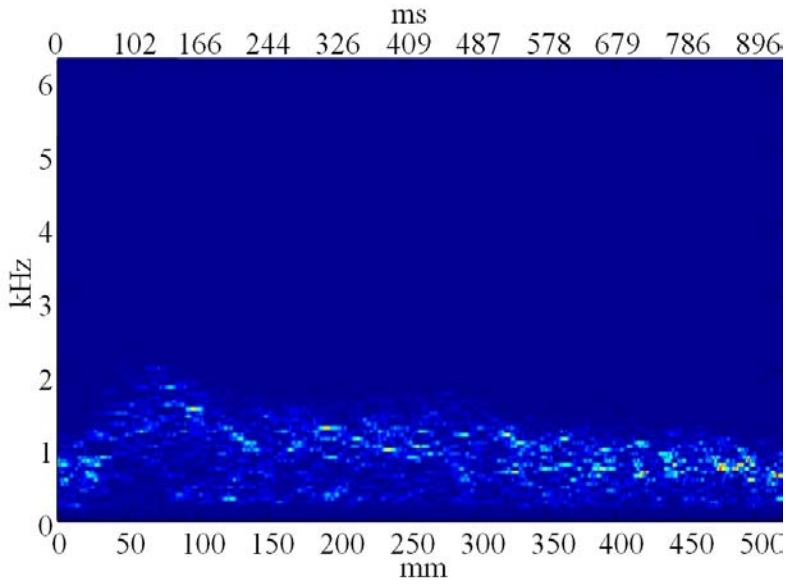

Figure 6.14 – MCA clinical Doppler signal spectral representation, considering the adaptive overlapping and increased spatial resolution (1mm).

6.4 MATHEMATICAL FORMULATION OF THE METHOD

This spectral representation can be defined as a function of the axial distance travelled by a group of cells occupying the sample volume. For that reason, it will be described for the rest of this work as Space-Frequency representation (SF).

The SF can be applied to all the spectral estimation methods described in Chapter 4.

Consider the traditional sample volume that is interrogated by the ultrasound probe, and assume it to have a rectangular shape in the axial direction; let the length of the rectangle be A_{vl}, and let s represent the total space travelled by a particular group of blood cells moving with the maximum velocity, measured from the first time instant t_{i-1} to instant t_i, after which that group of cells traverses the entire sample volume. Then, each *s* value is taken from the time domain Doppler signal according to

$$s_i = t(n_i) \tag{6.5}$$

and

$$n_i = n_{i-1} + \left(\frac{A_{vl}}{V_{i-1}} \right) \tag{6.6}$$

where t is the vector of times indexes in the time domain signal, and n_i and $n_i - 1$ are two time occurrences between which there is no significant information available.

Recalling expression (4.8) the form of the SF-STFT estimator can be defined as

$$\text{SF}-\text{STFT}(k,s) = \left| \sum_{k=0}^{N-1} x(s) w(s) e^{-\frac{j2k\pi}{N}} \right|^2 \tag{6.7}$$

The SF-STMC is given by

$$\text{SF}-\text{STMC}(k,s) = P_{AR}(k,s) w(s) \tag{6.8}$$

where $P_{AR}(k,s)$ is the power spectrum of the k frequency (as defined in Equation (4.39)) and for the space s.

Finally the SF-DCWD, according to (4.56), is

$$\text{SF}-\text{STFT}(k,s) = 2 \sum_{\tau=-\infty}^{+\infty} w_N(\tau) e^{-jk\tau} \sum_{\mu=-\infty}^{+\infty} w_M(\mu) \frac{1}{\sqrt{4\pi\tau^2/\sigma}} e^{-\frac{(\mu-s)^2}{4\pi\tau^2/\sigma}} x(\mu+\tau) x^*(\mu-\tau) \tag{6.9}$$

6.5 SPACE FREQUENCY SHORT TIME FOURIER TRANSFORM ESTIMATION OF SIMULATED EMBOLIC SIGNALS

To analyse the improvements that can be obtained with this method when ESs analysis is required, the SF-STFT was applied to the simulated ESs and subjected to the tests described in last chapter for time-domain processing and STFT.

The size of the window chosen to apply with SF-STFT, 110 time points, were considered the best option while equally considering the power and the maximum frequency estimation as studied in Chapter 4. The spatial resolution was considered equal to the axial sample volume length for each case.

The original method, written in Matlab, was replaced by a C language implementation. This newer code, built on an existing high performance implementation of STFT [Moura, 2004], performed the estimation of a 900ms signal very quickly (in less than 15 ms).

The results of the application of the SF-STFT to the two case studies considered in the last Chapter are described next. The figure presented in this Section considered the L codes defined in Table 5.3 for the first case study and Table 5.4 for the second case study.

The velocities were estimated from (3.18) and (2.5).

6.5.1 FIRST CASE STUDY

The first thing to be analysed is the estimation of the MEP when the maximum value of $P_E + P_B$ is considered.

The comparison of the MEP estimated using SF-STFT and the simulated MEP for emboli designated as A and $A_{vl} = 1$mm is presented in Figure 6.15.

Although the performance is inferior to the one obtained with the time-domain approach, it can be considered superior to the performance obtained with the use of the STFT.

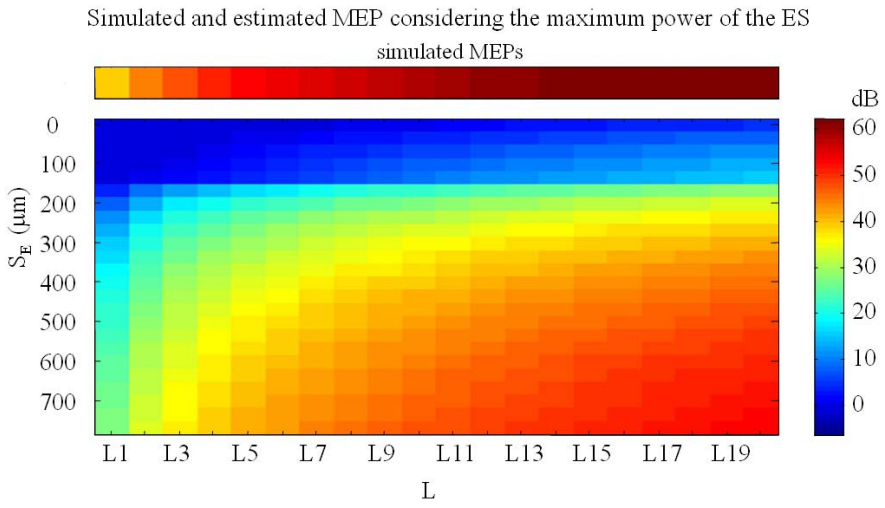

Figure 6.15 – First case study: Estimated MEP (maximum power) obtained with the SF-STFT. The upper bar represents the expected MEP values, the right bar represents the colour scales.

The same is true when the MEP is computed from the mean value of $P_E + P_B$, as it is shown in Figure 6.16.

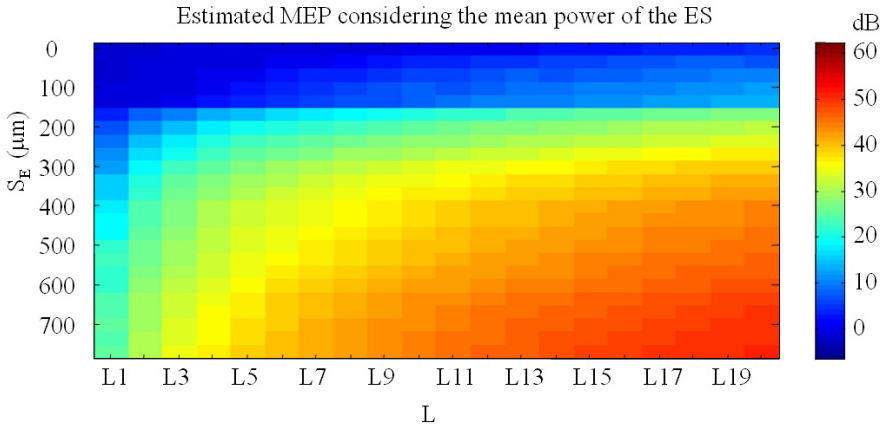

Figure 6.16 – First case study: Estimated MEP (mean power) obtained with the SF-STFT. The left bar represents the colour scales.

A detection threshold of 6dB was found to be enough to avoid false positives, as in the case of STFT.

Applying this threshold using $A_{vl} = 1$mm for emboli designated as A, there was, as in the other cases, a decrease on the accuracy of MEP estimation when the mean value of $P_E + P_B$ is considered (see Figure 6.17).

The number of emboli missed in this case was 59 in 480, as much as time-domain in the same situation, and much less than the 84 missed using STFT (as reported in Section 5.5.1).

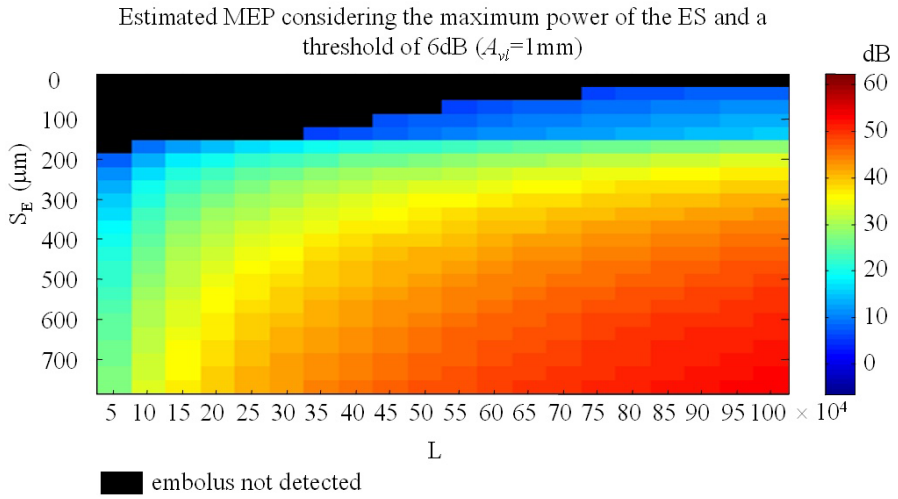

Figure 6.17 – First case study: Estimated MEP (maximum power) obtained the SF-STFT, A_{vl}=1mm, and a threshold for detection of 6dB.

However, when A_{vl} is simulated to be 10mm, the number of missed emboli increases to 210 in 480, which is better than the results obtained with time-domain (211 false negatives) processing but worse than the results obtained with the STFT (185 false negatives).

As in the other cases, the possibility of estimating accurate embolic powers has decreased with the increase of A_{vl}.

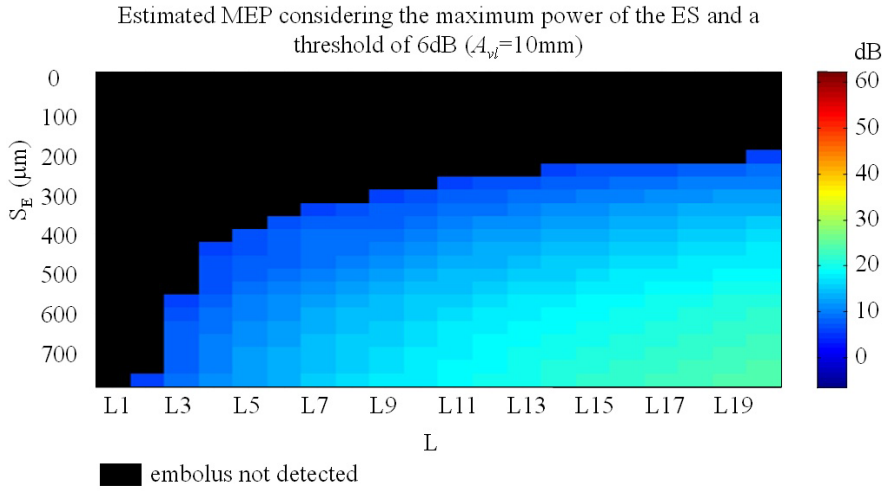

Figure 6.18 – First case study: Estimated MEP (maximum power) obtained with the SF-STFT, A_{vl}=10mm, a threshold for detection of 6dB.

Figure 6.19 shows the relationship between the increase of A_{vl} and the increase of false negatives.

The performance of the SF-STFT is much similar to the performance of time-domain (see Figure 5.14) processing and is worse than the performance of STFT only

when $A_{vl} = 1\text{cm}$ (see Figure 5.15). Each A_{vl} in the figure corresponds to 3360 simulated signals.

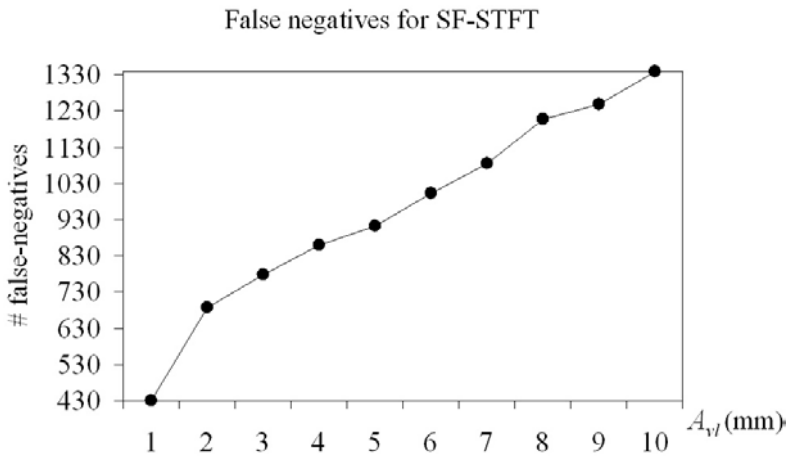

Figure 6.19 – First case study: Total number of false negatives found for the 10 values of A_{vl} using the SF-STFT with a threshold for detection of 6dB. For each A_{vl} the total number of emboli was 3360.

The estimated velocities when $A_{vl} = 1\text{mm}$ is shown in Figure 6.20. The SF-STFT seems to be a very irregular estimator of the velocity. In general, the velocities are estimated to be higher than the ones input into the simulator, but does not seem to be a relationship between the velocities and the power or the effective length of the emboli as occurred when time-domain estimation was studied.

This behaviour might be related with the nature of the space-frequency approach. As only independent samples are being considered, some of those samples may not occur in the centre of the embolus where the embolic power is higher.

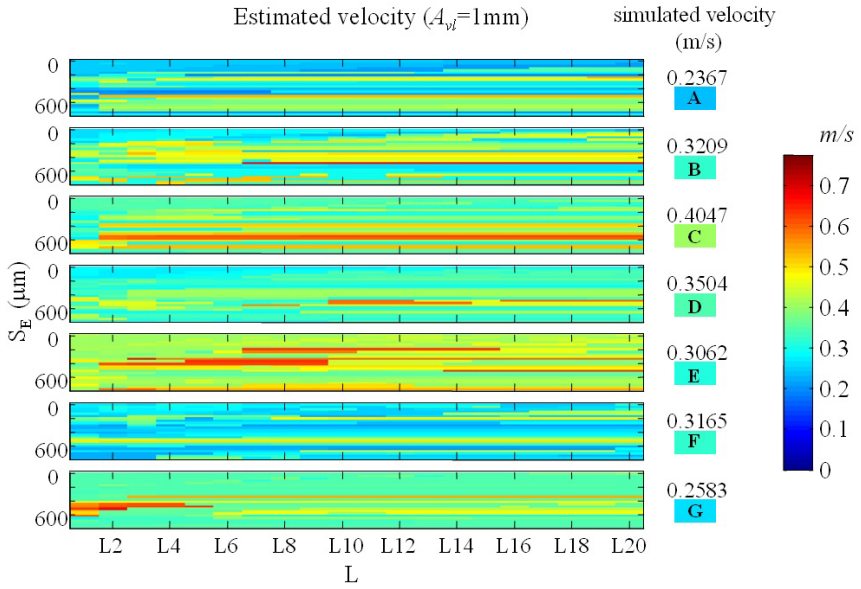

Figure 6.20 – First case study: Estimation of the velocities of the emboli using the SF-STFT for an A_{vl}=1mm.

Figure 6.21 shows the results of the estimation of v_E when A_{vl} is simulated to be 10mm. Although the results are now much improved there is still observed a worst performance of the SF approach when compared to the other methods. Notice that in this case it is possible to identify a relationship between the lower powers and the shorter S_E and the estimation of velocity.

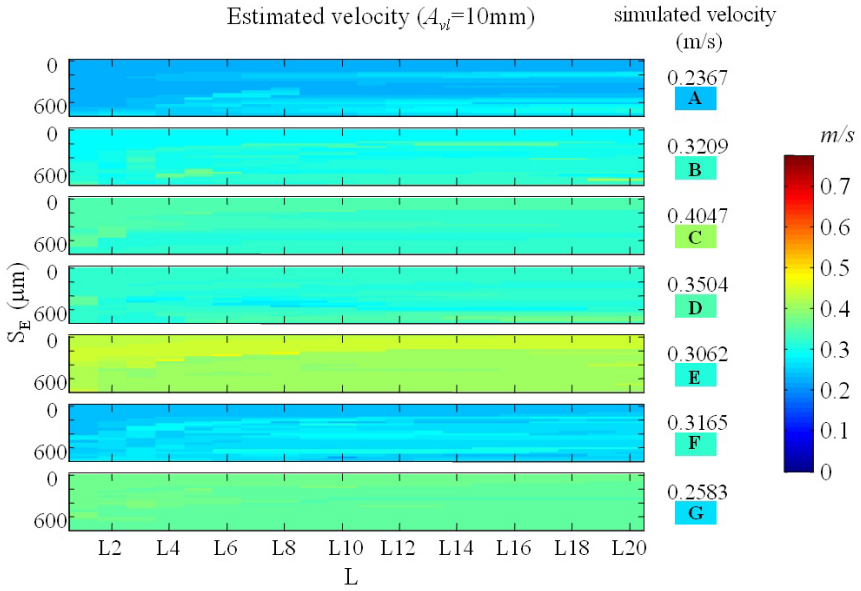

Figure 6.21 – First case study: Estimation of the velocities of the emboli using the SF-STFT for an A_{vl}=10mm.

Figure 6.22 and Figure 6.23 show the results obtained for the estimation of the velocities when the detection threshold is applied to respectively $A_{vl} = 1\text{mm}$ and $A_{vl} = 1\text{cm}$.

The same remarks that were drawn for the results obtained before the application of the detection threshold are still valid.

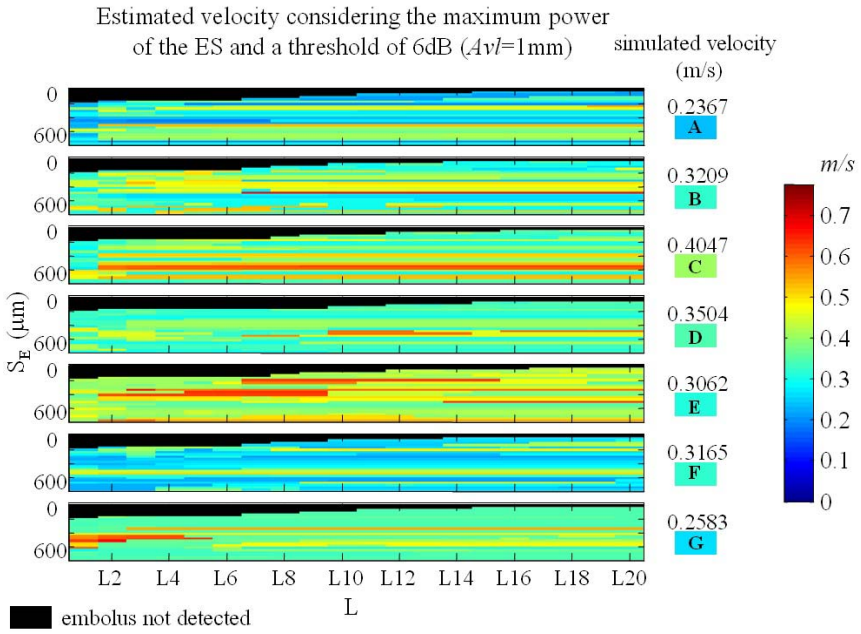

Figure 6.22 – First case study: Estimation of the velocities of the emboli using the SF-STFT for an A_{vl}=1mm, considering a threshold for detection 6dB.

An important feature that has not been observed before is now visible in Figure 6.23. Some of the missed emboli located in D position do not correspond to low L and short S_E. This behaviour suggests that the results could be improved with an increased spatial resolution.

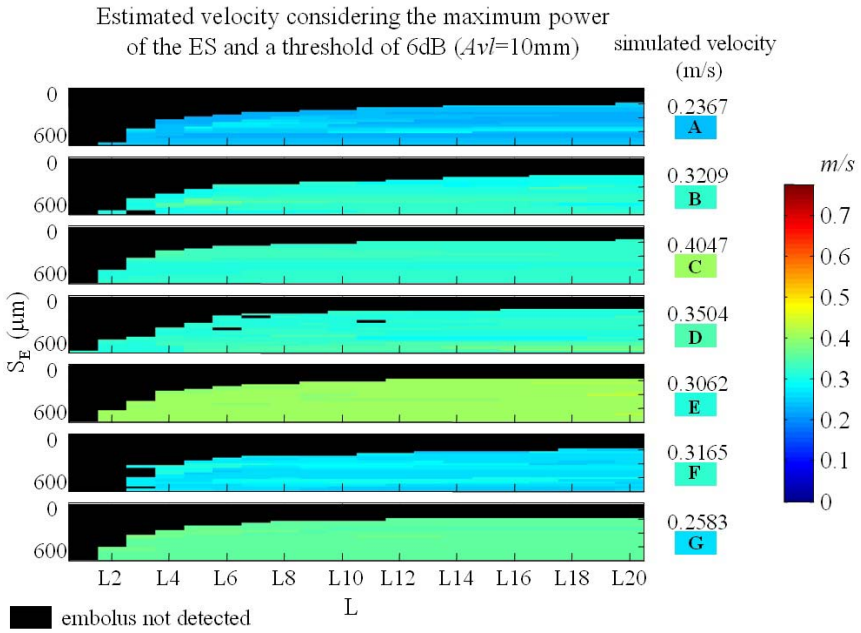

Figure 6.23 – First case study: Estimation of the velocities of the emboli using the SF-STFT for an A_{vl}=10mm, considering a threshold for detection of 6dB.

Figure 6.24 shows the improved velocity estimation obtained by duplicating the spatial resolution.

The estimated velocities are now much closer to the ones obtained with time-domain and STFT processing. It can also be seen that there are less missed emboli with this new resolution.

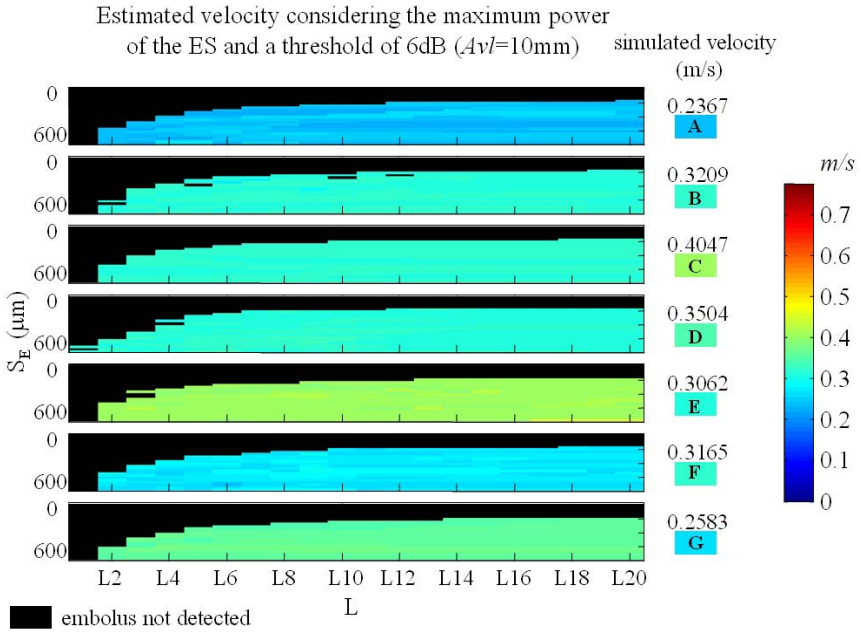

Figure 6.24 – First case study: Estimation of the velocities of the emboli using the SF-STFT for an A_{vl}=10mm, considering a threshold for detection of 6dB, and double space resolution.

To estimate SVL with SF-STFT it is necessary to apply a weighting factor given by,

$$w = \frac{v_E}{V_M} \tag{6.10}$$

as the space-frequency operates on the maximum frequency.

The results obtained for the estimation of SVL when $A_{vl} = 1\text{mm}$ are shown in Figure 6.25, and can be considered comparable to those obtained with time-domain processing. Although it is not much clear from the figure, there is a relationship between S_E and SVL. The reason why it is not clear is that the SVL values are relatively close to each other, but in general lower for shorter S_E and bigger for longer S_E.

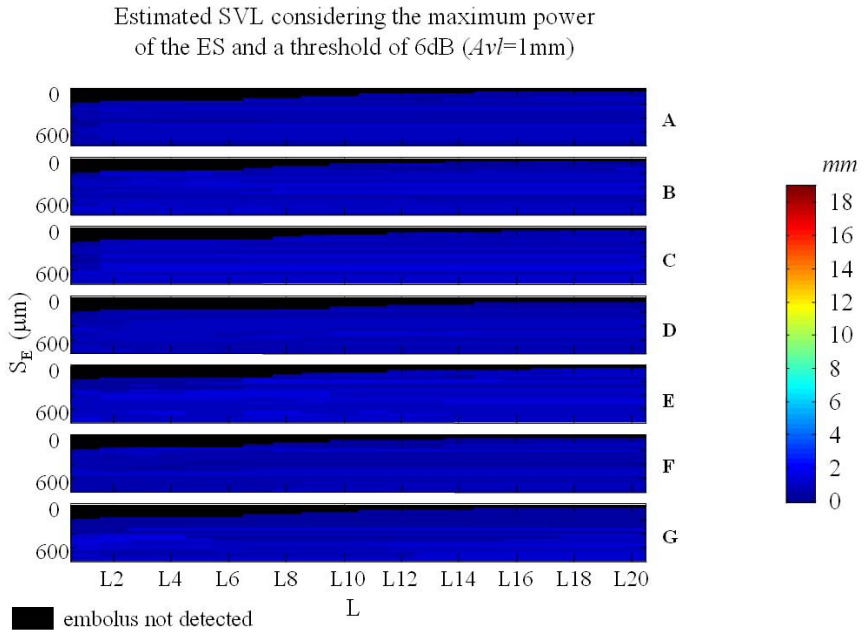

Figure 6.25 – First case study: Estimation of the SVL of the emboli the SF-STFT for an A_{vl}=1mm, considering a threshold for detection of 6dB.

However, the results obtained with $A_{vl} = 10\text{mm}$ are not similar to the results obtained with time domain processing for the same situation. On the contrary, the estimation of the SVL seems worsen with the increase of the A_{vl}. The estimated SVLs are much closer now, and it seems to be no way to relate SVL with S_E in this case.

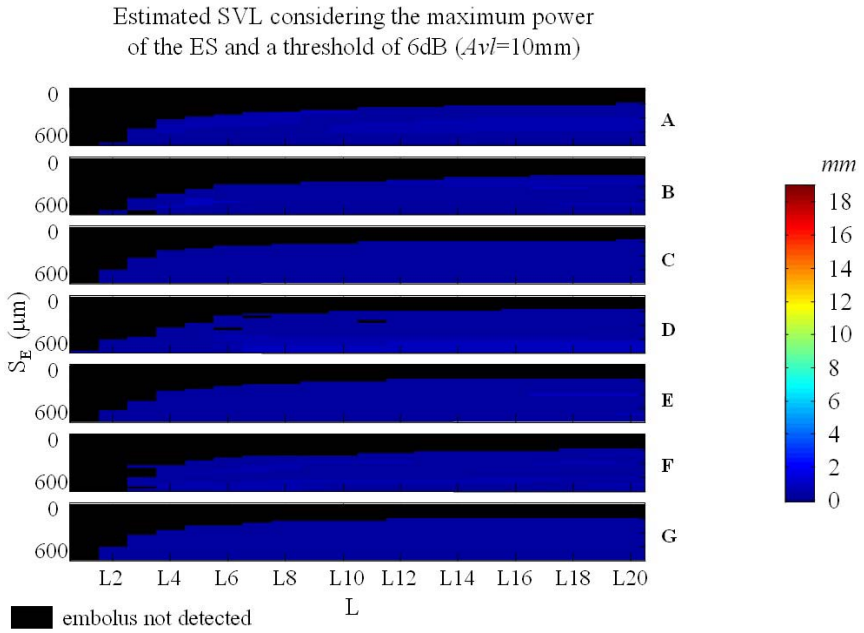

Figure 6.26 – First case study: Estimation of the SVL of the emboli using the SF-STFT for an A_{vl}=10mm, considering a threshold for detection of 6dB

Increasing the spatial resolution does help is this case as the graphs in Figure 6.27 show. Although the values of SVL are very close to each other, a relationship between SVL and S_E can be observed in the figure.

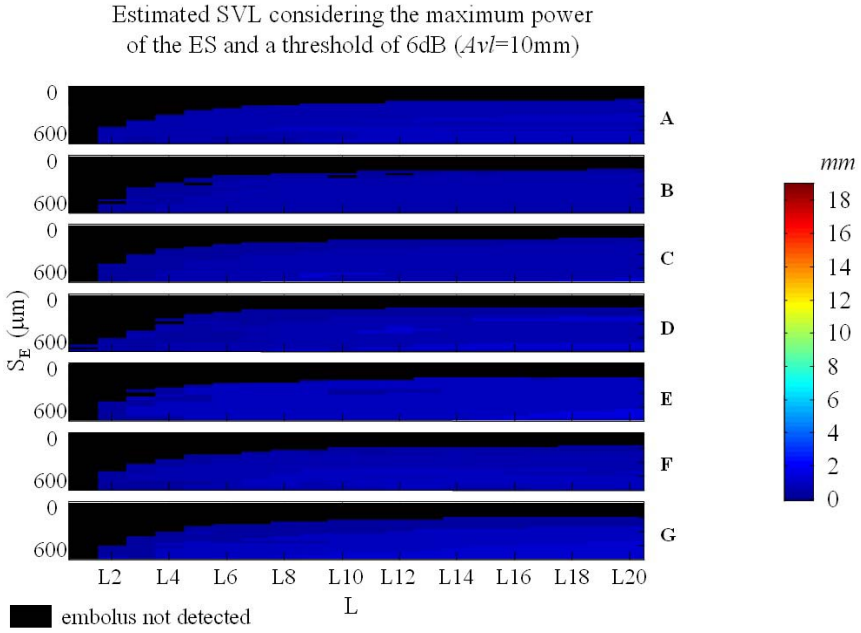

Figure 6.27 – First case study: Estimation of the SVL of the emboli using the SF-STFT with double resolution for an A_{vl}=10mm, considering a threshold for detection of 6dB.

6.5.2 SECOND CASE STUDY

Similarly to what happened in the first case study, the performance of the SF-STFT on estimating the MEP, is worst than the performance of the time-domain approach but better than the performance of STFT estimation.

This can be observed in Figure 6.28 when MEP is computed from the maximum value of $P_E + P_B$, and in Figure 6.29 when MEP is computed from the mean value of $P_E + P_B$. Both figures were generated with the simulation of emboli A and $A_{vl} = 1\text{mm}$.

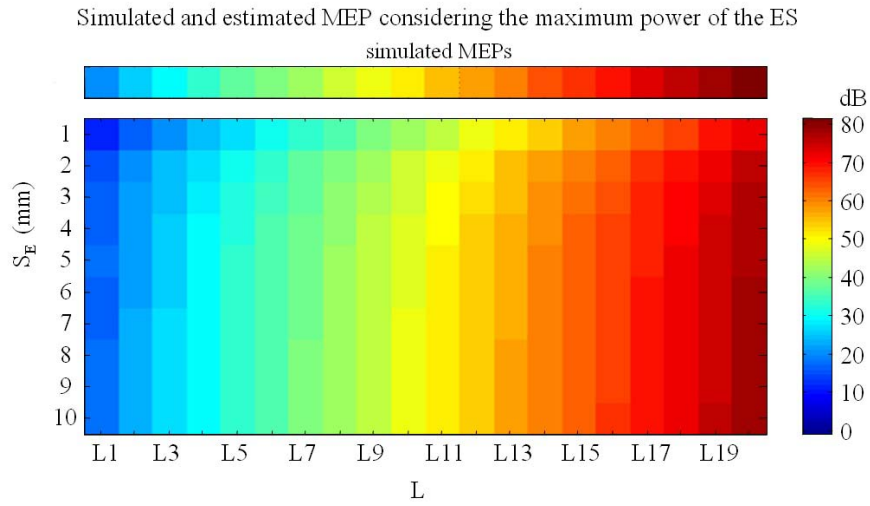

Figure 6.28 – Second case study: Estimated MEP (maximum power) obtained with the SF-STFT. The upper bar represents the expected MEP values, the right bar represents the colour scales.

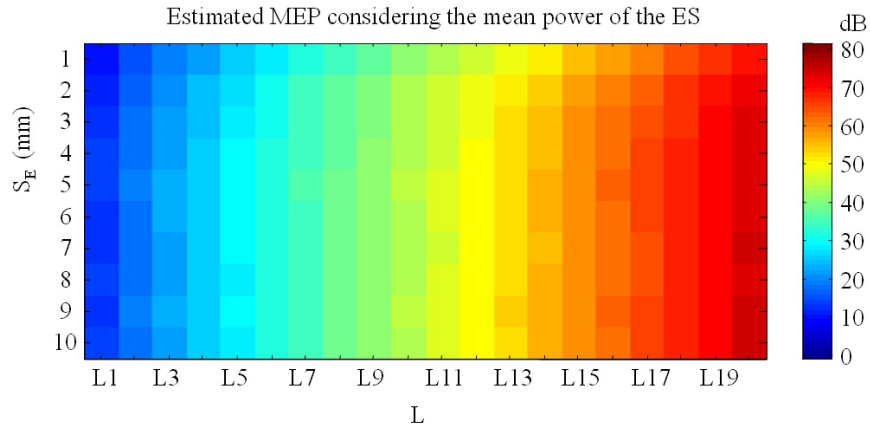

Figure 6.29 – Second case study: Estimated MEP (mean power) obtained with the SF-STFT. The left bar represents the colour scales.

The detection threshold of 6dB was still found appropriate for using with SF-STFT in the second case study.

With this threshold there are no missed emboli if $A_{vl} = 1$mm for emboli designated as A. However, if A_{vl} is simulated to be 10mm, there are 22 missed emboli in 200 simulated, whose parameters are showed in Figure 6.30. That corresponds to missing more emboli than time-domain (17 missed emboli) or STFT processing (15 missed emboli).

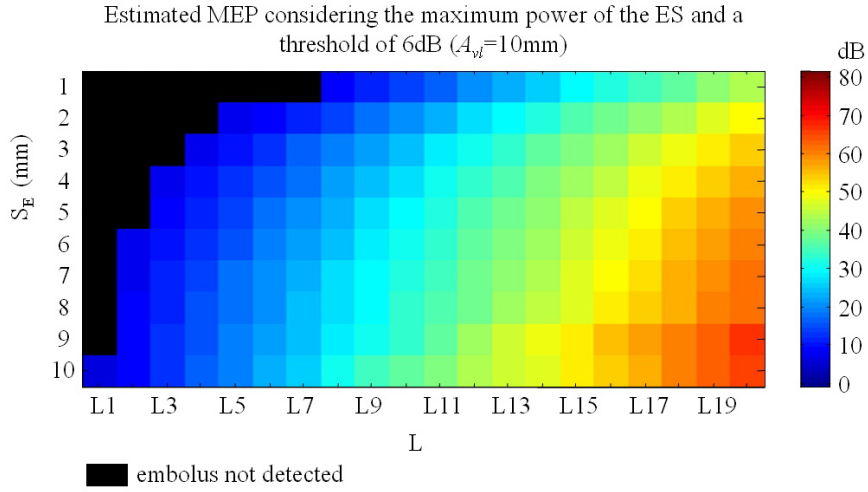

Figure 6.30 – Second case study: Estimated MEP (maximum power) obtained with the SF-STFT, A_{vl}=10mm, a threshold for detection of 6dB.

The total number of missed emboli observed in the second case study for each A_{vl} is showed in Figure 6.31. For each A_{vl}, 1400 ES were simulated.

Notice that the curve in the graph has a similar behaviour to the curve obtained with time-domain processing (see Figure 5.35), but presents general worst behaviour than the STFT (see Figure 5.44).

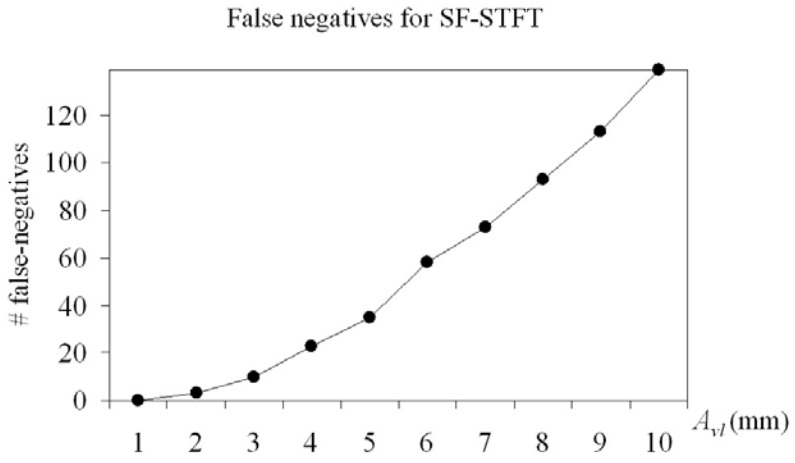

Figure 6.31 – Second case study: Total number of false negatives found for the 10 values of A_{vl} using the SF-STFT with a threshold for detection of 6dB. For each A_{vl} the total number of emboli was 3360.

The results obtained on the estimation of embolic velocities for $A_{vl} = 1\text{mm}$ and $A_{vl} = 10\text{mm}$ are shown respectively in Figure 6.32 and in Figure 6.33. There are no important differences between the two graphs, indicating that the choice of the A_{vl} does not have to rely on the accuracy of the velocity estimation.

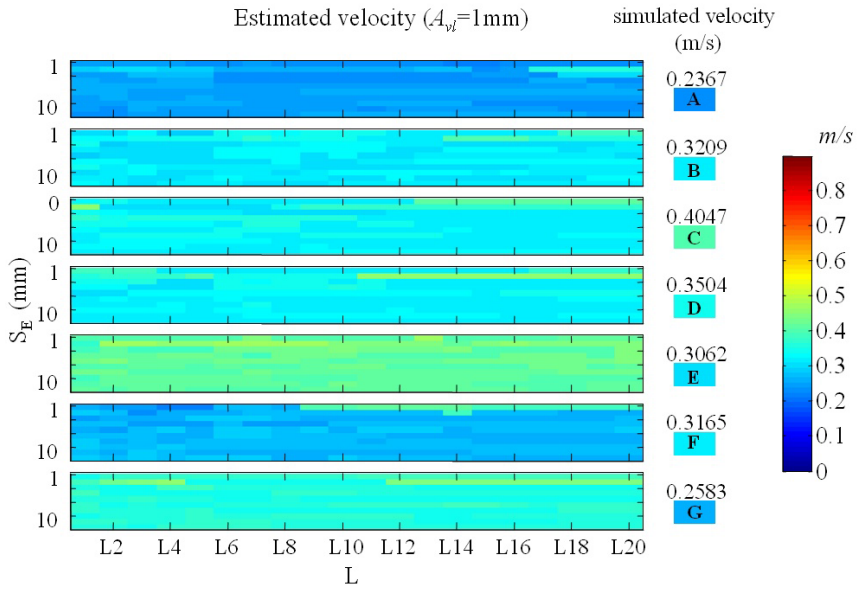

Figure 6.32 – Second case study: Estimation of the velocities of the emboli using the SF-STFT for an A_{vl}=1mm.

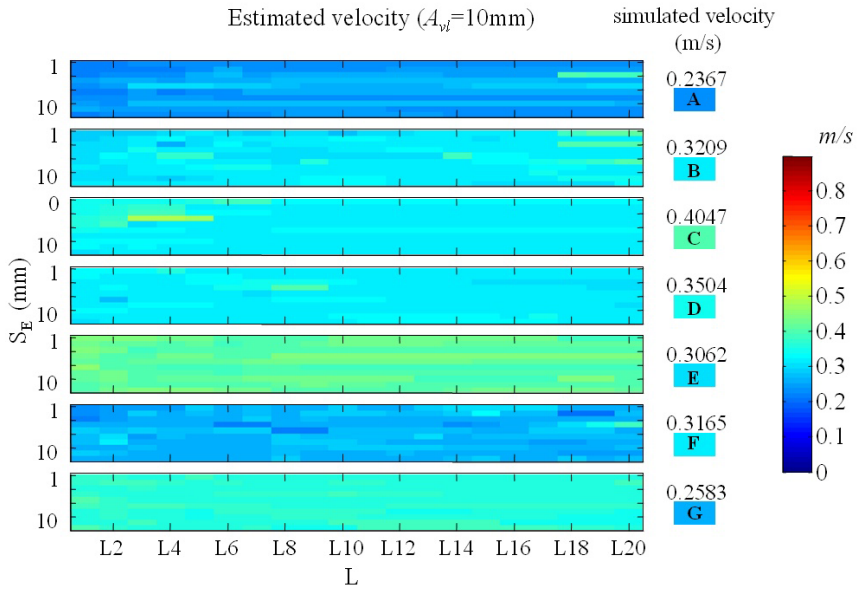

Figure 6.33 – Second case study: Estimation of the velocities of the emboli using the SF-STFT for an A_{vl}=10mm.

The results of the velocity estimation when the detection threshold is applied are similar to the results obtained before applying the threshold. However, the observation

of the graphs in Figure 6.34 obtained for the study of the estimation of velocities when the detection threshold is applied for $A_{vl} = 1$cm, also allows concluding that a higher spatial resolution could improve the general performance of the SF-STFT.

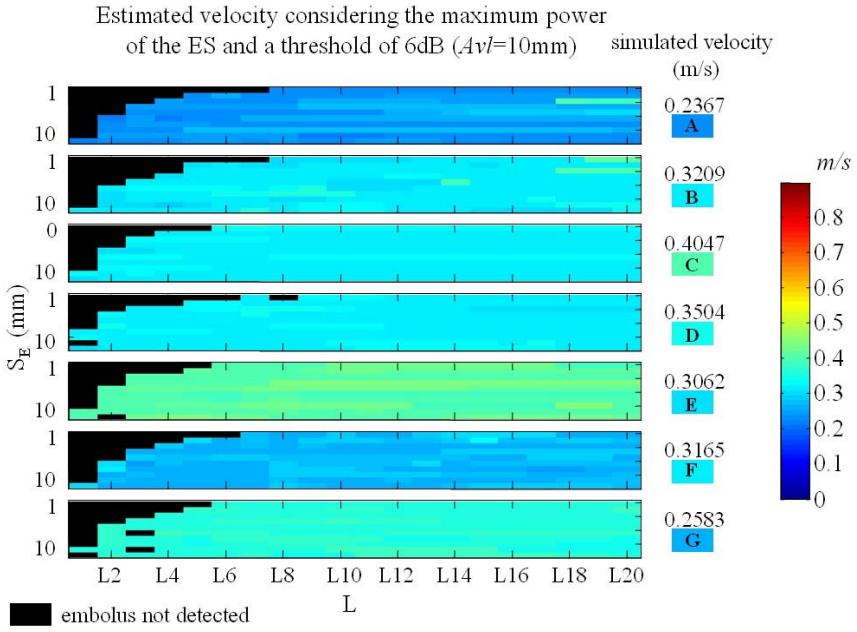

Figure 6.34 – Second case study: Estimation of the velocities of the emboli using the SF-STFT for an A_{vl}=10mm, considering a threshold for detection of 6dB.

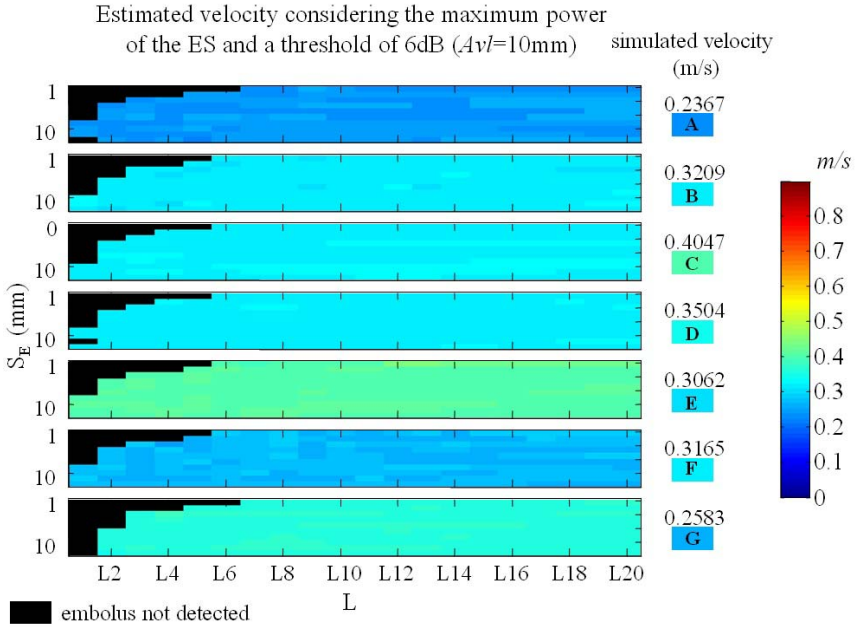

Figure 6.35 – Second case study: Estimation of the velocities of the emboli using the SF-STFT for an A_{vl}=10mm, considering a threshold for detection of 6dB, and double space resolution.

Figure 6.35 shows the estimated velocities for $A_{vl} = 1$cm, when the detection threshold is applied. Now the results of the velocity estimation are similar to the ones obtained with the other methods, and the probability of missing emboli decreased.

There is some improvement on the results obtained for SVL when the second case study is compared to the first.

Notice that the relationship between SVL and S_E is more easily observed in Figure 6.36, which was obtained using the 6dB detection threshold and $A_{vl} = 1$mm.

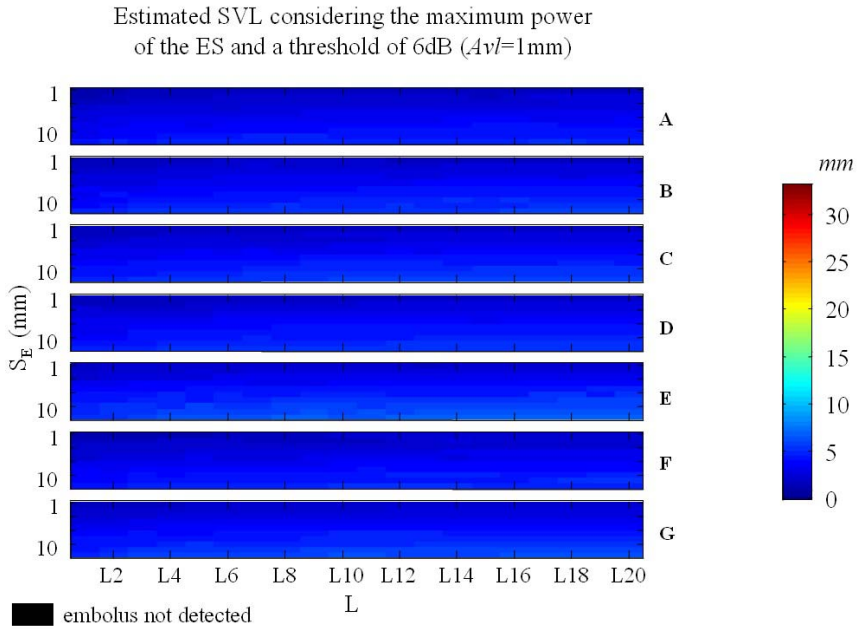

Figure 6.36 – Second case study: Estimation of the SVL of the emboli the SF-STFT for an A_{vl}=1mm, considering a threshold for detection of 6dB.

That relationship gets more confused when A_{vl} increases to 10mm, as Figure 6.37 shows.

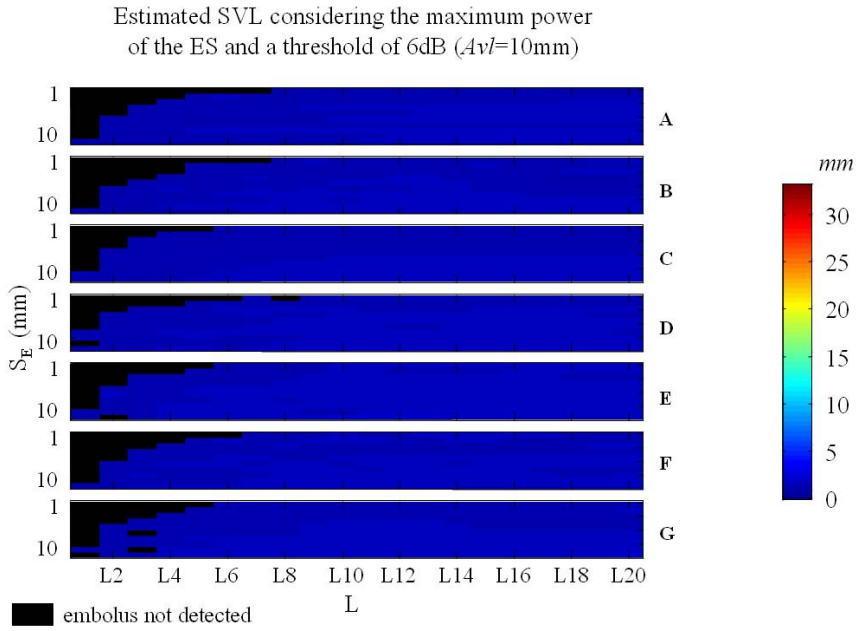

Figure 6.37 – Second case study: Estimation of the SVL of the emboli using the SF-STFT for an A_{vl}=10mm, considering a threshold for detection of 6dB.

Finally, Figure 6.38 shows that the improvement obtained by doubling the spatial resolution is not so clear in this case.

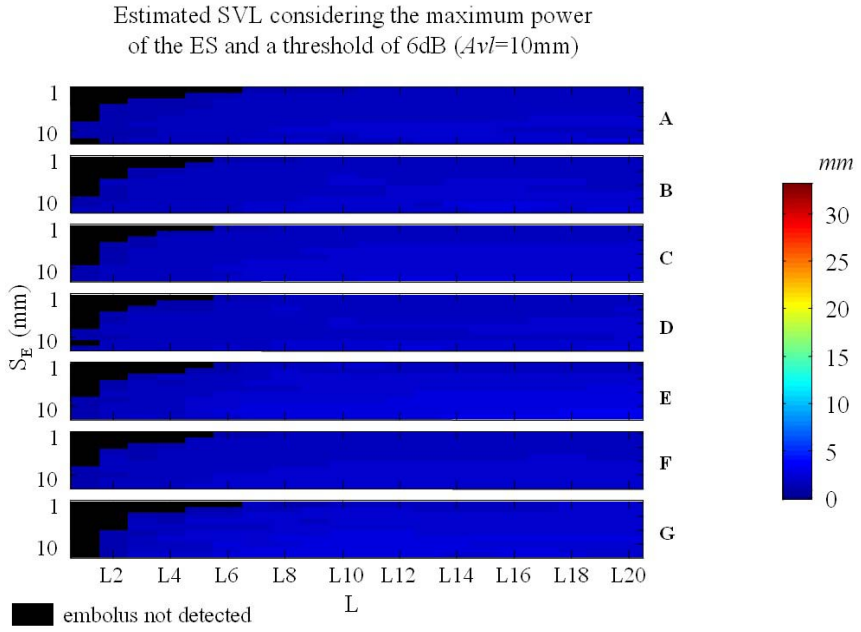

Figure 6.38 – Second case study: Estimation of the SVL of the emboli using the SF-STFT with double resolution for an A_{vl}=10mm, considering a threshold for detection of 6dB.

6.5.3 RESULTS

The comparison of SF-STFT with STFT and time-domain processing on the characterisation of emboli, leads to the clear preference of the SF methodology over the STFT and to the probable preference of the SF-STFT over the time-domain processing.

Although the MEP is still better estimated with the time-domain approach, that difference is not as relevant as it was in the case of the STFT.

The SF-STFT deteriorates the estimation of velocity, but as, in this case the computation of the SVL no longer depends on the accuracy of the velocity estimation, this disadvantage presents no relevant consequences.

The estimation of SVL is better estimated with the SF-STFT.

More evident is the improved performance of SF-STFT on the detection of emboli – the main goal of this study. Figure 6.39 and Figure 6.40 show the comparative performance of time-domain processing, STFT and SF-STFT, with single and double resolution, on detecting emboli, for first and second case studies, respectively.

The SF-STFT general performance is similar to the time-domain approach, better than STFT for the shorter S_E considered in the first case study, worst than STFT for the longer S_E considered in the second case study. However, if the spatial resolution is increased twice, the number of missed emboli is generally lower when SF-STFT is used.

Notice that the spatial SF-STFT resolution could be still much improved without becoming even close to the computational burden involved in the use of the STFT.

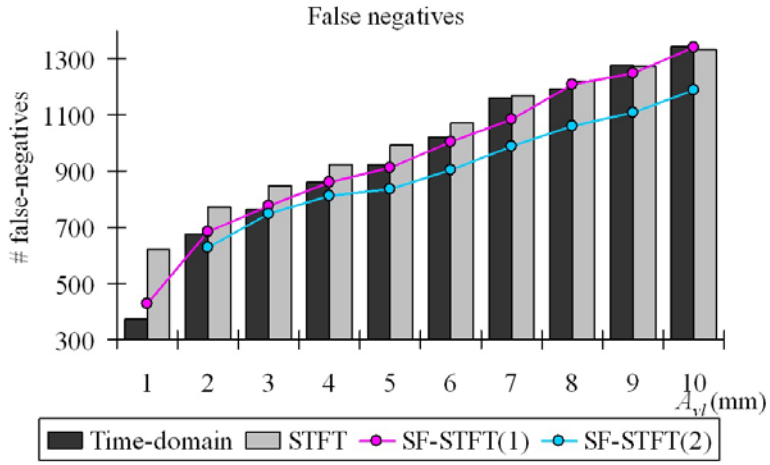

Figure 6.39 – First case study: amount of missed emboli for each A_{vl} for time-domain approach, STFT, and SF-STFT with simple and double resolution.

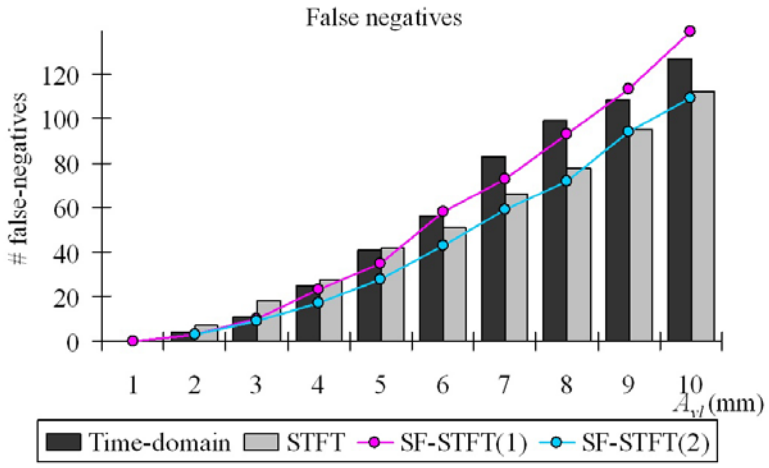

Figure 6.40 – Second case study: amount of missed emboli for each A_{vl} for time-domain approach, STFT, and SF-STFT with simple and double resolution.

6.6 CONCLUDING REMARKS

In an attempt to overcome the main drawbacks of spectral estimation for emboli detection and analysis, a new method, the SF representation is proposed.

This method uses adaptive overlapping based on the maximum velocities measured in the Doppler signal to estimate the spectrum.

As the time axis is not linear in this new approach, the method becomes a function of space travelled by the blood flow within a specific region in the artery.

It was expected that this method would present a performance as good as the STFT on estimating the MEP and an advantageous performance on estimating the SVL emboli regardless from its velocity.

The tests performed on the SF-STFT showed that the expected results were accomplished and even overcome, as the results obtained allow comparing its performance with the performance of the time-domain approach. The results also encourage the use of the SF approach on the detection of emboli.

However, the effective evaluation of this method must be done on clinical signals, and this will be studied in the next chapter.

7 OLD METHODS VS NEW METHODS APPLIED TO CLINICAL SIGNALS

7.1 INTRODUCTION

The application of the developed spectral estimation methods to clinical signals allows a more realistic evaluation of the improvements and/or drawbacks of the SF representation. This chapter reports a comparison of the proposed method with the STFT and time-domain approaches, and discusses the results obtained.

7.2 CLINICAL SIGNALS

The clinical signals used in this chapter were supplied by the Medical Physics Department of the University of Leicester. Table 7.1 shows a description of the files containing the signals.

Type of emboli	Channel one	Channel two	Number of files	Number of emboli[23]
Particulate	Doppler signal	Amplified Doppler signal	10	16
All (Frequency modulated)	Doppler signal	Amplified Doppler signal	10	16
Gaseous	Doppler signal	Amplified Doppler signal	8	30

Table 7.1 – Description of the files with clinical signals

[23] According to the time-domain signals.

The files were obtained with a probe of 2MHz, directed with an angle of approximately 0º to 30º. The sampling frequency was 12.5 kHz.

The SNR of the signals was estimated to be 27.2dB. This value was found from the average of the SNR of all the signals involved.

For each clinical signal the SNR, was computed from

$$SNR = 10\log_{10}\left(\frac{P_B}{P_N}\right) \tag{7.1}$$

where P_B and P_N stand for respectively the power of blood and the power of noise. P_N was estimated from an area of the spectrum of the signals where blood could be assumed absent, and P_B was estimated from an area of the spectrum where both blood and noise were present.

7.3 IMPLEMENTATION

The spectral parameters involved in the embolic analysis, are the mean frequency and the power variation that allow the computation of, respectively, S_E and the MEP. The analysis of the results presented in Chapter 4, led to the choice of windows of 60 bins without overlapping.

The use of the SF-STFT involves another spectral parameter, the maximum frequency. Figure 7.1 shows the normalized errors obtained with the several window lengths that have been considered in this work for the spectral parameters involved (from the results presented on Chapter 4). The graph was built considering the average error for each window length for each case. Each parameter (or combination of parameters) was normalized to the maximum value. The values were obtained considering SNR=20dB (only signals with ∞, 20 and 10dB were studied in this work).

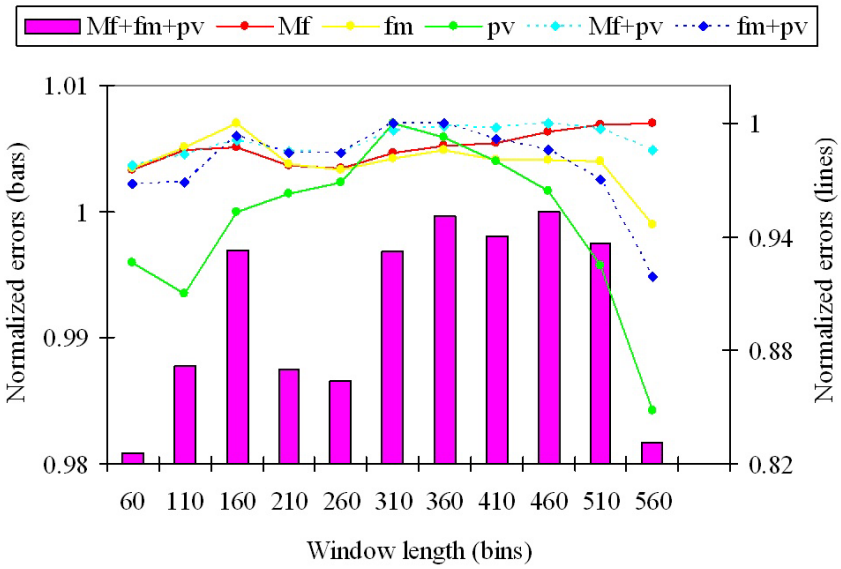

Figure 7.1 – Normalized errors obtained with the STFT for the average of different windows length. MF stands for maximum frequency, fm for mean frequency and pv for power variation. The circles indicate the minimum errors.

According to the graph, it was decided to use windows with 60-bin length, as it leads to the lowest errors considering that all the involved parameters are of equal importance.

The detection of emboli and the determination of its SVL were computed using an automatic procedure developed in Matlab.

7.4 RESULTS

As the time-domain signal contains all the available information in the signal, it was considered the reference. The STFT and the SF-STFT results are presented as a ratio relative to the time-domain processing results.

To study the behaviour of the SF-STFT on the detection and characterization of emboli, three spatial resolutions were considered: Δs of 1mm, 5mm and 1cm. Since the axial sample volume length of the probe employed was 1cm, the $\Delta s = 1$cm might loose some information, but is considered in this study as an extreme case.

Figure 7.2 shows the relationship of the average MEP from which emboli could be identified while avoiding false-positives, obtained from time-domain processing and each of the other approaches.

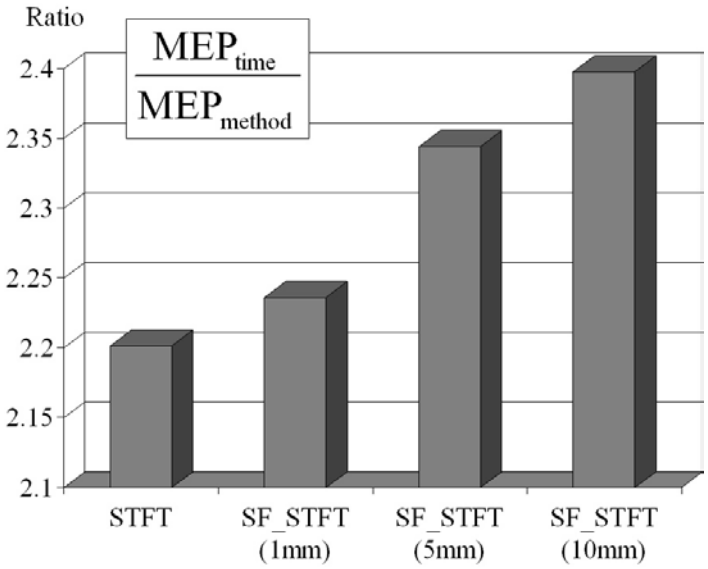

Figure 7.2 – Ratios of the average minimum MEPs that allow embolic detection and avoid false-positives.

In all the results used for generating Figure 7.2, only one of the MEPs (that was estimated with the SF-STFT for $\Delta s = 1\text{cm}$) presented a higher value than the one observed for time-domain processing.

From the above figure, the first conclusion is that spectral estimation allows enhancing the emboli over the background signal. Among the spectral estimators, the STFT is the one that presents the lowest improvement, as on average it depicts the emboli signals with approximately 2.2 times the MEP of the time-domain signals.

The SF-STFT presents even higher emboli MEP, and the ratio increases with the decrease of spatial resolution.

However, it is important to note that the STFT introduced a false-positive identification that could not be avoided. The choice of a lower threshold would imply loosing the identification of a possible embolus.

With the application of the SF-STFT with $\Delta s = 1\text{mm}$, four emboli were missed. The visual observation of the signals involved indicates that those missed occurrences could not be found at all, regardless the threshold used. The samples containing there are disguised by adjacent emboli.

Figure 7.3 shows the errors obtained with the SVL estimation. The errors are normalized to the results obtained with time domain processing.

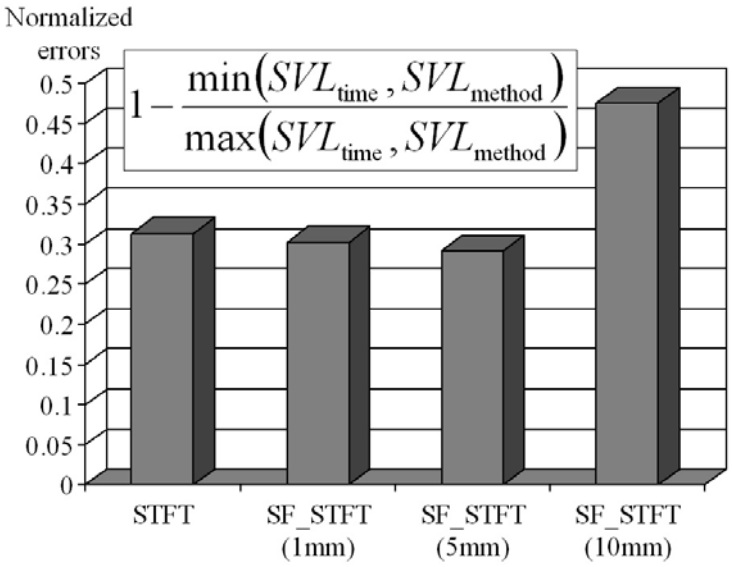

Figure 7.3 – Relationship between the estimated SVL with time domain processing and with the spectral estimation methods.

The lowest SVL detected by time domain processing was 0.395mm.

SVL estimated with the SF-STFT approach, were corrected with the factor w defined in Equation (6.10).

Figure 7.3 shows the lowest errors of the estimation are obtained with the SF-STFT using $\Delta s = 5\text{mm}$. The use of $\Delta s = 1\text{mm}$ presents the worst results, as it was already expected. However, the more important conclusion is that the SF-STFT shows an improved performance over the classical STFT.

It is also important to consider that STFT and SF-STFT with $\Delta s = 1\text{mm}$ underestimates the SVL (in Figure 7.3, 83% of results of the STFT and 90% of the results of SF-STFT with $\Delta s = 1\text{mm}$ correspond to an underestimation). Increased resolution of the SF-STFT tends to overestimate the SVL (around 98% of the results in Figure 7.3 are overestimated for both $\Delta s = 5\text{mm}$ and $\Delta s = 10\text{mm}$).

The results depicted in Figure 7.4 were obtained to the study of the impact of weighting the SVL estimated with the factor defined in Equation (6.10).

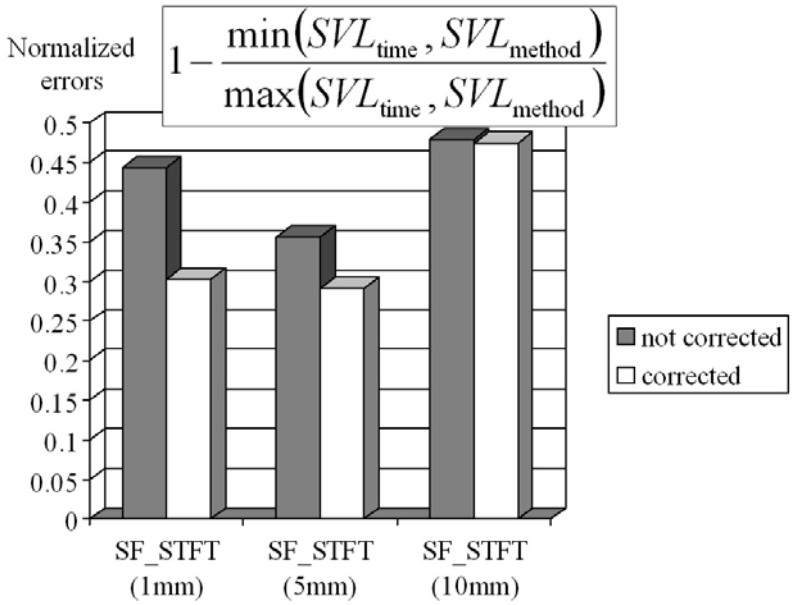

Figure 7.4 – Comparison of the accuracy on estimating the SVL of emboli using and not using the correction factor.

Without the weighting factor, the results of the SF-STFT are worse. In this case, the STFT would be preferred over the SF-STFT.

Moreover, the non-corrected version of the SF-STFT mainly overestimates the SVL if $\Delta s = 1\text{mm}$ (in Figure 7.4 around 98% of the results are overestimated) and to underestimate if $\Delta s = 5\text{mm}$ (that happens to around 74% of the emboli considered in the figure). If $\Delta s = 10\text{mm}$, only 47% of the emboli studied were overestimated.

7.5 CONCLUDING REMARKS

The application of the three methods to the analysis of ESs led to the conclusion that the STFT with an appropriate time resolution can be a tool as powerful as the time-domain approach. Moreover, the SF-STFT can perform even better than the STFT with the additional advantage of presenting less computational burden.

8 CONCLUSION

8.1 GENERAL CONCLUSIONS

The aim of the research work presented in this thesis was to improve the characterisation of emboli in blood flow signals.

The quality of the characterisation is strongly related to the accuracy of the estimation of some Doppler signal spectral parameters, namely, the maximum and mean frequency, the bandwidth, and the power variation over time.

Intrusive vessel lesions produce disturbances in the blood flow, thus affecting the velocity waveform and, consequently, the mean and maximum frequencies and the bandwidth. Embolic events are associated with power increases in a range of Doppler shifted frequencies.

Pulsed ultrasonic Doppler signals, such as the ones obtained using transcranial Doppler equipment applied to MCA, are characterised by a random nature with a Gaussian probability density function in the case of undisturbed flow. The spectrum is time varying determined by the blood velocity profile in the sample volume being analysed. Under steady heart rate conditions, the Doppler signal can be considered cyclo-stationary.

Taking into account the blood flow characterisation, the fact that emboli identification and classification would require testing different methods of spectral estimation, the use of testing-case signals, whose spectral parameterization was known, was envisaged. After performing a review of many blood flow signal simulators, the Wang and Fish method was chosen as the more appropriate for simulating the blood flow in the MCA when Doppler TCD is used (Chapter 3).

This simulator requires the input of theoretical spectral waveforms representing the behaviour of the signals to be generated. Those waveforms were obtained by averaging several clinical signals. To enable waveforms of different lengths to be

averaged, two algorithms were studied. One of the algorithms was adapted, from a published algorithm, to the current problem and the other is a new averaging method based on earlier work from Kitten and Giddens [Kitney, Giddens, 1983]. The performance of both the modified and the new method were studied in depth, leading to the selection of the new method for producing the average waveforms required for feeding the simulator.

The accuracy of the simulator was tested and its satisfactory performance on generating typical MCA signals' characteristics (mean frequency, bandwidth and power variation over time), was ascertained. However, the simulator performance on mimicking the maximum frequency behaviour could be improved.

According to the clinical parameters used for diagnosis, and the direct relationship between Doppler frequencies and blood from velocities, the most common procedure for computing the clinical parameters, is by processing the blood flow signal in the time-frequency domain. The first approach performed towards the selection of the most adequate spectral estimator method, made use of MCA signals previously simulated. Experiments with these reference signals were reported in Chapter 4.

Based on past experience, the STFT, the STMC and the DCWD were primarily considered as spectral estimation methods for MCA Doppler blood flow signals. To assure a realistic understanding of the effects of the methods on the signals, a set of scenarios, as complete as possible was created. The scenarios involved different noise conditions and several combinations of each method's parameters. Tests were performed evaluating the ability of the method to estimate the four relevant spectral parameters. This allowed the construction of a hierarchy of relevance of the parameters of the methods, for tuning each method by estimate each spectral parameter under different noise conditions. Once the estimators were tuned to their best performance, according to the averaged spectral waveforms obtained in Chapter 3, it was possible to select the STFT as the method to be used in subsequent research. This choice was mainly due to STFT ability to estimate the power variation over time.

Regarding the main goal of this work, spectral analysis of ESs, it was also proposed to include embolic events in the simulation. Chapter 5 reports the work concerning this goal.

The foundations of the embolic simulation process are that: the appearance of emboli varies according to their effective length, MEP, and velocity; that the axial

length of emboli in time-domain and time-frequency representations depend on the embolic velocity; and that the MEP may vary according to the embolus location in the cardiac cycle. According to this, emboli were considered moving at the mean velocity of the signal, at the time of its occurrence. The averaged waveform of the mean velocity was computed over a space axis instead of the time axis, to avoid the effect of the velocity on the estimation of the effective length of emboli. Additionally, the power was considered not to vary over time, to allow a correct characterisation of the MEP.

After the characterization of emboli according to the space axis, the ES is transformed back into the time domain to be added to the Doppler blood flow background signal.

Although not thoroughly extensively used in the current work, it should be noted that the embolic simulator developed allows the generation of emboli at any velocity in the range of velocities observed in the signal, and to produce ESs with time-varying power.

A range of effective embolic axial lengths, MEPs and velocities that could produce realistic ES was used for simulating signals with emboli. These simulated signals were used to analyse the effects produced by signal sampling. The application of STFT and time-domain processing was studied. Analysis of the results led to the conclusion that both methods produce comparable results as long as the STFT is used with the correct time resolution, i.e., the correct percentage of window overlap. Although the STFT produced acceptable results, in a real time implementation where further processing might be required, the computational burden, associated with the calculation for an adequate percentage overlap, might be excessive. Additionally, time analysis and time-frequency analysis suffer from a common problem: the same embolus presents different characteristics depending on the part of the cardiac cycle in which it occurs. Finally, if STFT is not provided with enough time resolution, an embolus capable of being detected during diastole could be missed during systole.

To overcome these limitations, a spectral estimator with adaptive overlapping was developed and named space-frequency representation. The fundamental concept of this representation is that the necessary and sufficient information contained in the time-domain signal is only renewed after a time interval that can be obtained from the (instantaneous) maximum velocity of that time-domain signal. Thus, a space-frequency distribution, treating all the important information and neglecting redundant information, was created.

The application of such an adaptive version of a time-frequency estimator to simulated signals and its statistical evaluation is reported in Chapter 6. The space-frequency representation of the simulated signals was obtained and the results of the estimation compared with those produced by the other methods. Identically performed results on the estimation of parameters were obtained. Particular attention must be drawn to the space-frequency graphical representation of ESs. The graphical spectrum conveys the SVL and frequency. Using time-frequency spectra, the SVL of an embolus can be obtained from embolus duration and frequency. Using space-frequency representations, the embolus size is proportional to its frequency thus more intuitive for a clinician.

Finally, the statistical evaluation and identification of the best spectral estimator, when clinical signals are considered, is reported in Chapter 7. The comparison of time-domain processing, STFT analysis and SF-STFT analysis to clinical data from the MCA containing embolic signals produced encouraging results towards a wider application of the new method.

8.2 FUTURE WORK

The contents of this research work enables pointing some lines of future work, such as:

- The study of the viability of the generalization of MCA blood flow simulator for using with other blood vessels. It is believed that the simulator input spectral parameters could be used, with the necessary adaptation, to the simulation of blood flow on other vessels. It is also believed that the inclusion of maximum frequency spectral parameter as input of the simulator could lead to global benefits.
- It is considered relevant to direct the investigation towards spectrogram visualization methods, by development and integration of the space-frequency methodology. However, this new visualization method must be consistent with the clinical conventional visualisation forms.
- More generally and according to the study described in this thesis and to some scientific publications [Lizzi *et al.*, 1996] [Oelze, O'Brien Jr, 2004] , it is also identified as relevant lines for future investigation

a) The study of interference factors not considered in this work, and related with emission and reception of ultrasound signals from blood, using methods of spectral analysis clinically evaluated.
b) Complement the study described in a) with the stochastic analysis of the signals.

- Other specific topics were identified along the thesis such as the search for alternative spectral estimators that can improve the power estimation, or, the improvement of the space-frequency representation to avoid the requirement of a weighting factor on the dimensioning of emboli.

9 BIBLIOGRAPHIC REFERENCES

[Aydin et al., 1999] Aydin Nizamettin, Padayachee Soundrie, Markus Hugh S., *The Use of the Wavelet Transform to Describe Embolic Signals*, Ultrasound in Med. & Biol., Vol. 25, No. 6, pp. 953-958, July 1999

[Aydin, Markus, 2000] Aydin Nizamettin, Markus Hugh S., *Directional Wavelet Transform in the context of Complex Quadrature Doppler Signals*, IEEE Signal Proc. Letters, Vol. 7, No. 10, pp. 278-280, October 2000

[Bascom, Cobbold, 1996] Bascom P. A. J., Cobbold R. S. C., *Origin of the Doppler Ultrasound Spectrum from Blood,* IEEE Trans. Biomed. Eng., Vol. 43, No. 6, pp. 562-571, June 1996

[Bastos *et al.*, 1996] Bastos C. A. C., Fish P. J., Vaz F., *A Model for Generating Doppler Ultrasound Signals from Pulsatile Blood Flow*, Proc. 18th Annual Conference of IEEE EMBS, Vol. 18, pp. 1.3.1, The Netherlands, October/November 1996

[Cardoso *et al.*, 1996a] Cardoso J., Ruano M. Graça, Fish P., *Non-Stationary Broadening Reduction in Pulsed Doppler Spectrum Measurements Using Time-Frequency Estimators*, IEEE Trans. Biomed. Eng., Vol. 43, No. 12, pp. 1176-1186, December1996

[Cardoso *et al.*, 1996b] Cardoso J., Fish P., Ruano M. Graça, *Choi-Williams Time-Frequency Estimator, a Parallel Implementation*, Vecpar'96 2nd Intern. Meeting on Vector and Parallel Processing (Systems and Applications), Oporto, Portugal, September 1996

[Cardoso, 1998] Cardoso J.C., *Investigation and Implementation of Real Time Spectral Estimation Techniques for use with Pulsed Doppler Blood Flow Detectors*, UCNW, UK, PhD Thesis, 1998

[Challis, Kitney, 1991a] Challis R.E., Kitney R.I., *Biomedical Signal Processing. Part II: The Frequency Transforms and Their Inter-Relationships*, Med. & Biol. Eng. & Comput., Vol.29, No.1, pp. 1-17, January 1991

[Challis, Kitney, 1991b] Challis R.E., Kitney R.I., *Biomedical Signal Processing. Part III: The Power Spectrum and Coherence Function*, Med. & Biol. Eng. & Comput., Vol.29, No.3, pp. 225-241, May 1991

[Choi, Williams, 1989] Choi Hyung-Ill, Williams William J., *Improved Time-Frequency of Multicomponent Signals using Exponential Kernels*, IEEE Trans. Acoust., Speech, Signal Processing, pp. 862-871,Vol.37, Nº6, June 1989

[Cohen, 1989] Cohen Leon, *Time-Frequency Distributions – A Review,* Proc. IEEE, Vol.77, No.7, pp. 941-981, July 1989

[Cohen, 1995] Cohen Leon, *Time-frequency Analysis*, Prentice-Hall, New Jersey, 1995

[Cohen, 1996a] Cohen L., *A General Approach for Obtaining Joint Representations in Signal Analysis. Part I: Characteristic Function Operator Method*, IEEE Trans. Signal Processing, Vol. 44, No.5, pp. 1080-1090, May 1996.

[Cohen, 1996b] Cohen L., *A General Approach for Obtaining Joint Representations in Signal Analysis. Part II: General Class, Mean and Local Values, and Bandwidth*, IEEE Trans. Signal Processing, Vol. 44, No. 5, pp. 1091-1098, May 1996.

[Consensus, 1995] Consensus Committee of the Ninth International Cerebral Hemodynamic Symposium, *Basic Identification Criteria of Doppler Microembolic Signals*, Stroke, Vol.26, No. 6, pp.1123, June 1995

[Culliane *et al.*, 2000] Cullinane Marisa, Reid Greg, Dittrich Ralf, Kaposzta Zoltan, Ackerstaff Rob, Babikian Viken, Droste Dirk W., Grossett Donald, Siebler Mario, Valton Luc, Markus Hugh S., *Evaluation of New Online Automated Embolic Signal Detection Algorithm, Including Comparison With Panel of International Experts*, Stroke, Vol.31, No.6, pp. 1335-1341, June 2000

[Culliane, Markus, 2001] Cullinane Marisa, Markus Hugh S., *Evaluation of a 1 Mhz Transducer for Transcranial Doppler Ultrasound Including Embolic Signal Detection*, Ultrasound in Med. & Biol., Vol. 27, No. 6, pp. 795–800, June 2001

[Devuyst *et al.*, 2001] Devuyst G., Darbellay G. A., Vesin J.-M., Kemény V., Ritter M., Droste D.W., Molina C., Serena J., Sztajzel R., Ruchat P., Lucchesi C., Dietler G., Ringelstein E.B., Despland P.-A., Bogousslavsky J., *Automatic Classification of HITS Into Artifacts or Solid or Gaseous Emboli by a Wavelet Representation Combined With Dual-Gate TCD*, Stroke, Vol. 32, No.12, pp. 2803-2809, December 2001

[Dietler, 2001] Dietler Giovanni, Neuroprotection Against Emboli. *The Automatic Detection and Classification of Brain Emboli Through Transcranial Doppler Ultrasound*, L'Institut de Physique de la Matière Condensée [on line], Jan 2001, [cited 2001-10-21], http://www.unil.ch/ipmc/docs/gd/home.html

[EstudMed.com, 2001] Equipe EstudMed.com, *Embolias*, EstudMed.com [on line], 2001, [cited 2001-10-21], http://www.estudmed.com/patologia/embolias_1.htm

[Evans, 1988] Evans D. H., *A Pulse-Foot-Seeking Algorithm for Doppler Ultrasound Waveforms*, Clin. Phys. Physiol. Meas., Vol.9, No.3, 267-271, August 1988

[Evans, 1999] Evans David H., *Detection of Microemboli, in: Transcranial Doppler Ultrasonography*, Babikian V. L., Welchser L. R. Ed., Butterworth-Heineman Medical, 2nd ed., Boston, USA, pp. 141-155, 1999

[Evans, 2003] Evans David H., *Ultrasonic Detection of Cerebral Emboli*, Proc. IEEE Symposium on Ultrasonics, Vol. 1, pp. 316-326, Honolulu, Hawaii, October 2003

[Evans, McDicken, 2000] Evans D.H., McDicken W. Norman, *Doppler Ultrasound: Physics, Instrumentation, and Clinical Applications*, 2nd ed., John Wiley & Sons, New York, 1992

[Fan *et al.*, 2001] Fan Lingke, Evans David H., Naylor Ross, *Automated Embolus Identification Using a Rule-Based Expert System*, Ultrasound in Med. & Biol., Vol. 27, No. 8, pp. 1065-1077, August 2001

[Fan, Evans, 1994] Fan Lingke, Evans David H., *Extracting Instantaneous Mean Frequency Information from Doppler Signals Using the Wigner Distribution Function*, Ultrasound in Med. & Biol., Vol.20, No.5, pp. 429-443, 1994

[Fish, 1990] Fish P., *Physics and Instrumentation of Diagnostic Medical Ultrasound*, UK, John Wiley & Sons,1990

[Fish, 1991] Fish P., *Nonstationary Broadening in Pulsed Doppler Spectrum Measurements*, Ultrasound in Med. & Biol. , Vol. 17, No. 2, pp. 147-155, 1991

[Fish, 1992] Fish P., *The Doppler Effect and Blood Flow: An Instrument Optimisation Programme*, Developments in Acoustics and Ultrasonics, Ed. M. J.W. Povey and D.J. McClements, IOP Publishing, Bristol, pp. 91-127, 1992

[Forsberg *et al.*, 1999] Forsberg Flemming, Oung Harry, Needleman Laurence, *Doppler Spectral Estimation using Time-Frequency Distributions*, IEEE Trans. Ultrason., Ferroelect., Freq. Contr., Vol.46, Nº3, pp. 595-606, May 1999

[Furui *et al.*, 1999] Furui Eisuke, Hanzawa Kazuhiko, Ohzeki Hajime, Nakajima Takashi, Fukuhara Nobuyoshi, Takamori Masaharu, Mohr J.P., Stapf C**.,** *"Tail Sign" Associated With Microembolic Signals*, Stroke, Vol. 30, No. 4, pp. 863-866, April 1999

[García-Nocetti *et al.*, 2001] García-Nocetti F., González J. Solano, Acosta E. Rubio, Hernández E. Moreno, *Parallel Processing in Time-Frequency Distributions For Signal Analysis*, Proc. BioEng'2001, ID46.pdf, Faro, Portugal, July 2001, CD-ROM

[Gardner, 1990] Gardner William A., *Introduction to Random Processes with Applications to Signals and Systems*, 2nd ed., New York, USA, McGraw-Hill,1990

[Georgiadis *et al.*, 2000] Georgiadis D., Uhlmann F., Lindner A., Zierz S., *Differentiation Between True Microembolic Signals and Artefacts Using an Arbitrary Sample Volume*, Ultrasound in Med. & Biol., Vol.26, No.3, pp. 493-496, March 2000

[Girault, 2000] Girault Jean-Marc, Kouamé Denis, Ouahabi Abdeldjalil, Patat Frédéric, *Micro-Emboli Detection : An Ultrasound Doppler Signal Processing View Point*, IEEE Trans. Biomed. Eng., Vol. 47, No. 11, pp. 1431-1439, November 2000

[Guetbi *et al.*, 1997] Guetbi C., Kouame D., Ouahabi A., Remenieras J. P., *New Emboli Detection Methods*, Proc. IEEE Ultrasonics Symposium, Vol. 2, pp. 1119-1122, Toronto, Canada, October 1997

[Guo *et al.*, 1994] Guo Zhenyo, Durand Louis-Gilles, Lee Howard C., *Comparison of Time-Frequency Distribution Techniques For Analysis of Simulated Doppler Ultrasound Signals of the Femoral Artery*, IEEE Trans. Biomed. Eng., Vol.41, No.4, pp. 1176-1186, April 1994

[Hademenos, 1997] Hademenos George J., *The Biophysics of Stroke*, American Scientist [on line], May/Jun 1997, [cited 2000-09-18], http://www.amsci.org/amsci/articles/97articles/Hademenos.html

[Holdsworth *et al.*, 1999] Holdsworth D. W., Norley C. J. D., Frayne R., Steinman D. A., Rutt B. K., *Characterization of Common Carotid Artery Blood-Flow Waveforms in Normal Human Subjects*, Physiol. Meas., Vol. 20, No. 3, pp. 219-240, August 1999

[Hoskins, 2003] Hoskins P. R., Thrush A., Martin K., Whittingham T. A., *Diagnostic Ultrasound: Physics and Equipment*. Hoskins PR, Thrush A, Martin K and Whittingham TA Ed., Greenwich Medical Media Ltd, London, 2003.

[Jain, 1964] Jain K. K., *Some Observations on the Anatomy of the Middle Cerebral Artery*, Canadian Jounal of Surgery, Vol. 7, pp. 134-139, April 1964

[Jensen, 1996] Jensen Jørden Arendth, *Estimation of Blood Velocities Using Ultrasound: A Signal Processing Approach*, Great Britain, Cambridge University Press, 1996

[Jeong, Williams, 1992] Jeong J., Williams W. J., *Kernel Design for Reduced Interference Distributions*, IEEE Transactions on Signal Processing, Vol. 40, No. 2, pp. 402-412, February 1992

[Jeong, Williams, 1992a] Jeong J. and Williams W. J., *Alias-Free Generalized Discrete-Time Time-Frequency Distributions*, IEEE Transactions on Signal Processing, Vol. 40, No. 11, pp. 2757-2765, November 1992

[Jones, Giddens, 1990] Jones S. A., Giddens D. P., *A Simulation of Transit Time Effects in Doppler Ultrasound Signals*, Ultrasound in Med. & Biol., Vol. 16, No. 6, pp. 607-619, 1990

[Kay, 1988] Kay Steven M., *Modern Spectral Estimation -Theory & Application*, Prentice-Hall, New Jersey, 1988

[Kay, Marple, 1981] Kay Steven M., Marple Jr. Stanley Lawrence, *Spectrum Analysis – A Modern Perspective*, Proc. IEEE, Vol.69, No.11, pp. 1380-1417, 1981

[Kitney, Giddens, 1983] Kitney R. I., Giddens D. P., *Analysis of Blood Velocity Waveforms by Phase Shift Averaging and Autoregressive Spectral Estimation*, ASME J. Biomech. Eng., Vol. 105, No.5, pp. 398-401, November 1983

[Krejza *et al.*, 1998] Krejza Jaroslaw, Mariak Zenon, Walecki Jerzy, Szydlik Piotr, Ustymowicz Andrej, Lewko Janusz, *Age Dependency of Blood Flow Velocities in Basal Cerebral Arteries: Transcranial Color Doppler Study*, Med. Sci. Monit., Vol. 4, No. 2, pp. 370-377, March 1998

[Kristoffersen, Angelsen, 1988] Kristoffersen Kjell, Angelsen Bjørn A. J., *A Time-Shared Ultrasound Doppler Measurement and 2-D Imaging System*, IEEE Trans. Biomed. Eng., Vol. 35, No. 5, pp. 285-295, May 1998

[Krongold *et al.*, 1999] Krongold B. S., Ramchandran K., Jones D. L., *Frequency-Shift-Invariant Orthonormal Wavelet Packet Representations*, IEEE Trans. on Signal Processing, Vol. 47, No. 9, pp. 2579-25782, September 1999

[Leeuwn *et al.*, 1986] Leeuwn G., Hoeks A., Reneman R., *Simulation of Real-Time Frequency Estimators for Pulsed Doppler Systems*, Ultrasonic Imaging, Vol. 8, No.4, pp. 252-271, October 1986

[Leiria *et al.*, 1999] Leiria Ana, Madeira M. Margarida, Ruano M. Graça, *Aortic Valve Analyser: A Cost/Benefit Study*, Proc. ICSPAT99, 325.pdf, Orlando, USA, November 1999, CD-ROM

[Leiria *et al.*, 2004] Leiria Ana, Moura M. M. M., Ruano M. Graça, *Time-Variable Blood Flow Averaged Waveforms*, Proc. Controlo 2004, Vol. 2, pp. 625-629, Faro, Portugal, June 2004

[Leiria, 2000] Leiria Ana, *Estimação Espectral do Sinal Doppler Ultrasom em Válvula Aórtica,* UCEH, ADEEC, Universidade do Algarve, Portugal, PAPCC Thesis, July 1992

[Lizzi *et al.*, 1996] Lizzi F. L., Astor M., Kalisz A., Liu T., Coleman D. J., Silverman R., Ursea R., Rondeau M., *Ultrasonic Spectrum Analysis for Assays of Different Scatterer Morphologies: Theory and Very-High Frequency Clinical Results*, Proc. IEEE Ultrasonics Symposium, Vol. 2, pp. 1155-1159, San Antonio, USA, November 1996

[Madeira *et al.*, 1999a] Madeira M., Bellis S.J., Aguilar Beltran L.A., Solano González J., García Nocetti D.F., Marnane W.P., Tokhi M.O., Ruano M.G., *High-Performance Computing For Real-Time Spectral Estimation*, Control Eng. Practice, Vol.7, pp. 679-686, July 1999

[Madeira *et al.*, 1999b] Madeira M., Tokhi M.O., Ruano M., *A Time-Frequency Spectral Implementation For Real Time Biomedical Application*, Preprints of 14th World Congress of IFAC, Vol.Q, pp. 635-694, Beijing, P. R. China, July 1999

[Markus *et. al*, 1997] Markus H. S., Ackerstaff R., Babikian V., Bladin C., Droste D., Levi D. Grosset, C., Russell D., Siebler M., Tegeler C., *Intercenter Agreement in Reading Doppler Embolic Signals : A Multicenter International Study*, Stroke, Vol.28, No.7, pp. 1307-1310, July 1997

[Marple, 1987] Marple Jr. S. L., *Digital Spectral Analysis with Applications*, Prentice-Hall, 1987

[Marple, 1989] Marple Jr. S. L., *A Tutorial Overview of Modern Spectral Estimation*, Proc. IEEE ICASSP, Vol. 4, pp. 2152-2157, Glasgow, UK, May 1989

[Matos *et al.*, 2000] Matos Sérgio, Leiria Ana, Ruano M. Graça, *Blood Flow Parameters Evaluation Using Wavelets Transforms*, Proceedings of World Congress on Medical Physics and Biomedical Engineering, 4235-52803.pdf, Chicago, USA, Jul 2000, CD-ROM

[Mo, Cobbold, 1986] Mo Larry Y. L., Cobbold Richard S. C., *A Stochastic Model of the Backscattered Doppler Ultrasound From Blood*, IEEE Trans. on Biomed. Eng., Vol. 33, No. 1, pp. 20-27, January 1986

[Mo, Cobbold, 1989] Mo Larry Y. L., Cobbold Richard S. C., *A Nonstationary Signal Simulation Model for Continuous Wave and Pulsed Doppler Ultrasound*, IEEE Trans. Ultrason. Ferroelect. & Freq. Contr., Vol.36, No.5, pp. 522-530, September 1989

[Mo, Cobbold, 1992] Mo Larry Y. L., Cobbold Richard S. C., *A Unified Approach to Modelling the Backscattered Doppler Ultrasound from Blood*, IEEE Trans. on Biomed. Eng., Vol. 39, No. 5, pp. 450-461, May 1992

[Moehring, Klepper, 1994] Moehring Mark A., Klepper John R., *Pulse Doppler Ultrasound Detection, Characterisation and Size Estimation of Emboli in Flowing Blood*, IEEE Trans. Biomed. Eng., Vol. 41, No.1, pp. 35-44, January 1994

[Moura, 2004] Moura M. M. M., *Processamento em Tempo-Real de Sinais Doppler de Fluxo Sanguíneo*, Universidade do Algarve, Portugal, PhD Thesis, 2004

[Müller *et al.*, 1998] Müller Martin, Pan Xudong, Walter Paul, Klaus Schimrigk, *Variability of Velocity and Duration of Microembolic Signals Detected by Bigated Transcranial Doppler Sonography in Carotid Endarterectomy*, Eur J Ultrasound, Vol. 8, No. 1, pp. 1-6, September 1998

[Oelze, O'Brien Jr, 2004] Oelze Michael L., O'Brien Jr William D., *Defining Optimal Axial and Lateral Resolution for Estimating Scatterer Properties from Volumes using Ultrasound Backscatter*, J. Acoust. Soc. Am., Vol. 115, No. 6, pp. 3226-3234, 2004

[Proakis, Manolakis, 1988] Proakis John G., Manolakis Dimitris G., *Introduction to Digital Signal Processing*, 2nd ed., Macmillan Publishing Company, New York, 1988

[Ringelstein *et. al*, 1998] Ringelstein E. Bernd, Droste Dirk W., Babikian Viken L., Evans David H., Grosset Donald G., Kaps Manfred, Markus Hugh S., Russell David, Siebler Mario, *Consensus on Microembolus Detection by TCD*, Stroke, Vol. 29, No. 3, pp. 725-729, March 1998

[Ringelstein, Droste, 1999] Ringelstein E. Bernd, Droste Dirk W., *Microembolic Signal Criteria*, Babikian V. L., Welchser L. R. Ed., Butterworth-Heineman Medical, 2nd Ed., Boston, USA, pp. 157-166, 1999

[Roy *et al.*, 2000] Roy Emmanuel, Abraham Pierre, Montrésor Silvio, Saumet Jean-Louis, *Comparison of Time-Frequency Estimators for Peripheral Embolus Detection*, Ultrasound in Med. & Biol., Vol.26, No.3, pp. 419-423, March 1998

[Ruano *et al.*, 2003] Ruano M. Graça, Moura M. M. M., Leiria Ana, García F., Moreno E., *A Framework for Blood Flow Analysis and Research*, Proc. of EMBC2003, P3165.pdf, Cancun, Mexico, September 2003, CDROM

[Ruano, 1992] Ruano M. Graça, *Investigation of Real Time Spectral Analysis Techniques for Use with Pulsed Ultrasound Doppler Blood Flow Detectors*, UCNW, Bangor UK, PhD thesis, 1992

[Schlaikjer *et al.*, 2003] Schlaikjer M., Torp-Pedersen S., Jensen J.A., *Simulation of RF Data with Tissue Motion for Optimizing Stationary Echo Canceling Filters*, Ultrasonics, Vol. 41, No. 6, pp. 415-419, August 2003

[Serrador *et al.*, 1993] Serrador Jorge M., Picot Paul A., Rutt Brian K., Shoemaker J. Kevin, Bondar Roberta L., *MRI Measures of Middle Cerebral Artery Diameter in Conscious Humans During Simulated Orthostasis*, Stroke, Vol. 31, No. 7, pp. 1672-1678, July 2000

[Smith *et al.*, 1994] Smith J. L., Evans D. H., Fan L., Thrush A. J, Naylor A. R., *Processing Doppler Ultrasound Signals from Blood-Borne Emboli*, Ultrasound in Med. & Biol., No.20, pp. 455-462, 1994

[Smith *et al.*, 1996] Smith Julia L., Evans David H., Lingke Fan, Bell Peter R. F., Naylor A. Ross, *Differentiation Between Emboli and Artefacts Using Dual-Gated Transcranial Doppler Ultrasound*, Ultrasound in Med. & Biol., Vol. 22, No. 8, pp. 1031-1036, 1996

[Smith *et al.*, 1997] Smith Julia L., Evans David H., Naylor A. Ross, *Analysis of the Frequency Modulation Present in Doppler Ultrasound Signals May Allow Differentiation Between Particulate and Gaseous Cerebral Emboli*, Ultrasound in Med. & Biol., Vol. 26, No. 5, pp. 727-734, 1997

[Smith *et al.*, 1998] Smith Julia L., Evans David H., Bell Peter R. F., Naylor A. Ross, *Time Domain Analysis of Embolic Signals can be Used in Place of High-Resolution Wigner Analysis when Classifying Gaseous and Particulate Emboli*, Ultrasound in Med. & Biol., Vol. 24, No. 7, pp. 989-993, 1998

[Talhami, Kitney, 1988] Talhami H. E., Kitney R. I., *Maximum Likelihood Frequency Traking of the Audio Pulsed Doppler Ultrasound Signal Using a Kalman Filter*, Ultrasound in Med. & Biol., Vol.14, No. 7, pp. 500-609, 1988

[Tokhi, Hossain, 1995] Tokhi M.O., Hossain M.A., *CISC, RISC and DSP Processors in Real-Time Signal Processing and Control*, Microprocessors and Microsystems, Vol. 19, No. 5, 1995

[Wang, Fish, 1996] Wang Y., Fish P., *Comparison of Doppler Signal Analysis Techniques for Velocity Waveform, Turbulence and Vortex Measurement: A Simulation Study*, Ultrasound in Med. & Biol., Vol. 22, No. 5, pp. 635-694, 1996

[Welch, 1967] Welch Peter D., *The Use of Fast Fourier Transform For the Estimation of Power Spectra: A Method Based on Time Averaging Over Short Modified Periodograms*, IEEE Trans. Audio and Electroacoust., Vol.AU-15, pp. 70-73, 1967

[Wendling *et al.*, 1992] Wendling F., Jones S. A., Giddens D. P., *Simulation of Doppler Ultrasound Signals for a Laminar, Pulsatile, Nonuniform Flow*, Ultrasound in Med. & Biol., Vol. 18, No. 2, pp. 179-193, 1992

[Zuilen *et al.*, 1998] Zuilen Erik V. Van, Gijn Jan Van, Ackerstaff Rob G. A., *The Clinical Relevance of Cerebral Microemboli Detection by Transcranial Doppler Ultrasound*, J. Neuroimaging, Vol.8, No. 1, pp.32-36, January 1998

[Zwan *et al.*, 1993] Zwan Albert van der, Hillen Berend, Tulleken Cornelis A. F., Dujovny Manuel, *A Quantitative Investigation of the Variability of the Major Cerebral Arterial Territories*, Stoke, Vol.24, No.12, pp. 1951-1959, December 1993